Fakultät für Physik
Technische Universität München

Multi-Messenger correlation study of Fermi-LAT blazars and high-energy neutrinos observed in IceCube

Matthias Johannes Huber

Vollständiger Abdruck der von der Fakultät für Physik der Technischen Universität München zur Erlangung des akademischen Grades eines

Doktors der Naturwissenschaften (Dr. rer. nat.)

genehmigten Dissertation.

Vorsitzender:
Prof. Dr. Andreas Weiler

Prüfende der Dissertation:
1. Prof. Dr. Elisa Resconi
2. Prof. Dr. Susanne Mertens

Die Dissertation wurde am 21.07.2020 bei der Technischen Universität München eingereicht und durch die Fakultät für Physik am 25.08.2020 angenommen.

Abstract

Since their first detection more than 100 years ago, the origin of ultra high-energy cosmic-rays remains an unresolved mystery in modern physics. Not only since the measurement of an astrophysical neutrino flux in 2013 and the first observation of a potential neutrino source in 2017, is it believed that neutrinos contribute the missing piece of the cosmic-ray puzzle.

In this thesis three different studies are presented that help to improve our current understanding of the neutrino puzzle. At first, a novel approach to model atmospheric leptons by means of hadronic interaction cross-sections measured by particle accelerators is reported. Detailed knowledge of the atmospheric lepton fluxes is not only essential for the search of astrophysical neutrinos and their sources but also for the investigation of low-energy neutrino phenomena. The method presented in this work allows the access of the dominating hadronic uncertainties of conventional atmospheric muon and neutrino fluxes in a mostly model-independent way.

The second analysis concentrates on astrophysical neutrinos hiding in the bulk of atmospheric particles. In order to discover the origin of these neutrinos, the correlation between different categories of blazars detected by the *Fermi* Large Area Telescope above 10 GeV and high-energy neutrinos observed by IceCube is tested. No significant neutrino emission from any of these blazar populations was found, with the strongest correlation being observed for LBL&IBL objects at a 1.9σ level. Based on this analysis, constraints on different models of neutrino emission from GeV gamma-ray emitting blazars can be placed. While, in general, high-energy neutrino emission from GeV gamma-ray emitting blazars is not ruled out, this population of sources cannot explain the bulk of neutrinos observed in IceCube.

With no sources of high-energy neutrinos discovered after 10 years of operation time in IceCube, different strategies can be pursued in the future. In this work the prospects of neutrino point source searches are discussed on the basis of a globally combined neutrino telescope network. By means of a collaboration of all currently planned observatories, every direction of the Universe becomes observable with local improvements of the sensitivity of factors up to $\sim$ 160 compared to IceCube. Hence, a global network will not only improve the chance to observe extragalactic sources of the highest-energy neutrinos but also allow detailed studies of phenomena apparent in our galaxy.

Zusammenfassung

Seit ihrem ersten Nachweis vor mehr als 100 Jahren ist der Ursprung der ultrahochenergetischen kosmischen Strahlung ein ungelöstes Rätsel der modernen Physik. Nicht erst seit der Messung eines astrophysikalischen Neutrinoflusses im Jahr 2013 und der ersten Beobachtung einer möglichen Neutrinoquelle im Jahr 2017 glaubt man, dass Neutrinos das fehlende Stück des Puzzles der kosmischen Strahlung beisteuern könnten.

In dieser Arbeit werden drei verschiedene Studien vorgestellt, die alle dazu beitragen können, unser gegenwärtiges Verständnis des Universums zu verbessern. Zunächst wird über einen neuartigen Ansatz zur Modellierung atmosphärischer Leptonen mit Hilfe von hadronischen Wechselwirkungsquerschnitten berichtet, die mit Teilchenbeschleunigern gemessen wurden. Eine detaillierte Kenntnis der atmosphärischen Leptonenflüsse ist nicht nur für die Suche nach astrophysikalischen Neutrinos und ihren Quellen, sondern auch für die Untersuchung von niederenergetischen Neutrinophänomenen unerlässlich. Die in dieser Arbeit vorgestellte Methode erlaubt den Zugang zu den dominierenden hadronischen Unsicherheiten der konventionellen atmosphärischen Myon- und Neutrinoflüsse auf weitgehend modellunabhängige Weise.

Die zweite Analyse konzentriert sich auf astrophysikalische Neutrinos, die sich in der Masse der atmosphärischen Teilchen verstecken. Um den Ursprung dieser Neutrinos zu entdecken, wird die Korrelation zwischen verschiedenen Kategorien von Blazaren und hochenergetischen Neutrinosgetestet. Es wurde keine signifikante Neutrinoemission von keiner dieser Blazar-Populationen gefunden, wobei die stärkste Korrelation für LBL&IBL-Objekte auf einem Niveau von $1,9\sigma$ beobachtet wurde. Auf der Grundlage dieser Analyse können Einschränkungen für verschiedene Modelle der Neutrinoemission von GeV-Gammastrahlen emittierenden Blazaren vorgenommen werden. Obwohl im Allgemeinen hochenergetische Neutrinoemission von GeV-Gammastrahlen emittierenden Blazars nicht ausgeschlossen wird, kann diese Quellenpopulation den Großteil der in IceCube beobachteten Neutrinos nicht erklären.

Zuletzt werden die Perspektiven der Suche nach Neutrino-Punktquellen auf der Grundlage eines global kombinierten Neutrino-Teleskopnetzes diskutiert. Durch eine Zusammenarbeit aller derzeit geplanten Observatorien wird jede Richtung des Universums beobachtbar mit lokalen Verbesserungen der Sensitivität um Faktoren bis zu ~ 160 im Vergleich zu IceCube. Somit bietet ein globales Netzwerk nicht nur die Chance, extragalaktische Quellen der hochenergetischen Neutrinos zu beobachten, sondern auch die Möglichkeit taillierter Studien der in unserer Galaxie auftretenden Phänomene.

Contents

List of Figures

List of Tables

1 Introduction

Albeit their first observation dates back more than 100 years, the origin of high-energy cosmic-rays remains a mystery [1]. While the exclusive information provided by these particles is limited, the study of additional astrophysical messengers might shed light on this puzzle. At the site of cosmic-ray acceleration, high-energy neutrinos can be generated in hadronic processes. Other than cosmic-rays, these neutrinos are almost unaffected on their path towards the Earth. Hence the identification of astrophysical neutrino sources can be a smoking gun indication for sources of high-energy cosmic-rays.

Since the discovery of a high-energy neutrino flux in 2013 by the IceCube Collaboration [2], the search for their sources is an abide field of study. While pure neutrino observations seem to be insufficient to reveal the origin of these particles, the IceCube Collaboration found first evidence for the neutrino emission from the direction of the gamma-ray emitting blazar TXS 0506+056 by means of multi-messenger observations [3–5]. Next to neutrinos, these high-energy photons can be generated at the site of astrophysical accelerators. Correlating the information from these multiple messengers can not only enhance the potential to discover the origin of high-energy neutrinos, but can also reveal unique details of the processes apparent at the site of these astrophysical objects.

The main focus of this work is on a multi-messenger correlation study of the population of GeV gamma-ray emitting blazars observed by the *Fermi-LAT* and high-energy neutrino data measured with the IceCube neutrino telescope. To build a comprehensive analysis framework, I aim to provide all information necessary to gain insight into the complete multi-messenger picture, from cosmic-rays to astrophysical photons and neutrinos.

Next to this multi-messenger correlation study, I report a novel approach to determine the flux of atmospheric leptons employing hadronic particle cross-sections measured with man-made particle accelerators. The interpretation of high-energy neutrino observations relies on the detailed understanding of this atmospheric background dilut-

ing the astrophysical signal. Hence the report of this method is embedded within the multi-messenger framework of this work.

Ultimately I will present a novel point source sensitivity study based on a global neutrino telescope network of all currently planned and existing neutrino observatories at the end of this thesis. In the following, the structure of the thesis is highlighted briefly.

- **Chapter 2** - The major part of this chapter focuses on the currently known information about cosmic-ray particles. At the end of this chapter the role of photons and neutrinos in the context of multi-messenger astronomy is emphasized.

- **Chapter 3** - The currently most accepted acceleration mechanism of cosmic-rays, photons, and neutrinos is summarized in this chapter. Besides, active galactic nuclei and their sub-category of blazars are introduced as potential sources of these particles.

- **Chapter 4** - This chapter focuses on neutrinos as astrophysical messengers. Next to the history of neutrino astronomy at the South Pole, a brief summary of the expected neutrino signal at the Earth as well as the special role of neutrinos in the context of multi-messenger astroparticle physics is emphasized.

- **Chapter 5** - In this chapter the lepton and in particular the neutrino production in atmospheric air-showers is discussed. Initially, the modeling of these lepton fluxes by means of coupled cascade equations is introduced. Afterward, we report a novel extension of this approach. With the aid of particle accelerator measurements, the dominating uncertainties of atmospheric lepton fluxes resulting from hadronic particle interactions in the shower can be accessed for the first time.

- **Chapter 6** - The observation principle of large volume neutrino detectors is introduced in this chapter. In this context, the main focus is on the IceCube Neutrino Observatory, while the major differences to neutrino telescopes build in water, are outlined as well.

- **Chapter 7** - In this chapter, the whole structure of the neutrino point source search in IceCube is introduced. While the reconstructions of characteristic event features, as well as the event selection, are summarized in the first part, the statistical method used for this search is outlined in the second part of this chapter.

- **Chapter 8** - The correlation study between blazar populations from the 3FHL catalog and 8 years of neutrino data from IceCube is summarized in this chapter.

Next to the analysis approach and the obtained results, implications for the neutrino emission, and more generally particle generation processes from the site of these blazars are discussed.

- **Chapter 9** - In the last chapter of this thesis, prospects of point source searches of high-energy neutrinos are discussed. After a brief summary of the current status of this scientific field, the vast potential of a global neutrino telescope network is outlined.

2

Cosmic-Rays & Multi-Messenger Astronomy

In 1912 Viktor F. Hess discovered the first cosmic-rays (CRs) in a balloon experiment [1], yielding the start of a new era in the field of astronomy. CRs bombard the atmosphere of the Earth at a rate of about 1000 events per square meter per second reaching ultra-relativistic energies up to $10^{20}\,\mathrm{eV}$ [6]. In the absence of large particle accelerators, cosmic-rays were a major source of information for elementary particle physics giving rise to many discoveries such as the positron and the muon in the early 20th century and neutrino oscillations in 1998 [7–9].

Even though the highest energy cosmic-rays can still offer novel insight into fundamental processes in the field of particle physics, the major scientific interest moved the astrophysical information they carry. Although their first detection was more than 100 years ago, the origin, as well as the acceleration of cosmic-rays (in particular at the highest energies) remains a mystery.

Using the information from additional astrophysical particles could provide the missing piece to solve the puzzle of cosmic-rays. In the first part, this chapter focuses on cosmic-rays and their known characteristics. Afterward, the motivation and the principle concept of multi-messenger astronomy is introduced.

2.1 Cosmic-Rays

Cosmic-rays are ionized particles bombarding the Earth's atmosphere almost isotropically due to their deflection in astrophysical magnetic fields (Subsection 2.1.4). The by far most abundant particle species are protons ($\sim 90\,\%$), followed by helium with the rest being heavier nuclei [6]. Even though the sources of cosmic-rays are not yet identified it is clear that the bulk of them originates from within the galaxy, yet from outside our solar system [6, 10].

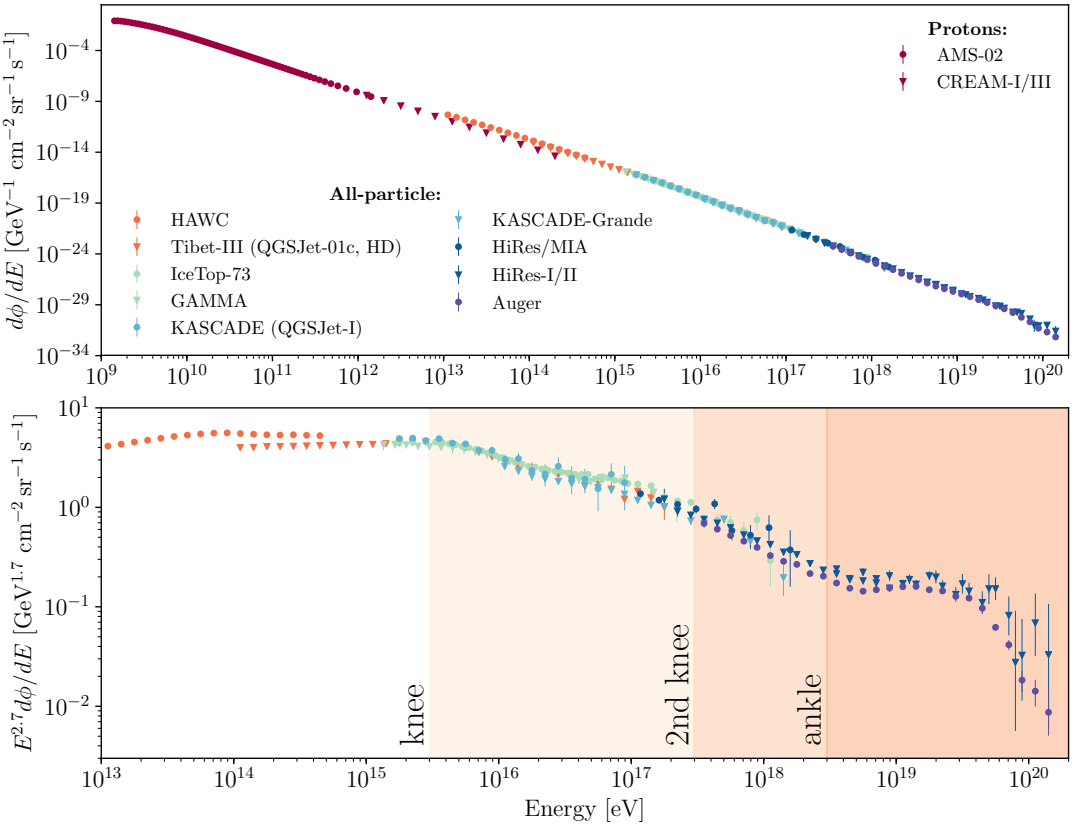

Figure 2.1: Cosmic ray flux incident at the Earth's atmosphere. The lower plot is multiplied by $E^{2.7}$ to highlight the features in the spectral distribution. The data is taken from [11–22].

2.1.1 The Observed Energy Spectrum of Cosmic Rays

The observed spectrum of cosmic-rays, illustrated in Figure 2.1, spans a vast range of energies from roughly 1 GeV to above 100 EeV. The spectrum is steeply falling with increasing energy, causing the need for different types of detector. While more than 1000 particles with energies above 10^9 eV penetrate each square meter of the upper layer of the atmosphere every second, the rate of particles above 10^{15} eV is only about 1 particle/year/m^2 [23]. The CR proton spectrum below a few hundred TeV is measured directly at the top of the atmosphere by experiments such as the space-borne experiment AMS-02 and the balloon experiment CREAM [11, 12]. Due to the low rate of high-energy CRs, large area detectors are required for their observation above $\sim 10^{14}$ eV. Hence, the all-particle spectrum above 100 TeV is measured by ground based air-shower experiments such as the Pierre-Auger or the HAWC observatory [13, 22].

At first glance, the energy spectrum of cosmic-rays appears remarkably simple, showing only few specific features. Over large orders of magnitudes the energy spectrum can be described by an inverse power-law distributions with spectral index γ according to

$$\frac{\mathrm{d}\phi}{\mathrm{d}E} \coloneqq \frac{\mathrm{d}^4 N}{\mathrm{d}E\,\mathrm{d}A\,\mathrm{d}\Omega\,\mathrm{d}t} \propto E^{-\gamma}. \tag{2.1}$$

In this way the differential cosmic-ray flux $\frac{\mathrm{d}\phi}{\mathrm{d}E}$ is defined as the number of particles N per energy E, per area A, per solid angle Ω as well as per time t. The power-law shape of the spectrum indicates that non-thermal processes are the driving mechanism to accelerate cosmic-rays to these enormous energies [6]. A more detailed understanding of this premise is subject of Chapter 3.

In the low GeV region the spectrum is locally influenced by solar modulations, with the sun being the primary source for cosmic-rays below $\sim 4\,\mathrm{GeV}$ [6, 23]. Using the simple power-law approach from above, the spectrum above 10 GeV can be divided in four main regions. Over five orders of magnitude, up to energies around 1 PeV the observed spectral index is approximately $\gamma = 2.7$. At around 3 PeV the spectrum steepens and a first transition region, known as the *knee* is visible. This region is supposed to indicate the beginning of the end of the population of galactic cosmic-rays [6]. Assuming shock acceleration of particles within astrophysical objects (Section 3.1), the particle creation in the environment of galactic supernova remnants reaches its limit close to the *knee* [6]. Moreover, the maximum energy of particles in such acceleration processes is proportional to their electric charge Z. In 1961 Peters was the first to follow up this idea, proposing that spectral features like the *knee* depend on the magnetic rigidity,

$$R \coloneqq \frac{pc}{Ze}, \tag{2.2}$$

with $pc \approx E$ being the total energy of a nucleus with charge Ze [24]. If acceleration processes reach a limit at a characteristic rigidity R_c, then this feature in the spectrum will be first visible for light particles. The maximum energy can be written as

$$E_c = Ze \cdot R_c. \tag{2.3}$$

Following this idea, spectral features like the *knee* can be interpreted as a successive cutoff of different nuclei at a characteristic rigidity R_c. The all particle spectrum from

such a particle population can be modeled by

$$\frac{\mathrm{d}\phi}{\mathrm{d}E} = \sum_i \phi_{0,i} \cdot E^{-\gamma_i} \cdot \exp\left(-\frac{E}{Z_i e R_c}\right), \tag{2.4}$$

where the summation index i represents the different groups of nuclei [25]. The association of such *Peter cycles* and the spectral shape in the region of the *knee* is supported by data from the KASCADE experiment [17].

From 10 PeV to about 1 EeV the spectrum can be explained by a spectral index $\gamma = 3.1$, before it flattens again in the second transition region [6]. This so-called *ankle* is commonly interpreted as the approaching end of galactic cosmic-ray particles and the emergence of an extragalactic contribution. This statement is supported when we consider current theories of the acceleration and propagation of cosmic-rays in the galaxy and more general in the entire Universe in Chapter 3. Above the *ankle* the spectrum softens to $\gamma = 2.6$ before it apparently cuts off at around 10^{20} eV. This cutoff could be the result of a maximal acceleration power in astrophysical environments [6, 26]. Yet, Greisen [27] and Zatsepin and Kuzmin [28] proposed an alternative explanation by realizing that photons from the cosmic microwave background (CMB) make the Universe opaque to very high energy protons due to energy losses in photo-pion production. The proton energy that is necessary for the first resonance

$$p\,\gamma_{\mathrm{CMB}} \rightarrow \Delta^+ \tag{2.5}$$

is ~ 50 EeV and thus in the order of the observed cutoff. This Greisen-Zatsepin-Kuzmin (GZK) effect is based on the assumption that protons are dominating the very high energy part of the cosmic-ray spectrum.

2.1.2 Composition of Cosmic Rays

The previous subsection introduced some basic conclusions on cosmic-ray physics that can be made from their energy spectrum. Another major source of information is the composition of cosmic-rays at different energies.

As mentioned before, direct measurement of cosmic-rays is feasible up to a few hundred TeV using satellite-borne and balloon experiments. The left panel of Figure 2.2 illustrates the relative abundance of different elements for cosmic-rays as well as the respective abundances in the solar system. Both distributions show remarkable similarities with most differences being in the range of 20-30 %. Yet, aside from the analogies, cosmic-rays show an extreme overabundance of lithium, beryllium, and boron and later

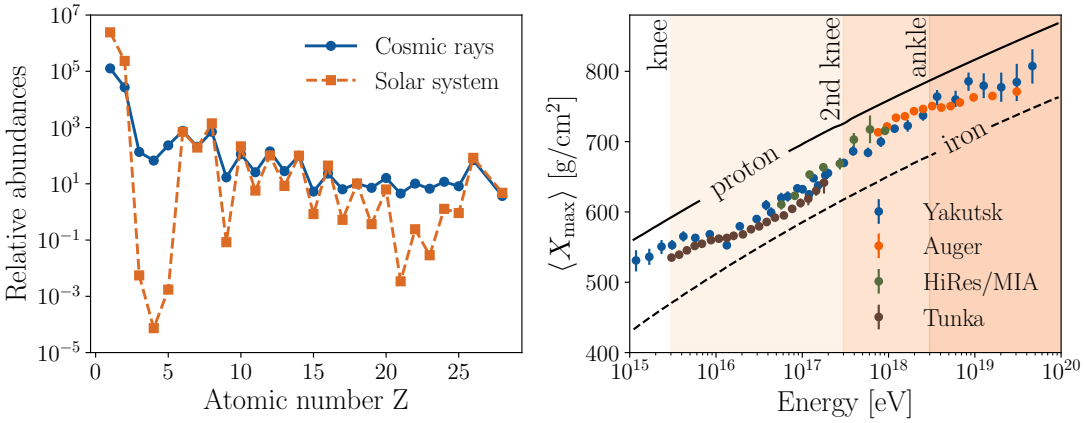

Figure 2.2: **Left:** Relative abundance of elements (represented by their nuclear charge Z) in cosmic-rays measured at $\sim 1\,\mathrm{GeV}/n$ [29]. All values are normalized with respect to silicon (Si=100). For comparison the frequency of elements in the solar system is added in a similar way [30]. **Right:** Distribution of the average shower maximum $\langle X_{\mathrm{max}} \rangle$. The solid (dashed) line illustrates the simulation of a composition of protons (iron) using the hadronic interaction model EPOSv1.99 [31]. The plot is reproduced from data shown in [32].

on also for the heavier isotopes Sc, Ti, V, Cr, and Mn. These elements are nearly absent as end-products of stellar nucleosynthesis [6]. Their overabundance can be explained as an effect of the propagation of cosmic-rays in the galaxy [23]. During the interaction of heavier elements with protons in the interstellar medium, these isotopes can be produced in so-called spallation processes. Comparing the ratio of Li, Be, and B compared to C, N, and O for both, cosmic rays and for the solar system, the average traveling distance x_{esc} of cosmic-rays in the Galaxy can be estimated. In order to compensate the absence of these elements in the solar system, cosmic-rays have to traverse on average a distance of

$$x_{\mathrm{esc}} = 10^{25}\,\mathrm{cm} = 3\,\mathrm{Mpc} \tag{2.6}$$

between production and the exit from the Galaxy [23]. This corresponds to an average escape time of $\tau_{\mathrm{esc}} = 10^7\,\mathrm{yr}$ [23]. Having a radius of around 15 kpc and a thickness of 300 pc the extent of our Galaxy is orders of magnitude smaller than the average distance traveled by cosmic-rays within this volume. Hence the propagation of cosmic-rays can be interpreted as a diffusive random walk, confining these particles within the galaxy before they can escape into the intergalactic space. Since this confinement is an effect of the galactic magnetic field, higher energy particles are less deflected and can escape

faster (Subsection 2.1.4).

In order to measure the composition of cosmic-rays above PeV energies large area air-shower experiments are necessary to compensate for the lack of cosmic-ray events. Once primary cosmic-ray particles enter the atmosphere they interact with molecules in the air initiating a cascade of particles propagating through the atmosphere with only the remnants being detected at the surface (Chapter 5). Since the primary particle is not measured directly, indirect information about the nuclear composition is used on a statistical basis. The development of a particle shower in the atmosphere depends on the mass of the primary nucleus. The cross-section for a nucleus with A particles is proportional to $A^{2/3}$ [33]. As a consequence heavier primary particles are on average supposed to interact at higher altitudes in the atmosphere, resulting in lower values for the shower maximum X_{max}[1]. In order to determine a precise correlation between the primary particle and the remnants measured at the surface a detailed understanding of all processes within the shower is essential (Chapter 5). Measurements of the mass composition of high energy cosmic-rays are highly susceptible to the theoretical uncertainties of hadronic interactions [32]. The right panel of Figure 2.2 shows the distribution of the average shower maximum $\langle X_{\mathrm{max}} \rangle$ for energies above 1 PeV. The solid line indicates the expected values for a composition purely consisting of protons, while the dashed line illustrates a scenario of cosmic-rays only being iron nuclei. While the measurements below 10 PeV do not agree well, they indicate a composition moving towards heavier nuclei from the *knee* to the *second knee*. This observation could be very well connected to a *Peters cycle* mentioned in the previous subsection. Above the *second knee* towards the *ankle* the distribution shifts towards a more proton-like composition before the average shower maximum decreases again towards the prediction of heavier primaries. Above 10^{19} eV the measurements from Yakutsk are highly susceptible to theoretical uncertainties of the hadronic interactions within the shower allowing no clear preference of neither a light nor a heavy primary mass composition [32]. Yet recent measurements from the Pierre Auger Observatory report evidence for a mixed mass composition above the *ankle* with the observations being inconsistent with a pure proton-like composition [34]. A mixed composition at the highest energies would disfavor the GZK effect being the responsible mechanism for the cutoff at 10^{20} eV (Subsection 2.1.1)

[1] X_{max} can be interpreted as the atmospheric depth with the highest particle density (Equation (5.2)).

2.1.3 Modeling the Observed Cosmic Ray Spectrum

Using both, the knowledge gained from the energy spectrum as well as the composition of cosmic-rays at different energies the spectrum can be modeled by the superposition of three main populations of cosmic-rays [35]. Up to the *knee* cosmic-rays from shock acceleration in supernova remnants represent the first component (Component A). A second galactic component of unknown origin (Component B) becomes dominant above the knee, while the highest energy particles are thought to be originating from extra-galactic acceleration environments (Component C) [25]. According to Peters each of these populations j can be modeled with single power law spectrum cutting off at a characteristic rigidity $R_{c,j}$ (Subsection 2.1.1) [24]. The total spectrum is modeled as the sum of the three populations

$$\frac{\mathrm{d}\phi_i}{\mathrm{d}E} = \sum_{j=1}^{3} \phi_0^{i,j} E^{-\gamma_{i,j}} \cdot \exp\left(-\frac{E}{Z_i R_{c,j}}\right), \tag{2.7}$$

where the subscript i indicates the respective type of the nucleus. The all-particle spectrum can be evaluated by summing up the contributions of all types of nuclei present in the cosmic-ray composition

$$\frac{\mathrm{d}\phi}{\mathrm{d}E} = \sum_i \frac{\mathrm{d}\phi_i}{\mathrm{d}E}, \tag{2.8}$$

where the nuclei are grouped into H, He, CNO, Mg-Si and Mn-Fe [25]. Two different realizations of such models are shown in Figure 2.3. The H3a model assumes a mixed composition for the third extragalactic component, while in the H4a model this population solely consists of protons [25].

2.1.4 Arrival Direction of Cosmic Rays

Due to their charge cosmic-rays are deflected by galactic and extragalactic magnetic fields on their travel through the Universe. In general the force on a particle of charge Ze, mass m and velocity v caused by a static magnetic field $\mathbf{B}$ can be written as

$$F_L = \Gamma m \frac{\mathrm{d}\mathbf{v}}{\mathrm{d}t} = \frac{Ze}{c}\mathbf{v} \times \mathbf{B}, \tag{2.9}$$

with Γ being the Lorentz factor of the particle motion. As a consequence, the particle travels in a helicoidal motion along the direction of the magnetic field [23]. The so-called

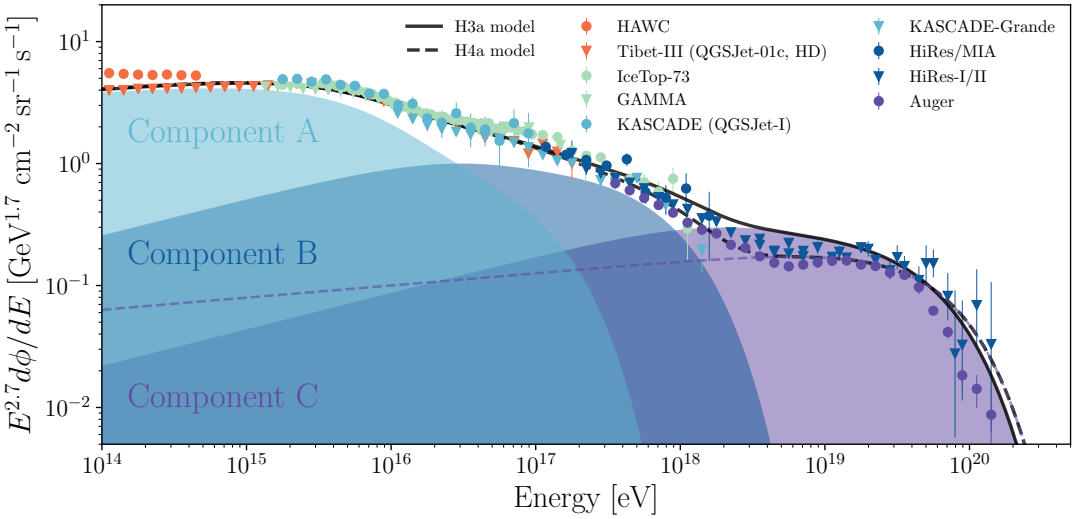

Figure 2.3: Cosmic ray models described by three populations of sources as proposed by Hillas [35]. In the H3a model the extragalactic component C is a mixture of light and heavier nuclei, while it only consists of protons in the H4a model [25]. The experimental data are taken from [11–21]. Credits to K. Krings.

Larmor radius of this circular motion is

$$r_L = \frac{pc}{ZeB} \simeq \frac{E}{ZeB}. \tag{2.10}$$

If cosmic-rays travel distances in the order of the Larmor radius, the deflection becomes a relevant bias for the directional information of their origin. The average intensity of the magnetic field in the Galaxy is $B_{Gal} \sim 4\,\mu\,\mathrm{G}$ [23]. The Larmor radius for a 1 PeV proton in the galactic magnetic field is around 0.3 pc, hence orders of magnitudes smaller than the volume of the Galaxy. Such cosmic-rays are not only confined in the galactic volume (Subsection 2.1.2) but also lose their directional information on their path towards the Earth. As implied by Equation (2.10) the deflection of cosmic-rays decreases with increasing energies. Cosmic ray protons with energies of 1 EeV have a Larmor radius of 300 pc in the order of the thickness of the galactic disk. Hence ultra-high-energy cosmic-ray particles (UHECRs) with energies greater than 1 EeV could in principle have the potential to point towards their sources if originated within the surrounding of our Galaxy or the nearby Universe. Anisotropies in the arrival direction at these energies have been studied by Pierre Auger and the Telescope Array (TA) experiment [36, 37]. Above $\sim$ 40 EeV indications for anisotropies at intermediate angular scales have been reported, yet could not be significantly verified due to the limited statistics

in this energy range [36, 38]. Lowering the threshold to 8 EeV allowed the discovery of a cosmic-ray anisotropy at a 5.2σ level [39]. Neither of the reported anisotropies did reveal any indication with an association with either the Galactic center or the Galactic plane, suggesting an extragalactic origin of these phenomena [36, 39].

2.2 Multi-Messenger Astronomy

With more than 100 EeV, cosmic-rays are by far the most energetic particles ever observed, orders of magnitude higher than particles from human-built accelerators. Even though measurements of cosmic-rays not only featured groundbreaking discoveries in particle physics but also gave insights in galactic and extragalactic phenomena, the fundamental question of their origin is still not answered. Due to the deflection in magnetic fields, cosmic-rays alone are challenging if not impossible to localize. Consequently, cosmic-ray particles alone might not provide the scientific information that is needed to resolve the mystery of their generation. The environments that are necessary to accelerate cosmic-ray particles to the highest energies potentially satisfy the requirements to generate auxiliary astrophysical messengers. In the following, we only consider three types of astrophysical messengers. Next to cosmic-ray protons and nuclei, photons (in particular gamma-rays, photons with $E >\sim$ keV) and neutrinos depict the most typical carriers of astrophysical information[2]. The research of gamma-rays and extraterrestrial high-energy neutrinos has been a large field of study during the last decades, with their respective spectra being measured over many years [40, 41]. Using the complementary information from gamma-rays and neutrinos in cooperation with cosmic-rays can provide the missing pieces to understand the origin of cosmic particles. The principle of this so-called *multi-messenger* approach is illustrated in Figure 2.4. In order to motivate these multi-messenger studies, the main features of gamma-rays and neutrinos as astrophysical messengers are shortly summarized in the next sections.

2.2.1 Gamma-Rays

Most current theories suggest that gamma-rays are either generated in leptonic processes involving interactions of high-energy electrons or in hadronic transactions of high-energy protons or heavier nuclei (Section 3.2). While none of these models is neither ruled out nor confirmed, both could potentially reveal a correlation between the generation of

[2]Note that despite being potential messengers, we do neither consider gravitational waves nor other exotic scenarios throughout this thesis.

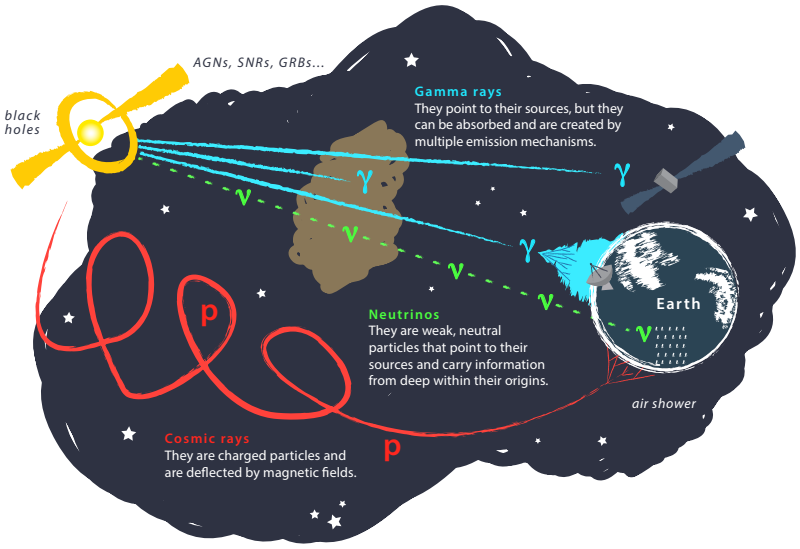

Figure 2.4: Illustration of the propagation of different messengers from an astrophysical source on their path towards the Earth. The Figure is taken from [42].

high-energy gamma-rays and the acceleration processes of high-energy cosmic-rays[3] [6].

In contrast to cosmic-rays, photons are not deflected by magnetic fields. Hence once they arrive at the Earth they directly point towards their site of generation. High energy gamma-rays are likely to interact with ambient radiation from the extragalactic background light (EBL) and the cosmic microwave background (CMB) via electron-positron pair production. The pair production interaction length (or gamma-ray attenuation length) with background radiation from the EBL and the CMB are illustrated in Figure 2.5. Starting from a few hundred GeV to approximately 100 TeV the absorption is dominated by interactions with the EBL. Above these energies radiation from the CMB become the prevalent target for attenuation. As a result of this attenuation, the observable distance of these photons is limited by their energy. The distance to the Galactic center and one of the closest blazars, Markarian 421 are also indicated in Figure 2.5. Above $\sim$ TeV energies, the observable universe is limited to our galaxy and the closest extragalactic objects with increasing opacity towards higher energies. Although the observable gamma-ray flux above a few TeV is strongly suppressed, the signal from these photons does not disappear completely. Pair-production and subsequent high-energetic leptons initiate electromagnetic cascades via inverse Compton

[3]Note that other than for neutrinos, photons can also be generated in leptonic processes which are not necessarily directly connected to high-energy cosmic-rays (Section 3.2).

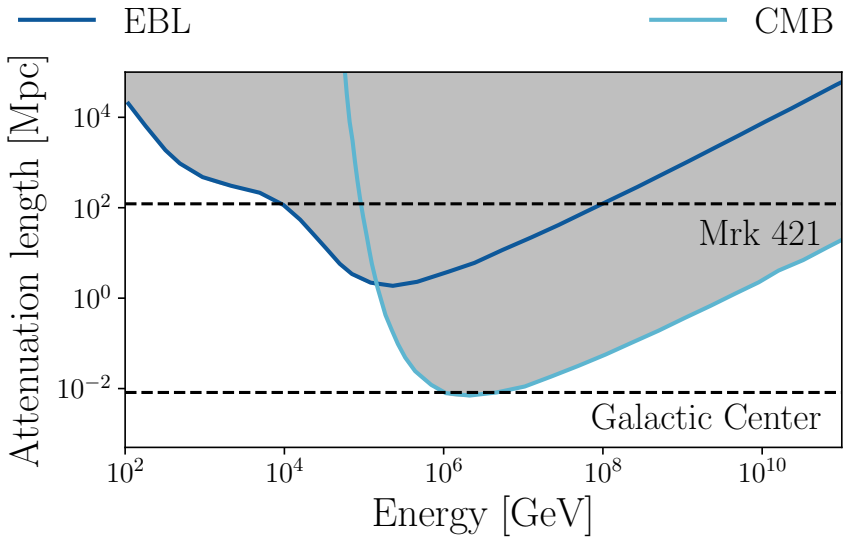

Figure 2.5: Attenuation length of gamma-rays versus their energy. The attenuation is caused by scattering with photons from the CMB and the EBL. The grey shaded area indicates the region of the Universe that is nearly opaque to photons. The data are taken from [43, 44].

scattering. The initial radiation is shifted to sub-TeV energies and complements the directly observable gamma-ray radiation in this energy region [43].

At energies from $\sim$ GeV to a few TeV a large variety of gamma-ray emitting objects are observed by means of numerous ground and space-based observatories [45]. Depending on energy range and the respective detector instrument, the location of these astrophysical objects can be determined with accuracies of less than $\sim 0.1^\circ$ [46].

2.2.2 Neutrinos

Similar to photons, neutrinos of all flavors are electrically neutral particles and hence are not deflected by magnetic fields. Their observed directions point directly back to their origin. Despite both potentially revealing the location of their origin, there are severe differences between neutrinos and photons as astrophysical messengers.

Astrophysical neutrinos are supposedly produced in the decay of charged mesons and in particular pions. The generation of these mesons requires interactions of protons or heavier nuclei with ambient protons or radiation target fields at the site of the source. In contrast to gamma-rays, neutrinos cannot be generated in purely leptonic processes[4]

[4]In principle neutrinos could be generated by decaying muons produced in pair-production processes of high-energy photons. Yet, this contribution of this effect is very sub-leading [33].

involving high-energy electrons.

A second major difference between both messengers becomes evident in the characteristics of their interactions. In the Standard Model of particle physics, neutrinos only interact weakly via the exchange of Z and W vector bosons. Due to the low cross-section of these processes neutrinos can traverse the Universe almost unimpeded. As a consequence, the observable distance of the Universe is in general not limited to neutrinos at any energy. While the low interaction cross-section of neutrinos is beneficial during the propagation, it depicts major challenges for their detection. Large volume neutrino detectors, such as the IceCube Neutrino Telescope aims to observe high-energy astrophysical neutrinos above the vastly exceeding terrestrial background. Although the flux of high-energy neutrinos has already been observed in 2013, no corresponding sources have been discovered yet.

Studying the interplay of multiple messengers from astrophysical environments can disclose detailed knowledge of on-going processes at the site of these sources. While the large statistics in gamma-ray, and generally photon observations allow detailed studies in this sector, additional information on neutrinos can help to determine the relevant generation models and access the acceleration at the highest energies that are opaque to photons. Determining a correlation with the acceleration processes of UHECRs could ultimately solve the mystery of their origin.

3

Astrophysical Particle Accelerators

In order to decode the origin of the highest energy cosmic-rays and the correlation with other astrophysical messengers, it is essential to understand the underlying generation processes. In the following two sections we will introduce the most commonly accepted theory of particle acceleration that implicates the generation of high-energy astrophysical messengers. Ultimately potential source candidates for the generation of these high-energy particles are summarized in Section 3.3.

3.1 Acceleration Mechanism

The power-law shape of the spectral distribution of cosmic-rays strongly disfavors a thermal origin of cosmic-rays[1], demanding other processes. While charged particles in most man-made accelerators gain energy in static electric fields, such electric fields are not feasible in most astrophysical environments [23]. In 1949 Fermi was the first to propose an alternative approach that could allow the generation of highly energetic particles in a stochastic process [47]. Due to *elastic* scattering with the magnetic field in moving plasma lower energetic particles can recursively gain energy. The particle spectrum resulting from this stochastic acceleration automatically follows a power-law distribution. This so-called *Fermi acceleration* mechanism will be introduced in the following section, where the logic follows the explanation as in [6].

3.1.1 Fermi Acceleration

Fermi proposed a stochastic acceleration process which allows charged particles to increase their energy by a factor of $\Delta E = \epsilon E$ in every *encounter*. In case of astrophysical objects these encounters could be depicted as *collisionless scattering* on irregularities

[1] Despite not showing any indication for a characteristics temperature scale, as expected for thermal radiation, the energies of the highest energy cosmic-ray particles are beyond the capabilities of thermal emission mechanisms [6].

within ambient moving magnetized plasma. More details on the mechanisms that can be responsible for the energy gain will follow later in this subsection. After n encounters the particle has an energy of

$$E_n = E_0 \left(1 + \epsilon\right)^n , \tag{3.1}$$

with E_0 being its initial energy. Assuming that in each step the particle has a chance P_{esc} to escape the acceleration region, the number of events with energies above E_{th} is proportional to

$$N(\geq E_{th}) \propto \sum_{m=n_{\mathrm{th}}}^{\infty} (1 - P_{\mathrm{esc}})^m = \frac{(1 - P_{\mathrm{esc}})^{n_{\mathrm{th}}}}{P_{\mathrm{esc}}}, \tag{3.2}$$

where n_{th} describes the number of encounters that are necessary for the particle to reach an energy E_{th}

$$n_{\mathrm{th}} = \ln\left(\frac{E_{th}}{E_0}\right) / \ln(1 + \epsilon). \tag{3.3}$$

Combining the last two formulas yields an expression for the number of particles directly depending on the threshold energy E_{th}

$$N(\geq E_{th}) \propto \frac{1}{P_{\mathrm{esc}}} \left(\frac{E_{th}}{E_0}\right)^{-\gamma+1}, \tag{3.4}$$

with $\gamma = 1 - \ln(1 - P_{\mathrm{esc}}) / \ln(1 + \epsilon)$. This formula nicely illustrates that the Fermi acceleration mechanism can naturally explain a power-law shape, that is observed for the spectrum of the cosmic-rays (Chapter 2.1.1).

As previously mentioned cosmic-ray particles can gain energy ΔE due to diffusion within moving magnetized plasma. For the Fermi mechanism, two different scenarios for the enhancement in energy exist. Both are schematically illustrated in Figure 3.1. In the original version proposed by Fermi (2nd order Fermi acceleration), relativistic cosmic-rays gain energy from encounters with moving clouds of plasma that are apparent within the galactic disc. Upon entering the cloud the particle coincides with the average motion of the moving gas, due to deflections caused by the magnetic fields. After leaving the cloud the particle gained an energy ΔE. Repeated collisions with magnetized clouds enable the stochastic acceleration mentioned above.

The second scenario (1st order Fermi acceleration) relies on a similar acceleration principle but caused by a different astrophysical environment. While the generation of energy is caused by independent clouds in the 2nd order Fermi mechanism, acceleration

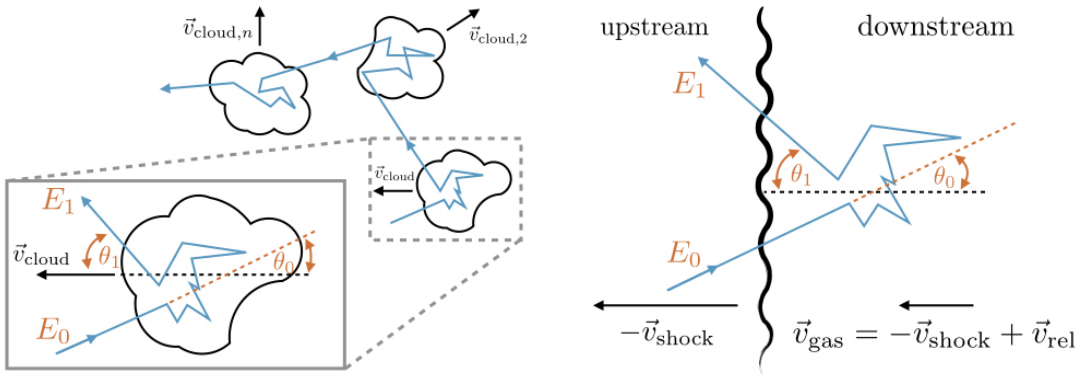

Figure 3.1: Illustration of the stochastic Fermi acceleration mechanism. **Left:** 2nd order Fermi acceleration due to collisions with moving clouds of gas. **Right:** 1st order Fermi acceleration at moving shock-front.

in this approach is caused by magnetized matter separated by an infinite plane shock-front (right panel of Figure 3.1). In this projection, the shocked gas in the *downstream* moves at the velocity $\mathbf{v}_{\text{gas}}$ with respect to the gas in front of the shock (*upstream*). Traversing the shock front back an forth yields an energy gain ΔE. In the following, we will derive the change in energy ΔE per encounter for both scenarios. Particle properties marked with an asterisk are defined in the rest frame of the magnetized cloud moving with velocity v_{cloud}, with all other properties being defined in the laboratory frame of an external observer.

If not explicitly mentioned otherwise, the following derivation is valid for both scenarios. The total energy of an incoming particle in the rest frame of the moving magnetized matter (true in both scenarios) is

$$E_0^* = \Gamma\left(E_0 - \beta p_x\right) \overset{1}{\approx} \Gamma E_0(1 - \beta\cos\theta_0) \tag{3.5}$$

where $p_x = |\mathbf{p}|\cdot\cos\theta_0$ describes the momentum of the particle along the direction of the moving magnetized matter. The Lorentz factor Γ and the velocity of the magnetized gas $\beta = \frac{|\mathbf{v}_{\text{cloud/gas}}|}{c}$ depict the parameters of the transformation from the laboratory frame of an external observer to the rest frame within the moving matter. The angles θ_0 and θ_1 are defined according to illustration in Figure 3.1. Assuming that all collisions caused by the magnetic field are elastic in the reference frame of the moving plasma, the particle can escape with the energy $E_1^* = E_0^*$. For the external observer the particle

[1] Assuming relativistic particles with $|\mathbf{p}| \gg m$, with m being the rest mass of the particle.

appears with energy

$$E_1 = \Gamma E_1^* \left[1 + \beta \cos\theta_1^*\right]. \tag{3.6}$$

According to Equation (3.1), the relative efficiency ϵ per encounter is

$$\epsilon = \frac{\Delta E}{E_0} = \frac{1 - \beta\cos\theta_0 + \beta\cos\theta_1^* - \beta^2\cos\theta_0\cos\theta_1^*}{1-\beta^2} - 1. \tag{3.7}$$

So far this derivation is valid for both scenarios. Yet, the average values for the relative efficiencies reveal significant differences. In the following all equations applying for the shock front scenario will be indicated with (1st) compared to the moving clouds (2nd). According to Equation (3.7), the average efficiency $\langle\epsilon\rangle$ depends on the angles between the particle and the moving matter at entry and exit. In case of the 2nd order Fermi mechanism, a relativistic particle can approach independent clouds of plasma either in head-on collisions or catch up the cloud of plasma moving in the same direction. The probability of a collision is proportional to the relative velocity between the particle and the cloud $p_0^{\mathrm{2nd}} = \frac{c - v_{\mathrm{cloud}}\cos\theta_0}{2c}$, yielding an expectation value for the incoming angle

$$\langle\cos\theta_0\rangle_{2nd} = \int_{-1}^{1} p_0^{\mathrm{2nd}} \cos\theta_0 \,\mathrm{d}\cos\theta_0 = -\frac{v_{\mathrm{cloud}}}{3c}. \tag{3.8}$$

On the other hand, in order to traverse the shock front into the downstream region the first order Fermi mechanism allows only head-on collision[2]. The projection of an isotropic flux in the upstream region onto the infinite plane yields an average incoming angle of

$$\langle\cos\theta_0\rangle_{1st} = \int_{-1}^{0} p_0^{\mathrm{1st}} \cos\theta_0 \,\mathrm{d}\cos\theta_0 = -\frac{2}{3}, \tag{3.9}$$

where $p_0^{\mathrm{1st}} = 2\cos\theta_0$ is the normalized probability distribution $\cos\theta_0$. In both scenarios elastic scattering in the rest frame of the magnetized matter influences the direction of the particle. In the scenario (2nd order) shown in the left panel of Figure 3.1, the particle can leave the matter distribution isotropically yielding

$$\langle\cos\theta_1^*\rangle_{2nd} = \int_{-1}^{1} \frac{1}{2}\cos\theta_1^* \,\mathrm{d}\cos\theta_1^* = 0. \tag{3.10}$$

In contrast, in the 1st order Fermi acceleration, the particle can only leave the shocked region if the outgoing angle θ_1^* projects again onto the shocked plane[1]. Consequently,

[2]Otherwise the particle would escape the acceleration region.

similar to Equation (3.9) the average outgoing angle in the shock wave scenario evaluates to

$$\langle \cos\theta_1^* \rangle_{1st} = \int_0^1 2\cos\theta_1^* \cos\theta_1^* \, \mathrm{d}\cos\theta_1^* = \frac{2}{3}. \tag{3.11}$$

Inserting these average angles in Equation (3.7) yields the average acceleration efficiency during each *encounter* for both processes

$$\langle \epsilon \rangle_{2nd} = \frac{1 + \frac{1}{3}\beta^2}{1 - \beta^2} - 1 \sim \frac{4}{3}\beta^2 \tag{3.12}$$

$$\langle \epsilon \rangle_{1st} = \frac{1 + \frac{4}{3}\beta + \frac{4}{9}\beta^2}{1 - \beta^2} - 1 \sim \frac{4}{3}\beta, \tag{3.13}$$

where the last approximation only holds if the relative velocities of the respective plasmas can be treated non-relativistically. The formulas above nicely illustrate the linear and second order dependence in the velocity β of the shock wave and the moving cloud scenario respectively. During the acceleration process in clouds the particle does not always gain but can even lose energy depending on the incoming and outgoing direction with respect to the movement of the clouds. On the other hand the shock wave scenario can be nicely visualized by a ball that is elastically bouncing between two mutually approaching trains. Similar to the ball and in contrast to the 2nd order Fermi acceleration, the particle gains energy in every *encounter* yielding on average the more effective acceleration mechanism.

3.1.2 The Power-Law Spectrum

In the previous subsection, we demonstrated that stochastic acceleration processes generate a particle spectrum following a power-law distribution. The spectral slope of the differential spectrum at the source is

$$\gamma_{\text{source}} = 1 - \ln(1 - P_{\text{esc}}) / \ln(1 + \epsilon) \sim 1 + \frac{P_{\text{esc}}}{\epsilon}. \tag{3.14}$$

This is similarly true for both scenarios of Fermi acceleration. Yet while astrophysical environments that are proposed by the second-order Fermi acceleration mechanism tend to induce very soft spectra [6], the particle acceleration induced by shock waves can recover the spectral index that is needed to describe the observed spectrum of cosmic-rays. The probability P_{esc} for particles to escape the acceleration cycle can be approximated by comparing the average rate of encounters R_{in} with the escape rate due to convection R_{out}. The former can be evaluated by the projection of an isotropic cosmic-ray flux on

the infinite plane of the shock, yielding

$$R_{\text{in}} = \int_0^{2\pi} \int_0^1 \mathrm{d}\cos\theta \, \frac{\rho_{\text{CR}} c \cos\theta}{4\pi} = \frac{\rho_{\text{CR}} c}{4}. \tag{3.15}$$

The escape rate from the downstream region is $R_{\text{out}} = \rho_{\text{CR}} \mathbf{v}_{\text{rel}}$[3], yielding

$$P_{\text{esc}} = \frac{R_{\text{out}}}{R_{\text{in}}} = \frac{4\mathbf{v}_{\text{rel}}}{c}. \tag{3.16}$$

Further making use of the kinetic energy of mono-atomic gases yields a universal expression for the spectral index

$$\gamma_{\text{source}} = 1 + \frac{3}{\mathbf{v}_{\text{shock}}/\mathbf{v}_{\text{rel}} - 1} \sim 2 + \frac{4}{M^2}, \tag{3.17}$$

where M represents the Mach number [6, 48]. The Mach number for strong shocks is $M \gg 1$, yielding a spectral distribution with $\gamma_{\text{source}} \sim 2$ for the generation of cosmic-rays at the site of the source [6]. Due to diffusion in ambient magnetic fields, the observable energy spectrum of galactic cosmic-rays is shifted with respect to the one at the site of generation. In the so-called *leaky box* model, this spectral displacement can roughly account for a factor of 0.6, yielding an expectation for the observable spectrum of

$$\gamma_{\text{obs}} \sim 2.6. \tag{3.18}$$

This is similar to what we can observe for the galactic part of the cosmic-ray spectrum (Subsection 2.1.1) [6].

3.1.3 Source Condition Criteria

The first-order Fermi mechanism is not only capable of recovering the observed spectral index. Connecting the principle of diffusive shock acceleration to Supernovas can explain the galactic component of the cosmic-ray spectrum up to the knee. Already in 1964 Ginzburg and Syrovatskii emphasized that shock acceleration of cosmic-rays in supernova explosions could be efficient enough to maintain a constant energy density in cosmic-rays [10]. The maximum energy in such supernova explosions is

$$E_{\text{SN}}^{\text{max}} \sim \frac{\mathrm{d}E}{\mathrm{d}t} \cdot T_{\text{SN}} \sim Z \cdot 300\,\text{TeV}, \tag{3.19}$$

[3] Assuming a supersonic gas flow in the rest frame of the shock, the mass flux into the shock is similar to the mass flux out, yielding $\rho_{\text{CR}} \cdot \mathbf{v}_{\text{shock}} = \rho_{\text{CR}} \cdot \mathbf{v}_{\text{rel}}$ [48].

where $\frac{\mathrm{d}E}{\mathrm{d}t}$ represents the differential energy gain in the stochastic process and T_{SN} gives the time interval during which particles are accelerated in supernova explosions [23]. Using typical values for the galactic magnetic field and the properties in supernova explosions, allows for the generation of cosmic-rays up to the region where the knee begins (Figure 2.1) [23]. Note that the maximum energy $E_{\mathrm{SN}}^{\mathrm{max}}$ depends on the atomic number Z of the particle motivating a successive cutoff in the region of the knee (Section 2.1.1).

The concept of a maximum particle energy that astrophysical objects can produce was generalized by Hillas in 1984 [26]. In order to keep a charged particle confined within the acceleration environment of size R, the Larmor radius r_L (Equation (2.10)) of the particle may not exceed R yielding a condition for the maximum energy of an object

$$E^{\mathrm{max}} = ZeBR \sim Z\beta \left(\frac{B}{\mu\,\mathrm{G}}\right)\left(\frac{R}{\mathrm{kpc}}\right) \cdot 10^{18}\,\mathrm{eV} \tag{3.20}$$

This expression allows the classification of different types of sources according to their potential to accelerate cosmic-rays to the highest energies observed. A summary of different types of sources in a so-called Hillas plot is shown in Figure 3.2. A short review of different types of astrophysical sources mentioned in this plot is given in Section 3.3.

3.2 Generation of other Messengers

The generation of high-energy cosmic-ray nuclei and electrons at the site of astrophysical objects implicates the generation of other astrophysical messengers (Section 2.2). Photons can either be produced by radiation from charged leptonic particles or in the decay of mesons and in particular pions [6]. In the second, so-called *hadronic* scenario also neutrinos will be generated in the vicinity of the source. The realization of both leptonic and hadronic generation processes of secondary particles strongly depends on the physical conditions at the site of acceleration.

Depending on the environment at the source the observed spectrum of photons could be explained by leptonic or hadronic acceleration models. On the other hand, the observation of a neutrino flux would automatically implicate the existence of hadronic generation processes. In the following, both models are shortly introduced.

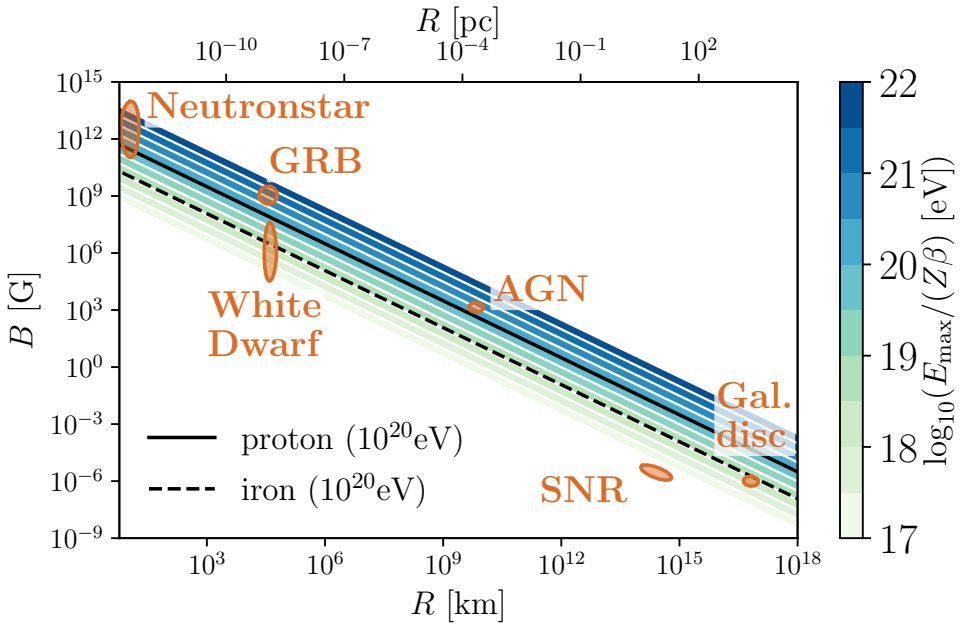

Figure 3.2: Illustration of the acceleration potential of cosmic-ray sources arranged according to their size R and ambient magnetic field strength B. Following the concept suggested by Hillas [26], the maximum particle energy that can be generated by a source depends on these quantities (Equation (3.20)). The colored lines indicate the parameter regions that provide the potential to accelerate protons ($Z = 1$) to the respective energy if $\beta = 1$. The data are adapted from [6].

3.2.1 Leptonic Model

Next to protons also cosmic-ray electrons are accelerated to relativistic energies in stochastic processes. Similar to the spectrum of protons, their spectral distribution at the source can be described by a simple power-law function with spectral index γ_e. In the presence of a magnetic field perpendicular to the motion of the electrons, photons are generated from synchrotron emission. Depending on the exact properties at the source the spectrum of these synchrotron photons peaks in the region between infrared and X-ray photons. The synchrotron radiation from protons and heavier elements is strongly suppressed with respect to radiation from electrons and can be ignored at these energies [6].

In the presence of low energy photons, the same relativistic electrons can transfer energy to these photons as a result of inverse Compton scattering. The low energy photons required for inverse Compton scattering can either be provided by the synchrotron radiation from the same population of electrons or external radiation fields.

Inverse Compton scattering can effectively generate high energy photons with a spectrum strongly depending on the spectral distribution of the parent electrons [23].

A schematic sketch of observed photons at different wavelengths from an active galactic nuclei (AGN) object (Subsection 3.3.1) is shown in the right panel of Figure 3.3. While purely leptonic models can usually describe the spectral energy distributions for such sources, the influence from hadronic generation models cannot be suspended [6].

3.2.2 Hadronic Model

While the origin of the low energy peak in the photon spectrum (e.g. Figure 3.3 for AGNs) is attributed to synchrotron radiation from accelerated electrons, the formation of the high energy bump in the photon distribution is still an open field of discussion. In hadronic models, photons are mainly generated in the decay of neutral pions, which can be either produced in interactions of protons with an ambient target of lower energetic protons or photons. Depending on the explicit environment at the site of the source either of these channels can be dominant [23]. Different to purely leptonic processes, neutrino production is possible through the decay of charged mesons which are generated likewise in interactions of high energy protons. Hence measuring neutrinos from the direction of a source would directly confirm the presence of hadronic acceleration processes.

In order to allow the generation of gamma-rays and neutrinos, the environment at the site of the source has to be transparent enough to produce the parent mesons, in a sense that the mean free path of protons needs to be smaller than the size of the object. Besides, the objects need to be smaller than the interaction length of these mesons, to allow the generation of high energy photons and neutrinos [23]. In such a scenario the generated flux of gamma-rays and neutrinos is strongly correlated to the flux of the cosmic-rays at the site of acceleration. The potential correlations between the generated neutrino flux and the flux of high-energy cosmic-rays and photons are studied in more detail in Section 4.2 and 4.3. Note that, even though the generated spectrum of these messengers is supposedly correlated, the correlation among their observed spectra is not obvious. While neutrinos can only be generated in hadronic models and arrive at the Earth without being influenced on their path, high-energy photons can be similarly generated in both models and their observable flux at high energies ($\gtrsim$ TeV) is attenuated and diluted due to pair-production with ambient background radiation in the Universe (Subsection 2.2.1). Ultimately the localization of cosmic-rays is very challenging due to their deflection in cosmic magnetic fields (Subsection 2.1.4).

It is worth noting that the production of gamma-rays and neutrinos is not limited to

the surrounding of the sources. In principle, high-energy cosmic-rays can also generate these messengers along their path in interactions with cosmic background radiation.

3.3 Candidate Sources of Cosmic Rays

Following the illustration shown in Figure 3.2 only few types of astrophysical objects posses all the ingredients to accelerate cosmic-ray particles and subsequent messengers to the highest energies that are observed at Earth.

Stochastic shock acceleration in galactic supernova remnants (SNR), resulting from explosions at the end of the evolution of stars can provide sufficient power to explain the isotropic flux of galactic cosmic rays in the region below the knee of the spectrum [6]. Nevertheless the conditions at the site of these sources do not allow the generation of cosmic-rays at the highest observed energies (Figure 3.2). According to Figure 3.2, amongst others extragalactic gamma-ray bursts (GRBs) posses the environment to accelerate cosmic-rays to energies of $10^{20}\,\mathrm{eV}$. GRBs can emerge from both the core collapse of a massive star or the merger of a binary system (e.g. neutron star - neutron star) and depict the most energetic transient objects in the Universe [6]. Disregarding the potential to generate UHECRs, no correlation between GRBs and high-energy neutrinos has been observed. As a consequence, not only their contribution to the observed high-energy neutrino flux but also to the flux of UHECRs is strongly constrained [49].

In the scope of this thesis, we want to study the neutrino emission from a different type of astrophysical sources, namely blazars, a sub-class of active galactic nuclei (AGN). Hence in the remaining part of this chapter, we will shortly introduce the relevant characteristics of AGNs and in particular blazars.

Note that similar to GRBs and AGNs, also other types of astrophysical objects might be able to produce UHECRs and subsequent messengers. Yet a description of these source types is beyond the scope of this work and the reader is relegated to other reviews for instance in [6, 23].

3.3.1 Active Galactic Nuclei

Active galactic nuclei offer different characteristics that turn them into interesting candidates for the emission of high-energy cosmic-rays. With luminosities up to $L_{\mathrm{bol}} \sim 10^{48}\,\mathrm{erg\,s^{-1}}$ they are the most powerful non-explosive objects in the Universe [50]. The observable photon emission from AGNs covers the full electromagnetic spectrum from radio to gamma-ray energies (Figure 3.3), allowing detailed studies of their properties. At the highest energies above $\sim 10\,\mathrm{GeV}$, AGNs and in particular the sub-class of blazars

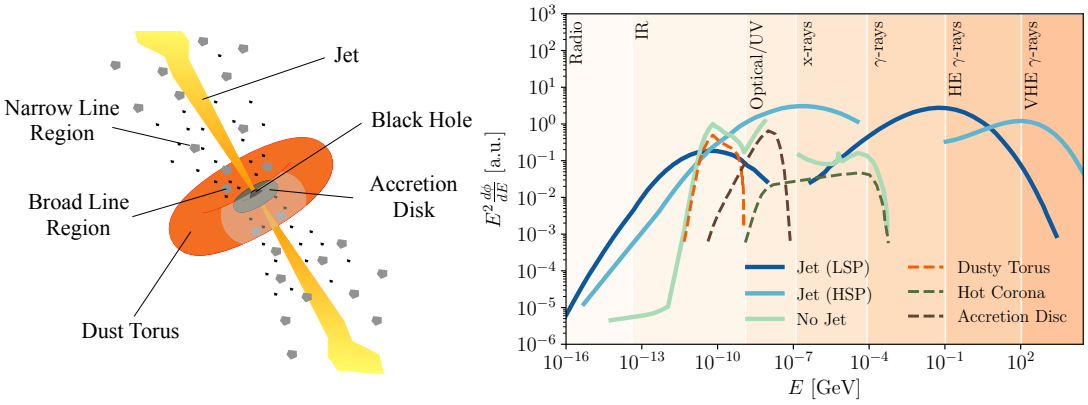

Figure 3.3: **Left:** Simplified view of the setup of AGNs. Figure adapted from [54]. **Right:** Schematic illustration of the typical spectral energy distribution for different classes of AGN. The figure is adapted from [50].

(introduced in the following subsection) dominate the observed photon emission [51, 52]. Due to the high luminosities, AGNs can be observed at far distances in the Universe, with the furthest AGN being detected at a redshift of $z \sim 7.1$ [53]. Around 1 % of all galaxies are supposed to host an AGN, making them a numerous class of astrophysical objects. At the moment roughly 10^6 AGNs are detected [50].

A sketch of a typical AGN object is illustrated in the left panel of Figure 3.3. The fundamental element common to every AGN is a spinning *supermassive black hole* (SMBH), with masses larger than 10^6 solar masses and extensions between 10^{-7} and 10^{-3} pc. The central source of energy in AGNs is caused by the accretion of particles around the SMBH and their subsequent release of gravitational energy. The accretion material is located in a thin disc around the SMBH, extending to distances of up to ~ 1 pc. The rate of the accretion flow might be connected to the launching of relativistic jets parallel to the spin axes of the central black hole. Despite being studied in great detail over many years, the physical nature of these relativistic jets is still poorly understood. Ultimately at distances from 1 to 10 pc a putative torus of dust of unknown composition surrounds the central region of the AGN [50, 55].

As previously mentioned, the observed spectral energy distribution (SED) of typical AGNs encloses many orders of magnitude in energy, ranging from radio to gamma-ray energies. Features appearing in different energy bands can be attributed to physical processes occurring in different regions of the source. Detailed studies of their characteristics at different wavelengths allow the exploration of the basic architecture of active galactic nuclei. A detailed summary of these multi-wavelength studies can be

found in [50]. In the following, we will only shortly outline the influence on the SED from different regions of the AGN. In the right panel of Figure 3.3 the typical SEDs for different types of AGN objects are illustrated.

The accretion disc surrounding the black hole in the center of every AGN generates radiation ranging from optical to low X-ray energies in the spectrum [42]. In case the the orientation of the AGN with respect to the observer at the Earth allows a direct investigation of the central region, it is possible to distinguish between optical features related to the presence of heated gas in the broad-line region between the SMBH and the inner wall of the dust torus and gas present in the narrow-line region located above the plane of the dust (left panel of Figure 3.3) [50]. The radiation from the accretion disc that is traversing the dust torus can interact with the ambient matter, with the resulting radiation shifted to the infrared (IR) regime. The details of these IR emission lines depend on both, the radiation coming from the accretion disc as well as the amount of obscuration provided by the dusty torus [50]. Inverse Compton scattering of photons from the accretion disc with the overlying atmosphere (called *corona*) is thought to be the primary process inducing the intrinsic X-ray emission of AGNs [56]. The most relevant component of AGNs for the neutrino phenomena studied in this thesis is the relativistic jet. Processes within the jet dominate the photon emission in the radio and gamma-ray band. In fact, AGNs without relativistic jets do not seem to provide the environments to produce photons at gamma-ray energies [57]. In case the orientation of the jet is aligned with the direction of an observer at the Earth, the emission from the jet can importantly contribute to every region across the SED [50].

3.3.2 Blazars

Blazars, a sub-class of active galactic nuclei hosting a relativistic jet at an angle smaller than 20° with respect to the line of sight depict one of the most promising source class for high-energy neutrinos and cosmic-rays [54, 58]. Despite intrinsically being a minority among AGN objects by definition, blazars dominate the bright radio and gamma-ray sky [59]. In fact above 50 GeV (10 GeV) these objects can explain $86^{+16}_{-14}\%$ ($42 \pm 8\%$) of the entire extragalactic background light [51, 52]. Consequently, blazars might potentially provide the environments to accelerate charged cosmic particles to the highest energies and generate high-energy neutrinos.

The photon emission from blazars typically emerges in a *double humped* shape that is strongly related to processes within the relativistic jet (Figure 3.3). While the first peak is commonly attributed to synchrotron radiation from relativistic electrons, the physical processes behind the second hump at higher energies is still unknown. In principle, both

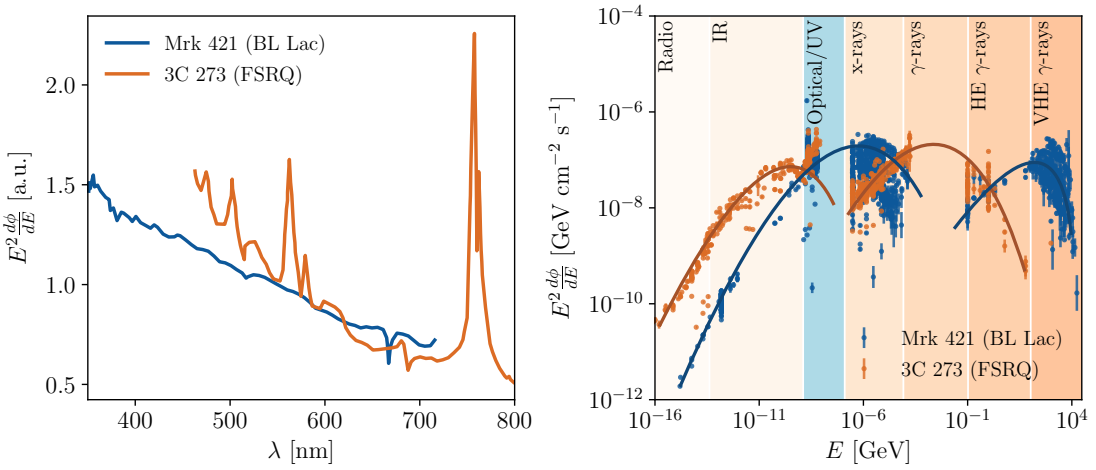

Figure 3.4: Comparison between the SED of a typical FSRQ (3C 273) and a typical BL Lac (Mrk 421). **Left:** Spectral distribution in the optical band. Figure adapted from [62], with data from [63, 64]. **Right:** Observed distribution over the entire electromagnetic spectrum, based on combined data from many space and ground-based observatories. The data have been collected by means of the SED builder tool of the ASI Science Data Center, available at `http://www.openuniverse.asi.it/`. The solid lines indicate a putative evolution of the double-humped structure connected to the relativistic jet.

leptonic and hadronic generation models within the jet could provide the gamma-ray emission typically observed for blazars (Section 3.2) [6].

According to features in their SED, blazars can be further divided into different sub-classes. Based on the location of the so-called synchrotron peak in the spectrum, blazars can be categorized into low synchrotron peaked (LSP) objects if $\nu_{\text{peak}} < 10^{14}\,\text{Hz}$ ($E_{\text{peak}} \lesssim 0.4\,\text{eV}$) or high synchrotron peaked (HSP) objects if $\nu_{\text{peak}} > 10^{15}\,\text{Hz}$ ($E_{\text{peak}} \gtrsim 4.1\,\text{eV}$). Blazars with synchrotron hump peaking in between both thresholds are designated as intermediate synchrotron peaked objects (ISP) [60, 61].

A complementary partition of blazars into Flat Spectrum Radio Quasars (FSRQ) and BL Lacs results from differences in their optical spectra. While FSRQs show broad emission lines in this energy region, BL Lac objects only display at most weak emission lines [50, 54]. The spectral energy distribution at optical wavelengths for a typical BL Lac (Mrk 421) and a typical FSRQ (3C 273) are shown in the left panel of Figure 3.4. Next to differences in the optical band that are used for the classification, FSRQ and BL Lac objects also show significant differences in their gamma-ray emission. This is again illustrated by means of the SED from the BL Lac Mrk 421 and the FSRQ 3C 273 shown in the right panel of Figure 3.4. While the latter shows a steeply falling

energy spectrum in the high energy (HE) region with almost no emission in the very high energy (VHE) band, the gamma-ray emission from the BL Lac is mostly flat in the HE region and extends to very high gamma-ray energies before dropping of [50]. Next to the major differences between FSRQs and BL Lacs, the SEDs in the right panel in Figure 3.4 both indicate another key characteristic of blazars. Blazars are found to exhibit a strong variability in their emission at different energies, with typical flares lasting from minutes to even months. The physical mechanisms behind the time variability at different energies are still unclear [50, 65].

4
Astrophysical Neutrinos

Neutrinos are electrically neutral particles interacting only through the weak force in the standard model of particle physics. The small cross-sections of neutrino interactions pose challenges for their detection, requiring large volume observatories as compensation. On the other hand these properties turn neutrinos into ideal astrophysical messengers. Having no electric charge and essentially no mass they are neither deflected by magnetic fields nor attenuated on their path towards the Earth. While photons above a few TeV are strongly attenuated in interactions with the cosmic background radiation (Subsection 2.2.1), the universe is transparent to neutrinos at these energies. Hence neutrinos can travel towards the Earth from the farthest reaches of the cosmos. The following chapter starts with a short summary of the historical evolution of neutrino astronomy at the South Pole. While no sources of astrophysical high-energy neutrinos have yet been discovered at a 5σ level, IceCube found multiple evidence for neutrino emission from the direction of the blazar TXS 0506+056 [4, 5]. The expected signal from astrophysical neutrino sources as well as the exceptional role of neutrinos in multi-messenger astronomy is discussed in Section 4.2 and 4.3. Finally the chapter concludes with a short summary of the multi-messenger observations from the direction of the blazar TXS 0506+056.

4.1 The Discovery of Astrophysical Neutrinos

High-energy neutrinos cannot be detected directly, but only through the measurement of the secondary products resulting from their interactions. In order to detect astrophysical neutrinos, large volume detectors are necessary to compensate their low interaction rate. Furthermore, these neutrino observatories have to be shielded against atmospheric neutrinos and muons showing similar signatures in the detector volume. This atmospheric background is continuously generated by particle showers induced by cosmic-rays in the atmosphere (Chapter 5). With KM3NeT in the Mediterranean sea,

GVD in Lake Baikal, P-ONE at Cascadia Basin and IceCube at the South Pole four sites with large volume neutrino telescopes are planed. While the completion of the final detector configuration is still in progress for the first three observatories, IceCube is successfully recording data by means of its complete detector configuration since 2011. In 2013 IceCube found first evidence for high-energy astrophysical neutrinos using the outer layers of the detector to shield the astrophysical signal from the atmospheric background [2]. This observation was later confirmed with the measurement of a diffuse muon neutrino flux from the Northern hemisphere [66]. While the first analysis used the outer layers of the detector to collocate an optimal sample of all-flavor neutrino events, the latter approach utilized the Earth as a natural shield against atmospheric background.

The experimental data of this, so-called through-going muon neutrino analysis from the Northern hemisphere are shown in the left panel of Figure 4.1. The conventional atmospheric flux dominates the sample up to $\sim 100\,\mathrm{TeV}$, with the fitted astrophysical component complementing the total flux above these energies. Commonly the astrophysical fluxes in IceCube analysis are presumed to follow a single unbroken power-law

$$\frac{\mathrm{d}\phi}{\mathrm{d}E} = \phi_{100} \cdot \left(\frac{E}{100\,\mathrm{TeV}}\right)^{-\gamma_{\mathrm{astro}}}, \tag{4.1}$$

although more complex models can not be ruled out yet [41]. If not clearly stated otherwise the flux values will account for the sum of neutrino and anti-neutrinos per neutrino flavor in the following.

The current flux parameters of the through-going muon neutrino as well all-flavor high-energy starting event (HESE) analysis are illustrated in the right panel of Figure 4.1. The result of a third analysis focusing on cascade-like events (Chapter 6) dominantly induced by electron and tau neutrino interactions are shown as well [67]. Despite the many differences, such as for instance the measurement signatures from different neutrino flavors, the results of all three analysis are in agreement at least within their 95 % confidence level uncertainties.

4.2 Expected Signal from Astrophysical Neutrino Sources

Although the discovery of the first high-energy astrophysical neutrinos happened already several years ago, the sources generating the collective astrophysical neutrino flux are still unidentified. The large atmospheric background in combination with the low interaction rate of neutrinos and the uncertainties of the reconstruction of their directional origin display only some of the challenges that have to be faced in order to

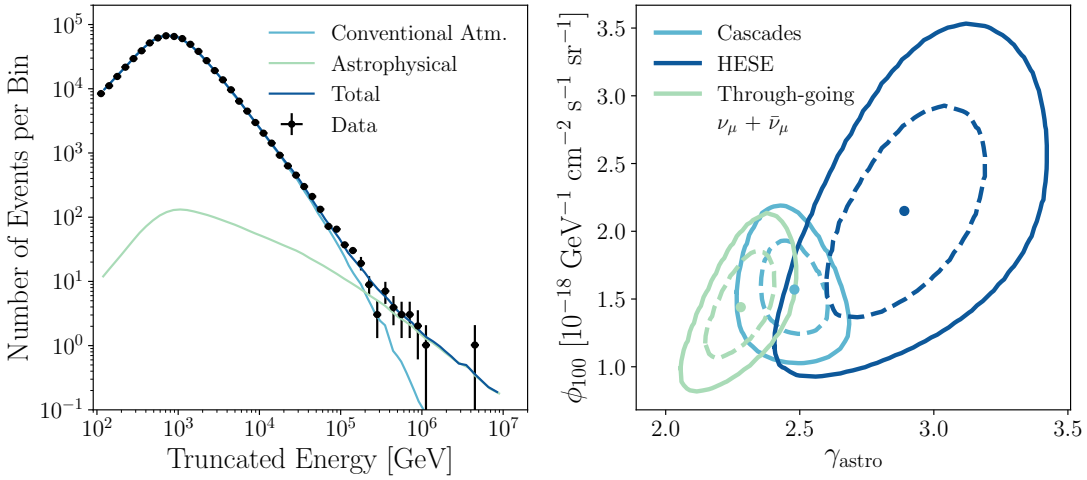

Figure 4.1: **Left:** Measured data in the through-going muon neutrino analysis compared to the MC predictions for the atmospheric background and the fitted astrophysical flux [41]. **Right:** Comparison of the best-fit likelihood contours of three complementary analysis measuring the astrophysical neutrino flux in IceCube. The dashed (solid) lines illustrate the 68 % (95 %) C.L. contours. The data are taken from [41, 67, 68].

find the sources of astrophysical neutrinos reaching the Earth.

4.2.1 Neutrino Generation in Hadronic Acceleration Models

Following the most common theories of particle acceleration in astrophysical objects, high-energy neutrinos are predominantly generated in the decay of charged mesons, with the largest contribution coming from pions

$$\pi^+ \quad \rightarrow \quad \nu_\mu + \mu^+ \quad \rightarrow \quad \nu_\mu \bar{\nu}_\mu + \nu_e + e^+ \tag{4.2}$$

$$\pi^- \quad \rightarrow \quad \bar{\nu}_\mu + \mu^- \quad \rightarrow \quad \bar{\nu}_\mu \nu_\mu + \bar{\nu}_e + e^-. \tag{4.3}$$

While in principle neutrinos could also be produced in the weak decay of neutrons or even more exotic scenarios involving non standard model physics [69], we will only focus on the *baseline* meson scenario in the following. As visible from Equation (4.3), the flavor ratio ($\nu_e : \nu_\mu : \nu_\tau$) of neutrinos from pion decay is (1 : 2 : 0) at the site of acceleration[1].

In astrophysical environments the parent mesons can only be produced in hadronic generation models (Section 3.2) involving interactions of high energy protons either

[1] Assuming that all muons can decay.

with surrounding matter or ambient photons. While meson production mostly occurs in inelastic proton proton collisions in the first case, in the latter scenario the pion production emerges through the Δ^+ resonance in photoproduction processes

$$p + \gamma \quad \rightarrow \quad \Delta^+ \quad \rightarrow \quad \pi^+ + n. \tag{4.4}$$

Although the cross-section of the proton-proton mechanism is about two orders of magnitude higher than the one for photoproduction, the probability for pion production from the latter can be dominant depending on the specific scenario at the source. The rate of pion generation in both mechanisms is proportional to the number density n_{bckg} of the respective background material. Depending on the environment surrounding the source, the photon density n_γ could be much higher than the density of non-relativistic matter n_p [6, 23].

Despite the fact that neutrinos are produced in pion decays in both scenarios mentioned above, their respective neutrino spectra can have different appearances. In principle the particle transport and generation in astrophysical accelerators can be treated similarly to the propagation of cosmic-rays in the atmosphere (Chapter 5). As mentioned above the interaction probability for both mechanisms depends on the number density of ambient target particles that are available for the interaction, yielding

$$\frac{1}{\lambda_{\mathrm{int,p}}} \propto n_{\mathrm{bckg}}, \tag{4.5}$$

where $\lambda_{\mathrm{int,p}}$ is the interaction length of protons for the respective mechanism. Assuming an idealized transparent source which is larger than $\lambda_{\mathrm{int,p}}$ but also smaller than the interaction length of pions[2], the neutrino spectrum can be approximated using Equation (5.14) and (5.18).

The proton energy threshold $E_{\mathrm{thr},p}$ for pion production in proton proton interactions is

$$E_{\mathrm{thr},p} = m_p + \frac{m_\pi \left(m_\pi + 4m_p\right)}{2m_p} \sim 1.2\,\mathrm{GeV}. \tag{4.6}$$

In principle all protons generated at the source exhibit similar interaction probability, independent of their energy. Hence the number density of the ambient target matter that is available for collisions is similarly independent of the energy of the relativistic protons. Using (5.14) and (5.18) the resulting spectrum of neutrinos will follow a power-law that is similar to generation spectrum of the primary cosmic-ray particles at the

[2] In this case the pions can on average decay before losing a fraction of their energy in interactions.

source

$$\gamma_{\nu}^{pp} \sim \gamma_{CR}. \tag{4.7}$$

Assuming stochastic Fermi shock acceleration of the parent protons (Section 3.1), the spectral index of neutrinos is supposed to follow an $\gamma_{\nu}^{pp} = 2$ spectrum in this scenario.

In contrast the energy threshold for protons in photoproduction processes inversely depends on the photon energy E_{γ}

$$E_{\mathrm{thr},p} \sim \frac{2m_p m_{\pi} + m_{\pi}^2}{4E_{\gamma}}. \tag{4.8}$$

Assuming a power-law distribution with spectral index α for the low-energy photon radiation, the number density of available photons can be expressed as $n_{\gamma} \propto \int_{E_{\mathrm{thr},\gamma}}^{\infty} E^{-\alpha} dE \propto E_{\mathrm{thr},\gamma}^{\alpha-1}$, where $E_{\mathrm{thr},\gamma}$ is the energy threshold for photons according to (4.8). As a consequence the spectral index of the emerging neutrinos is hardened by a factor of $(\alpha - 1)$ with respect to the parent cosmic-ray spectrum

$$\gamma_{\nu}^{p\gamma} \sim \gamma_{CR} - (\alpha - 1). \tag{4.9}$$

Hence while the spectral index of neutrinos from proton-proton interactions only depends on the parent proton spectrum, the neutrino spectrum induced by photoproduction processes also depends on the energy distribution of the low-energy target photons. Assuming a target photon spectrum with $\alpha = 2$ and relativistic protons from stochastic shock acceleration, the generated neutrinos will follow a hard $\gamma_{\nu}^{p\gamma} \sim 1$ power-law spectrum. Such scenarios could be realized for example in blazar jets (Subsection 3.3.2).

The average energy of a neutrino produced in photoproduction is roughly 5 % of the energy of the parent proton. This estimation is motivated by the fact that the pion carries on average 20 % of the proton energy while its energy in the decay (Equation (4.3)) is equally split between the four leptons [23]. Given an optimal astrophysical environment, the highest energy protons could produce neutrinos up to $\sim$ EeV energies [70].

4.2.2 Flavor Oscillations over Astronomical Distances

Due to their non-vanishing, diverging masses neutrinos can oscillate between their flavor eigenstates. This phenomenon becomes crucial for the understanding of the neutrino flavor composition generated at the site of astrophysical sources. During their propa-

gation towards the Earth, oscillations allow the transition between different neutrino flavors. The observable flavor ratios are modified accordingly. Using the approximation that matter induced influences are negligible [71], the effect of vacuum oscillations for neutrinos from astrophysical sources is shortly discussed in the following subsection. A more detailed summary can be found for instance in [6].

Neutrino oscillations arise from the mixing between their flavor eigenstates $|\nu_\alpha\rangle$ with $\alpha \in \{e, \mu, \tau\}$ and their mass $|\nu_j\rangle$ with $j \in \{1, 2, 3\}$. While the former eigenstates define their weak interactions with other particles in the standard model, the latter are used to describe their free propagation. The existence of a neutrino mass term in the standard model, implies a difference of these representations with both being connected according to unitary 3×3 *Pontecorvo-Maki-Nakagawa-Sakata* transformation matrix U [6, 72]

$$\begin{pmatrix} |\nu_e\rangle \\ |\nu_\mu\rangle \\ |\nu_\tau\rangle \end{pmatrix} = U \cdot \begin{pmatrix} |\nu_1\rangle \\ |\nu_2\rangle \\ |\nu_3\rangle \end{pmatrix}. \tag{4.10}$$

In this sense, flavor eigenstates can be expressed as linear combinations of mass eigenstates and vice versa. On the basis of this correlation we will evaluate the probability $P_{\alpha\beta}$ that a neutrino with original flavor α appears in flavor β after traveling a distance L. This probability can be phrased by means of the transition amplitude between both flavor eigenstates according to

$$P_{\alpha\beta} = |\langle \nu_\alpha | \nu_\beta(L) \rangle|^2. \tag{4.11}$$

In order to get an expression for $|\nu_\beta(L)\rangle$, we initially contemplate the propagation of a neutrino mass state that is characterized by the time-dependent Schrödinger equation, yielding a stationary solution in vacuum

$$|\nu_j(t)\rangle = e^{-\frac{iEt}{\hbar}} |\nu_j(0)\rangle, \tag{4.12}$$

where E is the energy of the relativistic neutrino that can be expressed as

$$E = \sqrt{p^2c^2 + m_j^2c^4} \sim pc + \frac{m_j^2c^4}{2E}. \tag{4.13}$$

The simplification on the right side of this equation makes use of the nearly vanishing magnitude of the neutrino mass m_j[3]. Combining both, the stationary solution for the

[3] Equation (4.13) uses the linear approximation of $\sqrt{1+x} \sim 1 + \frac{1}{2}x$ for small $x > 0$, which is valid due to $E \sim pc \gg m_j c^2$.

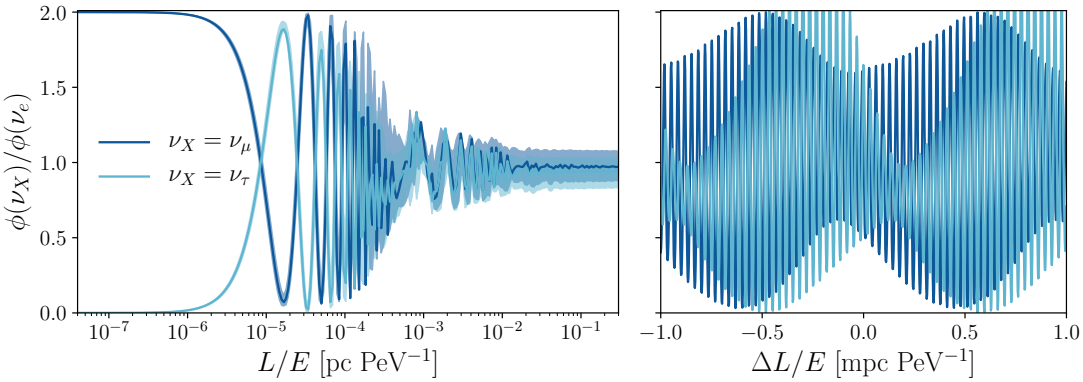

Figure 4.2: Illustration of the flavor oscillation effect for neutrinos traveling across astronomical distances. **Left:** The values on the y-axis depict the average ratio of flavor X with respect to electron neutrinos within finite but small bins in L/E (bin size $\Delta \log_{10}(L/E[\text{pc/PeV}]) \sim 0.03$). The shaded bands illustrate the deviations corresponding to the 1σ uncertainties of current oscillation parameters assuming no interior correlations. **Right:** Observable oscillation pattern from an extended region ΔL close to Mrk 421. In both panels the initial flavor composition represents the standard $(\nu_e : \nu_\mu : \nu_\tau) = (1 : 2 : 0)$ scenario resulting from pion decay (Subsection 4.2.1). The oscillation parameters and their corresponding uncertainties are taken from [73].

mass eigenstates from Equation (4.12) and (4.13) and the correlation between both eigenvector basis from Equation (4.10) yields the transition amplitude

$$\langle \nu_\alpha | \nu_\beta(L) \rangle = e^{-\frac{ipL}{\hbar}} \sum_j U^*_{\beta j} U_{\alpha j} e^{-\frac{im_j^2 c^3 L}{2E\hbar}}, \tag{4.14}$$

with $L \coloneqq ct$[4]. Ultimately the transition amplitude from Equation (4.11) evaluates to

$$\begin{aligned} P_{\alpha\beta} = &\sum_{j=1}^{3} |U_{\beta j}|^2 |U_{\alpha j}|^2 \\ &+ 2 \sum_{k>j} Re\left(U^*_{\beta j} U_{\alpha j} U_{\beta k} U^*_{\alpha k}\right) \cos\left(\frac{\Delta m^2_{kj} c^3 L}{2E\hbar}\right) \\ &+ 2 \sum_{k>j} Im\left(U^*_{\beta j} U_{\alpha j} U_{\beta k} U^*_{\alpha k}\right) \sin\left(\frac{\Delta m^2_{kj} c^3 L}{2E\hbar}\right), \end{aligned} \tag{4.15}$$

with $\Delta m^2_{kj} = m^2_k - m^2_j$. This transition probability can be utilized to estimate the

[4]The eigenvectors are by definition orthogonal, yielding $\langle \nu_j | \nu_k \rangle = \delta_{jk}$

evolution of the initial flavor composition generated at the source, according to

$$\begin{pmatrix} \phi(\nu_e) \\ \phi(\nu_\mu) \\ \phi(\nu_\tau) \end{pmatrix} = P \cdot \begin{pmatrix} \phi^0(\nu_e) \\ \phi^0(\nu_\mu) \\ \phi^0(\nu_\tau) \end{pmatrix}, \tag{4.16}$$

where P is the 3×3 matrix composed of $P_{\alpha\beta}$. The average evolution of the flavor composition from the pion decay scenario (Subsection 4.2.1) is illustrated in Figure 4.2. The oscillation pattern in the left panel shows that the observable flavor composition of neutrinos from source populations distributed at distances of more than $10^{-2}\,\mathrm{pc}$[5] matches a uniform distribution in this scenario. In fact this averaging effect arises due to a rapid increase of the oscillation frequency and for starters only applies for the cumulative signal from sources located at varying distances. In principle for point like sources located at a fixed distance L, Equation (4.16) predicts an exact flavor composition at the detector that can widely deviate from the uniform flavor mixture. Nevertheless in case the extension of the acceleration region exceeds the oscillation period, the averaged values from the left panel become valid again. The oscillation frequency for neutrinos from the distance of the blazar Mrk 421 ($\sim 120\,\mathrm{pc}$) is illustrated in the right panel of Figure 4.2. ΔL indicates the putative extension of the source. An equal number of observable neutrino flavors is expected, if the acceleration region at the site of this blazar exceeds at least a few 0.1 mpc. This is supposedly the case for blazars and in general AGN objects (Subsection 3.3.2). Since Mrk 421 is one of the closest blazars and the oscillation frequency is generally rising with increasing distance, this observation can be extended to all individual blazar sources.

More generally, the average observable flavor composition from distant astrophysical sources[6] can be approximated by taking the limit $L \to \infty$ in Equation (4.15). Both the average of the sine and cosine become zero yielding

$$P_{\alpha\beta}|_{L\to\infty} = \sum_{j=1}^{3} |U_{\beta j}|^2 |U_{\alpha j}|^2 \tag{4.17}$$

and eventually

$$P_{L\to\infty} = \begin{pmatrix} P_{ee}|_{L\to\infty} & P_{e\mu}|_{L\to\infty} & P_{e\tau}|_{L\to\infty} \\ P_{e\mu}|_{L\to\infty} & P_{\mu\mu}|_{L\to\infty} & P_{\mu\tau}|_{L\to\infty} \\ P_{e\tau}|_{L\to\infty} & P_{\mu\tau}|_{L\to\infty} & P_{\tau\tau}|_{L\to\infty} \end{pmatrix} \sim \begin{pmatrix} 0.55 & 0.24 & 0.21 \\ 0.24 & 0.38 & 0.38 \\ 0.21 & 0.38 & 0.41 \end{pmatrix}. \tag{4.18}$$

[5] For comparison, the galactic center is located roughly 8 kpc away from the Earth.
[6] If the acceleration region is larger than one oscillation period.

This transformation probability can be easily used to evaluate the observable flavor ratio for other more exotic neutrino generation scenarios. If neutron decay is the generating mechanism, only electron neutrino are produced, $(\nu_e : \nu_\mu : \nu_\tau) = (1 : 0 : 0)$. Due to the large mixing angles in the observable flux ratio at the Earth evaluates to $(\hat{\nu}_e : \hat{\nu}_\mu : \hat{\nu}_\tau) \sim (1 : 0.44 : 0.39)$ in this scenario. Similar considerations for a pure muon neutrino case at the source, yield $(\hat{\nu}_e : \hat{\nu}_\mu : \hat{\nu}_\tau) \sim (1 : 1.58 : 1.57)$.

4.2.3 Astrophysical Neutrinos at the Earth

In the previous subsections the potential properties of neutrino production induced by meson decays in astrophysical sources were introduced. In the context of such models the neutrino flux is supposed to follow a power-law distribution with a spectral index much harder then the distribution of the atmospheric background (Chapter 5). This expectation is supported by the measurements of the total astrophysical neutrino flux integrated over the whole sky shown in Figure 4.1.

Due to oscillations on the path towards the Earth a similar amount of neutrino flavors from astrophysical sources is expected at the Earth (Subsection 4.2.2). While the differentiation between electron and muon neutrinos is rather simple at higher energies, a distinct detection of τ neutrinos is more challenging in IceCube (Section 6.3). Evidence for the first two high-energy tau neutrino candidates was recently found, with both events showing indications for a unique double cascade structure [74]. The flavor ratio of high-energy neutrinos measured in IceCube within the same analysis is compatible with the expectation from meson decay scenarios [74].

In Figure 4.3 all high-energy track-like events measured in IceCube are shown [75]. These events are a composition of events from different IceCube analysis [41, 68], with the similarity that all are supposed to be high-energy muon neutrinos of non-atmospheric origin. The distribution of these events, reflects the detection properties of the IceCube detector, showing an accumulation of events around the horizon. In this region the Earth serves as a shield to absorb the atmospheric muon background, while the signal of the remaining neutrinos in the detector is optimal for the reconstruction of the most interesting event properties. The sensitivity of IceCube with respect to individual point sources is added in the background of Figure 4.3 [76].

4.3 The Role of Neutrinos in Multi-Messenger Astronomy

In currently established non-exotic models of astrophysical accelerators neutrinos can only be generated in hadronic interaction models (Subsection 4.2.1). In such scenarios

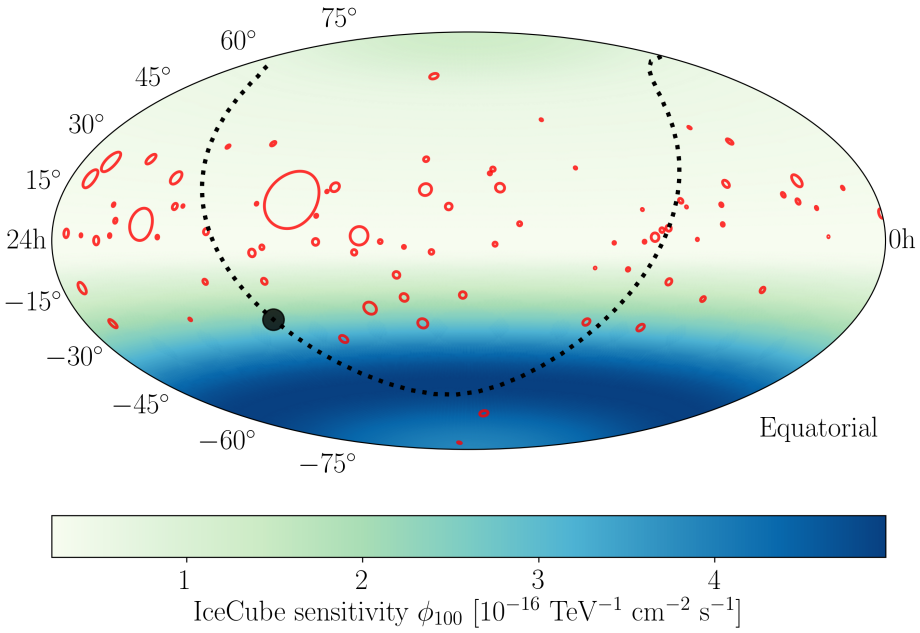

Figure 4.3: High-energy track-like events measured with the IceCube detector [75]. The red circles indicate the 90 % error contours of the events. In addition the IceCube sensitivity with respect to neutrino point sources with $\gamma_{\text{astro}} = 2$ is highlighted [76]. The black line/dot indicate the galactic plane/center.

neutrinos are predominantly produced in the decay of charged pions, which themselves can either be produced in proton-proton interactions or photoproduction processes of protons with ambient low-energy radiation. In both scenarios neutral pions are generated as well, decaying into two photons

$$\pi^0 \quad \rightarrow \quad \gamma + \gamma \tag{4.19}$$

with a branching ratio of $\sim 98\,\%$ [77]. In an idealized transparent source, all pions can decay and the generated gamma-ray flux is supposed to have a spectral shape similar to the one of neutrinos (Subsection 4.2.1).

Making use of some simple kinematics in pion decays we can find a connection between magnitudes of the resulting flux of photons and neutrinos. Neutrinos produced in the decay of charged pions (Equation (4.3)) and subsequent muons respectively obtain on average 1/4 of the energy of the parent pion [78, 79]. The total numbers of neutrinos

generated from charged pions with energies between $[E_{\pi,0}, E_{\pi,1}]$ is

$$\sum_{\alpha} \int_{E_{\pi,0}/4}^{E_{\pi,1}/4} \frac{\mathrm{d}\phi_{\nu_\alpha}}{\mathrm{d}E_\nu}\,\mathrm{d}E_\nu = 3 \int_{E_{\pi,0}}^{E_{\pi,1}} \frac{\mathrm{d}\phi_{\pi^{+(-)}}}{\mathrm{d}E_\pi}\,\mathrm{d}E_\pi\,, \tag{4.20}$$

where α indicates the summation index over all three neutrino flavors. The factor 3 on the right hand side arises from the fact that three neutrinos are produced in the decay of positively and negatively charged pions respectively (Equation (4.3)). Taking the derivative with respect to $E_{\pi,1}$ on both sides of the equation, directly yields a relation between the flux of neutrinos and pions at the source

$$\frac{1}{4}\sum_{\alpha} \frac{\mathrm{d}\phi_{\nu_\alpha}}{\mathrm{d}E_\nu}\bigg|_{E_\nu = E_{\pi,1}/4} = 3\frac{\mathrm{d}\phi_{\pi^{+(-)}}}{\mathrm{d}E_\pi}\bigg|_{E_{\pi,1}}\,. \tag{4.21}$$

The correlation between gamma-rays and neutral pions can be derived in a similar way. According to Equation (4.19) neutral pions decay into two photons, each carrying on average 1/2 of the energy of the parent pion. Hence the production rate of gamma-rays caused by neutral pions can be written as

$$\int_{E_{\pi,0}/2}^{E_{\pi,1}/2} \frac{\mathrm{d}\phi_\gamma}{\mathrm{d}E_\gamma}\,\mathrm{d}E_\gamma = 2 \int_{E_{\pi,0}}^{E_{\pi,1}} \frac{\mathrm{d}\phi_{\pi^0}}{\mathrm{d}E_\pi}\,\mathrm{d}E_\pi\,. \tag{4.22}$$

The resulting relation between the flux of gamma-rays and pions at the source is

$$\frac{1}{2}\frac{\mathrm{d}\phi_\gamma}{\mathrm{d}E_\gamma}\bigg|_{E_\gamma = E_{\pi,1}/2} = 2\frac{\mathrm{d}\phi_{\pi^0}}{\mathrm{d}E_\pi}\bigg|_{E_{\pi,1}}\,. \tag{4.23}$$

In order to connect the flux of neutrinos directly to one of pionic gamma-rays, the relative production rate $K_\pi = (N_{\pi^+} + N_{\pi^-})/N_{\pi^0}$ of charged pions with respect to their neutral counterparts is mandatory. While neutral and charged pions are approximately produced in similar amounts in photoproduction processes ($K_\pi(p\gamma) = 1$), all three charges are generated in equal numbers in interactions of protons with surrounding matter, yielding $K_\pi(pp) = 2$ [79]. Using these relative production rates, Equation (4.21) and (4.23) can be combined to obtain a direct relation between neutrino and gamma-ray production from pion decays

$$\sum_{\alpha} \frac{\mathrm{d}\phi_{\nu_\alpha}}{\mathrm{d}E_\nu}\bigg|_{E_\nu} = 3K_\pi \frac{\mathrm{d}\phi_\gamma}{\mathrm{d}E_\gamma}\bigg|_{E_\gamma = 2E_\nu}\,. \tag{4.24}$$

This powerful relation can be used to set limits on the neutrino production from astro-

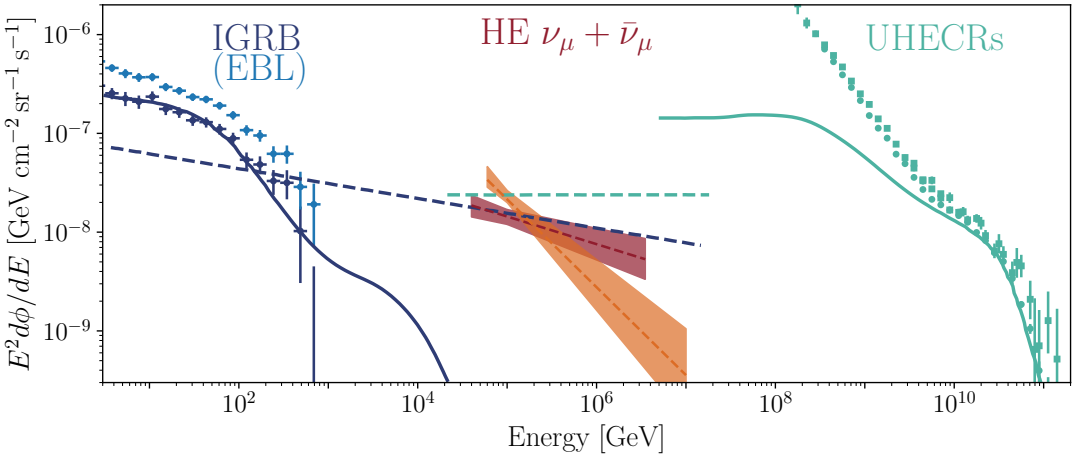

Figure 4.4: Observed spectral energy distribution of gamma-rays, high-energy neutrinos and UHECRs. The extragalactic background light above 100 MeV as well as the relative fraction of isotropic gamma-rays is measured by the Fermi-LAT [40]. The respective muon neutrino flux determined by the through-going muon neutrino (red) as well as the HESE (orange) analysis are illustrated [41, 68]. Finally also measurement of the ultra-high-energy cosmic-ray spectrum detected by the Pierre Auger collaboration (dots) and the HIRes experiment (square) are shown [19, 22]. The general idea of this plot and the corresponding fits are adapted from [79] and outlined in the text.

physical sources from their gamma-ray observations alone, without needing any particular reference to the production of cosmic-rays [79]. Similarly the fraction of gamma-rays produced by meson decay in astrophysical sources can be determined by neutrino flux measurements. In [79], the authors applied the relation from (4.24) to set a limit on the total neutrino flux connected to the isotropic gamma-ray background (IGRB) measured by the Fermi space telescope [40]. Assuming that the total diffuse gamma-ray background is induced by photons from the decay of neutral mesons within optically transparent sources[7], a maximally possible neutrino flux from the same population can be estimated according to Equation (4.24). While neutrinos can travel towards the Earth without sensing any deflection or absorption effects, gamma-rays above $\sim 100\,\mathrm{GeV}$ are strongly attenuated due to interactions with cosmic background radiation (Subsection 2.2.1). This effect is included in the calculation of the neutrino limit. In Figure 4.4 the spectral energy distribution of gamma-rays, neutrinos and high energy cosmic-rays measured at Earth are summarized. The dashed blue line illustrates the limit on the neutrino flux connected to the isotropic gamma-ray background in a pure proton-proton scenario.

[7] If the source is not transparent for high-energy photons, the correlation between between gamma-rays and neutrinos is diluted and becomes non-trivial.

Interestingly this bound resides in a similar order of magnitude as the astrophysical flux measurements in IceCube (Section 4.1). The neutrino flux from the through-going muon neutrino analysis nearly saturates this limit over the entire energy range, while the measured flux from the high-energy starting events (HESE) even exceeds the limit at lower energies. The neutrino limit from the isotropic gamma-ray background could be easily extended to the total extragalactic background light including also the gamma-ray flux from resolved sources. Since most of the high-energy photon flux can be explained by resolved sources this limit would clearly overshoot the current neutrino observations. Hence this relation between the high-energy EBL and IceCube neutrinos suggests that a significant contribution to the extragalactic gamma-ray background can be attributed to purely leptonic gamma-rays (Section 3.2). It is worth to note that these relations between observable high-energy gamma-rays and neutrinos only apply if the site of generation at the sources is transparent for high-energy photons. In fact in most putative acceleration environments high-energy photons can be absorbed by ambient radiation fields (e.g. the same radiation that serves as target for their acceleration in photohadronic processes), while neutrinos can escape unnoticed. The observable correlation between both messengers is non-trivial and can strongly deviate from their coherent generation (Equation (4.24)). Nevertheless while gamma-ray observations can hardly be used to constrain the putative amount of astrophysical neutrinos in such scenarios, neutrino observations can be utilized to constrain the maximal amount of hadronically produced gamma-rays. Correlating the observations of both messengers could reveal novel insights in the production mechanisms of astrophysical source populations.

Similar to gamma-ray observations, the measured flux of ultra high-energy cosmic-rays can be used to set limits on the total production rate of astrophysical neutrinos. Under the assumption that the sources of ultra high-energy cosmic-rays are cosmologically distributed, one can derive a locally constant production rate of these high energy protons above $1 \times 10^{19}\,\mathrm{eV}$ from the observed cosmic ray spectrum [80]. Assuming that all of these protons efficiently produce pions which subsequently decay into neutrinos results in a model-independent upper limit on the observed neutrino flux [81]. The authors in [79] compared this so-called *Waxman-Bahcall* limit to the total astrophysical neutrino flux measured with the IceCube detector (Figure 4.4). As visible the measured neutrino data do not contradict, yet approach this upper bound. This suggests that there might also be a connection between the sources of ultra-high-energy cosmic-rays and IceCube neutrinos.

Similar to the correlation to high-energy neutrinos, the observed spectrum of UHECRs can be correlated to gamma-ray measurements. While blazars dominate the gamma-ray flux above GeV energies [51, 52], a purely pionic origin of the high-energy

gamma-ray flux caused within their jets contradicts the Waxman-Bahcall bound [81]. This discrepancy could be resolved if some fraction of the high-energy emission of photons is instead induced by inverse-Compton scattering of relativistic electrons within the jet (Section 3.2). Neutrinos could be the smoking gun to determine this fraction and establish a possible connection between the three types of messengers.

4.4 First Evidence for an Extragalactic Neutrino Source

On 22. September 2017, the IceCube collaboration detected a neutrino event (IceCube-170922A) with a most-likely neutrino energy of $\sim 290\,\mathrm{TeV}$[8]. Despite not being remarkably interesting within the sample of observed high-energy neutrinos alone, it gave rise to a set of novel multi-messenger observations. As part of its *Realtime Alert System* [82], IceCube sent out an automated notification to a multitude of multi-messenger observatories[9] within less than a minute from the detection. Within one week of the observation of IceCube-170922A, the *Fermi-LAT* Collaboration reported an enhanced gamma-ray emission from the blazar TXS 0506+056 during the time of the neutrino alert. This blazar is located roughly 0.1° from the fitted direction of IceCube-170922A, while clearly being within the 50 % spatial uncertainty region of the neutrino. The region of the sky around the neutrino alert is illustrated in the left panel of Figure 4.5. The high gamma-ray emission during the time of the alert that was reported by *Fermi-LAT* was confirmed by further follow-up studies performed by for instance with the Major Atmospheric Gamma Imaging Cherenkov (MAGIC) telescope. An a posteriori probability construction revealed that the chance coincidence to find a high-energy neutrino in spatial and time coincidence with the gamma-ray flare of TXS 0506+056 can be rejected at a 3σ level [4].

The multi-messenger observations during the time of the alert initiated the investigation of the existing 9.5 years of archival neutrino data from the direction of TXS 0506+056. Although the time integrated neutrino emission prior to IceCube-170922A did not indicate a statistically significant neutrino emission, a neutrino flare was observed between September 2014 and March 2015 at a $\sim 3.5\sigma$ level. Both, the multi-messenger observations during the time of the neutrino alert as well as the neutrino flare during 2014 and 2015 suggest that the blazar TXS 0506+056 might indeed be a source of high-energy astrophysical neutrinos [5]. Since the 5σ threshold that is required to

[8] Assuming that the spectrum of the corresponding source follows a power-law with $\gamma = 2.13$, which is the best-fit spectrum of the astrophysical muon neutrino flux from the Northern Hemisphere at the time of the alert [66].

[9] And in particular a broad range of multi-wavelength telescopes for photons.

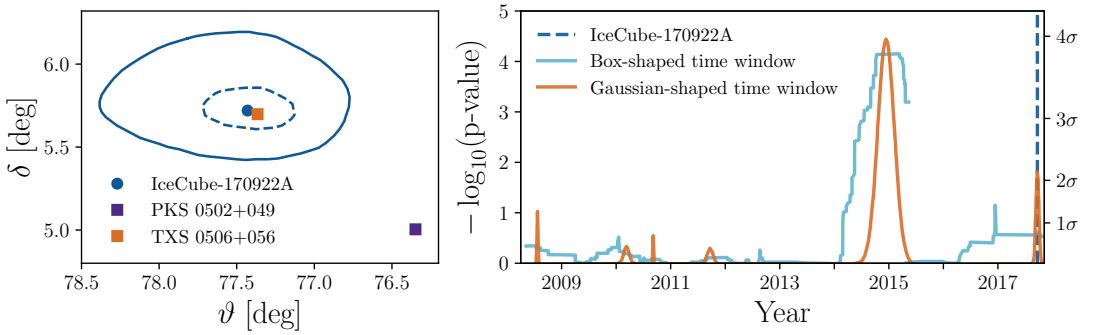

Figure 4.5: **Left:** Illustration of the region around the neutrino alert IceCube-170922A. The lines illustrate the 50 % (dashed) and 90 % (solid) containment region resulting from the directional reconstruction. The data are taken from [4]. **Right:** P-value distribution for the time-dependent neutrino emission from the direction of TXS 0506+056. The data are taken from [5].

claim a discovery in neutrino astroparticle-physics is not attained in neither of the studies, the blazar TXS 0506+056 is not officially the first confirmed source of high-energy neutrinos. Nevertheless from now on it is entitled as the first source showing strong evidence for the emission of high-energy neutrinos.

While the observations described in this section clearly indicate evidence for the neutrino emission from position of TXS 0506+056, it is not obvious to combine all the information into one coherent picture. In fact, while the neutrino alert in 2017 was accompanied by an associated gamma-ray flare, no gamma-ray enhancement from TXS 0506+056 was seen during the period of the neutrino flare. In addition to the missing gamma-ray increment from TXS 0506+056, the nearby blazar PKS0502+049 (left panel in Figure 4.5) was found in a gamma-ray flaring state in the period between 2014 and 2015. In order to shed light on the underlying physics, the authors in [75] performed a detailed dissection in space, energy and time of the region around neutrino alert. They found that TXS 0506+056 dominates the observable photon emission in this region at all gamma-ray energies. During the period between 2014 and 2015, PKS0502+049 contaminates the gamma-ray emission at lower energies. At energies above a few GeV the gamma-ray emission from PKS0502+049 drops and the contribution from TXS 0506+056 becomes prevalent. In fact, data from the *Fermi-LAT* suggest that the average spectral index for the gamma-ray emission from TXS 0506+056 above $\sim 2\,\mathrm{GeV}$ is in a very hard state during that time, indicating the putative contribution from a hadronic flare. The SEDs of TXS0506+056 and the observed neutrino fluxes during both time periods are illustrated in Figure 4.6. As expected for lepto-hadronic generation models (Section 3.2) [84], the high-energy gamma-ray and neutrino fluxes reside at a similar

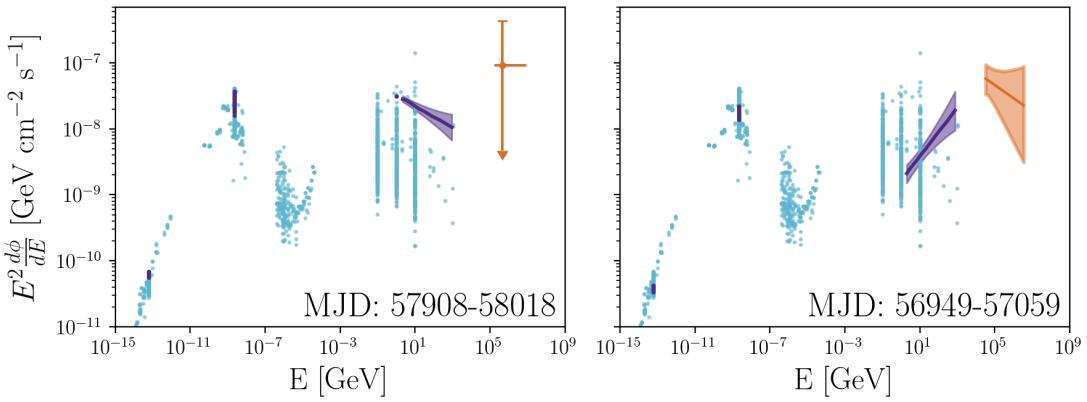

Figure 4.6: Hybrid photon neutrino SED during different time windows (MJD). The purple points/lines show the photon emission simultaneous with the high-energy neutrino flux (orange dots/lines). The purple line/band represents a fit to the gamma-ray data from the *Fermi-LAT*. In order to allow a proper comparison to the neutrino data, the gamma-ray data were de-absorbed to correct for attenuation with cosmic background radiation (Subsection 2.2.1) [83]. **Left:** Time period during the neutrino alert: June 4-September 22, 2017. **Right:** Time period during neutrino flare: October 19, 2014 - February 6, 2015. The data for both plots is taken from [4, 5, 75].

level during both time periods. In summary, these observations made in [75] support a coherent picture in which TXS 0506+056 is the only source of the neutrino emission in this region. In order to further investigate the underlying generation mechanism in such sources, more multi-messenger observations are mandatory in the future.

5

Cosmic Ray Showers in the Atmosphere

Cosmic rays entering the atmosphere interact with nuclei in the air initializing an avalanche of secondary particles cascading down to the surface of the Earth. In this process, the primary hadron can either interact with nuclei producing a sub-cascade at lower energies or decay into leptons or other hadrons. A schematic sketch of a particle cascade induced by one primary cosmic-ray is illustrated in Figure 5.1.

Measurements of secondary leptons with large area ground-based detectors can give insight on the properties of the primary cosmic ray particle that started the cascade. Moreover, atmospheric leptons can be utilized as signal to extract information about neutrino oscillations, the neutrino mass hierarchy, and further low-energy phenomena [85, 86]. On the other hand, cosmic-ray air showers induce background for other astrophysical messengers such as neutrinos. Atmospheric muons and neutrinos constitute the major background for astrophysical measurements with large volume neutrino detectors.

Both purposes, knowledge about the primary cosmic ray as well as a proper description of the fluxes coming from secondary particles require detailed knowledge about the physics occurring within the cascade. The transport of secondary particles towards the surface is influenced by decays, interactions, and continuous energy losses. Using this simple principle, the expansion of fluxes of secondary particles can be modeled by coupled cascade equations [6]. This semi-analytical approach, as well as a brief summary of the characteristics of atmospheric muons and neutrinos, are introduced in the first two sections of this chapter.

Since lepton fluxes at the surface of the Earth depend on interaction and decay properties of all particles involved in the cascade as well as properties of the surrounding atmosphere, theoretical estimates of these fluxes suffer from all deviations from the actual physical properties. In particular, the interactions of hadrons with ambient air molecules constitute a major source of systematic uncertainties. In the context of

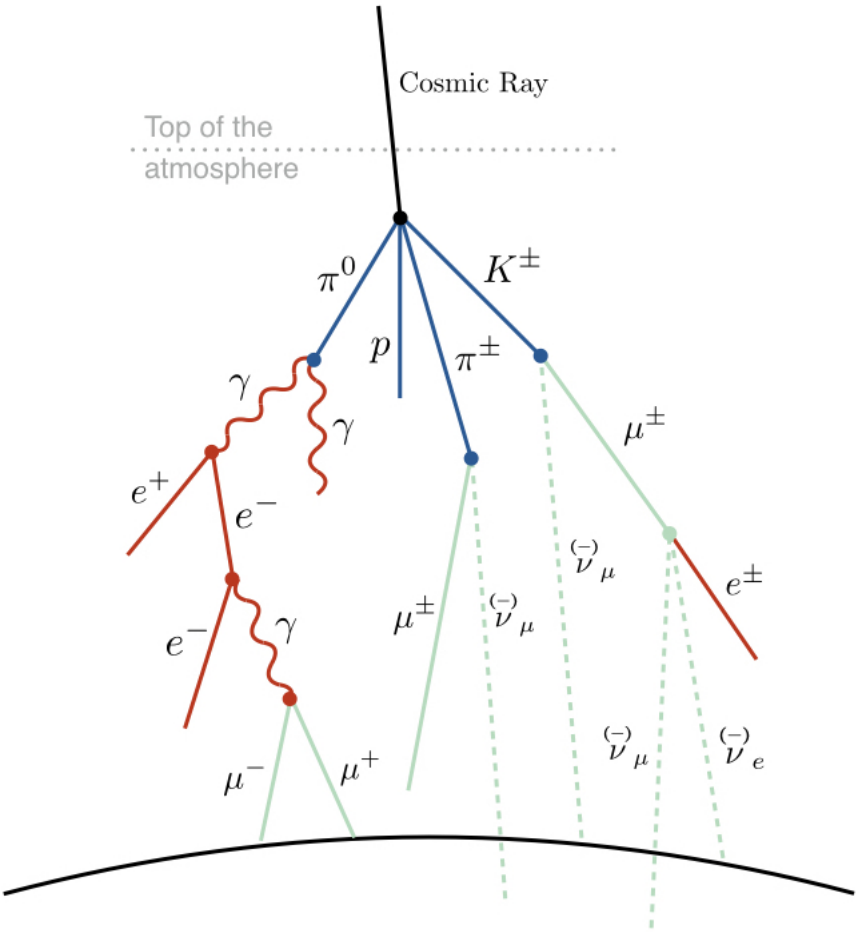

Figure 5.1: Schematic illustration of a cosmic ray air shower.

particle cascades induced by relativistic cosmic-rays, the interactions of hadrons with small momentum transfer with respect to the shower axis become most relevant. Due to the large coupling constant, ordinary perturbation theories can not be applied for these processes [87]. Hence the majority of the currently present theoretical models attempt to describe hadronic interactions based on phenomenological arguments.

While experimental data of soft hadronic collisions above TeV energies are not accessible with current man-built particle accelerators, measurements of certain particle interactions exist at energies of hundreds of GeV and below. These data can be used to test and tune the theoretical models at lower energies. On the other hand these measurements can also be used directly to describe the hadronic interactions within atmospheric air showers. Section 5.3 gives a short summary of the most dominant sources of uncertainties in atmospheric cascades. Moreover, a maximally model-independent treatment

of hadronic interactions based on experimental measurements is proposed and the results are shown. The chapter concludes with a discussion of the current status and prospects of the determination of the accuracy and consequently the uncertainties of atmospheric lepton fluxes.

5.1 Modeling of Cosmic Ray Air Showers

Cosmic-rays in the atmosphere trigger a cascade of particles that propagate towards the Earth. On this path, particles can either interact with nuclei in the air, decay, or suffer constant energy losses. In a straight forward approach, the flux of secondary particles can be estimated by means of Monte Carlo simulations, propagating each individual particle generated within the cascade. Yet, particle showers induced by high-energy cosmic-rays contain billions of particles making full Monte Carlo simulations very time and storage consuming.

Instead of using full simulations of the particle cascade, a set of coupled cascade equations can be used to describe the development of the average particle fluxes in the cascade [6]. This semi-analytic approach is not only beneficial in terms of memory consumption but also allows the calculation of secondary fluxes at the surface of the Earth within the order of seconds [88]. Different to full air shower simulations, this methodology enables detailed studies of different parameters influencing the development of the cascade. The following section will briefly introduce the concept of coupled cascade equations to describe the particle evolution caused by cosmic-ray particles in the atmosphere.

5.1.1 Coupled Cascade Equations

In the following the differential flux of particles of type h is defined as

$$\phi_h = \frac{\mathrm{d}N_h}{\mathrm{d}E\,\mathrm{d}A\,\mathrm{d}\Omega\,\mathrm{d}t}, \tag{5.1}$$

where N is the number of particles per unit area A, per solid angle Ω, per time t and energy E. Since the propagation of particles depends on the properties of the surrounding matter it is convenient to write the evolution of particles in terms of the slant depth variable

$$X(l_{\mathrm{Obs}}) = \int_0^{l_{\mathrm{Obs}}} \rho_{\mathrm{atm}}(l)\,\mathrm{d}l\,, \tag{5.2}$$

representing the history of the geometric trajectory l through the atmosphere with density $\rho_{\mathrm{atm}}(l)$. Following these conventions the linear evolution of the flux of type h particles in the atmosphere can be described by

$$\begin{aligned}
\frac{\mathrm{d}\phi_h(E,X)}{\mathrm{d}X} = &- \frac{\phi_h(E,X)}{\lambda_{\mathrm{int},h}(E)} && (a)\\
&- \frac{\phi_h(E,X)}{\lambda_{\mathrm{dec},h}(E)} && (b)\\
&+ \sum_k \int_E^\infty \mathrm{d}E_k \, \frac{\mathrm{d}N^{\mathrm{int}}_{k(E_k)\to h(E)}}{\mathrm{d}E} \frac{\phi_k(E_k,X)}{\lambda_{\mathrm{int},k}(E_k)} && (c)\\
&+ \sum_k \int_E^\infty \mathrm{d}E_k \, \frac{\mathrm{d}N^{\mathrm{dec}}_{k(E_k)\to h(E)}}{\mathrm{d}E} \frac{\phi_k(E_k,X)}{\lambda_{\mathrm{dec},k}(E_k)} && (d)\\
&- \frac{\partial}{\partial E}\left(\mu(E)\phi_h(E,X)\right). && (e) \qquad (5.3)
\end{aligned}$$

Both terms, (a) and (b) represent *loss* terms due to interactions with nuclei in the air as well as particle decays. While the interaction lengths λ_{int} only vary slowly with energy, the decay lengths λ_{dec} change by orders of magnitude over the energy range interesting for cosmic-ray physics. This energy dependence of λ_{dec} causes some challenges in the numerical approach of solving the cascade equations from above [88].

The source terms (c) and (d) describe the *gain* in flux due to interactions and decays of additional particles creating particles of type h with energy E. The summation index k in both terms embraces all particles present in the air shower. The second part of the integrand defines the flux of particles k with energy E_k that interact (or decay respectively) at a depth X, while the first component describes the average number of particles h and energy E that are created by interactions (or decays) of a particle k with energy E_k. The lower bound on the integral illustrates the fact that only particles k with energies $E_k \geq E$ can generate particles h with energy E. The last term (e) accounts for continuous energy losses such as ionization and radiative losses, with $\mu(E)$ defining the stopping power of the respective effect [6].

It is worth noting at this point that despite the many positive aspects like the low time and memory consumptions the cascade equation formalism also shows some downsides compared to full Monte Carlo simulations. In Equation (5.3) all generated particles are forced to propagate along the direction of the primary particle, completely ignoring any transverse dispersion of the cascade. Since such so-called 3D effects are sub-dominant for energies above a few GeV, the outcome of the cascade equations is still valid above these energies. Next to ignoring the transverse spread of the particle shower, cascade

equations only propagate average fluxes of particles. Applications that require the full distribution around the mean values rely on details from Monte Carlo simulations.

5.1.2 Analytic Solutions and Feynman Scaling

In order to get some basic insight into the methodology of cascade equations, a simplified example of nucleon, meson, and neutrino propagation will be introduced in the following subsection. In order to have a simplified notation, we will restrict the incoming flux of cosmic rays to consist of protons only. The extension to a more complex composition can be carried out in a straight forward way.

Nucleons in the Atmosphere

Assuming that the initial flux of protons follows a simple power-law distribution

$$\phi_p(E, X) = \phi_0(X) \cdot E^{-\gamma}, \tag{5.4}$$

with a flux normalisation $\phi_0(X = 0) = \phi_0$, the resulting flux of protons after traversing a thin atmospheric target with thickness $\mathrm{d}X$ can be written as

$$\frac{\mathrm{d}\phi_p(E, X)}{\mathrm{d}X} = -\frac{\phi_p(E, X)}{\lambda_{\mathrm{int},p}(E)} + \int_E^\infty \mathrm{d}E_p \, \frac{\mathrm{d}N^{\mathrm{int}}_{p(E_p)\to p(E)}}{\mathrm{d}E} \frac{\phi_p(E_p, X)}{\lambda_{\mathrm{int},p}(E_p)}. \tag{5.5}$$

Here we presume that protons are only produced in interactions of protons with nuclei in the air.

In the following we will use some basic assumptions to further simplify this equation. Since the interaction cross section of protons with nuclei in the air varies only very slowly with energy we will presume it to be constant in energy $\lambda_{\mathrm{int},p}(E) \sim \lambda_{\mathrm{int},p}$. In 1969 Richard Feynman proposed that the interaction yield of a particle h with energy E_h from particles k with energy E_k is independent of the absolute energies of both particles but only depends on the ratio [89]

$$x_{\mathrm{Lab}} = \frac{E_h}{E_k}, \tag{5.6}$$

where the subscript indicates that this variable is based on variables defined in the laboratory frame of an external observer. This so-called *Feynman scaling* is an important and powerful assumption that allows the description of hadronic interactions even for the highest primary energies E_k in phenomenologically motivated interaction models.

The respective interaction yields from Equation (5.5) simplify to

$$\frac{\mathrm{d}N^{\mathrm{int}}_{k(E_k)\to h(E_h)}}{\mathrm{d}E_h} = \frac{\mathrm{d}N^{\mathrm{int}}_{k\to h}(x_{\mathrm{Lab}})}{\mathrm{d}x_{\mathrm{Lab}}} \cdot \frac{x_{\mathrm{Lab}}}{E_h}. \tag{5.7}$$

Using the *Ansatz* from Equation (5.4) and the assumptions from above, the proton flux in Equation (5.5) can be simplified to

$$\begin{aligned}
\frac{\mathrm{d}\phi_p(E,X)}{\mathrm{d}X} &= \frac{\phi_0(X)}{\lambda_{\mathrm{int},p}(E)} \left[-E^{-\gamma} + \int_E^\infty \mathrm{d}E_p \, \frac{\mathrm{d}N^{\mathrm{int}}_{p(E_p)\to p(E)}}{\mathrm{d}E} \cdot E_p^\gamma \right] \\
&= -\frac{\phi_0(X) E^{-\gamma}}{\lambda_{\mathrm{int},p}(E)} \left[1 - \int_0^1 \mathrm{d}x_{\mathrm{Lab}} \, \frac{\mathrm{d}N^{\mathrm{int}}_{p\to p}}{\mathrm{d}x_{\mathrm{Lab}}} \cdot x_{\mathrm{Lab}}^{\gamma-1} \right] \\
&= -\frac{\phi_0(X) E^{-\gamma}}{\lambda_{\mathrm{int},p}(E)} \left[1 - Z_{pp} \right],
\end{aligned} \tag{5.8}$$

where Z_{pp} characterizes the *spectrum-weighted moment* of inclusive proton production caused by a spectrum of primary protons [6]. Since this depicts a linear differential equation of first order for the normalisation $\phi_0(X)$, a solution for the propagated proton flux can be written as

$$\phi_p(E,X) = \phi_0 \exp\left(-\frac{X}{\lambda_{\mathrm{int},p}}(1 - Z_{pp}) \right) \cdot E^{-\gamma} = \phi_0 \exp\left(-\frac{X}{\Lambda_p} \right) \cdot E^{-\gamma}, \tag{5.9}$$

with $\Lambda_p \coloneqq \lambda_{\mathrm{int},p}/(1 - Z_{pp})$. From this solution, we can conclude that the flux of protons, and even more generally the flux of all nucleons follows the same spectral shape as injected from the primary cosmic rays.

Although this simplified view on the propagation of protons in the atmosphere ignores the energy dependence of interaction length, changing properties in the atmosphere as well as other little details, it is a nice example of how easy a solution for the average particle fluxes in cosmic ray showers can be calculated. It is worth noting, that this solution for nucleons is not restricted to the atmosphere but is valid for all environments with energy independent interaction lengths and primary spectra that allow the factorization *ansatz* used in Equation (5.4).

Mesons in the Atmosphere

The vast majority of atmospheric leptons are produced in the decay of charged mesons. Analytic expressions for the flux of these secondary mesons in the atmosphere can be evaluated nearly similar to the flux of nucleons above. Different to nucleons we assume that mesons are not only produced in interactions of nucleons but also in collision of

higher energetic mesons. Moreover the suppression of the meson flux is caused by interactions as well as decays. For simplicity we will derive the atmospheric flux for charged pions only(indicated as π) whereas the general formalism is valid for all other mesons as well. Analogous to the protons, the cascade equation for charged pions in the atmosphere can be written as

$$\begin{aligned}\frac{\mathrm{d}\phi_\pi(E,X)}{\mathrm{d}X} &= -\frac{\phi_\pi(E,X)}{\lambda_{\mathrm{int},\pi}} - \frac{\phi_\pi(E,X)}{\lambda_{\mathrm{dec},\pi}(E)} + \frac{\phi_p(E,X)}{\lambda_{\mathrm{int},p}} Z_{p\pi} + \frac{\phi_\pi(E,X)}{\lambda_{\mathrm{int},\pi}} Z_{\pi\pi} \\ &= -\phi_\pi(E,X)\left[\frac{1}{\Lambda_\pi} + \frac{\epsilon_\pi}{EX\cos(\theta)}\right] + \frac{\phi_p(E,X)}{\lambda_{\mathrm{int},p}} Z_{p\pi}. \end{aligned} \tag{5.10}$$

In the last step the decay length is approximated with $\lambda_{\mathrm{dec},\pi}(E,X) \sim \frac{EX\cos(\theta)}{\epsilon_\pi}$, where ϵ_π is the characteristic pion decay constant and θ the incoming zenith angle[1] of the primary cosmic-ray [23, 77]. Using the solution for protons from Equation (5.9), the cascade equation for pions can be analytically solved for two extreme cases [23].

In the high energy limit, where $E \gg \epsilon_\pi$, the effect of pion decays becomes irrelevant and the formula from above reduces to

$$\left.\frac{\mathrm{d}\phi_\pi(E,X)}{\mathrm{d}X}\right|_{E\gg\epsilon_\pi} = -\phi_\pi(E,X)\frac{1}{\Lambda_\pi} + \frac{Z_{p\pi}}{\lambda_{\mathrm{int},p}}\phi_0 \exp\left(-\frac{X}{\Lambda_p}\right)\cdot E^{-\gamma}. \tag{5.11}$$

Using some algebra and the fact that pions are not part of the primary cosmic radiation yields

$$\phi_\pi(E,X)|_{E\gg\epsilon_\pi} = \phi_0 \frac{Z_{p\pi}}{1-Z_{pp}} \frac{\Lambda_\pi}{\Lambda_p - \Lambda_\pi}\left[\exp\left(-\frac{X}{\Lambda_\pi}\right) - \exp\left(-\frac{X}{\Lambda_p}\right)\right]\cdot E^{-\gamma}. \tag{5.12}$$

As a consequence the flux of atmospheric mesons in this high-energy limit can be factorized in a depth dependent and an energy dependent part, with the latter following the same spectral shape as the atmospheric nucleons and hence also the original cosmic-rays.

Similar to the high-energy case, Equation (5.10) can be solved in the low-energy limit with $E \ll \epsilon_\pi$. In contrary to the high-energy case, the decay of pions becomes dominant while the impact of their interactions can be ignored. Hence Equation (5.10) reduces to

$$\left.\frac{\mathrm{d}\phi_\pi(E,X)}{\mathrm{d}X}\right|_{E\ll\epsilon_\pi} = -\phi_\pi(E,X)\frac{\epsilon_\pi}{EX\cos(\theta)} + \frac{Z_{p\pi}}{\lambda_{\mathrm{int},p}}\phi_0 \exp\left(-\frac{X}{\Lambda_p}\right)\cdot E^{-\gamma}. \tag{5.13}$$

[1] The zenith angle represent the angular difference between the direction of the primary particle and the axis perpendicular to the Earth's surface.

The resulting pion flux in this low-energy limit is

$$\phi_\pi(E,X)|_{E\ll\epsilon_\pi} = \left[\frac{Z_{p\pi}}{\lambda_{\mathrm{int},p}}\exp\left(-\frac{X}{\Lambda_p}\right)X\right]\frac{\phi_0\cos(\theta)}{\epsilon_\pi}\cdot E^{-\gamma+1}. \tag{5.14}$$

Similar to before, the pion flux can be factorized in a depth and an energy dependent term. While the flux in the high-energy limit follows the same spectral index as the original cosmic-rays, the spectral index in the low-energy limit is one power harder.

Muons and Neutrinos from Charged Meson Decays

Finally, also an analytic solution for atmospheric leptons can be evaluated based on the outcomes above. In the following we will exemplary show an analytic approximation for atmospheric muons caused by pion decay. Neutrinos can be treated in a mostly similar way. According to Equation (5.3), the flux of muons caused by the decay of pions can be written as

$$\frac{\mathrm{d}\phi_\mu(E,X)}{\mathrm{d}X} = -\frac{\phi_\mu(E,X)}{\lambda_{\mathrm{int},\mu}(E)} - \frac{\phi_\mu(E,X)}{\lambda_{\mathrm{dec},\mu}(E)} + \int_E^\infty \mathrm{d}E_\pi \frac{\mathrm{d}N^{\mathrm{dec}}_{\pi(E_\pi)\to\mu(E)}}{\mathrm{d}E}\frac{\phi_\pi(E_\pi,X)}{\lambda_{\mathrm{dec},\pi}(E_\pi)}. \tag{5.15}$$

Note that this of course only results in the total muon flux if the decay of pions is the only or at least dominating process generating muons. The relative contribution from kaons or heavier mesons can be evaluated in similar way. Since the interactions and constant energy losses of muons only contribute a minor correction, we will neglect the first term in Equation (5.15) in the following. Charged pions almost exclusively decay into a muon and a muon neutrino pair [77], with the larger fraction of energy being transferred to the muon. Disregarding some kinematic effects that are caused by the relativistic progression of the pion, the decay yield in Equation (5.15) can be represented by a delta function

$$\frac{\mathrm{d}N^{\mathrm{dec}}_{\pi(E_\pi)\to\mu(E)}}{\mathrm{d}E} \approx \delta\left(a_\mu E_\pi - E\right), \tag{5.16}$$

where the factor a_μ describes the fraction of the pion energy that is transmitted to the muon.

A 10 GeV muon can travel on average $\sim$ 62 km through the atmosphere before it decays. Hence considering only muons that are relevant for IceCube we can roughly approximate this equation by neglecting the muon decay term. Inserting all the as-

sumptions mentioned mentioned in Equation (5.15), yields

$$\frac{\mathrm{d}\phi_\mu(E,X)}{\mathrm{d}X} \approx \frac{\phi_\pi(E/a_\mu,X)}{\lambda_{\mathrm{dec},\pi}(E/a_\mu)} = \frac{\phi_\pi(E/a_\mu,X)\cdot\epsilon_\pi}{X\cos(\theta)E/a_\mu}. \tag{5.17}$$

Hence the spectral shape of the pionic part of the muon flux is about one power softer than the original pion flux. In the previous subsection we have calculated analytic approximations for the atmospheric pion flux for two extreme cases. In the energy region where the meson decay dominates over their interactions, the spectral slope of the atmospheric muons is supposed to follow the cosmic ray spectrum

$$\phi_\mu(E,X)|_{E\ll\epsilon_\pi} \propto E^{-\gamma}. \tag{5.18}$$

On the other hand, in the region where meson interactions with air molecules outweigh the effect of their decays the spectrum is proportional to

$$\phi_\mu(E,X)|_{E\gg\epsilon_\pi} \propto E^{-(\gamma+1)}. \tag{5.19}$$

A mostly similar derivation can be made for atmospheric neutrinos. Nevertheless as noted above, this is a very simplified view on the generation of muons and neutrinos since their generation is reduced to the decay of a single particle species. Nevertheless, despite this fact and the usage of further approximations this outcome can give a first hint on the spectral shape of muons and neutrinos in particular in the energy ranges where the respective mesons dominate the leptonic production. In order to get a proper distribution for atmospheric leptons, all relevant production and decay channels have to be considered. A numerical cascade equation based solver involving multiple particle species will be presented in the following subsection.

5.1.3 Numerical Implementation

In order to solve Equation (5.3) simultaneously for multiple particle species, a set of these cascade equations can be structured in a matrix differential equation defined on a discrete energy grid. This functionality is implemented in a code called *Matrix Cascade Equations* (MCEq), handling ~ 70 hadron and lepton species [88]. Using this numerical cascade equation solver, particle fluxes from cosmic ray air showers can be calculated within less than 1 s.

The following subsection gives a brief summary of the implementation used in MCEq. A more detailed explanation can be found in [88]. In order to numerically solve Equation (5.3), MCEq uses a discrete energy grid in logarithmic scale having N bins in total.

Making the transition to a discrete formalism, Equation (5.3) evolves to

$$\begin{aligned}\frac{\mathrm{d}\phi^h_{E_i}}{\mathrm{d}X} =& -\frac{\phi^h_{E_i}}{\lambda_{\mathrm{int},h}(E_i)} + \sum_k \sum_{E_k \geq E_i}^{E_N} \frac{c_{k(E_k)\to h(E_i)}}{\lambda_{\mathrm{int},k}(E_k)} \phi^k_{E_k} \\ & - \frac{\phi^h_{E_i}}{\lambda_{\mathrm{dec},h}(E_i, X)} + \sum_k \sum_{E_k \geq E_i}^{E_N} \frac{d_{k(E_k)\to h(E_i)}}{\lambda_{\mathrm{dec},k}(E_k, X)} \phi^k_{E_k},\end{aligned} \tag{5.20}$$

where the secondary particle distributions from interactions and decays are described by

$$c_{k(E_j)\to h(E_i)} = \Delta E_j \frac{\mathrm{d}N^{\mathrm{int}}_{k(E_j)\to h(E_i)}}{\mathrm{d}E_i} \tag{5.21}$$

and

$$d_{k(E_j)\to h(E_i)} = \Delta E_j \frac{\mathrm{d}N^{\mathrm{dec}}_{k(E_j)\to h(E_i)}}{\mathrm{d}E_i} \tag{5.22}$$

respectively.

Structuring all relevant quantities of Equation (5.20) in a smart way as vectors and matrices allows the formulation of one matrix differential equation accounting for all particles at once. In this sense, the fluxes of all particles involved in the cascade are listed in one global flux vector

$$\boldsymbol{\Phi} \coloneqq \begin{pmatrix} \phi^p & \phi^n & \phi^{\pi^+} \cdots \end{pmatrix}^T, \tag{5.23}$$

with

$$\phi_{\mathbf{h}} \coloneqq \begin{pmatrix} \phi^h_{E_0} & \phi^h_{E_1} \cdots \phi^h_{E_N} \end{pmatrix}^T, \tag{5.24}$$

being the flux vector of a particle h discretized on the energy grid defined above. Hence the dimension d_ϕ of this flux vector is the product of the total number of particles and the size of the energy grid N. Similar to the particle fluxes the interaction and decay coefficients can be summarized in one $d_\phi \times d_\phi$ matrix. The full interaction matrix is

$$C_{d_\phi \times d_\phi} \coloneqq \begin{pmatrix} \boldsymbol{C}_{p\to p} & \boldsymbol{C}_{n\to p} & \boldsymbol{C}_{\pi^+\to p} & \cdots \\ \boldsymbol{C}_{p\to n} & \boldsymbol{C}_{n\to n} & \boldsymbol{C}_{\pi^+\to n} & \cdots \\ \boldsymbol{C}_{p\to \pi^+} & \boldsymbol{C}_{n\to \pi^+} & \boldsymbol{C}_{\pi^+\to \pi^+} & \cdots \\ \vdots & \vdots & \vdots & \ddots \end{pmatrix}. \tag{5.25}$$

The $N \times N$ sub-matrices contain the secondary particle distribution coefficients describing the production of a particle h in interactions of particles k. Evaluated on the same energy grid these matrices can be written as

$$C_{k\to h} \coloneqq \begin{pmatrix} c_{k(E_0)\to h(E_0)} & \cdots & c_{k(E_N)\to h(E_0)} \\ & & c_{k(E_N)\to h(E_1)} \\ & \ddots & \vdots \\ 0 & & c_{k(E_N)\to h(E_N)} \end{pmatrix}. \tag{5.26}$$

The decay coefficients are arranged similarly in the decay matrix $D_{d_\phi \times d_\phi}$. Finally the energy dependent interaction and decay lengths of all particles are arranged respectively in diagonal matrices, with the first being defined as

$$\mathbf{\Lambda}^{\text{int}}_{d_\phi \times d_\phi} \coloneqq \text{diag}\left[\frac{1}{\lambda_{\text{int},p}(E_0)}, \cdots, \frac{1}{\lambda_{\text{int},p}(E_N)}, \frac{1}{\lambda_{\text{int},n}(E_0)}, \cdots, \frac{1}{\lambda_{\text{int},n}(E_N)} \cdots\right]. \tag{5.27}$$

For the decay length a factorization *ansatz* is used to separate the dependencies on the energy and the density in the atmosphere. Hence the decay length of a particle h with energy E_i can be written as

$$\lambda_{\text{dec},h}(E_i, X) = \rho(X) \cdot \hat{\lambda}_{\text{dec},h}(E_i). \tag{5.28}$$

The density independent part of the decay lengths are arranged in the diagonal matrix $\mathbf{\Lambda}^{\text{dec}}_{d_\phi \times d_\phi}$ similar to the decay lengths above.

Using all variables defined above the transport equation for a set of particles becomes

$$\frac{\mathrm{d}\mathbf{\Phi}}{\mathrm{d}X} = \left[\left(-\mathbb{1} + \boldsymbol{C}_{d_\phi \times d_\phi}\right) \mathbf{\Lambda}^{\text{int}}_{d_\phi \times d_\phi} + \frac{1}{\rho(X)} \left(-\mathbb{1} + \boldsymbol{D}_{d_\phi \times d_\phi}\right) \mathbf{\Lambda}^{\text{dec}}_{d_\phi \times d_\phi}\right] \cdot \mathbf{\Phi} \tag{5.29}$$

Using some minor approximations to overcome numerical issues, MCEq solves Equation (5.29) for around 70 particle species simultaneously. Since most matrices in this formalism are very sparse a fast calculation of atmospheric lepton fluxes at the surface of the Earth is possible.

5.2 Atmospheric Muons and Neutrinos

Cosmic-rays constantly bombard the atmosphere from every direction, creating cascades of secondary particles reaching the surface of the Earth. Due to their relatively long lifetime and their low interaction cross-section, muons are the most abundant species of charged particles. Next to additionally generated atmospheric neutrinos, these muons

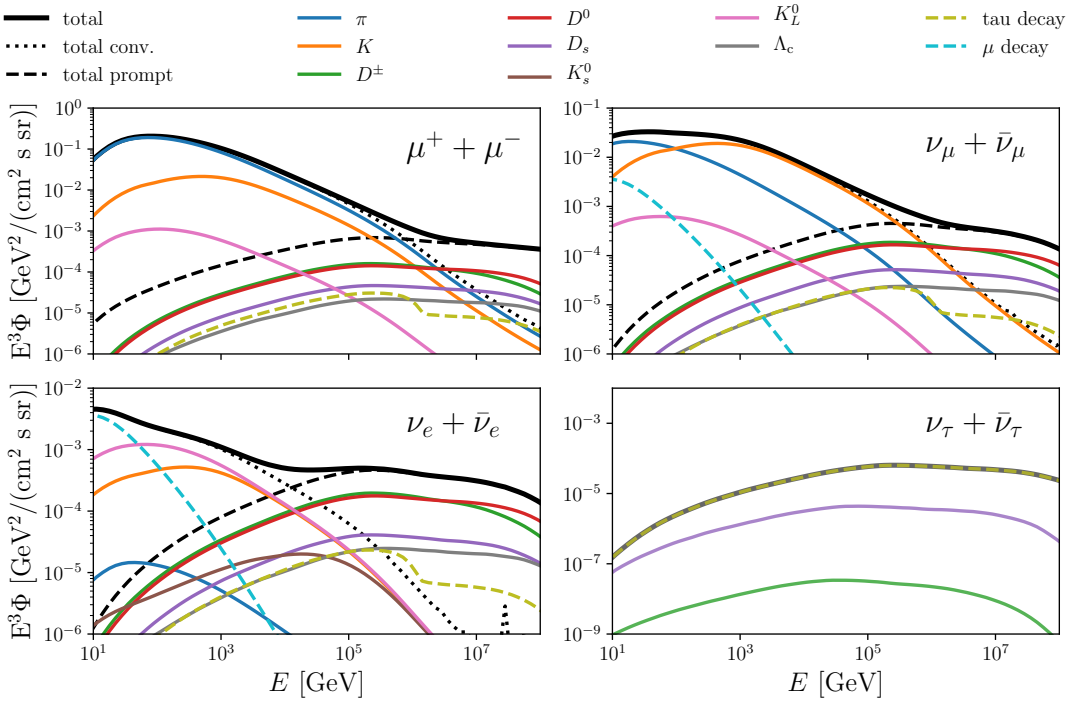

Figure 5.2: Illustration of the atmospheric lepton fluxes and their relative contributions calculated with MCEq. The cosmic ray spectrum is based on the H3a model (Subsection 2.1.3), while the hadronic interactions are described by the model SIBYLL 2.3c [90].

depict the major background for neutrino experiments. Hence it is crucial to have a proper understanding of atmospheric lepton fluxes.

In general both muons and neutrinos are generated in the decay of atmospheric mesons. While conventional muons and neutrinos, mainly produced by pions and kaons dominate at energies below $\sim 100\,\text{TeV}$, so-called *prompt* leptons are expected to become important above this energy. Prompt muons and neutrinos originate from the decay of charmed mesons. Due to the short lifetime of charged particles, prompt leptons are basically produced instantly after the production of the charmed meson, yielding a prompt spectrum following approximately the shape of the original cosmic ray spectrum (refer to Equation (5.18)). As the mother particles of conventional leptons can travel through the air for some time they can interact with the ambient molecules in the atmosphere. Hence the spectral shape of the conventional leptons can be up to one power softer than the cosmic-ray flux arriving at the top of the atmosphere (refer to Equation (5.19)).

In the previous section, it was shown that the linear propagation of particles in the atmosphere initiated by a primary cosmic-ray can be modeled by coupled cascade equa-

tions. Similarly, the inclusive flux of leptons at the Earth coming from the collectivity of cosmic-rays can be modeled. Figure 5.2 illustrates the vertically down-going atmospheric fluxes of muons and all three neutrino flavors respectively based on the cosmic-ray model H3a (Subsection 2.1.3). The thin lines indicate the relative contributions of different mother particles to the total fluxes (thick black lines).

5.3 Uncertainties in the Modeling of Cosmic Ray Showers

The calculation of atmospheric particle fluxes relies on a detailed knowledge of the interaction and decay properties of all particles involved in the cascade. Next to the physics happening within the cascade the distribution of the primary cosmic-rays has a major impact on the particle fluxes at the surface of the Earth. Additionally, atmospheric features such as local characteristics as well as the geometry of the Earth can affect the outcome. While the latter can be determined and implemented accurately in atmospheric shower models, the accurate knowledge of hadronic interactions and the primary cosmic-ray flux is limited. Hence these two dependencies depict the main sources of uncertainty in the estimation of atmospheric particle fluxes at energies above $\sim 10\,\mathrm{GeV}$. At lower energies also so-called *3D effects* caused by the geomagnetic field start to become important. Yet, since we are mostly interested in atmospheric muon and neutrino fluxes relevant for high energy neutrino physics we will not discuss the last point throughout this work.

Monte Carlo simulations of atmospheric particle fluxes are extremely time-consuming. As a consequence these simulations are inapplicable for the study of uncertainties coming from different components influencing the outcome of atmospheric fluxes. The methodology of cascade equations, on the other hand, provides a simple approach to investigate such effects. The intrinsic uncertainties of individual models can be propagated throughout the whole shower yielding the determination of the respective effect at the surface.

The cosmic-ray spectrum spans over many order of magnitudes reaching energies up to $100\,\mathrm{EeV}$. In order to get a full spectrum over all these energies, data from many different experiments have to be combined. Due to this combination of different measurements as well as the limited statistics at higher energies, the identification of a correct model describing all these data can be challenging. As a consequence, multiple theoretical approaches exist to model this primary cosmic-ray spectrum. The left panel of Figure 5.3 shows the atmospheric muon neutrino flux calculated with MCEq for four different cosmic-ray models. At around $10\,\mathrm{TeV}$ one can already see deviations of $\sim 20\,\%$ with increasing tendency towards higher energies. While the H3a, the H4a,

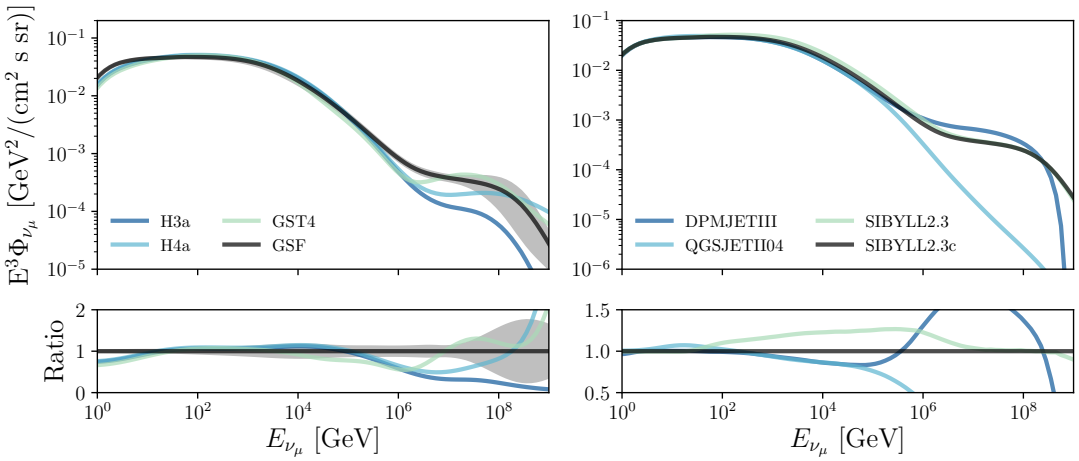

Figure 5.3: Muon neutrino flux averaged over all incoming angles above the horizon. **Left:** Spectrum for different primary cosmic ray spectra. The H3a and H4a models are introduced in Subsection 2.1.3. The Global Spline Fit (GSF) spectrum is based on a global fit of combined datasets from different measurements [91]. The hadronic interactions for all lines are described by the model SIBYLL 2.3c [90]. **Right:** Variations due to different hadronic interaction models [90, 92–94].

and the GST4 model mostly rely on theoretically motivated arguments, the GSF model characterizes the cosmic ray spectrum based on a mostly data-driven approach [91]. In their work, the authors combine data from multiple experiments and perform a global fit taking into account the statistical and systematic uncertainties of available experimental observations. Propagating the resulting uncertainties throughout the particle cascade yields dedicated uncertainties for atmospheric lepton fluxes. The grey band in Figure 5.3 illustrates the uncertainties of the muon neutrino flux caused by the uncertainties of the data-based GSF model.

Aside from inaccuracies in the initial flux of cosmic-rays, hadronic interactions depict the main source of uncertainty of atmospheric lepton fluxes above 10 GeV. While the effect of the cosmic-ray spectrum is nicely taken care of in the GSF model, the influence of hadronic interactions is still an open field of investigation. Since every particle cascade starts with a hadronic interaction of the primary cosmic-ray with nuclei in the air, even little deviations of these cross-sections will propagate recursively through the shower. In order to accurately describe all these interactions within the cascade, detailed knowledge of the relevant inclusive particle cross-sections over a large phase-space region of the projectile and secondary particle energies is mandatory. High-energy cosmic-rays arrive at energies orders of magnitude higher than typical particle

energies from man-made accelerators. Hence, current applications that are used to model cosmic-ray showers are based on theoretical interaction models. Since hadronic interactions in air showers are dominated by collisions with low transverse momentum transfer between the interacting particles, perturbative modeling within the framework of QCD is not sufficient [95]. Hence theoretical descriptions of hadronic interactions within particle showers commonly rely on phenomenological theories in combination with predictions from perturbative QCD [95]. Resultant models can be fine-tuned to comparable data measured at lower energies, while they solely rely on phenomenological arguments to extend to higher primary energies [96]. The evaluation of the atmospheric muon neutrino flux with different hadronic interaction models is shown in the right panel of Figure 5.3. The deviations between the individual outcomes are in the order of 20 % at 100 GeV with an increasing tendency towards higher energies.

Over the past decades, hadronic interactions of different particles have been measured with the successive fixed target experiments NA49 and NA61/SHINE located at the CERN SPS accelerator complex [97, 98]. Instead of using theoretically motivated interaction models, these data can be used directly to investigate the influence of hadronic interaction on detectable atmospheric fluxes at the surface. In the following section, we will concentrate on the uncertainties coming from hadronic interactions, introducing a new data-driven approach to replace current interaction models.

5.3.1 Hadronic Interactions from Particle Accelerators

The NA49 and the NA61/SHINE experiment were designed to study the nonperturbative sector of hadronic interactions. With both being set up in a fixed target configuration multiple collisions of different hadrons and nuclei have been studied over the years [97, 98].

In the context of atmospheric air showers, we are interested in extracting the experimental data describing the interaction of proton, light nuclei, and subsequent hadrons with the air in the atmosphere. Hence measurements with nitrogen or oxygen targets would be ideal. While no such data have been measured yet, hadronic interactions with a carbon target exist for multiple projectile particles. With an atomic number of 6, carbon is directly beside nitrogen and oxygen in the periodic table. Hence these measurements are supposed to introduce only a minimal bias compared to hadronic interactions within the atmosphere (Subsection 5.3.3).

In order to describe the evolution of particles caused by cosmic-rays, the inclusive production cross-sections of the relevant secondary particles are necessary. While conventional muons and neutrinos are essentially generated in the decay of pions and kaons

Experiment	Primary	Target	E_{beam} [GeV]	Secondaries	Variables
NA49	p	C	158	$\pi^{\pm}, \overline{\text{p}}, n$	x_F
NA61/SHINE	p	C	31	$\pi^{\pm}, K^{\pm}, K^0_S, \Lambda$	p, θ
NA61/SHINE	π^-	C	158, 350	$\pi^{\pm}, K^{\pm}, \overline{\text{p}}$	p, p_T
NA61/SHINE	p	p	20, 31, 40, 80, 158	$\pi^{\pm}, K^{\pm}, \overline{\text{p}}$	y, p_T

Table 5.1: Selection of experimentally measured inclusive particle yields $\mathrm{d}N \,/\, \mathrm{d}X$ (Equation (5.21)). The last column indicate the variables X in which the experimental data are elaborated. The experimental data are extracted from [99–102].

and their subsequent products, the atmospheric lepton fluxes at higher energies rely on additional information about the production of charmed mesons (see Figure 5.2).

For the study in this chapter we aim to gather as many experimental observations[2] as possible. The available inclusive particle yields used within this work are summarized in Table 5.1. As visible from the last column in Table 5.1 each of these data sets is evaluated in different sets of variables. In order to use these data within the formalism of cascade equations (Equation (5.21)), we have to convert the measured particle yields to values in terms of x_{Lab}. A detailed summary of the conversion procedures and their subsequent uncertainties can be found in Appendix A and B. Figure 5.4 shows the converted inclusive production yields $\mathrm{d}N \,/\, \mathrm{d}x_{\text{Lab}}$ of different mesons in proton carbon collisions. The yields on the y-axes are multiplied with $x_{\text{Lab}}^{1.7}$. Hence the distributions form the integrand given in the definition of the spectrum weighted moments (Equation (5.8)) for a cosmic ray spectrum with spectral index $\gamma = 2.7$. Since the spectrum weighted moments basically cover the impact of hadronic interactions in the cascade equation formalism (Subsection 5.1.2), it is most indispensable to accurately determine the integral of the distributions in Figure 5.4. Besides, these distributions allow for the determination of the most relevant energy phase-space regions (which correspond to regions in x_{Lab}) of the respective particle interaction. The spectrum weighted moments, also called Z-factors, for $\gamma = 2.7$ for all interactions in Figure 5.4 and 5.5 are summarized in Table E.1.

The data points in Figure 5.4 are fitted with a model-independent spline fit, taking into account the statistical and systematic uncertainties of the data points. In the region towards higher x_{Lab} values the uncertainties of the fits naturally blow up due to the missing phase-space coverage of the measurements. Next to the experimental data, comparable lines from the interaction models SIBYLL2.3c and DPMJET are

[2]The experimental data are required to obtain static and systematic uncertainties.

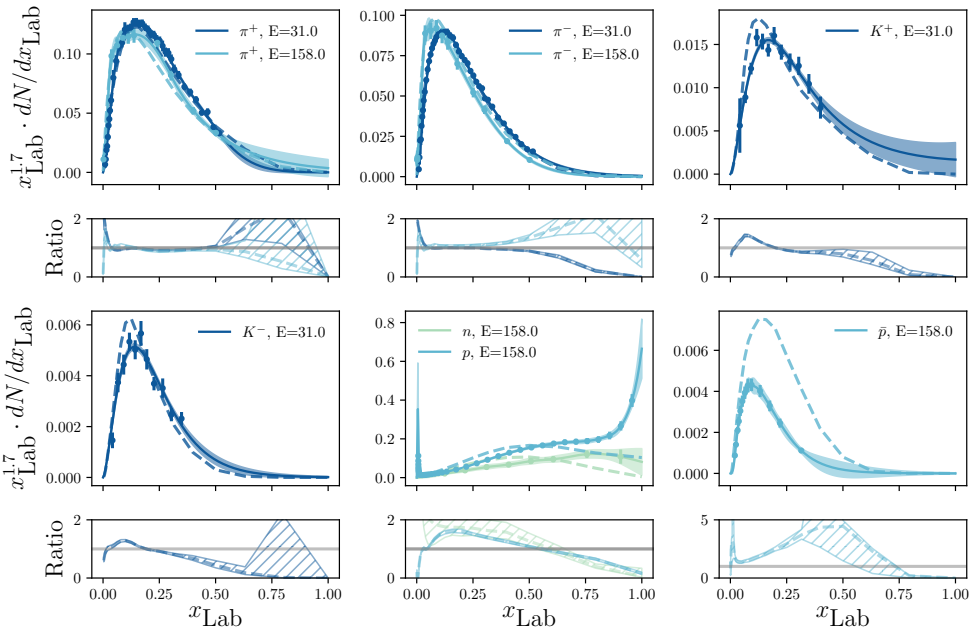

Figure 5.4: Inclusive production yields of different mesons in proton-carbon interactions. The points illustrate the results measured by the fixed-target experiments NA49 and NA61/SHINE (Table 5.1) with the error bars including systematic and statistical uncertainties of the respective experiment. The solid lines show a spline fit to these data where the shaded band represents the uncertainty of the fit. For comparison the inclusive particle yields in proton-air collisions from SIBYLL 2.3c (at 31 GeV the yields from DPMJET are shown instead) (dashed lines) are shown [90, 92].

illustrated. None of the two theoretical models can describe all data points within their uncertainties. While the pion distributions exhibit deviations of 10 % to 20 % at the peak, deviations for e.g. anti-protons can reach more than 100 %. Similar plots are shown in Figure 5.5 for the inclusive yields of pions, kaons, and protons resulting from interactions of negatively charged pions with carbon.

5.3.2 Data-based Model for Hadronic Interactions

Current calculations of atmospheric lepton fluxes rely on hadronic interaction models based on phenomenological arguments. The estimation of the atmospheric muon neutrino flux with different interaction models in Figure 5.3 (right panel) exemplary illustrates the strong dependency on the actual choice of the respective hadronic model.

In order to get a handle on the uncertainties of the atmospheric lepton fluxes caused by hadronic interactions, different attempts have been made. The authors in [103] divided

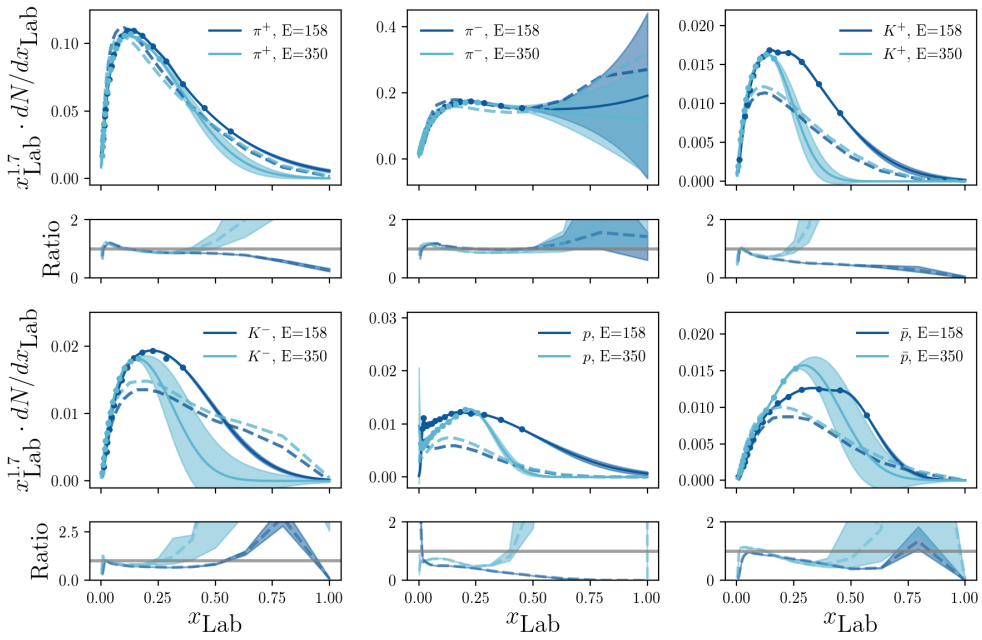

Figure 5.5: Inclusive production yields of different mesons in interactions of negative pions with a carbon target. The points illustrate the results measured by the fixed target experiment NA61/SHINE (Table 5.1) with the error bars including systematic and statistical uncertainties of the experiment. The solid lines show a spline fit to these data where the shaded band represents the uncertainty of the fit. For comparison the inclusive particle yields in pion-air collisions from SIBYLL 2.3c (at 31 GeV the yields from DPMJET are shown instead) (dashed lines) are shown [90].

the energy phase space of the hadron productions into multiple regions. In a next step, they assigned independent errors to each region based on the availability of experimental data. Using, for instance, MCEq, the influence of these uncertainties on atmospheric lepton fluxes can be calculated (see Appendix D). Despite allowing the evaluation of principle hadronic uncertainties, this approach also contains several downsides. The uncertainties in the phase-space regions are not connected to the uncertainties of the respective interaction models but are based on the quality of available data. Hence, these denoted uncertainties might simultaneously suffer both, over and under-coverage of the actual errors. Moreover, only uncertainties for pion and kaon production are available from this approach, neglecting possible deviations coming from further interactions. In a different attempt, the authors derive correction factors to hadronic interaction models by calibrating the computed muon fluxes and ratios with existing measurements [104].

While both approaches aim to adjust the current interaction models to existing mea-

surements, we propose a maximally model-independent approach to get a handle on the characteristics of hadronic interactions. Instead of using the experimentally measured distributions to calibrate theoretical models, we will use these data directly to describe the hadronic part of air showers. A proper hadronic model requires the inclusive particle yields of all relevant hadron interactions with ambient matter in the atmosphere at projectile energies between a few GeV up to the highest cosmic-ray energies. The inclusive yields that are experimentally measured up to now are listed in Table 5.1. The decay of pions, kaons, and their subsequent products dominate the flux of atmospheric muons, muon and electron neutrinos at energies up to $\sim 10\,\text{TeV}$-$100\,\text{TeV}$ (see Figure 5.2). Most of these *conventional* hadronic interactions are covered by the aforementioned experimental data. Consequently, these measurements allow the construction of a data-driven model (DDM) of *conventional* hadronic interactions on the following conditions.

Experimental measurements of the cross-sections of hadronic interactions only exist at projectile energies that are feasible with current particle accelerators. From Table 5.1 we can see that maximum energy of the primary energies is in the order of hundreds of GeV. Besides the missing data for higher primary energies, full phase-space coverage in terms of x_{Lab} of the existing measurements is not possible for all interactions with the current detector setups. Ultimately, as mentioned in the previous subsection no measurements with nitrogen or oxygen targets, mimicking the air in the atmosphere have been performed yet. In addition, experimental data for koan and further subdominant interactions do not exist yet. To overcome these limitations we construct the DDM based on the following assumptions:

- **Feynman Scaling**: In order to access the full range of primary energies, we assume Feynman scaling being valid for all energies. As mentioned in Subsection 5.1.2, Feynman scaling suggests that the properties of hadronic collisions only depend on the ratio of the primary and the secondary particle energy instead of their absolute values. In this way the existing data from Table 5.1 can be extended to all projectile energies.

- **Carbon Target**: Due to the absence of air-like target data we assume that hadron-air collision can be approximated by hadron interactions with carbon.

- **Missing Phase-Space Coverage**: The phase space in x_{Lab} is not completely covered by data for all secondary particle yields (Figure 5.4 and 5.5). We aim to access these uncovered regions with a model-independent spline fit.

- **Missing interactions**: The interaction of kaons and all further particles that

Primary	Secondaries
p	$\pi^{\pm}$, $K^{\pm}$, $\overline{\mathrm{p}}$, n
n	$\pi^{\pm}$, $K^{\pm}$, $\overline{\mathrm{p}}$, n
$\pi^{\pm}$	$\pi^{\pm}$, $K^{\pm}$, $\overline{\mathrm{p}}$

Table 5.2: Hadron production yields covered in the data-driven hadronic interaction model.

can not be covered by experimental data are modeled with SIBYLL 2.3c.

Following these assumptions we build a hadronic interaction model based on the proton carbon data from Table 5.1. The inclusive production yields of the charge conjugate primaries n and π^+ can be accessed by theoretical isospin symmetry arguments [105]. The isospin symmetries used within the DDM follow the implementation in MCEq [106]. A summary of all interaction yields that are covered by experimental data in our model can be found Table 5.2. Note that heavier cosmic ray nuclei are also covered within this approach since their interactions can be treated as the superposition of protons and neutrons [88].

5.3.3 Verification of the Remaining Model Assumptions

Before we apply the DDM to the evaluation of atmospheric lepton fluxes by means of MCEq, we aim to verify the validity of the model assumptions mentioned in the previous subsection.

As previously mentioned, the spectrum weighted moments (Equation (5.8)) approximately cover the impact of the hadronic interactions in the air-shower development (Subsection 5.1.2). In case the scaling assumption in the DDM is correct, these Z-factors are independent of the projectile energy of the respective hadronic interaction. Hence scaling in the DDM can be approximately validated by observing constant spectrum weighted moments for different projectile energies. Since experimental data only exist for few and in particular low projectile energies, these Z-factor distributions can only be accessed by means of theoretical interaction models. The Z-factor distributions resulting from SIBYLL 2.3c for different projectile energies for all inclusive particle interactions mentioned in Figure 5.4 are illustrated in Figure 5.6 (the Z-factor distribution for the particle yields from Figure 5.5 are shown in Figure E.1). As expected, the Z-factors change with increasing energy which clearly indicates a violation of Feynman scaling. Nevertheless if we compare the values at 158 GeV where experimental observations are available with the values at the highest energies, we can see that these deviations reside roughly within 10 % for pions and 20 % for kaons. For protons and anti-protons hardly

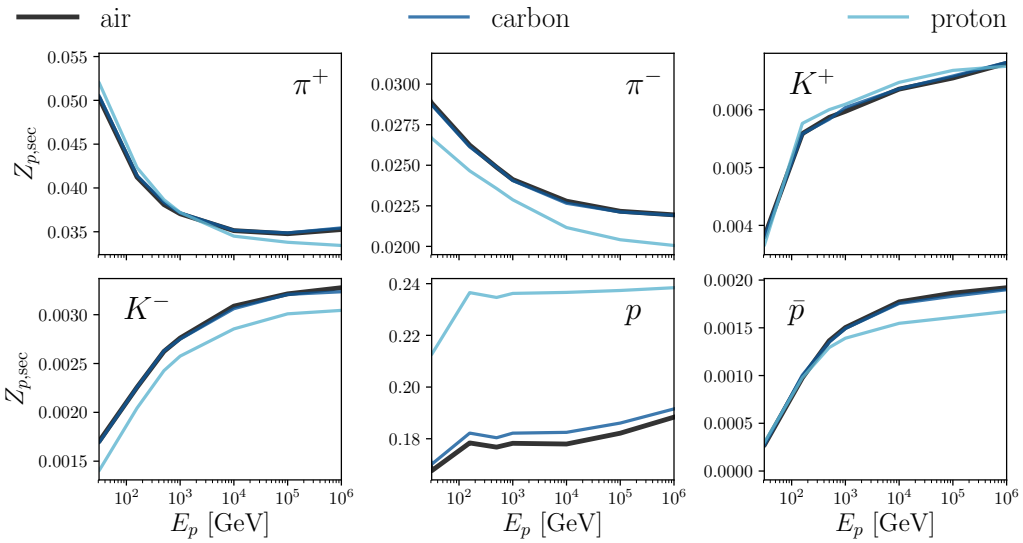

Figure 5.6: Z-factor distributions for the inclusive particle interactions shown in Figure 5.4. The colors indicate the different target materials for the respective interaction. Note that the values in these plots are calculated by means of the interaction model SIBYLL 2.3c [90].

any change is visible. As a consequence, we can state that the scaling assumption in the DDM is not correct, yet it most likely only introduces additional uncertainties of up to 20 % at higher energies. The effect of additional scaling uncertainties in the DDM is studied in Subsection 5.3.5.

Next to the spectrum weighted moments within the air, similar distributions for carbon and proton targets are shown in Figure 5.6. The Z-factors for carbon targets nearly completely coincide with the ones produced in air. Hence experimental data elaborated on carbon targets might be used in the DDM without introducing any significant bias for the evaluation of atmospheric air-showers. On the other hand, the secondary particle yields elaborated with simple proton targets can show significant deviations from the ones obtained with carbon or air. According to SIBYLL 2.3c these differences depend strongly on the exact type of the secondary resulting particle type and the projectile energies. Nevertheless, the Z-factor distributions for proton targets also show a similar trend. Hence experimental observations made with this target material could still be used to test the general scaling behavior of the respective interaction.

Other than the Feynman scaling and the different target materials, the last two model assumptions cannot be verified by means of the spectrum weighted moments shown in Figure 5.6. The determination of the influence of the missing phase-space coverage of

the experimental observations is not trivial. Yet, since we used a most generic spline fit to access the values in these regions, the uncertainties of these fits naturally blow up in the regions where no data is available. Although it is not guaranteed that the true values are covered within these uncertainties, they most likely depict a conservative estimate of the discrepancies. Moreover, it is worth noting, that for most of the particle yields the missing phase-space coverage resides within regions that only marginally contribute to the evaluation of atmospheric lepton fluxes[3] (Figure 5.4 and 5.5). The DDM is limited to the available experimental measurements (Table 5.2). In order to get a feeling for the potential effects of particle interactions that are not covered in the DDM is seems reasonable to consider Figure 5.2 again. In the conventional energy regime, these particle fluxes are vastly dominated the pion and kaon decays. Except for kaon interactions within the atmosphere, all particle yields in this energy range are covered by the DDM. At the current stage, the relative influence from the kaon-air interactions can only be studied by means of theoretical interaction models. This faint effect is illustrated in Figure E.4 and E.5. Once the decay of additional charmed mesons becomes relevant (roughly 10^5 GeV for muons and muon neutrinos and GeV for electron neutrinos) the current implementation of the DDM alone can not be applied to estimate the resulting atmospheric lepton fluxes and their uncertainties correctly.

5.3.4 Atmospheric Lepton Fluxes based on the Data-Driven Hadronic Interaction Model

Similar to the theoretically motivated models, the data-driven approach can be applied to the coupled cascade equation solver MCEq to compute the flux of atmospheric muons and neutrinos. The technical procedure that is required to process the experimental production yields $\mathrm{d}N \,/\, \mathrm{d}x_{\mathrm{Lab}}$ to the discrete values required in MCEq is summarized in Appendix C. The statistic and systematic uncertainties provided by the data can be propagated along the particle cascade in MCEq, allowing for detailed studies of the impacts on atmospheric leptons. The technical procedure of the uncertainty propagation in MCEq is explained in Appendix D.

The atmospheric fluxes of vertically down-going leptons and their corresponding uncertainties resulting from the DDM are illustrated in Figure 5.7. Comparable outcomes using SIBYLL 2.3c and assigned uncertainties according to [103] (Subsection 5.3.2) are shown in addition. The median results of the DDM clearly deviate from the evaluation with the theoretical model SIBYLL 2.3c for all lepton quantities in this figure. Yet, it

[3] As mentioned before, the integral of the distributions in Figure 5.4 and 5.5 constitute the spectrum weighted moments and hence depict the influence of the respective hadronic interaction.

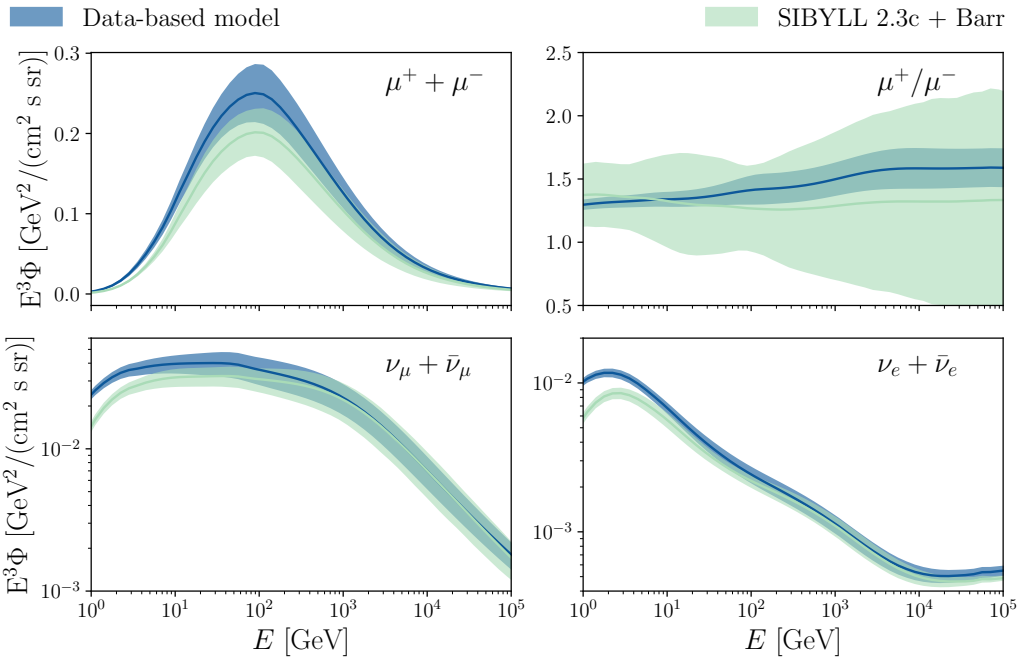

Figure 5.7: Modelling of the flux of vertically down-going atmospheric leptons. Both the outcomes of the data-based model as well as the results with the hadronic interaction model SIBYLL 2.3c are shown. The uncertainty bands of the SIBYLL 2.3c curve are based on the approach from [103], including only uncertainties from pion and koan production in CR-air interactions.

is nicely visible that all outcomes agree within their uncertainties above 10 GeV. At lower energies, the total lepton fluxes do not agree within the given uncertainties. These deviations might indicate the incorrect description of the hadronic particle interactions in the theoretical model at lower energies. Nevertheless, it is worth noting that geomagnetic effects can significantly influence the distributions at energies below 10 GeV. While these effects might shift the absolute flux values for both approaches it cannot account for the totality of the relative deviations.

From Figure 5.7 we can conclude that the data-driven approach yields consistent outcomes[4] with total uncertainties[5] in the range of roughly 5 % to 25 %. In the next step, we want to investigate the emergence of the atmospheric fluxes and their uncertainties based on the DDM.

At first, we want to study which uncertainties from the experimental data contribute most the total uncertainties of the atmospheric fluxes. The contributions to the lepton

[4]In a sense that the flux values are comparable to the ones obtained with SIBYLL 2.3c.
[5]Based on the presumption that the model assumptions of the DDM are all correct.

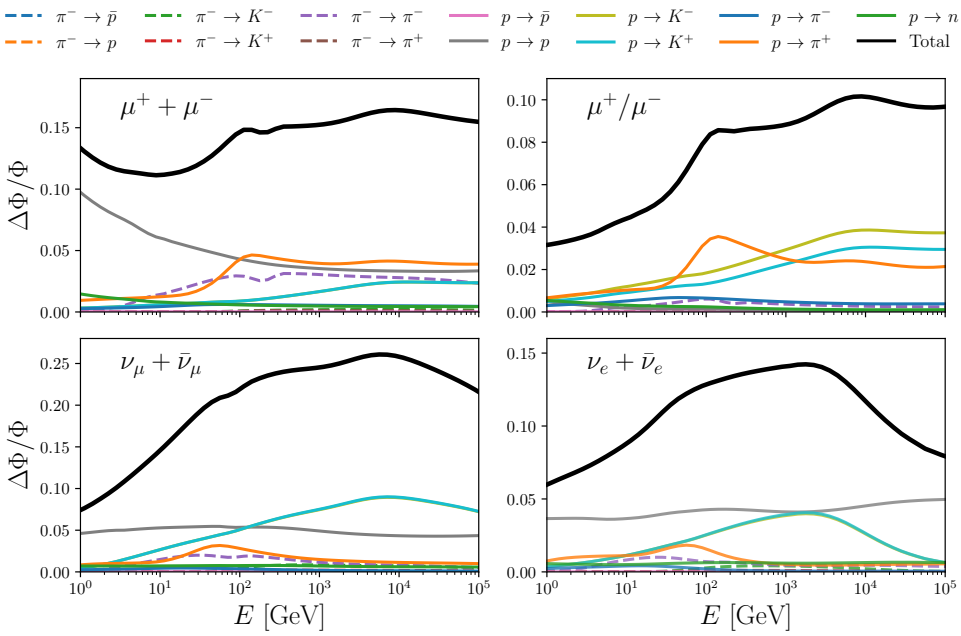

Figure 5.8: Uncertainties of atmospheric lepton fluxes resulting from the statistical and systematic errors of the hadronic interactions covered in the data-based interaction model. The colored lines show the contribution to the total uncertainty from individual interactions.

fluxes in Figure 5.7 from different hadronic interactions are illustrated in Figure 5.8. These outcomes assemble both the relative importance of the respective interactions (Figure 5.2) and the experimental uncertainties from the observation. For the total muon flux, the largest contributions arise from inclusive proton and π^+ production in interactions of protons within the atmosphere. It is worth noting that also pion production from pion interactions in the air introduces a non-negligible source of uncertainty for muons. Uncertainties from these interactions have not been treated at all in any of the previous approaches mentioned in Subsection 5.3.2. For the muon charge ratio, the proton production yields become less important because they simultaneously influence both the generation of positively and negatively charged muons. The absolute uncertainties for this charge ratio are driven by the production of kaons and pions in proton-air interactions. For the muon and electron neutrino fluxes, the uncertainties are dominated by the uncertainties of the proton, the K^+ and the π^+ production yields. In summary, these plots indicate nicely which particle production yields need to be measured more accurately in order to reduce the uncertainties of the resulting atmospheric lepton fluxes.

Next to the contribution to the respective uncertainties, we are interested in the

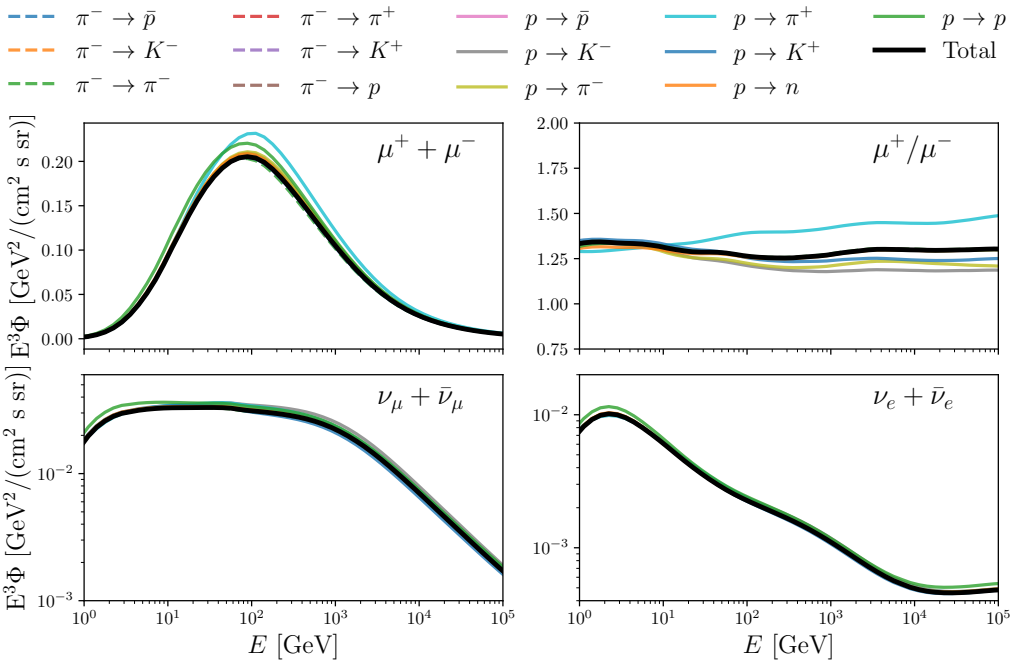

Figure 5.9: Influence of individual experimentally observed particle production yields. The black solid lines represent the outcomes based on the interaction model SIBYLL 2.3c, whereas for all other lines only the respective interaction from the DDM is replaced in SIBYLL 2.3c.

average atmospheric flux changes caused by replacing individual particle interactions with respect to SIBYLL 2.3c. Similar to before, this effect is illustrated for the total muon, muon and electron neutrino flux and the muon charge ratio in Figure 5.9. Other than before, these outcomes indicate which experimentally observed particle production yields cause the largest deviations with respect to the default interaction model SIBYLL 2.3c. The relative changes with respect to the fluxes based on SIBYLL 2.3c are illustrated in Figure 5.10. The changes for the total lepton fluxes are dominated by pion, kaon and proton production in interactions of protons with the air in the at atmosphere. Similar to before, the proton production is less relevant for the observable muon charge ratio.

From the discussion of the outcomes of the DDM in this subsection we have learned that it is not sufficient to only consider uncertainties from pion and carbon production in interactions of protons and heavier nuclei. In fact in order to evaluate accurate and complete uncertainties of atmospheric lepton fluxes caused by hadronic interactions all relevant processes have to be considered. Finally we want to compare the atmospheric lepton fluxes modeled by means of the DDM with available measurements. The muon

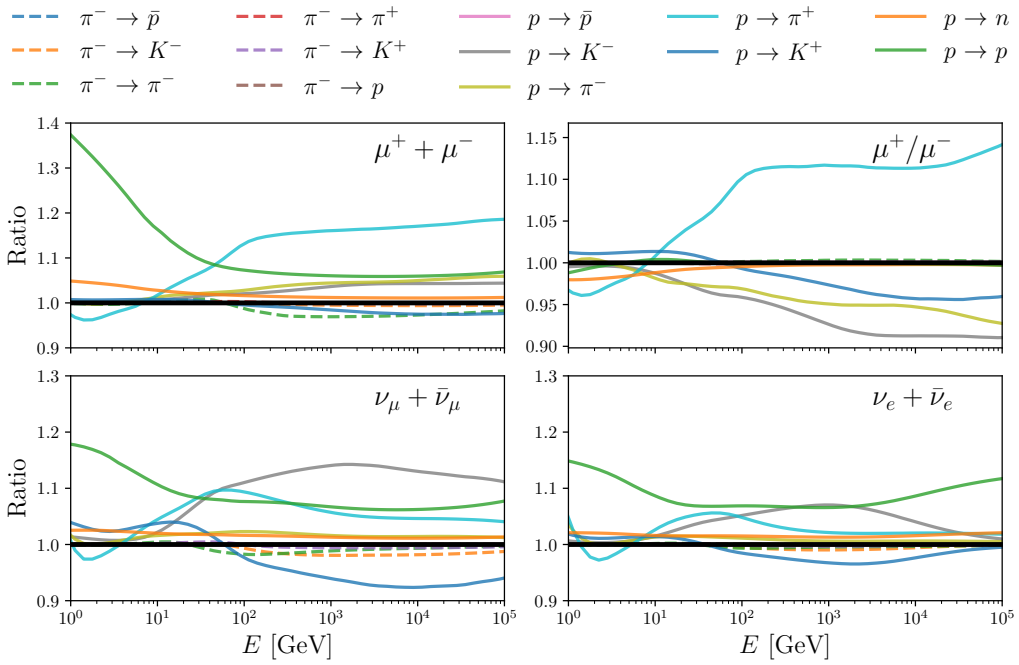

Figure 5.10: Relative Influence of individual experimentally observed particle production yields. All lines represent the ratio of the fluxes from Figure 5.10 with respect to the interaction model SIBYLL 2.3c.

fluxes for different incoming angles θ of the primary cosmic-rays are illustrated in Figure 5.11. While the atmospheric flux models based on SIBYLL 2.3c cannot explain the experimental observation of the vertically down-going muon flux, the flux model based on the DDM can, in fact, cover these data points within the uncertainties. The data points for the horizontally incoming muon flux show large variations. Nevertheless, even for these observations, the DDM seems to describe the experimental data better than the interaction model SIBYLL 2.3c. This is in particular visible for the observations between 10 GeV and 1 TeV.

The comparison of the DDM and experimental observations of the muon charge ratio are illustrated in Figure 5.12. Other than before SIBYLL 2.3c seems to describe the muon charge ratio better at lower energies for down-going particles, while the experimental observations are still covered within the uncertainties of the DDM. At energies above 1 TeV the DDM fits the data more accurately than SIBYLL 2.3c.

The atmospheric muon and electron neutrino fluxes for the DDM are shown again in Figure 5.13. At energies above 50 GeV both models seem to describe the observed data within their uncertainties. In order to compare hadronic models in the neutrino sector in more detail, more accurate measurements of the neutrino fluxes would be necessary. The

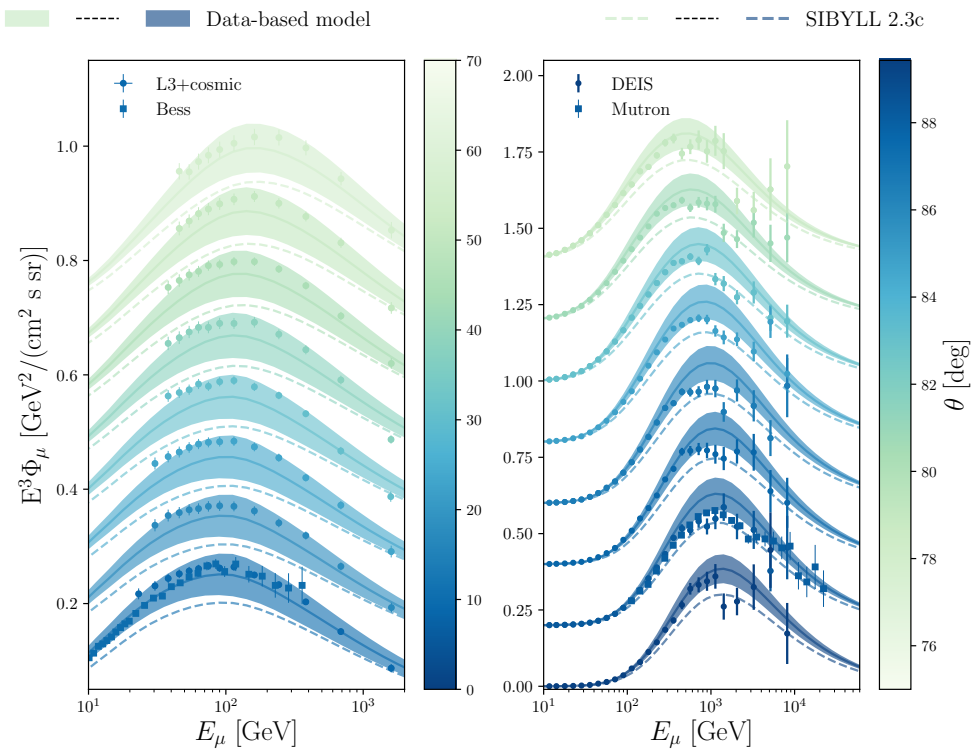

Figure 5.11: Atmospheric muon fluxes for different incoming angles θ. The shaded bands show the outcomes based on the data-based model, while the dashed lines show the results with the interactions model SIBYLL 2.3c. For comparison, experimental data from different experiments are illustrated. For better discrimination of the individual curves, the absolute values in the left (right) panel are respectively shifted by a factor of 0.1 (0.2). The experimental data are taken from [107–110].

data points from Super-K at a few GeV are affected by neutrino oscillations. Since the modeling of the atmospheric cascade in MCEq does not account for these oscillations, a direct comparison between the models and the data is not possible at these energies.

From the comparison with experimental observations, we can conclude that the DDM nicely describes the outcome of these measurements. In fact, the DDM can even explain the deficit of vertically down-going muons that results from SIBYLL 2.3c. Nevertheless, it is worth noting at this point that despite being maximally model-independent, the accuracy of the currently implemented data-driven approach still relies on the accuracy of the remaining model assumptions. The limitations caused by these presumptions are discussed in the following subsection.

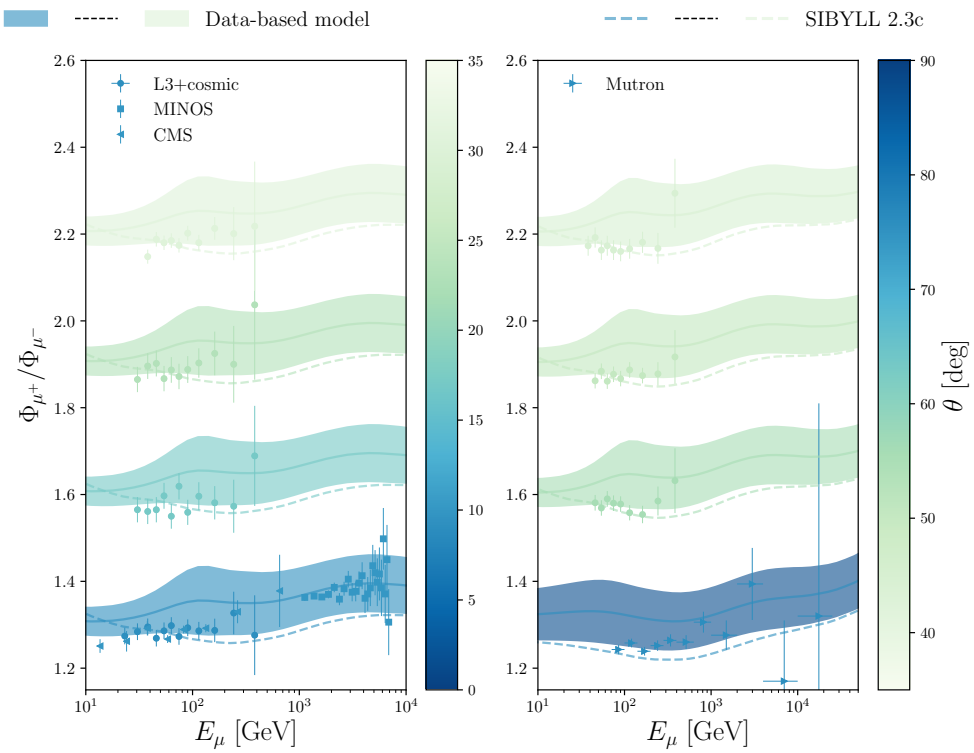

Figure 5.12: Atmospheric muon flux ratio for different incoming angles θ. The shaded bands show the outcomes based on the data-based model, while the dashed lines show the results with the interactions model SIBYLL 2.3c. For comparison experimental data from different experiments are illustrated. For better discrimination of the individual curves, the absolute values in the left panel are respectively shifted by a factor of 0.3. The experimental data are taken from [107, 110–112].

5.3.5 Limitation and Prospects of Data-Driven Interaction Models

The data-driven approach to describe hadronic interactions in MCEq seems to fit nicely to experimental observations. Moreover, it covers all statistic and systematic uncertainties of the underlying interactions and hence yields a nearly complete description of the hadronically induced uncertainties of atmospheric lepton fluxes. Nevertheless, the DDM does not cover any uncertainties that could arise from deviations of the model assumptions mentioned in Subsection 5.3.2. While the influence of the missing interactions, the false target material, and the missing phase-space coverage was already discussed in Subsection 5.3.3, we want to concentrate on the possible effects that might arise from scaling violations. As mentioned in Subsection 5.3.2, Feynman scaling is the key element in order to access the particle production yields in the DDM from the experimentally

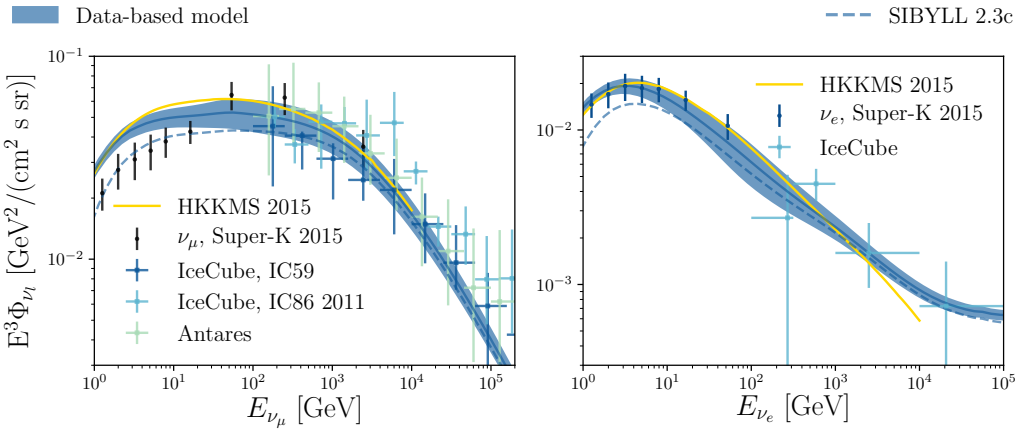

Figure 5.13: Atmospheric neutrino fluxes averaged over all incoming angles θ. Experimental data from IceCube, Antares and Super-K are added for comparison [113–116]. The yellow line indicates the result of the competing atmospheric neutrino flux calculation model from [117]. **Left:** Atmospheric muon neutrinos. **Right:** Atmospheric electron neutrinos.

observed production channels. In Subsection 5.3.3 we have seen that Feynman scaling is not valid at the energies necessary for the evaluation of conventional lepton fluxes. Yet, from the distribution of the spectrum weighted moments in Figure 5.6 we also observed that possible deviations at high energies from the values measured at 158 GeV might be in the order of 10 % to 20 %. Since the particle production yields in the DDM are obtained from experimental observations up to projectile energies 158 GeV (or 350 GeV for pion projectiles), we are interested in the effect of scaling violations above these energies. These effects are shown in Figure 5.14 and 5.15. In these plots, four scenarios of scaling violations are illustrated. At first, an additional uncertainty of 10 % is introduced for all particle production yields with projectile energies above 158 GeV. This roughly corresponds to a scenario with 10 % scaling violation above the projectile energies where experimental data are available. From the outcomes in both figures, we can conclude that these scaling deviations introduce additional uncertainties of a few percents at all energies for all lepton fluxes. In the second scenario, more conservative scaling uncertainties of 50 % above 158 GeV are introduced. In this case, the total uncertainties blow up significantly at all energies above $\sim$ 10 GeV for all atmospheric lepton fluxes. Ultimately we want to test how additional experimental data might influence the outcome of this study. Assuming that we possess experimental data up to projectile energies of 1 TeV in the future, we can repeat the previous study. Having scaling violations of 10 % above projectile energies of 1 TeV yields only minor additional

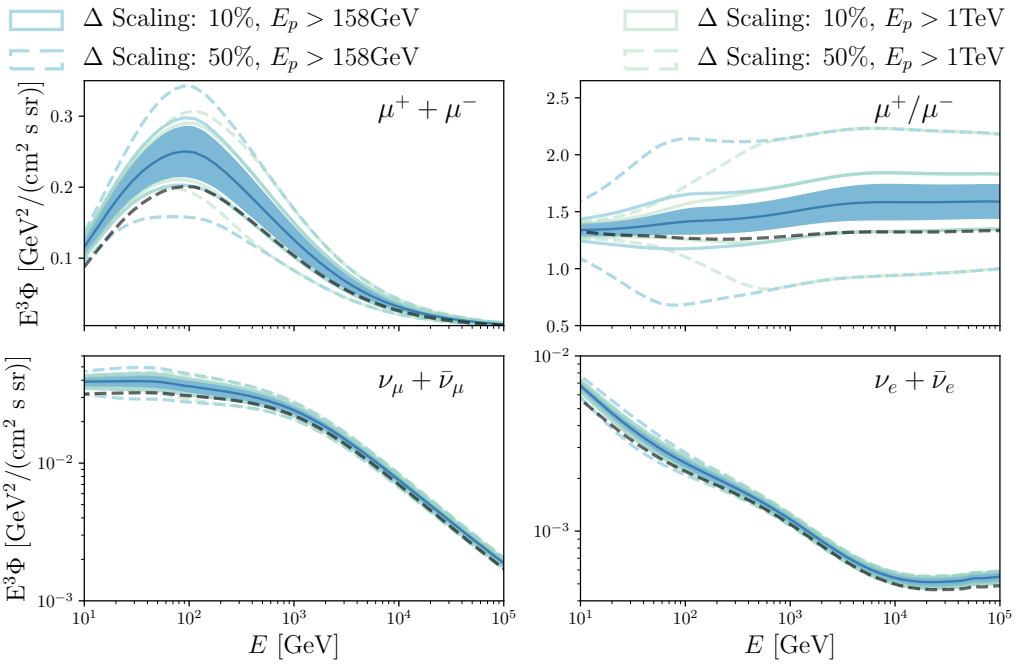

Figure 5.14: Atmospheric lepton fluxes based on the data-based hadronic model. The influence of additional scaling uncertainties for primary energies in different energy ranges is illustrated. The dedicated colored dashed lines illustrate the uncertainty band of these scaling violations in addition to the uncertainty band from the data-based model (blue filled band). The dashed line illustrates the outcomes using the interaction model SIBYLL 2.3c.

uncertainties of a few percent above $\sim 100\,\text{GeV}$. Below these energies, the atmospheric lepton fluxes are hardly affected by these deviations. A similar behavior appears if the additional scaling uncertainties of the hadronic interactions extend to 50 %. In this case, the total uncertainties of the atmospheric fluxes significantly increase at higher energies, while only minor influences are visible at lower energies.

In summary, we can conclude that deviations from the scaling assumption in the DDM might introduce additional non-negligible uncertainties for atmospheric fluxes at all energies. Following the theoretically motivated Z-factor distributions from Figure 5.6, these deviations might be in the order of 10 % to 20 % (depending on the projectile and secondary particle type and the projectile energy). Hence the resulting outcomes of a realistic scenario might reside somewhere in between the two scenarios with projectile energy thresholds at 158 GeV. Additional data at higher projectile energies might further reduce uncertainties at energies below 100 GeV.

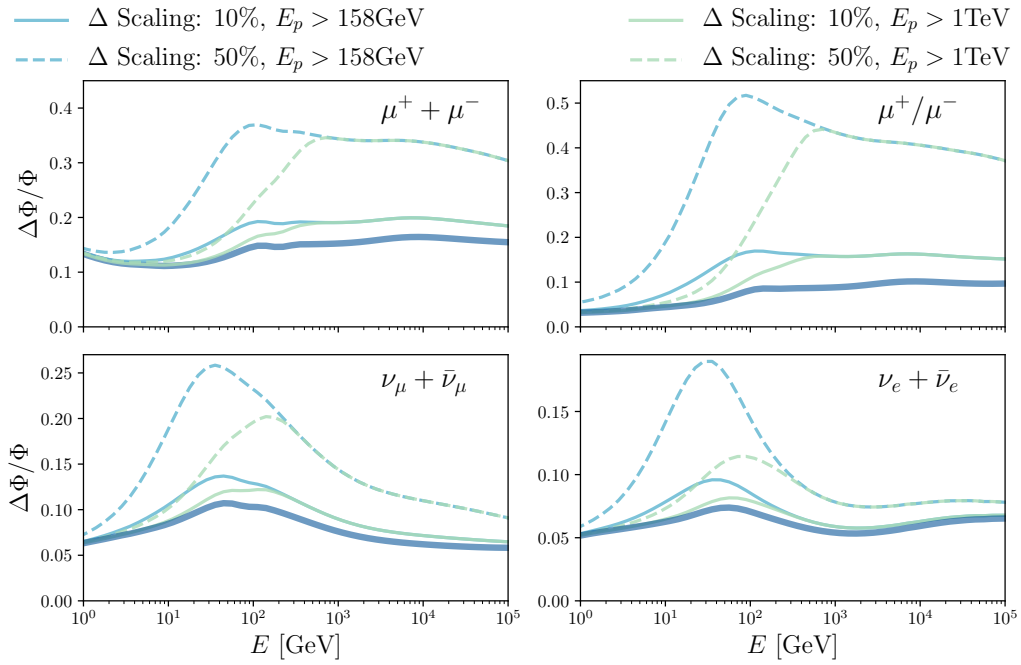

Figure 5.15: Uncertainties of atmospheric lepton fluxes based on the data-based hadronic model and its corresponding errors. The influence of additional scaling uncertainties for primary energies in different energy ranges is illustrated. The dedicated colored dashed lines illustrate the uncertainties of these scaling violations in addition to the uncertainties from the data-based model (blue thick line).

5.3.6 Summary & Outlook

The data-driven hadronic interaction model introduced in the previous section allows for the first time a detailed description of the dominating hadronic uncertainties of atmospheric lepton fluxes. Different to previous approaches, the DDM depends as little as possible on theoretical interaction models while covering nearly all interactions that are relevant for the accurate estimation of conventional lepton fluxes. Despite the fundamental constraints mentioned in Subsection 5.3.2, the DDM covers all hadronic uncertainties for energies up to $\sim 100\,\text{TeV}$ for muons and muon neutrinos ($\sim 10\,\text{TeV}$ for electron neutrinos). The current implementation of the DDM is limited by the availability of experimental measurements. The missing knowledge for projectile energies is most likely the strongest constraint of the model. Feynman scaling is supposed to overcome this lack of knowledge. Additional uncertainties that might be caused by the scaling assumptions might reside in the order of a few up to roughly 20 % (Subsection 5.3.5).

As visible in Figure 5.14 and 5.15 additional measurements at higher projectile energies can significantly reduce the uncertainties resulting from scaling violations. In fact, the deviations of the spectrum weighted moments at higher energies only deviate by a few percents from the values at 1 TeV. Moreover, these Z-factor distributions for all particles follow a clear distribution. Hence it might even be feasible to model the high-energy effects from multiple observations at lower projectile energies.

Besides the accuracy limitation due to the scaling assumption, the current implementation of the DDM is limited to particle energies that are dominated by conventional pion and kaon decays. Nevertheless, if experimental observations for the production of charmed particles would be available, the data-driven approach introduced in this work can be easily extended to higher lepton energies as well.

We can conclude, that even very few supplementary experimental data could eliminate most of the constraints resulting from the missing observations at the highest projectile energies, leaving a completely theory independent description of hadronic interactions in the evaluation of conventional atmospheric lepton fluxes. In order to access the high-energy tails of these leptons distributions, additional data for the production and propagation of charmed particles is necessary.

6

Large Volume Neutrino Detectors

High-energy neutrinos are unique astrophysical messengers that can carry information from the farthest reaches of the Universe. Since neutrinos are only weakly interacting neutral particles they are neither deflected by magnetic fields nor significantly influenced by interactions with ambient matter on their path. Despite this behavior being a major benefit during their travel towards the Earth, it generates severe challenges for the detection of these particles. In the following chapter we will introduce the general detection principle that is employed by all currently existing neutrino telescopes (Section 6.1). The detector requirements and the explicit implementation of this concept in case of the IceCube detector and other large volume neutrino detectors in water is summarized in Section 6.2 to 6.4. Ultimately this chapter closes with a brief summary of the data acquisition system used for the IceCube experiment.

6.1 High-Energy Neutrino Detection

Neutrinos are weakly interacting particles that can not be observed directly, but have to be measured via their secondary products. Above 100 GeV the neutrino interactions with matter are dominated by deep inelastic scattering processes with individual quarks inside ambient nucleons [118]. In this sense neutrinos can either interact with a quark in the nucleon N via the exchange of a charged W boson

$$\nu_l + N \rightarrow l + X \tag{6.1}$$

or a neutral Z boson

$$\nu_l + N \rightarrow \nu_l + X. \tag{6.2}$$

While in the first, so-called charged current (CC) scenario, a charged lepton l of the same flavor as the neutrino is generated, a neutrino of the same flavor with a fraction

of the primary neutrino energy is created in the latter neutral current (NC) case. In both cases the nucleon N fragments into a hadronic shower X. While neutrino electron scattering is generally negligible at these energies, the resonant production of a W boson in interactions of electron anti-neutrinos with electrons bound in the ambient atoms

$$\bar{\nu}_e + e^- \rightarrow W^-, \tag{6.3}$$

depicts a mentionable exception. This resonance formation becomes prominent at the Glashow resonance energy [119]

$$E_{\nu,GR} = \frac{m_W^2 - m_\nu^2 - m_e^2}{2m_e} \sim 6.3\,\mathrm{PeV}. \tag{6.4}$$

The resulting W boson can either decay into hadrons or a neutrino-lepton pair [77].

The aforementioned inclusive cross-sections of neutrinos in this high energy regime are illustrated in Figure 6.1. At lower energies the deep inelastic nucleon cross-sections grow almost linearly with the neutrino energy. Above 10 TeV the momentum transfer starts to dominate over the mass of the gauge boson in the propagation term leading to a suppression of the cross-section. While neutrinos and anti-neutrinos can be distinguished due to valence quark composition of the nucleons at lower energies, scattering at sea quarks becomes dominant above 100 TeV making both cross-sections nearly identical [118, 120]. The Glashow resonance production of W bosons is subdominant at all energies except from region around 6.3 PeV where this mechanism outshines the effect of the deep inelastic nucleon interactions.

Large volume neutrino detectors use optical methods to measure the light emission of the secondary products generated in these neutrino interactions. Along their path charged relativistic particles cause local polarizations in a dielectric medium. If the velocity of the particle exceeds the speed of light in the medium, these asymmetric polarizations can not relax back to equilibrium but electromagnetic radiation is emitted in the so-called Cherenkov effect. The photons emitted along the path of the charged particle forms a light cone with opening angle ϑ defined as

$$\cos(\vartheta) = \frac{1}{\beta n}, \tag{6.5}$$

where $\beta = v/c$ is proportional to the velocity v of the charged particle and n the refractive index of the medium. This effect is illustrated in Figure 6.2. Assuming relativistic particles with $\beta \sim 1$, the expected Cherenkov angle in ice ($n_{ice} \sim 1.309$) is approximately $\vartheta_{ice} \sim 41°$ while it is $\vartheta_w \sim 43°$ for sea water with refractive index

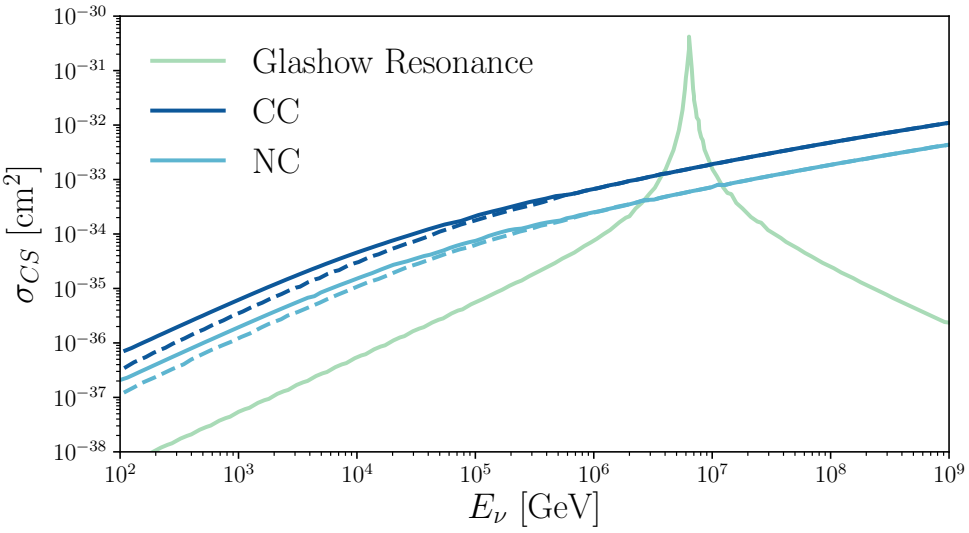

Figure 6.1: Relevant neutrino cross sections in the high-energy regime. The deep inelastic cross sections of neutrinos are illustrated as solid line, while anti-neutrinos are marked as dashed lines. Data are taken from [120].

$n_w = 1.364$ [23, 77].

The number of photons N generated along the path dx of the relativistic particle can be analytically estimated by the Franck-Tamm formula [121]

$$\frac{\mathrm{d}^2 N}{\mathrm{d}x\,\mathrm{d}\lambda} \sim \frac{2\pi\alpha}{\lambda^2}\left(1 - \frac{1}{\beta^2 n(\lambda)^2}\right), \tag{6.6}$$

where λ is the wavelength of the radiation and α depicts the fine structure constant. Since this number of photons is inversely proportional to their wavelength, shorter wavelengths dominate the contribution to the total light emission making the Cherenkov radiation appear mostly blue at visible wavelengths in water and ice.

For wavelengths below $\sim 300\,\mathrm{nm}$ the refractive index $n(\lambda)$ obtains values below unity, suppressing the emission of Cherenkov light in these regions. This decline is even more intensified by the characteristics of commonly used optical detection modules as well as the light transmission properties of the medium. Consequently the most significant light output in ice and water appears in the ultra-violet and optical wavelength regions between $300\,\mathrm{nm} - 600\,\mathrm{nm}$ [23].

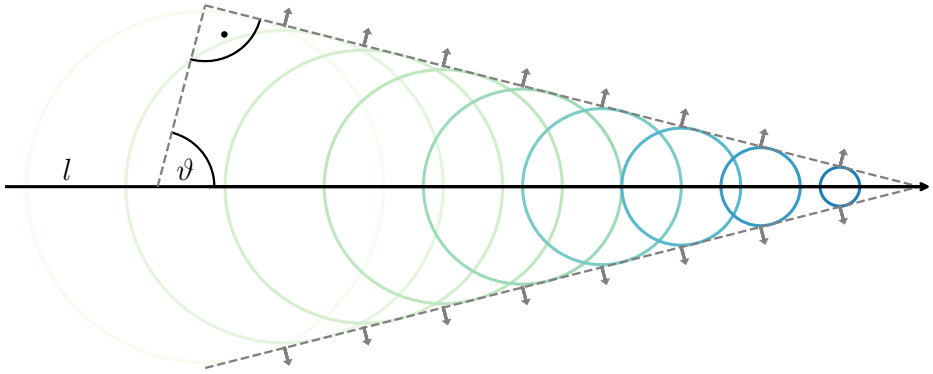

Figure 6.2: Illustration of the Cherenkov effect of a relativistic particle l. The round circles represent the spread of the light emission at the respective position seen from the location of the charged particle. Their superposition yields a wave front of photons with opening angle $\vartheta_w = 43°$.

6.2 Detector Requirements

The detection of high-energy neutrinos faces many challenges. Since neutrinos are solely weakly interacting particles they can only be detected by signatures of secondary particles generated in their interactions with ambient matter. The electromagnetic radiation from these neutrino induced secondaries can be observed by means of optical detection techniques. In order to guarantee reasonable performance, neutrino telescopes have to unify various essential characteristics.

Experiments targeting high-energy astrophysical neutrinos have to encompass a large mass and volume of target material to compensate the low neutrino cross sections as well as the faint astrophysical signal. Since high-energy neutrinos require the presence of very high energetic hadrons, an upper bound on the high-energy neutrino flux can be derived from the energy density of extra-galactic UHECRs (Section 4.3) [81, 122]. Assuming that neutrinos are either produced in $p-p$ or photohadronic interactions, the measured energy density of extragalactic cosmic-rays implicates an upper limit of [79]

$$E^2 \frac{\mathrm{d}\phi_{\nu_\mu}}{\mathrm{d}E} \sim 2 \times 10^{-8}\,\mathrm{GeV\,cm^{-2}\,s^{-1}\,sr^{-1}}. \tag{6.7}$$

Given a detector volume V in an optically transparent medium with density ρ, the average rate of events from a certain neutrino interaction process ν_i within an observation

time T is

$$N_{\nu_i} = \int_T \mathrm{d}t \int_{\Delta\Omega} \mathrm{d}\Omega \int_{\Delta E} \mathrm{d}E \, N_A \rho V_{\mathrm{eff}}(E) \sigma_{\nu_i}(E) \frac{\mathrm{d}^3\phi_{\nu_i}}{\mathrm{d}t \, \mathrm{d}\Omega \, \mathrm{d}E}, \tag{6.8}$$

with N_A being the Avogadro constant, ρ the density of the material and σ_{ν_i} the cross section for the process of interest. The effective volume V_{eff} accounts for detector related effects such as selection efficiencies. For a perfectly efficient detector the effective volume approximately corresponds to the geometrical detector volume V. The expected event count from the neutrino flux given in Equation (6.8) can be used to determine the required size of the neutrino detector. In case of a $1\,\mathrm{km}^3$ scale neutrino telescope the expected rate of neutrino induced muons with energies above 200 TeV is ~ 60 per year. Hence in order to observe extragalactic astrophysical neutrinos at an acceptable rate neutrino telescopes have to cover detector volumes of $1\,\mathrm{km}^3$ or larger.

Next to the absolute rate of astrophysical neutrino events, the purity of these event samples is crucial. Since the observation of neutrinos is based on optical detection mechanisms it is inevitable to shield the detector against any possible background radiation that might appear similar to the neutrino signal. Hence large volume neutrino detectors are built deep within ice or water to have a natural delimitation of preventable background radiation. In this way direct radiation and most charged particles cannot penetrate the detector anymore. Nevertheless muons and neutrinos that are largely produced in the atmosphere can still reach the detector, depicting a nearly irreducible source of background radiation for astrophysical neutrino searches (Section 7.2).

While the size and location of the telescope is fundamental to obtain a large and pure observation rate of high-energy neutrinos, the optical transparency of the detector material is crucial to allow the undisturbed observation of the neutrino induced Cherenkov radiation. The light propagation in optically transparent media is predominantly affected by scattering and absorption. Both material dependent effects can be quantified by the average geometric scattering and absorption length, Λ_{sct} and Λ_{abs}, respectively describing the average distances x, that light at a wavelength λ can travel within the medium before its intensity I is reduced by a factor of $1/e$ according to

$$I(\lambda, x) = I_0 \exp\left(-\frac{x}{\Lambda_i}\right). \tag{6.9}$$

The coefficient Λ_i can represent both, the scattering and absorption lengths. Since photon scattering in ice and water is strongly forward peaked[1], we can typically record light that experienced multiple scatters. Hence it is often beneficial to contemplate the

[1]The average deflection angle ϑ_{sct} at each scattering point is small.

average effective scattering length $\Lambda_{\text{sct}}^{\text{eff}}$ instead

$$\Lambda_{\text{sct}}^{\text{eff}} = \frac{\Lambda_{\text{sct}}}{1 - \langle \cos(\vartheta_{\text{sct}}) \rangle}, \tag{6.10}$$

where ϑ_{sct} represents the deflection angle of photons at each scatter point. While the geometric scattering length describes the average distance between to scatters, the effective scattering length specifies the average propagation scale of photons along an incident direction incorporating the non-isotropic scattering behavior within the medium [123, 124]. The interplay of both, scattering and absorption effects can be described by the effective attenuation length which relates to the latter according to

$$\Lambda_{\text{att}}^{\text{eff}} = \frac{\Lambda_{\text{sct}}^{\text{eff}} \cdot \Lambda_{\text{abs}}}{\Lambda_{\text{sct}}^{\text{eff}} + \Lambda_{\text{abs}}}. \tag{6.11}$$

On the basis of these light propagation characteristics, the optimal detector composition for a particular physical problem can be extracted. In case of vast light dispersion along the path of the relativistic particles, a sparse segmentation of detection modules is sufficient to capture an adequate fraction of the signal. Hence the optimal setup for a neutrino detector within a given volume depends not only on the respective neutrino energies of interest (Section 6.3), but also on the optical properties of the surrounding medium. Considering all these premises, all current neutrino telescopes are composed of a set of optical modules containing one or more photo-multiplier tubes, with their exact distribution depending on the typical energy range of the physical phenomenon and the optical characteristics of the surrounding area.

6.3 Event Topologies

Depending on the respective interaction process, neutrinos of different flavors can produce different signatures within a detector volume. While light production in neutral current neutrino interactions is solely induced by the hadronic cascade from the fragmenting nucleon, additional Cherenkov radiation from generated leptons illuminates the detector medium in charged current neutrino collisions. In general the light signatures from all high-energy neutrino interactions can be categorized into two main classes according to their geometry. While this classification is not complete, it covers all neutrino interaction processes that are relevant throughout this thesis.

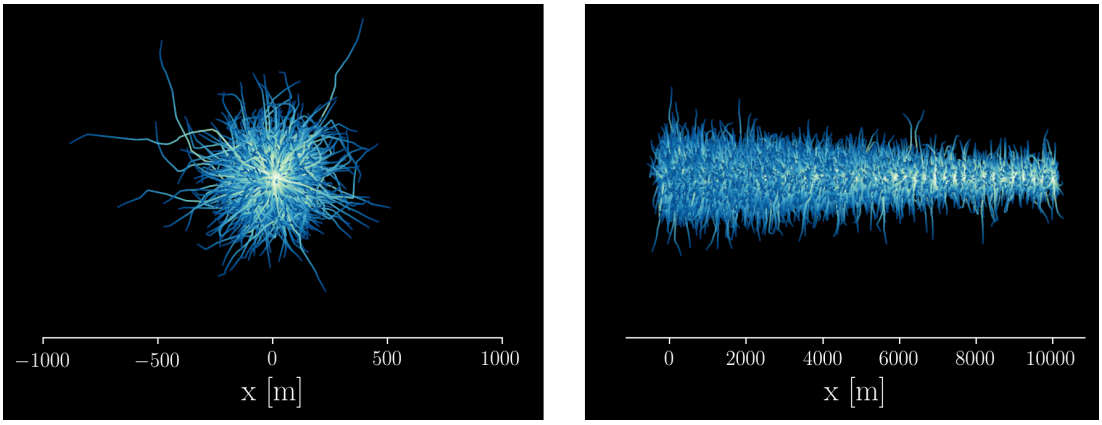

Figure 6.3: Simulation of typical neutrino interaction signatures in ice. This toy simulation shows the Cherenkov light emission from charged particles traveling in the positive x direction in a random walk approximation. The optical properties of the medium are characterized by an average scattering length of $\Lambda_{\text{sct}} = 2.5\,\text{m}$ and an average absorption length of $\Lambda_{\text{abs}} = 100\,\text{m}$, which is a typical parameterization for the Antarctic ice in IceCube (Table 6.1) [125]. The distribution of the photon scattering angle ϑ_{sct} for Mie scattering in ice is modeled by a linear combination of a Henyey-Greenstein and a simplified Liu function [123, 125]. The color indicates the time difference between the production and absorption of the photon. **Left:** Cascade-like event signature typical for NC processes and CC interactions of ν_e and ν_τ. **Right:** Track-like event signature from a high energy muon produced in CC ν_μ interactions.

6.3.1 Cascade-like Events

In optically transparent media charged current interactions of electron and tau neutrinos as well as neutral current collisions of all neutrino flavors induce nearly spherical symmetric light patterns. While the secondary electron or the immediate decay of the tau initiate an electromagnetic cascade that superimposes with the hadronic cascade from the fragmented nucleon, the photon emission in neutral current interactions is exclusively created by the hadronic shower. An electron-neutrino pair generated in Glashow Resonance interactions produces a signal similar to its CC correspondent, yet without the occurrence of a hadronic cascade (Section 6.1). In general, the total light emission persists of the superposition of Cherenkov photons from the primary lepton as well as all charged particles from subsequent particle showers. A typical spherical light emission profile of a CC electron neutrino interaction in the vicinity of Antarctic ice is shown in the left panel of Figure 6.3.

The spherical light signature of the neutrino interactions mentioned above arises due

to the short path lengths of electrons and all other charged particles within both kinds of particle showers [126]. In transparent media such as ice or water, the longitudinal expansion of such particle showers is in the order of a few meter [127]. In addition the directional information of the initiating particle is smeared out by scattering effects of the emitted Cherenkov photons, yielding a nearly spherically symmetric light pattern. While the homogeneous light production in electromagnetic cascades is directly proportional to its deposited energy, the light pattern from hadronic showers show larger variations in their dispersion and energy deposition [126]. These fluctuations appear due to the generation of neutral particles which do not further contribute to the light emission.

Despite these minor deficits from the hadronic shower, the neutrino energy in charged current interactions is entirely deposited within a finite volume around the interaction vertex. Since the measurable Cherenkov radiation is proportional to this energy, these interactions allow for a good energy reconstruction if they are contained within the detector volume. On the other hand neutrinos in NC interactions dispense only a fraction of their energy to the hadronic shower while the remaining energy is escaping with the outgoing neutrino.

6.3.2 Track-like Events

Unlike electrons, high-energy muons produced in CC interactions of muon neutrinos can travel large distances in water and ice due to their larger mass. While passing through the ambient matter muons lose energy through ionization and stochastic processes such as bremsstrahlung, pair production and nuclear interactions [33, 128]. Note that the auxiliary emitted Cherenkov radiation depicts an insignificant contribution to the total energy loss and can be neglected in the following consideration. The average energy loss of muons per path length $\mathrm{d}x$ is illustrated in the left panel of Figure 6.4. As visible, it can be parameterized by

$$\left\langle -\frac{\mathrm{d}E_\mu}{\mathrm{d}x} \right\rangle = a_\mathrm{I} + a_\mathrm{St} E_\mu, \tag{6.12}$$

where a_I represent the ionization term which is roughly constant above 1 GeV and a_St combines the remaining stochastic effects. The average energy loss of muons in the Antarctic ice can be characterized by $a_\mathrm{I} \sim 0.259\,\mathrm{GeV\,m^{-1}}$ and $a_\mathrm{St} \sim 0.363 \times 10^{-3}\,\mathrm{m^{-1}}$ [77, 129]. Following Equation (6.12), we can calculate the average path length $L_\mu(E_\mu)$

of a muon with energy E_μ before it looses all its energy according to

$$\langle L_\mu(E_\mu)\rangle = \frac{1}{a_{\mathrm{St}}} \log\left(1 + \frac{a_{\mathrm{St}}}{a_{\mathrm{I}}} \cdot E_\mu\right). \tag{6.13}$$

Hence muons with an energy of 10 TeV travel on average ~ 7.5 km through the ice, while the most probable path length of a 1 PeV muon logarithmically increases to ~ 20 km. Above ~ 500 GeV the stochastic energy losses begin to dominate over the continuous ionization processes leading to an increased variance of the muon path length [130].

Along the path of the muon, Cherenkov light is produced by the muon itself and by electromagnetic cascades that are produced by continuous and stochastic processes along the track. Since the Cherenkov light yield is proportional to the total track length of all contributing particles, higher-energy muons appear brighter. Above ~ 500 GeV the light emission is dominated by stochastic energy losses [126]. Hence the original light dispersion of the primary muon is distorted by overlaying photons from the subsequent electromagnetic cascades at these energies. In the vicinity of the neutrino interaction vertex additional Cherenkov radiation emerges from the hadronic cascade caused by the fragmentation of the target nucleon. The typical time integrated light pattern of a ~ 30 TeV muon in ice is illustrated in the right panel of Figure 6.3.

The elongated lever arm of muons with energies above a few hundred GeV allows for a precise reconstruction of the muon direction. Additionally, the direction of the incoming muon neutrino deviates from this muon track by the kinematic scattering angle between the two particles at their interaction vertex

$$\langle \sphericalangle(\nu_\mu, \mu)\rangle \sim \frac{1.5^\circ}{\sqrt{E_{\nu_\mu}/100\,\mathrm{GeV}}}. \tag{6.14}$$

The exact distribution and the corresponding 68 % confidence interval of the this kinematic angle for different neutrino energies is illustrated in the right panel of Figure 6.4. For incoming neutrinos with energies above a few TeV this angle becomes smaller than 1° and typically resides below the angular resolution of existing neutrino telescopes [131].

Similar to the charged current collisions of ν_e and ν_τ, muon neutrinos performing CC interactions deposit all of their energy in the surrounding medium. Yet due to the extensive path length of high-energy muons, only segments of their paths will be contained within the detection volume. The measurable deposited energy of this track segment will only allow the computation of lower limits to the total neutrino energy. In order to evaluate such energy limits, it is moreover essential to know the fraction of

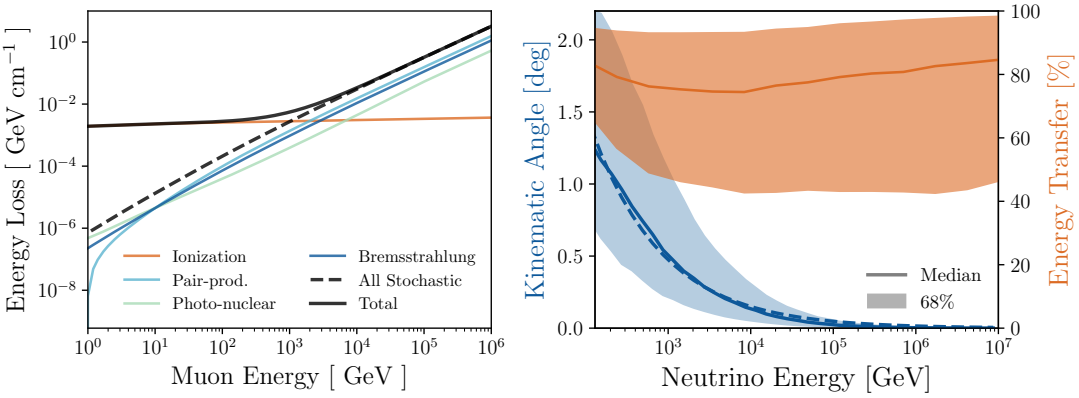

Figure 6.4: **Left:** Contribution from ionization and stochastic processes to the muon energy loss in ice [77]. The total muon energy loss can be accurately approximated by Equation (6.12). **Right:** Distribution of the median kinematic angle between muon neutrinos and the corresponding muons generated in CC interactions for different neutrino energies (blue solid line, values referenced on the left-side axis). Above 100 GeV this angle approximately follows the distribution given in Equation (6.14) (dashed line). The fraction of the neutrino energy that is attributed to the muon is illustrated by means of the second y-axis on the right.

energy that is transmitted from the neutrino to the muon[2]. This is illustrated in the right panel of Figure 6.4. On average the muon obtains $\sim 80\,\%$ of the neutrino energy at all energies, while showing significant variations in the exact values.

Depending on the location of the neutrino interaction inside the detector, we can further divide these track-like events into through-going and starting tracks, with the latter having the interaction vertex within the detector volume and the former traveling through the full detector after interacting outside its volume.

6.4 Large Volume Neutrino Observatories

As mentioned in the previous section, interactions of high-energy astrophysical neutrinos leave a distinct trace of Cherenkov radiation within optically transparent media such as ice and water. In order to guarantee a reliable detection of these signatures, neutrino telescopes have to equip large volumes of these media with optical detection apparatus in surroundings isolated from any kind of background radiation (Section 6.2). As to synergize an optimal detection performance with cost-efficiency, all existing high-energy neutrino observatories consist of optical detection modules sparsely arranged over large

[2]The remaining part is contained within the hadronic cascade.

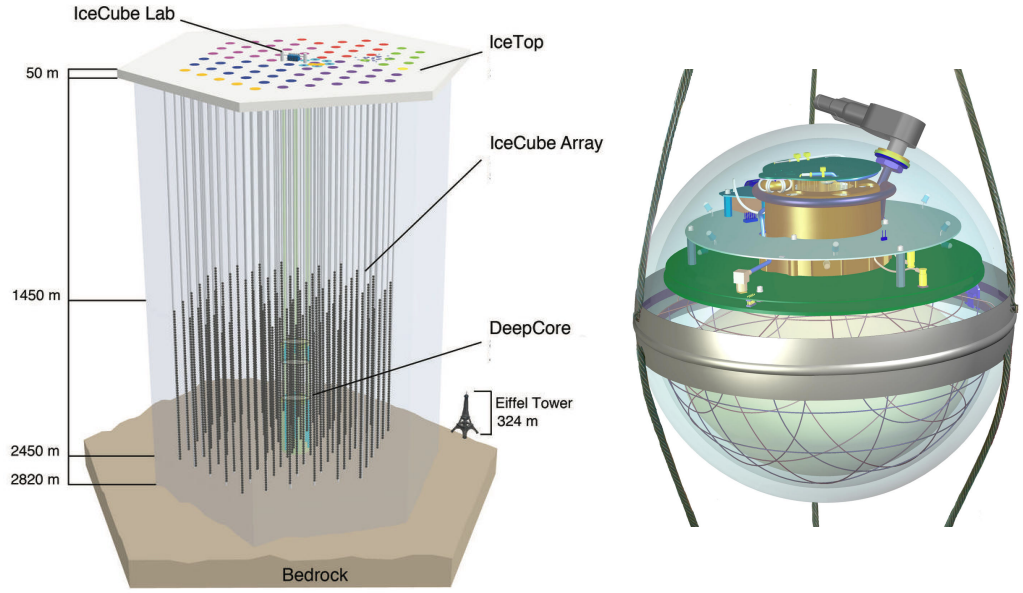

Figure 6.5: **Left:** Schematic sketch of the IceCube detector. Figure taken from [138]. **Right:** Illustration of an IceCube DOM, containing a photo-multiplier tube and a circuit board for data acquisition, high-voltage generation, etc. (Section 6.5) [136, 139]. Figure taken from [140].

volumes. The exact distribution of these modules depends on the precise characteristics of the surrounding medium as well as the physical hypothesis of interest. To date, four different high-energy neutrino detection sites exist. The IceCube neutrino observatory is the only telescope array arranged in ice, while the KM3NeT, P-ONE and GVD detectors reside in water [132–135]. In the following the IceCube neutrino observatory is introduced. Subsequently some fundamental differences of neutrino detection in ice and water are listed in the last part of this section.

6.4.1 The IceCube Neutrino Observatory

The IceCube Neutrino Observatory is the world's largest neutrino telescope, instrumenting one cubic kilometer of Antarctic ice at a depth between 1450 m to 2450 m [136]. While preliminary data taking started already in 2005 throughout the construction phase, the full detector is operating successfully since 2011 [132].

In addition to the in-ice array of optical detection modules, the observatory includes the IceTop detection array at the surface of the Antarctic ice [137]. A schematic sketch of the IceCube detector is illustrated in the left panel of Figure 6.5.

The detector volume within the ice is instrumented with 86 strings, each equipped

with 60 digital optical detection modules (DOMs). Except from the 8-string DeepCore array in the middle part of the detector [141], the vertical separation between the individual modules is 17 m. The strings are arranged in hexagonal formation with horizontal distances of 125 m. The design of this part of the in-ice array was chosen to achieve the primary science goal of measuring astrophysical neutrinos in the range between TeV and PeV energies, given the optical characteristics of the Antarctic ice [136]. The average optical properties between depths of 1450 m to 2450 m inside the Antarctic ice are summarized in Table 6.1. While the average absorption length Λ_{abs} is of the order of 100 m, the scattering of photons with an effective scattering length $\Lambda_{\text{sct}}^{\text{eff}}$ of 25 m dominates the attenuation of Cherenkov radiation within the ice [142]. Based on this structuring of detection modules, the cubic-kilometer in-ice array is sensitive to neutrino events above 100 GeV [136]. Note that the Antarctic ice is pervaded by different horizontal layers of dust that were composed during its formation, with the most prominent being located at a depth of $\sim$ 2050 m. As a consequence the optical properties in these region differ significantly from the values mentioned above [142].

The IceCube detector can resolve the incoming direction of neutrinos yielding cascade-like event structures with a median angular resolution of 10° - 15°, while the origin of muon neutrinos above 1 TeV with a subsequent muon track can be traced with a median uncertainty of less than 1° [2, 143].

The denser vertical spacing of the modules and the string spacing of the DeepCore sub-array allows more detailed studies of phenomena at a lower energies, with a lower bound at $\sim$ 10 GeV [141]. Since we are mostly interested in extragalactic phenomena of neutrinos at high energies, throughout this thesis this sub-part of the detector is of no particular interest and can just be integrated in the total 86 string in-ice array.

6.4.2 Large Volume Detectors in Water

Similar to the telescopes located in ice, the detection principle for neutrino detectors in water relies on the observation of Cherenkov radiation. Regardless of the many similarities, neutrino detectors in water and ice also face diverse challenges.

One major difference resides in the optical properties of the two media. While scattering from crystal point defects and air bubbles is pervasive in ice, light scattering in water is less prominent. On the other hand light absorption due to electronic and molecular excitation processes happens on a more frequent basis in water than in ice [144]. As previously mentioned in Section 6.2, these optical properties can be characterized by the scattering and absorption lengths. The characteristic values for both measures at different observation sites in water and ice are summarized in Table 6.1.

Experiment	Medium	λ[nm]	Λ_{abs} [m]	$\Lambda^{\text{eff}}_{\text{scat}}$ [m]	$\Lambda^{\text{eff}}_{\text{att}}$ [m]
IceCube	ice	400	~ 100	$\sim$ 25	~ 20
Baikal-GVD	fresh water	475	$\sim$ 22	~ 480	~ 21
KM3NeT	sea water	475	$\sim$ 60	~ 265	~ 49
P-ONE	sea water	465	-	-	~ 35

Table 6.1: Average optical properties for wavelengths λ measured at different neutrino observation sites. The values are taken from [134, 142, 145–147]. The effective attenuation lengths $\Lambda^{\text{eff}}_{\text{att}}$ for IceCube, Baikal-GVD and KM3NeT are evaluated from the respective effective scattering and absorption lengths according to Equation (6.11). For the P-ONE site only preliminary measurements of the attenuation length exist.

While scattering dominates the light propagation in ice, absorption effects determine the spread of Cherenkov photons in water. As a consequence, the detection of direct un-scattered light is feasible over limited distances in water, allowing for a very good angular resolution. As a consequence of the different properties of the two media, the spacing of the optical modules has to be adapted differently for ice and water detectors.

Next to the optical characteristics, general properties of the surrounding medium yield varying challenges. While in-situ background radiation in ice is almost exclusively introduced by the detector itself, bioluminescent organisms and decays of radioactive isotopes induce additional background light in water [144]. Hence, neutrino telescopes in water require more sophisticated methods to suppress this background. Lastly, ambient currents in water can shift the position of the optical modules in water, while the location of the detection modules in ice is fixed. A detailed tracking of the position of the optical modules in water is inevitable to guarantee an optimal directional resolution.

6.5 Data Acquisition in IceCube

The digital optical modules (right panel of Figure 6.5) are the fundamental observation units in IceCube, performing both light detection and data acquisition [136]. As mentioned above, they consist of a downward facing photo-multiplier tube (PMT) and a corresponding circuit board, that controls data acquisition, communication and low-voltage power conversion.

If a photon hits a PMT it induces an electric charge. In case this charge exceeds a threshold 0.25 pe the DOM registers a *hit*, recording the PMT waveform for 6.4 μs (1 pe is defined as the most likely charge deposit caused by a single photon at a typical PMT gain of 10^7) [136]. To ensure optimal data taking over this time window and large

dynamic ranges, each PMT is complemented with two different types of digitizers: an Analog Transient Waveform Digitizer (ATWD) and a Fast Analog to Digital Converter (FADC) [136]. The ATWDs sample the waveform at ~ 3.3 ns intervals for a total time of 427 ns. To provide a wide dynamic range each ATWD contains multiple channels with different amplification gains. Each DOM is equipped with two independent ATWDs operating alternately to reduce readout dead time. While the recording time of the ATWDs is optimized for photons generated close to the respective DOM, the characteristics of the additional FADC are selected to cover the time range of the remaining light production. As such the FADC observes the PMT waveform at a continues sampling rate of 25 ns over a total readout time of $6.4\,\mu$s [136].

Once a hit is recorded, the corresponding information is sent to the IceCube Laboratory (ICL) at the surface. The amount of information that is transmitted depends on the presence of locally coincident hits at nearest or next to nearest neighboring DOMs from the same string. If such local coincident hits are launched within $\pm 1\,\mu$s, they are flagged as a hard local coincident hits (HLC). For HLC hits the fully digitized waveform information from the ATWD and the FADC are transmitted to the ICL. Isolated hits with no HLC are referred to as soft local coincidence (SLC). In this case only three sample points from the FADC waveform centered around the peak of the distribution are saved and transmitted. This data acquisition format is motived by the fact that HLC hits indicate regions with a high probability to observe multiple photons. While these waveforms assembled from multiple photons can have complex devolutions, the distribution from single photon hits (as presumably the case for SLC hits) can be usually characterized by a limited amount of parameters [136].

At the surface these hits are searched for multiplicity criteria in order to reconstruct the potential light pattern induced by charged particles. While SLC hits are dominantly generated by dark noise, only HLC hits are utilized for these selections. The Simple Multiplicity Trigger 8 (SMT8) illustrates the first selection criteria for events used throughout the following thesis. This trigger condition requires at least eight HLC hits within a sliding time window of $5\,\mu$s. Ultimately a IceCube event is made up of HLC hits with trigger windows overlapping within sliding time differences of $-4\,\mu$s to $6\,\mu$s. SLC hits that reside within the total time window complement the event. The event rate at the SMT8 trigger level is vastly dominated by atmospheric muons and typically varies between 2.5 kHz to 3 kHz (left panel in Figure 7.7).

In order to provide scientists from outside the South Pole station with the observed data, IceCube uses the transmission via a satellite. The rate of events from SMT8 trigger vastly exceeds the bandwidth of this satellite. Hence the data volume at the South Pole is further reduced by processing and filtering of the triggered events. As

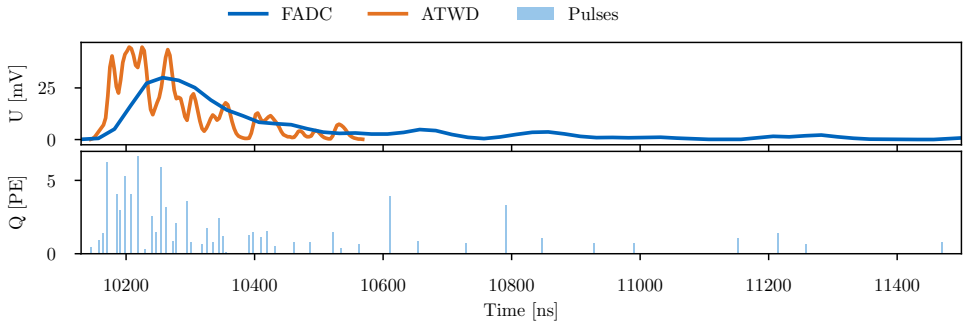

Figure 6.6: Illustration of the conversion of the observed ATWD and FADC waveforms (top panel) into a series of pulses (bottom panel) at one DOM. The time on the x-axis depicts the absolute time within the event trigger window. The data in the figure was elaborated by T. Glauch.

such, the digitized waveforms are calibrated and converted into a more compact series of so-called *pulses*. Each pulse contains a charge amplitude, a pulse width and the corresponding leading edge time. This conversion is illustrated in Figure 6.6. Besides this data compression the events are further filtered according to specific requirements of interest. Since we are interested in correlating the direction of neutrino induced events with astrophysical events, the so-called muon filter is most relevant in this work. Based on fast and computationally inexpensive reconstructions, this filter selects good reconstructed track-like events from both hemispheres (Subsection 6.3.2). For down-going events from the Southern hemisphere ($\delta < -5°$) an additional zenith dependent cut on the total deposited charge is applied to reduce the dominating part of the background coming from atmospheric muons. Applying the data processing and the muon filter reduces the event rate to $\sim 34\,\mathrm{Hz}$ [136]. After the transfer to the north, these events build the starting point for many high level analyses in IceCube (Section 7.2).

7

Search Methods for Neutrino Point Sources

High-energy astrophysical neutrinos leave a designated light signature when they interact in optically transparent media (Section 6.3). While the low interaction cross-sections depict severe challenges in their detection, they make neutrinos perfect pointers towards their origin. As such, high-energy neutrinos can be considered as astrophysical messengers, providing information from the farthest reaches of the Universe. In principle, a single astrophysical neutrino could be enough to identify the location of its site of generation. Unfortunately, this straight forward correlation between the astrophysical neutrino signatures and the position of their sources is diluted in actual observations.

Large area neutrino telescopes, such as the IceCube Observatory are built deep within the ground to be shielded against obvious electromagnetic radiation. Nevertheless, atmospheric muons and neutrinos can reach these detectors and generate light patterns that are nearly indistinguishable from the signal of astrophysical sources. These atmospheric leptons depict the major background in the observation of astrophysical neutrinos and in particular in the discovery of their sources. They dominate the rate of triggered events in IceCube by orders of magnitude above the expected astrophysical signal (left panel of Figure 7.7). While it is nearly impossible to rule out an atmospheric background origin on an event by event basis, IceCube applies a different strategy to overcome the vast atmospheric background contamination in the search for astrophysical neutrino sources on a statistical basis.

Neutrinos generated at the site of astrophysical point-like objects are supposed to cluster on small angular scales around the location of the source. The angular spread of these events depends on the accuracy of their directional reconstruction inside the detector. On the other hand, cosmic-rays bombard the Earth uniformly from all directions, yielding a locally uniform distribution of the overall dominating atmospheric background. Hence a high local density of events is a typical signature of astrophysical

neutrino generators. The average number of background events decreases with decreasing size of the cluster window, allowing a better signal to background discrimination for accurately reconstructed events. As a consequence we will only use track-like events throughout the following thesis, permitting the best directional accuracy (Section 6.3). Next to the directional information of triggered events, their energy information can be utilized to differentiate between astrophysical signal and atmospheric background. According to the most common shock acceleration models at the site of astrophysical objects, neutrino sources are supposed to generate neutrinos following a simple power-law spectrum with spectral index of ~ 2 or even harder (Subsection 4.2.1). Neutrinos and muons from atmospheric air showers, on the other hand, present a much softer spectrum, approximately following a ~ 3.5 power-law distribution above a few GeV (refer to Figure 5.2). In such a scenario the rate of background events drops much faster with increasing energy than the corresponding astrophysical signal.

Both directional and energy information of events can be used in cooperation to discriminate between the signal of astrophysical point sources and atmospheric background fluctuations. In order to quantify the significance of a potential signal, we make use of unbinned likelihood ratio tests in the following. Since the analyses performed in this thesis seek for local accumulations of events, they operate best on large statistical samples with a high astrophysical signal purity and well-defined event characteristics. The latter can be achieved by the reconstruction of the light patterns appearing within the detector volume. The proceeding of the directional and energy reconstruction for track-like events in IceCube is summarized in Section 7.1. The selection of the event sample optimizing the performance of point source searches in IceCube follows in Section 7.2. Ultimately the statistical method and their performance in IceCube are introduced in Section 7.3 and 7.4.

7.1 Reconstructions of Characteristic Event Features

The direction and the energy of muons in ice are strongly correlated with the Cherenkov radiation emitted along the path. Hence both event characteristics can be reconstructed from the combined light patterns measured by the optical modules in the detector. These reconstructions suffer several disturbances in IceCube. Scattering and absorption in the ice influences the dispersion of the emitted Cherenkov photons. Additionally, noise from radioactive decays inside the glass sphere of the DOMs affects the correlation between the observed light patterns and the true physics parameters of the incident

particles [139]. The directional and energy reconstruction methods for muons[1] that are introduced in the following aim to overcome these challenges.

7.1.1 Directional Reconstructions

Muons traveling through the Antarctic ice induce Cherenkov light along their path. In an ideal scenario, the time evolution of this radiation forms a Cherenkov cone with an opening angle ϑ along the path of the muon (Section 6.1). In combination with the long traveling distance of high-energy muons (on average multiple kilometers for muons above a few TeV), the detectable Cherenkov light allows for accurate directional reconstructions. As visible in Figure 6.3 the time-integrated light emission in ice has a cylindrical spread around the path of the muon. Once a high-energy muon traverses the detector volume, nearby DOMs record a series of pulses characterizing the detection time t_i and the charge q_i of the observed light at the position of the respective module $\mathbf{d}_i$ (Section 6.5).

In the following, the evolution of a muon in the detector will be parameterized by a straight line

$$\mathbf{x}(t) = \mathbf{x}_0 + \mathbf{v}_\mu \cdot (t - t_0), \tag{7.1}$$

where $\mathbf{x}_0$ is the support vector of the muon at time t_0 and $\mathbf{v}_\mu$ is the velocity of the muon. For high-energy muons, the track length exceeds the maximal detection range ($\sim 1\,\mathrm{km}$ for IceCube). Hence most muons observed within the detector originate from outside this volume and we will assume an infinitely long muon track in the following. Due to this supplement, the support vector $\mathbf{x}_0$ can be chosen arbitrarily along the path. High-energy muons nearly travel at the speed of light in vacuum ($\|\mathbf{v}_\mu\| \gtrsim 0.99c$ for $E_\mu > 1\,\mathrm{GeV}$). Hence the number of free parameters a of the geometrical coordinates (Equation (7.1)) for muons can be reduced from six to five. In IceCube a commonly used representation is $a = \{x_0, y_0, z_0, \theta, \phi\}$.

Due to the limited computing power at the South Pole and the convergence stability of the algorithms, IceCube performs a consecutive chain of reconstruction algorithms. At the site of the detector, fast and simplified reconstruction methods are applied to the data. Their outcomes are then used to filter the data and seed more complex algorithms that are applied after the data transfer.

[1] Muons from astrophysical neutrinos are mainly generated in CC interactions of muon and tau neutrinos (Section 6.1).

Linefit

The simplest directional reconstruction algorithm that is used is called *LineFit*. This method aims to minimize the distance between the first hit at each triggered DOM and the hypothetical muon track, ignoring the shape of the Cherenkov cone and any impacts of the surrounding media. In this sense the position of the hit DOMs are projected on the path of the muon

$$\widetilde{\mathbf{d}}_i = \mathbf{x}_0 + \mathbf{v}_\mu \cdot t_i^{\mathrm{1st}}, \tag{7.2}$$

where t_i^{1st} is detection time of the first photon hit a DOM i. The evolution of the muon track can be evaluated by minimizing

$$\sum_i^{N_{\mathrm{DOM}}} \left(\mathbf{d}_i - \widetilde{\mathbf{d}}_i\right)^2 \tag{7.3}$$

with respect to the support vector x_0 and the velocity $\mathbf{v}_\mu$, where N_{DOM} is the number of hit DOMs. This problem can be solved analytically allowing for a very fast evaluation of a simplified first guess for the direction of the muon. Unlike in the infinite track approximation from above, this algorithm does not require the assumption that the muon travels at the vacuum speed of light but actually is sensitive to the velocity of the particle. As such, in the ideal case, *LineFit* recovers the speed of light c for muons while the particle velocity is approaching 0 for spherically symmetric events [148].

Maximum Likelihood Estimators

More sophisticated reconstructions incorporate the physics of the light propagation in ice. This mainly includes the time emission profile corresponding to the Cherenkov cone as well as scattering and absorption effects in the ice. Assuming again an infinitely long muon track moving at the speed of light in vacuum, we can estimate the geometrical arrival time of Cherenkov photons at DOM k according to

$$t_{\mathrm{geo}}^k = t_0 + \frac{d_\mu}{\|\mathbf{v}_\mu\|} = t_0 + \frac{\mathbf{e}_\mu \cdot (\mathbf{d}_k - \mathbf{x}_0) + d_\perp \tan(\vartheta)}{c}, \tag{7.4}$$

where $\mathbf{e}_\mu$ is the direction of the muon and ϑ is the Cherenkov angle [148]. The remaining variables follow the definitions given in the left sketch of Figure 7.1. This geometrical time corresponds to the arrival time of Cherenkov photons unaffected by scattering and absorption. The time delay t_{res} that a photon i experiences on its way to DOM k due

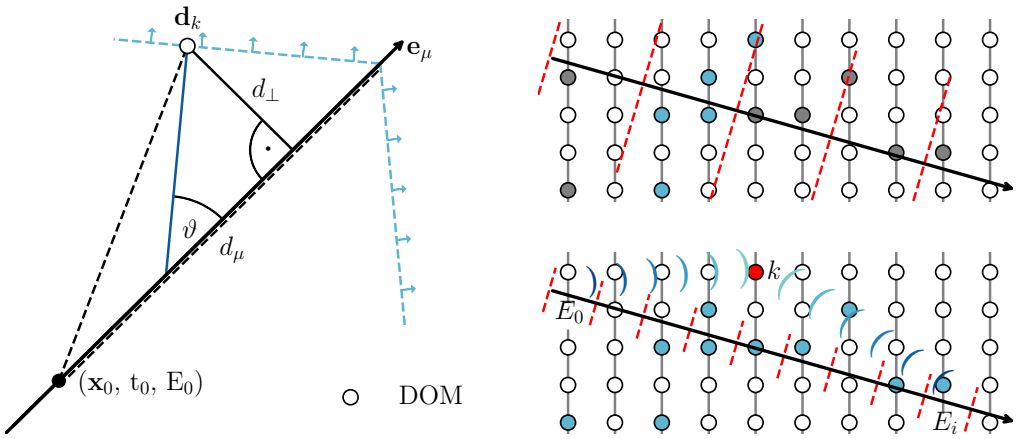

Figure 7.1: **Left:** Illustration of the photon propagation along a high-energy muon track ($\|\mathbf{v}_\mu\| = c$) in an optically perfect medium. The sketch includes all observable quantities that are necessary to estimate the geometrical arrival time t_{geo} of a photon at DOM k. **Right:** Illustration of the segmented (top panel) and the unfolding (bottom panel) muon energy reconstruction principle used in IceCube.

to these effects can be defined as

$$t_{\text{res}}^{ik} \coloneqq t_{\text{hit}}^{ik} - t_{\text{geo}}^{k}, \tag{7.5}$$

where t_{hit}^{ik} is the observed time of the hit [148]. Based on the knowledge of the probability distribution p of these time residuals we can determine a single photo-electron (SPE) likelihood function

$$\mathcal{L}_{\text{SPE}} = \prod_{k} \prod_{i \text{ at } k} p\left(t_{\text{res}}^{ik} | \{a_\mu\}, \{a_{\text{Det}}\}\right), \tag{7.6}$$

where the index k loops over all triggered DOMs with respective photo-electron hits i [148, 149]. Maximizing the likelihood with respect to $\{a_\mu\}$ yields the description of the corresponding muon path according to Equation (7.1). The parameter set $\{a_{\text{Det}}\}$ includes all relevant detector properties, such as the position and orientation of the individual DOMs and the properties of the surrounding ice.

While the formulation of the single photo-electron likelihood in Equation (7.6) is optimal in theory, it suffers limitations due to the finite time resolution of the detector modules. The arrival times of individual photons from the same muon cannot be distinguished at a specific DOM, but only the arrival time of the first pulse is recorded

[148]. Hence only the first photon hit at each DOM can be used in the SPE approach in IceCube. In order to incorporate the available information of the remaining photon hits we can adapt the SPE likelihood to a multi photo-electron likelihood (MPE) according to

$$\mathcal{L}_{\mathrm{MPE}} = \prod_{k}^{N_{\mathrm{DOM}}} N_k \cdot p\left(t_{\mathrm{res}}^{0k} | \{a_\mu\}, \{a_{\mathrm{Det}}\}\right) \cdot \left(\int_{t_{\mathrm{res}}^{0k}}^{\infty} p\left(t | \{a_\mu\}, \{a_{\mathrm{Det}}\}\right) \mathrm{d}t\right)^{N_k - 1} . \tag{7.7}$$

At each triggered DOM k the MPE method makes use of a first order stoachstic distribution, describing the probability to observe the first photon at t_{res}^{0k} followed by $N_k - 1$ subsequent hits [148].

In the ideal case, the probability distribution p of these time residuals should be a delta function at zero. Yet in realistic scenarios, the arrival times of photons originating from high-energy muons are delayed due to their generation in radiative processes and the scattering processes in the ice. While the first distortion can be added to the probability distribution on a stochastic basis, the latter effect depends on the distance between the muon and the respective DOM as well as the respective ice conditions on that photon path [148]. In addition, random noise hits and the limited timing resolution of the modules symmetrically broaden the distribution around $t_{\mathrm{res}} = 0$, allowing also for negative time residuals.

A fast analytic approximation for these pdfs is realized by

$$p_{\mathrm{ana}}(t_{\mathrm{res}}) \propto \frac{\tau^{-d_\perp/\lambda_s} \cdot t_{\mathrm{res}}^{d/\lambda_s - 1}}{\Gamma(d_\perp/\lambda_s)} \cdot \exp\left(-\frac{d_\perp}{\lambda_a} - t_{\mathrm{res}} \cdot \left(\frac{1}{\tau} + \frac{c}{n\lambda_a}\right)\right), \tag{7.8}$$

where λ_a represents the average absorption length in ice and n the refractive index. The free parameters τ and λ_s are determined by Monte Carlo simulations [148]. For low distances $d_\perp$ this function sharply peaks close to $t_{\mathrm{res}} = 0$ corresponding to mostly unscattered photons. For larger distances between the muon and the detection module it allows scattering and subsequently yields larger delay times. The analytic distribution p_{ana} for different distances is illustrated in the left panel of Figure 7.2. While reconstructions relying on this analytic distribution incorporate generic ice properties without making concessions in the computational performance, local characteristics of the surrounding media are ignored. The optical properties in IceCube perceive drastic depth dependent fluctuations due to contamination with dust (Subsection 6.4.1). In order to incorporate such information into the reconstructions, tabulated simulations of detailed light propagation in the Antarctic ice are used. These simulations are interpolated with multi-dimensional splines allowing for efficient storage and fast access throughout

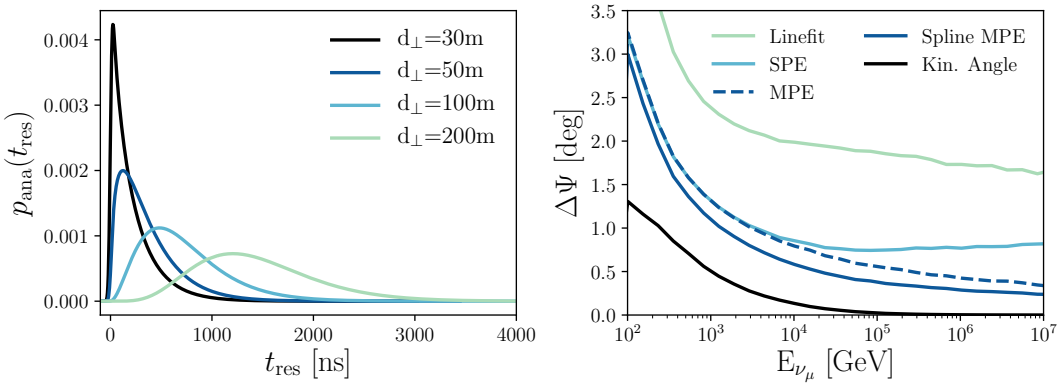

Figure 7.2: **Left:** Analytic distribution of the photon delay time for different distances to the muon track. In order to account for the limited timing resolution of the PMTs, the pdfs from Equation (7.8) are convoluted with a gaussian distribution around t_{res} and standard deviation of 15 ns [150]. **Right:** Median angular resolution $\Delta\psi$ for different directional reconstructions. The black line indicates the influence from the kinematic angle between the neutrino and the muon (Figure 6.4).

the reconstruction. The reconstruction based on these simulated spline tables, called SplineMPE, yields the best performance at the expense of an intensive computational effort [151]. To account for the limited timing resolution of the PMTs in the individual DOMs all pdfs mentioned above are convoluted with a gaussian distribution

$$p(t_{\mathrm{res}}) = \int_0^\infty p_X(t_{\mathrm{res}}) \cdot \frac{1}{\sqrt{2\pi}\sigma_t} e^{-(t_{\mathrm{res}}-x)^2/2\sigma_t^2} dx \tag{7.9}$$

where p_X can represent both, the analytic as well as the tabulated description of the delay time probability [150]. The parameter σ_t depicts the standard deviation of the gaussian distribution. The performance of different direction reconstructions mentioned in this subsection are illustrated in the right panel of Figure 7.2. Note that although the likelihood reconstructions are based on the assumption of an infinite muon track, these algorithms are also used for events starting within the detector volume in this thesis.

The capability and the accuracy of the directional reconstructions in IceCube can be tested by means of measurements of the muon deficit from the direction of the moon. While the incoming direction of atmospheric muons should, in general, mimic the almost isotropic distribution of their generating cosmic-ray particles, a muon deficit is expected from the direction of the moon. The lower rate from this direction is caused by the absorption of cosmic-rays in the moon and the subsequently missing production

of secondary muons in the atmosphere. Since muons above TeV energies are strongly aligned with the incoming direction of their generating cosmic-ray, they can optimally reveal the location of this cosmic-ray absorption. Making use of the most advanced directional reconstruction mentioned above, IceCube observes the location of this so-called *moon shadow* within 0.2° of its expected position. This outcome serves as a simulation independent validation of the average capability of the directional reconstructions in IceCube [143].

Uncertainty Estimation

Based on the aforementioned likelihood reconstructions, an angular uncertainty estimate of the muon direction can be evaluated on an event-by-event basis. While in principle a detailed scan of the likelihood space around the maximizing[2] values $\{\bar{a}_\mu\}$ would be desirable for the uncertainty estimation[3], it is computationally not feasible for the high-level reconstructions in IceCube.

Instead, in order to access the uncertainty from the likelihood space, IceCube makes use of several simplifying assumptions. Primarily, the dimension of the problem is reduced by marginalizing over the vertex parameter $\mathbf{x}_0$ (Equation (7.1)), leaving a two dimensional likelihood landscape $\mathcal{L}(\mathbf{a}_{\text{red}})$ with $\mathbf{a}_{\text{red}} = (\theta, \phi)$. Secondly this two dimensional likelihood space is supposed to be normal distributed around the maximum values $\lambda = (\bar{\theta}, \bar{\phi})$ with

$$\mathcal{L}(\mathbf{a}_{\text{red}}) \sim \frac{1}{\sqrt{4\pi^2 \det(\Sigma)}} \exp\left(-\frac{1}{2}(\mathbf{a}_{\text{red}} - \lambda)^\intercal \Sigma^{-1} (\mathbf{a}_{\text{red}} - \lambda)\right), \tag{7.10}$$

where Σ depicts the covariance matrix of the distribution

$$\Sigma = \begin{pmatrix} \sigma_\theta^2 & \sigma_{\theta\phi} \\ \sigma_{\theta\phi} & \sigma_\phi^2 \end{pmatrix}. \tag{7.11}$$

As a consequence, the negative logarithm of this likelihood function follows a bi-dimensional parabolic distribution in the region around λ

$$-\log \mathcal{L}(\mathbf{a}_{\text{red}}) \sim \log\left(\sqrt{4\pi^2 \det(\Sigma)}\right) + \frac{1}{2}(\mathbf{a}_{\text{red}} - \lambda)^T \Sigma^{-1} (\mathbf{a}_{\text{red}} - \lambda). \tag{7.12}$$

The so-called *paraboloid* uncertainty estimate makes use of these assumptions. Since a

[2] In fact, instead of maximizing the likelihood function itself, the negative logarithm of the likelihood function is minimized in IceCube.

[3] Applying Wilks theorem this would directly yield an approximation for any uncertainty contour [152].

full likelihood scan is not feasible, the $-\log\mathcal{L}$ values are solely evaluated on 8 points on each of three rings around the minimum λ. Using the method of least squares a paraboloid function is fit to these points. As the full covariance information is contained within the paraboloid representation, the resulting gaussian uncertainties for both angles can be read directly from the covariance matrix Σ. In general these uncertainties form a confidence ellipse. To simplify the employment in point source analyses, in the following the elliptical uncertainties are approximated by a single circular uncertainty estimate σ_p according to

$$\sigma_\mathrm{p} = \sqrt{\frac{\sigma_1^2 + \sigma_2^2}{2}}, \tag{7.13}$$

where σ_1 and σ_2 depict the major and minor axis of the ellipse[4]. By means of the paraboloid uncertainty, the angular distribution around the true direction λ can be described by a normal distribution according to

$$f(\theta, \phi|\lambda, \sigma_\mathrm{p}) = \frac{1}{2\pi\sigma_\mathrm{p}^2} \exp\left(-\frac{1}{2\sigma_\mathrm{p}^2}((\theta, \phi) - \lambda)^2\right) \tag{7.14}$$

In this scenario σ_p illustrates the one dimensional uncertainty for both angles θ and ϕ, in a sense that it respectively describes the 68 % probability that the true angle i is within the range σ_i, with $i \in \{\theta, \phi\}$. In order to estimate the probability for both variables to be within the error circle we have to integrate the underlying normal distribution from Equation (7.14) over the area of the circle, yielding

$$\int_0^{\sigma_\mathrm{p}} \int_0^{2\pi} f(r\cos\nu, r\sin\nu) r \,\mathrm{d}r \,\mathrm{d}\nu = -\exp\left(-0.5r^2/\sigma_\mathrm{p}^2\right)\Big|_0^{\sigma_\mathrm{p}} \sim 0.39 \tag{7.15}$$

where we used the polar coordinate representation ($\theta = r\cos\nu, \phi = r\sin\nu$) for the integration. Hence the chance for both true angles to be within the error circle is only $\sim$ 39 %. For the point source analysis in this thesis we are interested in the median angular resolution of individual events. According to Equation (7.15) the original paraboloid value has to be extended by a factor of $\sqrt{-2\log(0.5)} \sim 1.17$ to fully cover this 50 % contour. In this sense the true direction of the event resides within the contour defined by $\sigma_\mathrm{p}^\mathrm{corr} \coloneqq 1.17\sigma_\mathrm{p}$ in 50 % of the cases. More detailed information about the paraboloid reconstruction can be found in [153, 154].

Within the framework of the point source analysis, the paraboloid value is used as an uncertainty estimate for the angular difference $\Delta\psi$ between the direction of the neutrino

[4]The correlation term from the covariance matrix is ignored in this circular approximation.

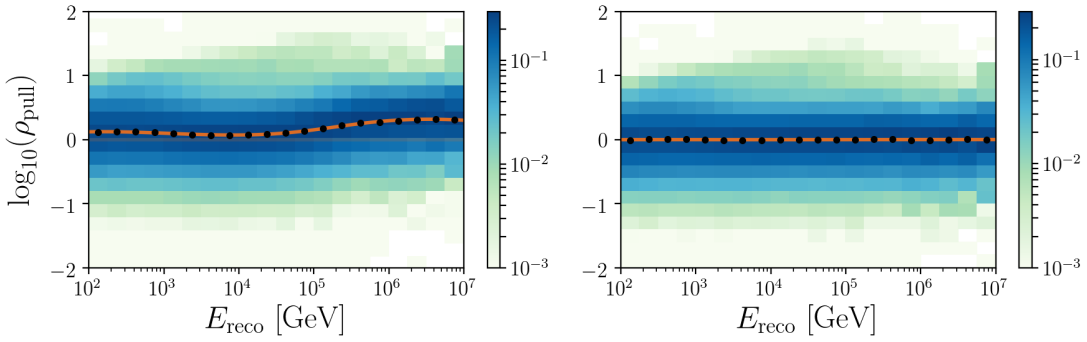

Figure 7.3: Illustration of the pull correction for a neutrino source following a power-law spectrum with γ. The color indicates the probability density normalized along each energy bin. The black dots indicate the median pull value in each energy bin, with the orange line being a spline fit through these median points. **Left:** Pull distribution before the correction. **Right:** Pull distribution after the application of the event-by-event correction from Equation (7.16).

and the observed event (Equation (7.41)). In order to verify this application, two more points have to be considered. At first, it is worth noting that the angular distance defines the angle between two unit vectors on a sphere. This definition is not similar to the projection of a circular contour on a sphere. In fact, while both interpretations are nearly identical[5] at the horizon, major differences occur in the region of the poles where both angles are distorted. In the construction of the paraboloid uncertainty, this problem is prevented by a rotation of the best fit angles λ to the horizon. For not too large error contours, the definition of the paraboloid uncertainty matches that of the angular difference. The back transformation to the original coordinates of the event preserves that correlation. As a consequence, the application of the paraboloid uncertainty $\sigma_{\mathrm{p}}^{\mathrm{corr}}$ as an estimate for the median angular uncertainty seems legitimate for track-like events in IceCube.

In an ideal world, where all previous approximations are satisfied, the paraboloid uncertainty is similar to the median angular difference between the true and the observed direction of the muon. In order to get an estimate for the angular difference between the reconstructed direction and the parent neutrino we have to account for the kinematic angle between both particles (Subsection 6.3.2). Since this angle is generally not observable in IceCube, the respective correction is done on a statistical basis. The so-called *pull* correction relates the paraboloid uncertainty $\sigma_{\mathrm{p}}^{\mathrm{corr}}$ to the true median angular difference $\Delta\psi^{\mathrm{True}}$ between the neutrino and the reconstructed direction in

[5] This is only true if the radius of the circle is not too large.

different energy bins

$$\rho_{\text{pull}}(\log E_\nu) = \frac{\Delta\psi^{\text{True}}}{\sigma_{\text{p}}^{\text{corr}}}. \tag{7.16}$$

In the ideal case, the paraboloid uncertainty depicts a correct representation of the true distribution, their pull values ρ_{pull} are exactly one. In order to account for deviations from the ideal case, the paraboloid uncertainty σ_i for each event i is corrected according to the pull at its energy

$$\sigma_i(\log E_\nu) = \rho_{\text{pull}}(\log E_\nu) \cdot \sigma_i(\log E_\nu). \tag{7.17}$$

The pull correction is illustrated in Figure 7.3.

While the pull correction is mainly thought to account for the kinematic angle between the muon and the neutrino, it is also capable to compensate discrepancies of the paraboloid approach on a large statistical basis. In fact, while the paraboloid construction seems to work fine on a statistical basis it is not optimal on an event-by-event basis. The issues with the approach can be attributed to multiple causes. Due to sparse sampling, the likelihood landscape of individual events might not be accurately described and the paraboloid fit might not even be possible. On the other hand, also an incorrect description of the track hypothesis in the likelihood might yield incorrect outcomes. A full study of the paraboloid construction is beyond the scope of this thesis. More detailed information can be found for instance in [155].

7.1.2 Energy Reconstructions

Similar to the directional information, the energy of a high-energy muon is correlated with the Cherenkov light emitted by the muon itself and subsequent products along its path. Muons traveling through the ice lose energy due to ionization and stochastic processes (Figure 6.4). The average energy loss can be quantified by Equation (6.12). While high-energy muons travel long distances through the ice, the IceCube observatory can only observe the Cherenkov radiation of the segment L appearing within the detector volume. Hence according to Equation (6.12), the average muon energy at entry in the detector can be estimated as

$$E_\mu^{\text{entry}} \sim \frac{\frac{\mathrm{d}E_\mu}{\mathrm{d}L} - a_{\text{I}}}{a_{\text{St}}}, \tag{7.18}$$

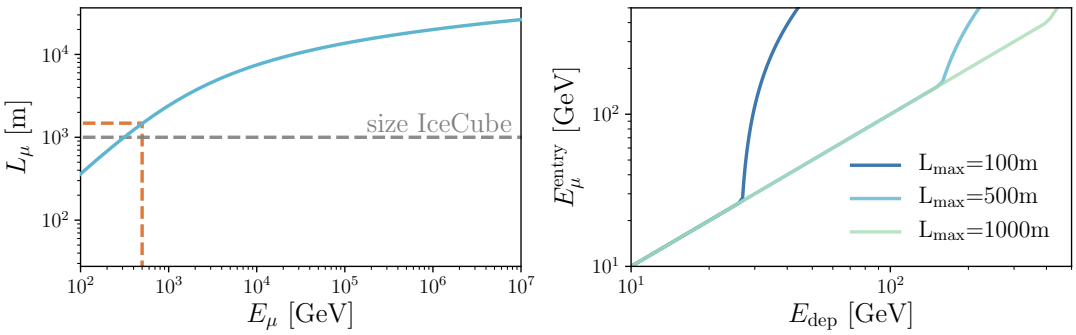

Figure 7.4: **Left:** Muon track length (blue line) in ice according to Equation (6.13). The orange dashed line indicates the energy threshold from the ionization dominated region at low energies to the high-energy regime where stochastic losses dominate. **Right:** Correlation between the total deposited energy and the muon energy at entry for different maximally possible track lengths L_{max} in the detector.

where $\frac{\mathrm{d}E_\mu}{\mathrm{d}L}$ is the deposited energy along the segment L. If the muon starts outside the detector volume this energy only displays a lower limit on the actual muon energy. Note that in principle, this approach is limited to the region above $\sim 500\,\mathrm{GeV}$ where stochastic losses induce deviations from the constant emission due to ionization. For muons that are dominated by ionization losses, Equation (7.18) does not seem to have discrimination power between different energies. Yet, as a matter of fact the average traveling distance of muons within the ice is at a similar scale as the detector size at these energies. The average traveling distance of muons within ice for different energies is illustrated in the left panel of Figure 7.4. If the muon path is shorter than the maximally possible length within the detector, the total deposited energy in the detector E_{dep} decreases even within the ionization regime. Even without knowing the actual length within the detector, the deposited energy in the detector can be used to estimate the muon energy E_μ^{entry} in such scenarios. The correlation between the deposited energy and E_μ^{entry} at low energies is shown in the right panel of Figure 7.4.

The deposited energy within the detector can be reconstructed from the observed Cherenkov light. Similar to the directional reconstruction, the deposited energy is estimated by the use of a maximum likelihood approach where the likelihood to see k_j hits at DOM j is given by a poissonian distribution

$$\mathcal{L}_j = \frac{\lambda_j^{k_j}}{k_j!} \cdot e^{-\lambda_j}. \tag{7.19}$$

The expected number of photon hits λ_j strongly depends on the optical properties of the ice surrounding the detection modules. Using Monte Carlo simulations the expected amount of photons can be estimated from the muon energy E_μ according to

$$\lambda_j = \Lambda_j \cdot E_\mu + \rho_j, \tag{7.20}$$

where Λ_j depicts the light production yields and ρ_j the noise expectation, both coming from simulations [126]. In principle, the average muon energy loss along the path L in the detector could be estimated by maximizing the product of likelihoods at all DOMs with respect to E_μ. Yet this approach suffers significant biases due to the stochastic processes that dominate the light yields for muons above a few TeV [126]. The stochasticity of the energy deposition can be included in the reconstruction by segmenting the muon track into little pieces that can catch up these variations.

This can be achieved by separating the muon track into different pieces and assigning the light yields from each DOM to one of these segments. This approach is illustrated in the top right panel of Figure 7.1. The energy depositions in the respective segment l can be evaluated similarly to above by maximizing

$$\log \mathcal{L}_{E_l}^{\text{seg}} = \sum_{j \in S_l} \left(k_j \log \left(\Lambda_j E_l + \rho_j \right) - \left(\Lambda_j E_l + \rho_j \right) - \log(k_j!) \right) \tag{7.21}$$

with respect to E_l. S_l depicts all DOMs belonging to segment l. Each segment can be treated as an individual detector system in this approach (top right panel of Figure 7.1). The optimal length of the segments depends on the spacing of the DOMs as well as the optical properties and it is typically in the order of $\sim 100\,\text{m}$ [126]. The energy loss $\frac{\mathrm{d}E}{\mathrm{d}L}$ within the detector can be estimated by taking the sum of the outcomes of the individual segments. Eliminating the segments with the highest energy losses removes biases due to large statistical fluctuations from the reconstruction and yields results more closely correlated to the muon energy at entry in the detector [130]. The accuracy of the segmented muon energy reconstruction in IceCube is shown in the left panel of Figure 7.5. Above $\sim$ TeV energies the reconstruction nicely recovers the muon energy at entry. At lower energies stochastic losses become subdominant and the segmented reconstruction, although theoretically possible, can not distinguish between these energies anymore. The right panel in Figure 7.5 shows the comparison between the reconstructed muon energy at entry and the original neutrino energy for a $\gamma = 2$ power-law spectrum. At the lowest energies, the muon travel distance is in the order of the size of the detector. Hence the muon energy at entry could give on average a measure for the absolute neutrino energy. Yet due the sub-optimal performance of the segmented

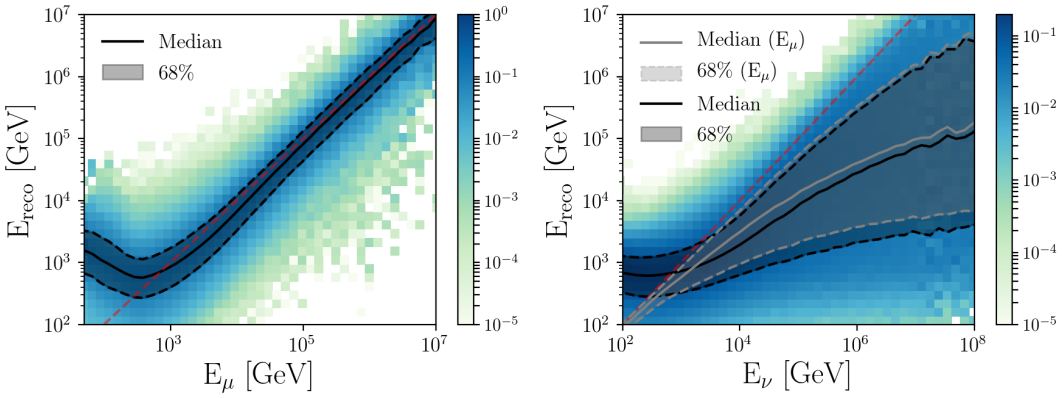

Figure 7.5: Illustration of the accuracy of the truncated muon energy reconstruction used in the point source searches in IceCube. **Left:** Comparison between the reconstructed and the true muon energy at entry in the detector. **Right:** Comparison between the reconstructed muon energy at entry and the original neutrino energy for an unbroken $\gamma = 2$ power-law spectrum (black). In addition, the average deviation between the actual muon energy at entry and the neutrino energy is shown (grey). The red dashed lines in both plots indicates the region of perfect agreement between reconstructed and true values.

algorithm, this correlation is diluted and the reconstructed values overshoot the actual neutrino energies on average. For higher energies, the performance of the reconstruction improves while the average travel distance of the muon exceeds the detector volume. Consequently, as expected, the reconstructed muon energy at entry only serves as a lower limit on the primary neutrino energy for such events.

Despite being fast, the spatially segmented approach can not describe the physics of the energy depositions along the muon track perfectly. While stochastic energy losses can happen at scales much smaller than the segmentation, their light yields could travel much further than the distances assigned by the separation of the detector. Instead of spatially segmenting the detector along the path of the muon, we can split the energy production along the track into different individual sources. In this physically more realistic scenario the expected light yield at each DOM j is a superposition of light from all stochastic losses

$$\lambda_j = \sum_s \Lambda_j(\mathbf{x}_j, \mathbf{x}_s) \cdot E_s + \rho_j = \mathbf{\Lambda}_j^T \cdot \mathbf{E} + \rho_j, \tag{7.22}$$

where s indicates the sources of energy depositions in the detector and $\mathbf{x}_s$ their position along the track. This approach is schematically illustrated in the lower right panel of

Figure 7.1.

The energy depositions along the muon track can be evaluated by maximizing

$$\log \mathcal{L}^{\text{unfold}} = \sum_j \left(k_j \log \left(\mathbf{\Lambda}_j^T \cdot \mathbf{E} + \rho_j \right) - \left(\mathbf{\Lambda}_j^T \cdot \mathbf{E} + \rho_j \right) - \log(k_j!) \right) \tag{7.23}$$

The main difference between this energy unfolding and the spatial segmentation relies on the fact that the energy depositions in the unfolded energy vector $\mathbf{E}$ are correlated with the whole detector while they were only connected to the corresponding detector segment in the spatial separation approach. The evaluation of $\mathbf{E}$ comes at high computational costs. Since the analysis performed in this thesis are based on high statistic samples this reconstruction technique is not applied. Hence the spatial segmentation technique is used in the following.

7.2 Through-going Track Selection

The searches for astrophysical neutrino point sources in IceCube use statistical techniques to filter out subleading astrophysical signals from the dominating atmospheric background. To ensure optimal performance of such tests the data transmitted from the South Pole is further purified. The main goal of this selection is the reduction of the atmospheric background without losing astrophysical signal events in order to achieve a high statistic neutrino sample with high purity. The event selection used for the analyses in this work is described in detail in [156, 157]. The main aspects and the general approach are summarized in the following section.

Muons generated in CC interactions of muon neutrinos within the ice induce light along their elongated travel path allowing for optimal directional reconstructions (Subsection 6.3.2). Hence the following analyses searching for neutrino point sources are based on samples of such track-like events. As previously mentioned in Section 6.5, events triggering the IceCube detector are rudimentarily filtered at the South Pole for track-like appearances using the muon filter selection. After the data transmission via satellite, these events constitute the starting point for more advanced selections.

Due to the large amount of data and the numerous different requirements of various analyses, the event selections in IceCube progressively run through multiple levels. In the case of this work, the pre-selected muon sample from the South Pole gets primarily reduced by the Muon Level 3 selection before more advanced reconstructions can be applied. The subsequent analysis specific selection finally aims to achieve a pure sample of neutrino events by removing most of the contribution of atmospheric muons. The

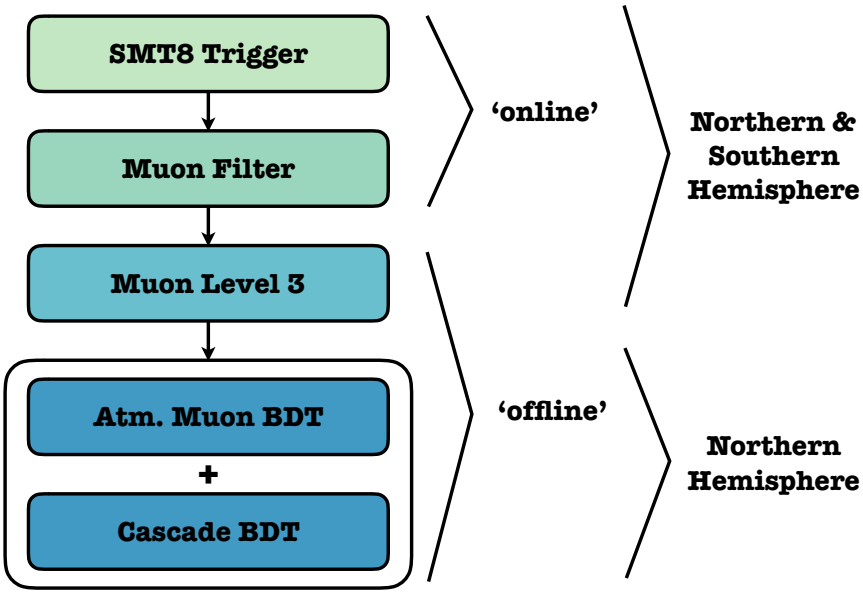

Figure 7.6: Schematic Illustration of the Event Selection Chain. The label *online* corresponds to the filtering done at the South Pole site, whereas *offline* indicates the event selection steps after the data transfer to the north. The figure is adapted from [156].

general steps of the event selection used for the event sample used in this thesis are schematically illustrated in Figure 7.6. Due to the exceptional location of the detector at the geographic South Pole, events coming from different hemispheres traverse different media before reaching the detector. While events coming from the southern hemisphere hit the detector nearly directly, events from the north pass through the Earth first. In order to account adequately for these differences, the offline event filtering is divided into a selection of events from the northern hemisphere ($\delta > -5°$) and the southern hemisphere respectively. The respective selection strategies for both hemispheres are shortly summarized in the following subsection. The Muon Level 3 selection, as well as the ultimate selection of the final sample used for the analysis, are summarized in Subsection 7.2.2 and 7.2.3.

7.2.1 Neutrino Selection Strategies: Northern vs. Southern Hemisphere

The IceCube neutrino observatory detects events from every direction in the sky. At the SMT8 level, the rate is dominated by atmospheric muons (left panel in Figure 7.7).

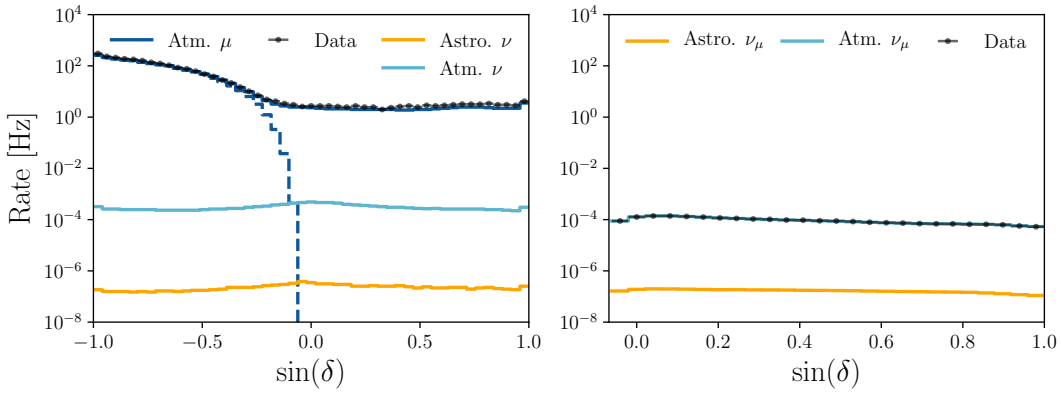

Figure 7.7: Event rates in IceCube at different reconstructed declinations δ_{reco}. **Left:** Event rate at the SMT8 trigger level (data from [158]). **Right:** Event rate from the Northern Hemisphere at the final analysis level.

While the dominant part of the rate in the southern hemisphere is actually generated by atmospheric muons from the same direction, the muon rate in the northern sky is induced by mis-reconstructed muons from the south. Atmospheric muons from the Northern Hemisphere are absorbed within the Earth and consequently cannot penetrate the detector. Hence a negligible rate of atmospheric muons from this part of the sky can be achieved by requiring good directional reconstruction quality. In this sense the dashed blue line in the left panel of Figure 7.7 illustrates the rate of atmospheric muons in bins of their true direction. Above $\delta \gtrsim -5^\circ$ the rate drops drastically below the one of atmospheric and astrophysical neutrinos. The signatures from atmospheric and astrophysical neutrinos from the Northern Hemisphere cannot be further distinguished.

In the Southern Hemisphere, the rate is dominated by well-reconstructed muon bundles. In cosmic-ray induced air-showers many low energy muons and neutrinos are produced. If multiple of these muons reach the detector simultaneously they mimic single high energy muons in the detector. Removing a significant fraction of these events can only be achieved by sacrificing some amount of the neutrino signal. Besides these bundles, atmospheric muons and neutrinos cannot be distinguished for events starting outside the detector. Hence the dominating rate of atmospheric muons cannot be eliminated as done in the north. For events starting inside the detector, additional vetoing techniques exist to lower the fraction of atmospheric muons and even neutrinos. As mentioned above, atmospheric muons and neutrinos are generated in large numbers in cosmic-ray air showers in the atmosphere. The rate of muons can be simply eliminated by requiring the events to start within the detector volume. Since muons, produced in the atmosphere, generate light along their whole path, such track-like events can

only be induced by neutrinos interacting within the detector volume. Going one step further, the air shower argument can be applied to reduce the atmospheric neutrino probability for individual events. Both atmospheric neutrinos and muons are produced in air showers. If we detect such neutrinos in IceCube, we are supposed to see one of the accompanying muons as well with a certain probability. This probability depends on the energy and the incoming direction of the neutrino. Using again the starting condition of the events in combination with energy and declination dependent conditions allows to deduce the selected sample to events with a low atmospheric background probability [159, 160]. Note that since both veto conditions depend on the measurement of atmospheric muons, they can only be applied to events from the Southern Hemisphere. For the analyses in the following thesis, we want to use the largest possible sample of track-like events with a high purity of astrophysical events. Since we do not want to constrain this sample to the small sub-sample of starting events we will not make use of the vetoing techniques applicable in the Southern Hemisphere. Nevertheless, other analyses looking for neutrino sources by means of this sub-sample exist in IceCube and outside the collaboration [75, 161].

7.2.2 Muon Level 3

The application of the most advanced reconstruction methods is computationally intense and hardly feasible for the large amount of track-like events transmitted from the South Pole. Hence the Muon Level 3 filter is applied first to significantly reduce the rate of atmospheric muons while keeping most of the neutrinos. This selection uses the available information about the deposited charge and the low-level directional reconstructions (LineFit, SPE and MPE using analytic parametrizations for the residual time probability distributions). Similar to the whole event selection chain also the Muon Level 3 filter progresses consecutively. The accurate selection criteria are documented in detail in [156]. In the following only the basic concept is summarized. In a first pre-selection step, mis-reconstructed events are removed by applying the online muon filter restrictions to the latest reconstructions. Additionally lower limits of 100 pe on the total charge $Q_{\mathrm{tot}} = \sum_k q_k$ and upper limits of 90 m on the average weighted distances

$$d_Q = \frac{1}{Q_{\mathrm{tot}}} \sum_k q_k \|\mathbf{d}_k - \mathbf{x}\|_{\mathrm{min}} \tag{7.24}$$

of the measured charges q_k at each DOM $\mathbf{d}_k$ with respect to the track hypothesis $\mathbf{x}$ are applied. While these cuts mainly remove uninteresting low energy events, the remaining sample is still dominated by atmospheric muon bundles (previous subsection).

These events can be separated by algorithms searching for causal connections between individual hits [156, 162]. After splitting, all low-level directional reconstructions as well as the pre-selection criteria are applied to the newly traced sub-events. Finally the so-called Muon Level 3 cut is used to solely keep events with potentially good reconstruction quality in both hemispheres. This is achieved by the use of quality criteria inferred from the maximum likelihood values $\mathcal{L}_{\max}$ of the directional reconstructions

$$\frac{-\log\left(\mathcal{L}_{\max}\right)}{N_{\mathrm{DOM}}-5} < 9 \quad \vee \quad \frac{-\log\left(\mathcal{L}_{\max}\right)}{N_{\mathrm{DOM}}-3} < 7.5. \tag{7.25}$$

As previously mentioned in Subsection 7.1.1, the parametrization of through-going tracks contains five free parameters. Hence the denominator $N_{\mathrm{DOM}} - 5$ corresponds to the degrees of freedom in the likelihood maximization. Empirically it was observed that the scale $N_{\mathrm{DOM}} - 3$ can give better separation power of well-reconstructed events. Events not passing these cuts can still be recovered by means of subsequent cuts on additional measures connected to direct photon hits [6]

$$\left(\frac{l_{\mathrm{dir}}}{180\,\mathrm{m}}\right)^2 + \left(\frac{n_{\mathrm{dir}}}{10}\right)^2 > 2 \quad \wedge \quad n_{\mathrm{dir}} > 6, \tag{7.26}$$

where n_{dir} is the number of DOMs measuring direct photons and l_{dir} is the distance of the DOM with the earliest and the latest direct hit. In addition to these restrictions a declination dependent charge cut is applied to the Southern hemisphere. The selection thresholds in the Muon Level 3 filter are chosen to eliminate large fractions of atmospheric muons while still being loose enough to retain most neutrino events. After the filtering, the all-sky event rate is reduced from 34 Hz to about $\sim$ 3 Hz, allowing the application of the more advanced reconstruction methods mentioned in Section 7.1 [156].

7.2.3 Neutrino Selection in the Northern Hemisphere

The aim of the final event selection is the generation of a large sample of track-like events with a high purity of astrophysical neutrinos. While the Muon Level 3 selection eliminated a large amount of background, the sample in both hemispheres is still dominated by atmospheric muons. In general, the signatures of such muons and neutrinos cannot be distinguished for events starting outside the detector. Yet, while muons in the Northern hemisphere only appear due to failed directional reconstructions, they naturally dominate in the south by more than three orders of magnitude. Hence their

[6] The time window for direct photons is defined as $[-15\,\mathrm{ns}, 250\,\mathrm{ns}]$

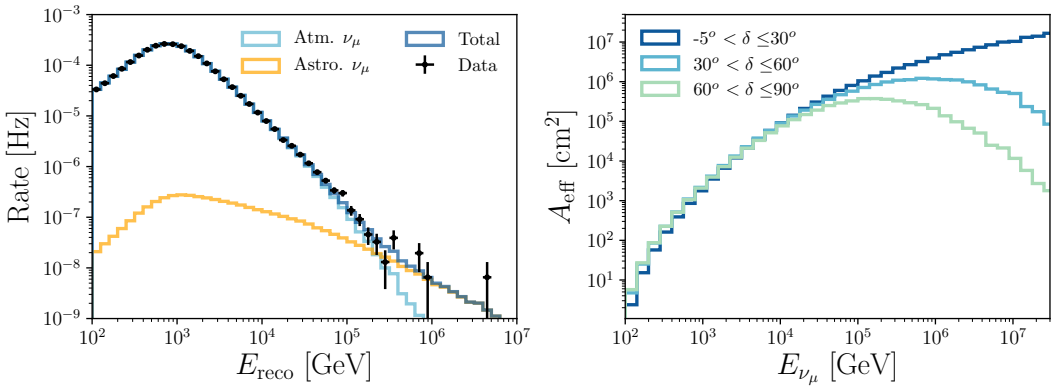

Figure 7.8: **Left:** Event rate in reconstructed energy bins for the final event sample. **Right:** Effective area A_{eff} of the final sample for different declination regions.

rate in the Northern Hemisphere can be further diminished by requiring a high directional reconstruction quality. In contrast, the different origins of through-going tracks in the Southern Hemisphere cannot be separated further. Consequently, we restrict the analyses in this thesis to events from the Northern hemisphere. Note that in principle the rate of atmospheric events can be vastly diminished by allowing only the highest energy events (left panel Figure 7.8). Since this restriction also removes a lot of astrophysical events it significantly reduces the sample size. While we do not make use of this approach for the Southern Hemisphere[7] other point source analysis in IceCube do [3, 76].

In order to efficiently diminish atmospheric muons from the sample, the final neutrino selection operates on the basis of supervised learning methods with boosted decision trees (BDT) [8]. The input variables for the BDT consist of reconstruction quality parameters such as the ones mentioned above and additional topological event characteristics. A complete list of all variables can be found in [156]. Next to this selection, an additional cascade BDT is applied to reject the remaining fraction of cascade-like events. Due to the usage of a false infinite track assumption, the likelihood reconstructions from Subsection 7.1.1 perform poorly on such events. As a consequence cascade-like events can be characterized as well-reconstructed very-high-energy tracks in the final sample. After the application of this additional BDT, the cascade contamination of the sample is reduced to a negligible fraction [156].

Ultimately, the total event rate in the Northern Hemisphere amounts to $\sim 2.4\,\text{mHz}$

[7] Due to the significantly lower sensitivity in the south.
[8] The python-based implementation from the scikit-learn toolkit is used here [163].

Season	Lifetime [d]	Rate [mHz]	δ	E_{reco}
IC59	348	0.7	$[\pm 0°, 90°]$	[3.2 MeV/m, 24 GeV/m] [4]
IC79	310	1.4	$[-5°, 90°]$	[158 GeV, 0.95 PeV]
IC86, 2011	342	2.4	$[-5°, 90°]$	[100 GeV, 0.66 PeV]
IC86, 2012-16	1773	2.4	$[-5°, 90°]$	[100 GeV, 4.55 PeV]

Table 7.1: Characteristics of the experimental data used for all point source searches in this thesis.

with a neutrino purity of 99.7 % [66, 156]. The event rate per declination bin is shown in the right panel of Figure 7.7. At all incoming angles, atmospheric neutrinos dominate over the astrophysical contribution by approximately three orders of magnitude. The distribution of the reconstructed energies is shown in the left panel of Figure 7.8. While atmospheric neutrinos dictate the rate at lower energies, the contribution of astrophysical events exceeds this background at $\sim 200\,\text{TeV}$ and becomes dominant afterwards. Note that the contribution of astrophysical events in all previous plots is modeled by a simple unbroken power-law with the best-fit parameters measured by IceCube (Equation (4.1)) [41]. The neutrino effective area A_{eff} for different incoming regions is shown in the right panel of Figure 7.8. In IceCube the effective area is defined by the number of observed neutrino events

$$N_{\nu_\mu+\nu_{\bar{\mu}}} = \int_T \mathrm{d}t \int_{\Delta\Omega} \mathrm{d}\Omega \int_{\Delta E} \mathrm{d}E\, A_{\text{eff}}(E,\delta) \frac{\mathrm{d}^3\phi_{\nu_\mu+\nu_{\bar{\mu}}}}{\mathrm{d}t\,\mathrm{d}\Omega\,\mathrm{d}E}, \tag{7.27}$$

within a solid angle $\Delta\Omega$ resulting from a flux $\frac{\mathrm{d}^3\phi_{\nu_\mu+\nu_{\bar{\mu}}}}{\mathrm{d}t\mathrm{d}\Omega\mathrm{d}E}$ within the energy range ΔE during a time T. As such, the effective area contains detector related characteristics as well as propagation and interaction effects of neutrinos on their way and inside the detector volume [9]. Note that since we do not distinguish between neutrinos and anti-neutrinos, the effective area A_{eff} contains the effects of both. The effective area around the horizon increases with increasing neutrino energy. On the other hand the effective areas for more vertically incoming events drops at higher energies. This effect is caused by the absorption of high-energy neutrinos along their path through the Earth.

The final event sample used for the analysis contains selected experimental data measured over eight years of total lifetime. Relevant characteristics for each of the experimental data samples from each year are summarized in Table 7.1. Note that the

[9] The effective area is closely related with the effective volume introduced in Equation (6.8) by $A_{\text{eff}} = N_A \rho \sigma_{\nu_\mu+\nu_{\bar{\mu}}} V_{\text{eff}}$.

[4] In the IC59 selection only the average energy deposition per meter $\langle \frac{\mathrm{d}E}{\mathrm{d}x} \rangle$ from the truncated likelihood approach is calculated.

event selections from above slightly differ for the individual years, with X in the name ICX indicating the respective number of operating strings in each season. The detector configuration and the event selection between 2012 and 2016 do not differ, yielding the combined sample IC86, 2012-16.

7.3 Statistical Search Methods

High-energy neutrinos from astrophysical point sources cluster at small scales around the direction pointing towards the source. In order to identify this signal event clustering in the previously selected sample, we construct a likelihood ratio test.

7.3.1 Unbinned Likelihood Ratio Test for a Single Source

In the following we aim to distinguish between two scenarios for the data observed with the IceCube telescope.

- $\mathbf{H}_b$**:** The observed data is the sum of events solely induced by atmospheric air-showers and a diffuse astrophysical component.
- $\mathbf{H}_s$**:** The observed data is the combined sum of events induced by atmospheric air-showers, a diffuse astrophysical component and a point-like neutrino source located at $\mathbf{x}_{\mathrm{src}} \coloneqq (\delta_{\mathrm{src}}, \vartheta_{\mathrm{src}})$[10]. The spectrum of the source is supposed to follow an unbroken power-law spectrum $\frac{\mathrm{d}\phi}{\mathrm{d}E_\nu} \propto E_\nu^{-\gamma}$.

The test statistic for this likelihood ratio test is defined as

$$\Lambda = -2 \log \left(\frac{\sup_{\theta \in \mathbf{H}_b} \mathcal{L}(\theta|\{x\})}{\sup_{\theta \in \mathbf{H}_s} \mathcal{L}(\theta|\{x\})} \right), \tag{7.28}$$

where $\{x\} = \{\mathbf{x}, N\}$ illustrates the set of observables from all events passing the selection criteria from the previous section. $\mathbf{x}$ contains the reconstructed quantities $x_i = (\log_{10}(E_i), \mathbf{x}_i^{\mathrm{reco}}, \sigma_i)$ of each event i, where E_i depicts the reconstructed energy, $\mathbf{x}_i^{\mathrm{reco}} = (\sin(\delta_i), \vartheta_i)$ the reconstructed direction and σ_i the corresponding uncertainty estimate. Finally the total number of observed events in the sample is N. The likelihood function in equation describes the probability to measure the set of observables $\{x\}$ for a given realization θ of either the hypothesis

$$\mathcal{L}(\theta|\{x\}) = p(\{x\}|\theta). \tag{7.29}$$

[10] δ and ϑ depict the declination and right ascension angle defined on the unit sphere with $\delta \in [-90°, 90°]$ and $\vartheta \in [0°, 360°]$.

In the following we will derive an expression for this likelihood function based on $\{x\}$. Using the principle of conditional probabilities we can divide Equation (7.29) in

$$p(\{x\}|\theta) = p(\mathbf{x}|N, \theta) \cdot p(N|\theta), \tag{7.30}$$

where the second term depicts the probability to observe N events in a given realization θ. In the most general configuration of the scenarios from above, events can either be generated by background from atmospheric events and a diffuse astrophysical component or by an astrophysical point source. Hence the probability distribution for N can be expressed by a poisson distribution

$$p(N|\theta) = \frac{(\lambda_s + \lambda_b)^N e^{-(\lambda_s+\lambda_b)}}{N!} \tag{7.31}$$

where λ_s and λ_b are the expected number of detected signal and background events respectively. Note that with $\lambda_s = 0$, this expression also holds for the putative realizations of the background hypothesis $\mathbf{H}_b$. Assuming an independent observation of all events, the first term in Equation (7.30) can be written as the product of the probabilities of the observables x_i from the individual events

$$p(\mathbf{x}|N, \theta) = \prod_{i=1}^{N} p(x_i|\theta). \tag{7.32}$$

Using the generalized source argument from above, the probability densities $p(x_i|\theta)$ of the individual observations can be further accessed. In general, events can either be generated by background or an astrophysical point source. In this sense, we introduce a variable ϵ indicating whether an event is generated in either of the two scenarios. The respective probability can be written as

$$p(\epsilon|\theta) = \begin{cases} \frac{\lambda_s}{\lambda_s+\lambda_b} & \text{if } \epsilon = \epsilon_s \\ \frac{\lambda_b}{\lambda_s+\lambda_b} & \text{if } \epsilon = \epsilon_b \end{cases} \tag{7.33}$$

Note that similarly to above, this expression also holds for realizations of the background hypothesis with $\lambda_s = 0$. Applying the law of total probability, the probability densities $p(x_i|\theta)$ can be separated in a part connected to point sources and a part connected to atmospheric and diffuse astrophysical background

$$\begin{aligned} p(x_i|\theta) &= p(x_i|\epsilon_s, \theta) \cdot p(\epsilon_s|\theta) + p(x_i|\epsilon_b, \theta) \cdot p(\epsilon_b|\theta) \\ &= p(x_i|\mathbf{x}_{\text{src}}, \gamma) \cdot p(\epsilon_s|\theta) + p(x_i|\eta_b) \cdot p(\epsilon_b|\theta), \end{aligned} \tag{7.34}$$

where η_b represents the established knowledge about the background relevant for the construction of the probability distribution functions (pdfs) later in this section. Inserting Equations (7.30)-(7.34) into Equation (7.29) yields an expression for the likelihood function

$$\mathcal{L}(\lambda_s, \gamma|\{x\}) = \frac{\lambda_{\text{tot}}^N e^{-\lambda_{\text{tot}}}}{N!} \cdot \prod_{i=1}^{N} \left[\frac{\lambda_s}{\lambda_{\text{tot}}} p(x_i|\mathbf{x}_{\text{src}}, \gamma) + \frac{\lambda_b}{\lambda_{\text{tot}}} p(x_i|\eta_b) \right], \tag{7.35}$$

with $\lambda_{tot} = \lambda_s + \lambda_b$. This likelihood can then be inserted into the test statistic from Equation (7.28). The characteristics of the background η_b and λ_b are established from characteristics from other measurements. Hence the likelihood in the realization of the background hypothesis $\mathbf{H}_b$ can be described without any free parameter and $\lambda_s = 0$. Differently, in the scenario of the signal hypothesis $\mathbf{H}_s$, the likelihood contains the two free parameters λ_s and γ, yielding the test statistic

$$\begin{aligned}
\Lambda =& 2 \log \left(\frac{\sup_{\lambda_s, \gamma} \mathcal{L}(\lambda_s, \gamma|\{x\})}{\mathcal{L}(\lambda_s = 0|\{x\})} \right) \\
=& 2 \sup_{\lambda_s, \gamma} \left[\log \left(\left(\frac{\lambda_s + \lambda_b}{\lambda_b} \right)^N \frac{e^{-\lambda_s - \lambda_b}}{e^{-\lambda_b}} \right) \right. \\
& \left. + \sum_{i=0}^{N} \log \left(\frac{\lambda_s}{\lambda_s + \lambda_b} \left(\frac{p(x_i|\mathbf{x}_{\text{src}}, \gamma)}{p(x_i|\eta_b)} - 1 \right) + 1 \right) \right]
\end{aligned} \tag{7.36}$$

Note that we only allow for $\lambda_s \geq 0$ in this thesis. The test statistic will be used in the following to evaluate the compatibility of the observed data with respect to the null hypothesis. The principle construction of the significances of outcomes based on this formalism is outlined in Subsection 7.3.4. In order to evaluate the test statistic we have to construct the signal point source $p(x_i|\mathbf{x}_{\text{src}}, \gamma)$ and the background $p(x_i|\eta_b)$ probabilities for the observables x_i. The background pdfs used for the analysis in this thesis are based on experimental data. Hence the expected number of background events λ_b is not known. Since the total number of events is dominated by atmospheric background by roughly three orders of magnitude we use the following approximation

$$\lambda_b \sim \lambda_{\text{tot}} \sim N. \tag{7.37}$$

As a consequence the poisson term for N in Equation (7.36) cancels, yielding a simplified test statistic

$$\Lambda = 2 \sup_{\lambda_s, \gamma} \sum_{i=0}^{N} \log \left(\frac{\lambda_s}{N} \left(\frac{p(x_i|\mathbf{x}_{\mathrm{src}}, \gamma)}{p(x_i|\eta_b)} - 1 \right) + 1 \right). \tag{7.38}$$

7.3.2 Signal and Background Probabilities

The signal and background probabilities of the observables x_i are calculable quantities by means of using physical assumptions on the respective scenario. The set x_i contains four observables for each event, yielding four-dimensional probability densities in both scenarios. In the following, we will reshape and if possible simplify both distributions to make them accessible for an IceCube analysis.

Signal Point Source Probability

Using again the rule of conditional probabilities, the signal probability can be separated in a spatial and an energy term according to

$$\begin{aligned} p(x_i|\mathbf{x}_{\mathrm{src}}, \gamma) &= p(\mathbf{x}_i^{\mathrm{reco}}| \log_{10}(E_i), \sigma_i, \mathbf{x}_{\mathrm{src}}, \gamma) \cdot p(\log_{10}(E_i), \sigma_i|\mathbf{x}_{\mathrm{src}}, \gamma) \\ &= p(\sin(\delta_i), \vartheta_i| \log_{10}(E_i), \sigma_i, \mathbf{x}_{\mathrm{src}}, \gamma) \cdot p(\log_{10}(E_i), \sigma_i|\mathbf{x}_{\mathrm{src}}, \gamma). \end{aligned} \tag{7.39}$$

Events from neutrino point sources are supposed to cluster around the direction of their origin. Motivated by this fact, we approximate the spatial term with a two dimensional gaussian distribution around the direction of the source $\mathbf{x}_{\mathrm{src}}$

$$p(\sin(\delta_i), \vartheta_i| \log_{10}(E_i), \sigma_i, \mathbf{x}_{\mathrm{src}}, \gamma) \sim \frac{1}{2\pi\sigma_i^2} \cdot \exp\left(\frac{-\boldsymbol{\psi}_i^2}{2\pi\sigma_i^2} \right), \tag{7.40}$$

where $\boldsymbol{\psi}_i$ depicts the angular difference between the reconstructed event direction and $\mathbf{x}_{\mathrm{src}}$ according to

$$\begin{aligned} \boldsymbol{\psi}_i &= \arccos(\mathbf{x}_i^{\mathrm{reco}} \cdot \mathbf{x}_{\mathrm{src}}) \\ &= \arccos\left(\sin(\delta_{\mathrm{src}}) \sin(\delta_i) + \cos(\vartheta_{\mathrm{src}} - \vartheta_i) \cos(\delta_{\mathrm{src}}) \sqrt{1 - \sin^2(\delta_i)} \right). \end{aligned} \tag{7.41}$$

It is worth to note that the gaussian function ignores the dependence of the reconstructed energy in Equation (7.40)[11]. The approximate validity of this simplification can be verified by comparing the gaussian distribution to simulated probability distri-

[11] In fact the pull correction for σ_i accounts for some part of the energy dependence.

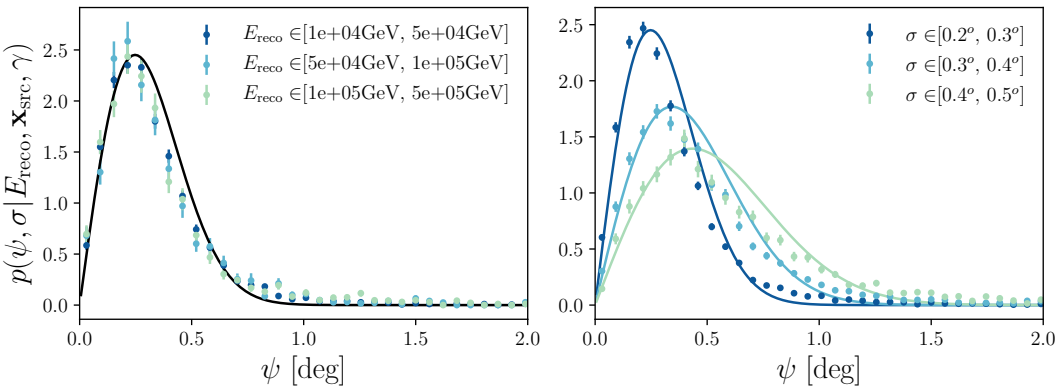

Figure 7.9: **Left:** Probability distributions of the angular distance ψ for different reconstructed energies. σ is set to 0.25°. The solid line illustrates the gaussian approximation from Equation (7.40). **Right:** Probability distributions for different angular uncertainty estimates given an energy of $E_{\mathrm{reco}} \sim 50\,\mathrm{TeV}$. The solid lines illustrate the gaussian approximation (Equation (7.40)) for the respective scenario. For both plots the source is fixed at $\delta = 5°$, with $\gamma = 2$.

butions. Similar to the gaussian approximation, the access to simulated distributions at reasonable statistics requires a simplification of the spatial probability. Assuming that the spatial probability only depends on the angular distance $\boldsymbol{\psi}_i$ we can write

$$\begin{aligned} p(\sin(\delta_i), \vartheta_i | \log_{10}(E_i), \sigma_i, \mathbf{x}_{\mathrm{src}}, \gamma) &\sim \frac{1}{2\pi} p(\cos(\boldsymbol{\psi}_i) | \log_{10}(E_i), \sigma_i, \mathbf{x}_{\mathrm{src}}, \gamma) \\ &= \frac{1}{2\pi \sin(\boldsymbol{\psi}_i)} p(\boldsymbol{\psi}_i | \log_{10}(E_i), \sigma_i, \mathbf{x}_{\mathrm{src}}, \gamma), \end{aligned} \tag{7.42}$$

where the factor $\frac{1}{2\pi}$ on the right side arises from the independence of ϑ_i. A comparison between the gaussian approximation and simulated pdfs for different energies is shown in the left panel of Figure 7.9. The gaussian distribution roughly fits the peak of the distribution, while underestimating the less relevant tails towards large angular differences in this scenario. The energy dependence seems to be negligible. The right panel of Figure 7.9 illustrates the comparison between the gaussian approximation and simulated distributions at $\sim 50\,\mathrm{TeV}$ for different reconstructed uncertainties. While not describing the simulated distributions perfectly, the gaussian approximation covers the general shape of the pdfs correctly.

The second term in Equation (7.39) can be separated according to

$$\begin{aligned} p(\log_{10}(E_i), \sigma_i | \mathbf{x}_{\mathrm{src}}, \gamma) &= p(\log_{10}(E_i) | \sigma_i, \mathbf{x}_{\mathrm{src}}, \gamma) \cdot p(\sigma_i | \mathbf{x}_{\mathrm{src}}, \gamma) \\ &\sim p(\log_{10}(E_i) | \mathbf{x}_{\mathrm{src}}, \gamma) \cdot p(\sigma_i | \mathbf{x}_{\mathrm{src}}, \gamma), \end{aligned} \tag{7.43}$$

where we ignore the σ_i dependence of the energy term in the second step. The energy term can be evaluated according to

$$p(\log_{10}(E_i) | \mathbf{x}_{\mathrm{src}}, \gamma) = \int_0^\infty p(\log_{10}(E_i) | E_\nu, \mathbf{x}_{\mathrm{src}}, \gamma) \cdot p(E_\nu | \mathbf{x}_{\mathrm{src}}, \gamma) \, \mathrm{d}E_\nu \,, \tag{7.44}$$

with both terms in the integral being constructed from Monte Carlo simulations.

Background Probability

Similar to the signal point source probability, the probability connected to atmospheric neutrinos and a diffuse astrophysical component can be separated into an energy and a spatial term

$$p(x_i | \eta_b) = p(\log_{10}(E_i), \sigma_i | \sin(\delta_i), \vartheta_i, \eta_b) \cdot p(\sin(\delta_i), \vartheta_i | \eta_b). \tag{7.45}$$

Due the rotation of the Earth and the geographical location of the detector, the spatial background distribution is uniform in right ascension[12] yielding

$$p(\sin(\delta_i), \vartheta_i | \eta_b) = \frac{1}{2\pi} \cdot p(\sin(\delta_i) | \eta_b). \tag{7.46}$$

The declination dependent distribution can be approximated from the experimental data. Since atmospheric muons dominate the rate of events by more than three orders of magnitude at every incoming angle, the potential influence of events from a neutrino point source are a negligible disturbance in the construction of the spatial background pdf. The distribution is shown in the left panel of Figure 7.10. Similarly to the signal pdf, the first term in Equation (7.45) can be divided according to

$$\begin{aligned} p(\log_{10}(E_i), \sigma_i | \mathbf{x}_i^{\mathrm{reco}}, \eta_b) &= p(\log_{10}(E_i) | \sigma_i, \mathbf{x}_i^{\mathrm{reco}}, \eta_b) \cdot p(\sigma_i | \mathbf{x}_i^{\mathrm{reco}}, \eta_b) \\ &\sim p(\log_{10}(E_i) | \mathbf{x}_i^{\mathrm{reco}}, \eta_b) \cdot p(\sigma_i | \mathbf{x}_i^{\mathrm{reco}}, \eta_b). \end{aligned} \tag{7.47}$$

Using the same argument as above the energy term can be evaluated from experimental data.

[12] Note that this is only valid for neutrino emission studies over observation times larger than at least a few days.

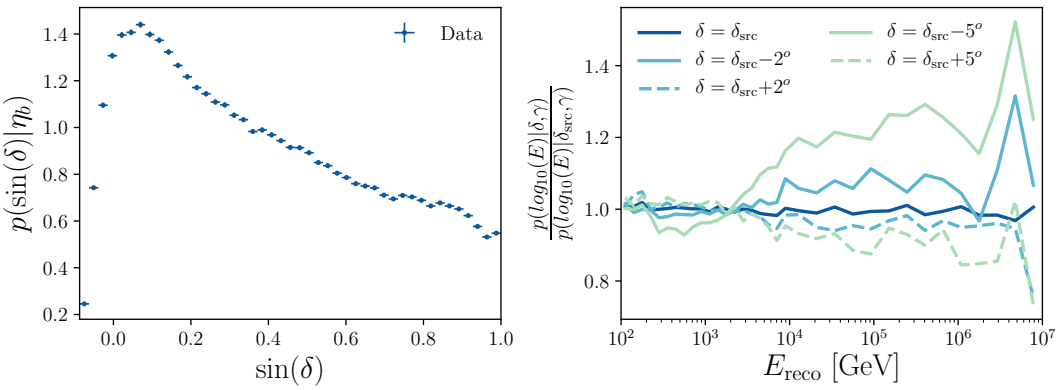

Figure 7.10: **Left:** Spatial part of the background probability distribution evaluated from data. **Right:** Illustration of the effect of the approximation in Equation (7.48) on the signal energy pdf. In this scenario the source with spectral index $\gamma = 2$ is located at $\delta_{\rm src} = 5°$.

These probability distributions can be combined in the test statistic Λ according to Equation (7.38). In order to allow for a fast evaluation of Λ we introduce the following two additional approximations

$$p(\log_{10}(E_i)|\mathbf{x}_{\rm src}, \gamma) \sim p(\log_{10}(E_i)|\mathbf{x}_i^{\rm reco}, \gamma) \tag{7.48}$$

$$\wedge$$

$$p(\sigma_i|\mathbf{x}_i^{\rm reco}, \eta_b) \sim p(\sigma_i|\mathbf{x}_{\rm src}, \gamma). \tag{7.49}$$

The first allows the pre-calculation and fast evaluation of the energy pdf ratio of the signal and the background component, while the latter cancels out the contribution of the σ probability in the definition of the test statistic. The validity of the first approximation is shown in the right panel of Figure 7.10 showing the ratio of the energy pdfs for events located at different distances to the source. For events close to the source there is hardly any deviation visible at any energy. The deviations grow with larger distances to source, up to 20 % at higher energies. Since the contribution of such events is strongly suppressed by the spatial probability densities, this approximation causes only minor disturbances in the final outcome. Inserting everything in Equation (7.38) yields

$$\Lambda = 2 \sup_{\lambda_s, \gamma} \sum_{i=0}^{N} \log \left(\frac{\lambda_s}{N} \left(\frac{\frac{1}{2\pi\sigma_i^2} \cdot \exp\left(\frac{-\psi_i^2}{2\pi\sigma_i^2}\right)}{\frac{1}{2\pi} p(\sin(\delta_i)|\eta_b)} \cdot \frac{p(\log_{10}(E_i)|\mathbf{x}_i^{\rm reco}, \gamma)}{p(\log_{10}(E_i)|\mathbf{x}_i^{\rm reco}, \eta_b)} - 1 \right) + 1 \right). \tag{7.50}$$

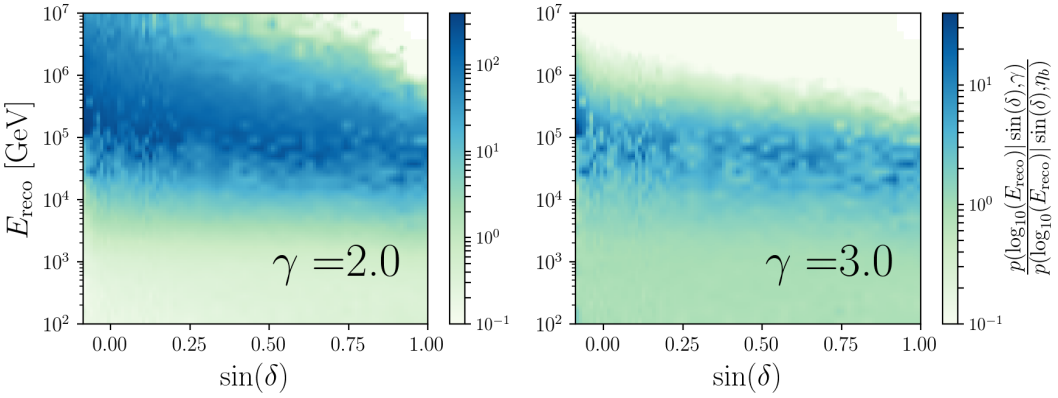

Figure 7.11: Ratio of the signal and background energy probabilities for different event declinations δ and different source spectra γ.

The ratio of the signal and background energy probabilities are shown for two different spectra in Figure 7.11. In order to validate all the assumptions and simplifications made in the previous section several performance tests of the analysis procedure were conducted. These checks are summarized in Appendix F.

7.3.3 Multiple Sources

In the previous section a likelihood ratio test was introduced to discriminate between the background hypothesis and the scenario of a single neutrino point source on top of this background. This statistical method can be easily extended to the scenario of multiple neutrino sources. The relevant adjustments with respect to the single source scenario are outlined in the following. While the background hypothesis remains similar the signal hypothesis is extended to

- **$\mathbf{H}_b$:** Similar to the definition in Subsection 7.3.1.

- **$\mathbf{H}_s$:** The observed data is the combined sum of events induced by atmospheric air-showers, a diffuse astrophysical component and M point-like neutrino sources located at $\{\mathbf{x}^j_{\mathrm{src}}\}_{j\in M}$. The spectrum of each individual source j is supposed to follow an unbroken power-law spectrum $\frac{\mathrm{d}\phi^j}{\mathrm{d}E_\nu} = \phi^j_0 \cdot E_\nu^{-\gamma}$.

The general structure of the likelihood function and the definition of the test statistic in Equation (7.38) remains unchanged. Yet, the description of the signal probability in Equation (7.39) expands to the hypothesis of multiple point sources. Using the law of

total probability the single source description modifies to

$$p(x_i|\{\mathbf{x}^k_{\mathrm{src}},\phi^k_0\}_{k\in M},\gamma) = \sum_{j=1}^{M} p(x_i|\mathbf{x}^j_{\mathrm{src}},\phi^j_0,\gamma)\cdot p(\mathbf{x}^j_{\mathrm{src}},\phi^j_0|\{\mathbf{x}^k_{\mathrm{src}},\phi^k_0\}_{k\in M},\gamma). \tag{7.51}$$

The first term in the sum illustrates the signal probability of the observables x_i for source j defined in Equation (7.39). The second term depicts the probability that a signal event is generated by source j. In principle the latter is represented by the relative event rate of each source. This can be evaluated by separating the pdf into

$$\begin{aligned} p(\mathbf{x}^j_{\mathrm{src}},\phi^j_0|\{\mathbf{x}^k_{\mathrm{src}},\phi^k_0\}_{k\in M},\gamma) =& p(\mathbf{x}^j_{\mathrm{src}}|\phi^j_0,\{\mathbf{x}^k_{\mathrm{src}},\phi^k_0\}_{k\in M},\gamma) \\ & \cdot p(\phi^j_0|\{\mathbf{x}^k_{\mathrm{src}},\phi^k_0\}_{k\in M},\gamma), \end{aligned} \tag{7.52}$$

where the first component indicates the relative detection efficiency of the detector at the position of the source j. The second part depicts the relative production rate of neutrinos from source j at the surface of the Earth. Hence it can be written as

$$p(\phi^j_0|\{\mathbf{x}^k_{\mathrm{src}},\phi^k_0\}_{k\in M},\gamma) = \frac{\phi^j_0}{\sum_{k=1}^{M}\phi^k_0} \coloneqq w_j. \tag{7.53}$$

The flux normalisations ϕ^j_0 are part of the signal hypothesis. Consequently they are either fixed within the analysis or appear as free parameters in the likelihood. The relative detection efficiencies at source j can be derived from

$$p(\mathbf{x}^j_{\mathrm{src}}|\phi^j_0,\{\mathbf{x}^k_{\mathrm{src}},\phi^k_0\}_{k\in M},\gamma) = \frac{\int A_{\mathrm{eff}}(\delta^j_{\mathrm{src}},E_\nu)E_\nu^{-\gamma}\,\mathrm{d}E_\nu}{\sum_{k=0}^{M}\int A_{\mathrm{eff}}(\delta^k_{\mathrm{src}},E_\nu)E_\nu^{-\gamma}\,\mathrm{d}E_\nu} \coloneqq r_j(\gamma), \tag{7.54}$$

where A_{eff} illustrates the effective area of the IceCube detector (Equation (7.27)).

7.3.4 Significance Calculation

In the previous section, an unbinned likelihood ratio test and the dedicated test statistic Λ was introduced to distinguish between two underlying scenarios for the observed data. The compatibility of the observed data and the corresponding test statistic value Λ_{Obs} with the background hypothesis can be quantified by the p-value p_0

$$p_0(\Lambda_{\mathrm{Obs}}) = \int_{\Lambda_{\mathrm{Obs}}}^{\infty} p(\Lambda|\mathbf{H}_b)\,\mathrm{d}\Lambda\,, \tag{7.55}$$

where $p(\Lambda|\mathbf{H}_b)$ is the probability distribution of the test statistic given that the background hypothesis is true. According to *Wilks Theorem* this probability density approaches a $\chi^2_{n_{\mathrm{dof}}}$ distribution with n_{dof} degrees of freedom in the limit of an infinite large sample size $N \to \infty$. The number of degrees of freedom n_{dof} depends on the difference in dimensionality of free parameters between the signal and the background hypothesis [152]. Applying this theorem to the test proposed in the previous sections, predicts

$$p(\Lambda|\mathbf{H}_b) \sim \begin{cases} 0.5 & \text{if } \Lambda = 0 \\ 0.5 \cdot \chi^2_{n_{\mathrm{dof}}=2}(\Lambda) & \text{else .} \end{cases} \tag{7.56}$$

The factor of 0.5 at zero arises from the fact that we only allow for positive λ_s in Equation (7.38), yielding an accumulation of the negative part of the distribution at $\Lambda = 0$[13]. The correctness of Wilks Theorem not only depends on the diverging size of the underlying sample, but also on the accuracy of the probability distributions evaluated in Subsection 7.3.2. Hence the distribution from Equation (7.56) is only used for fast evaluations of p-values. The final p-values are calculated on the basis of the actual background distribution, evaluated from trials mimicking samples of background events. In the case of this thesis the background event samples are generated from experimental data with randomized ϑ information for all events.

In IceCube, the background hypothesis of dedicated likelihood ratio test can be rejected if the p-value passes a threshold of $p_0 = 2.87 \times 10^{-7}$ (corresponding to one-sided $+5\sigma$ standard deviation threshold).

7.4 Sensitivity, Discovery Potential and Limits on Observations

Prior to the evaluation of the ultimate significance, it is interesting to get information about the capability of the hypothesis test. Within IceCube, these informative quantities are depicted by the sensitivity and the discovery potential of the analysis.

The sensitivity is defined as the flux of a neutrino source with spectral index γ that yields a p-value smaller than 0.5 in 90 % of the cases. On the other hand, as anticipated by the name, the discovery potential corresponds to the flux that results in p-value smaller than $n\sigma$ in 50 % of the cases. In IceCube usually either values for $n = 3$ or $n = 5$ (yielding the 3σ or the 5σ discovery potentials) are quoted.

[13] Note that in principle Wilks Theorem is not defined at the boundaries of the free parameters. Yet the factor 0.5 mostly relies on observations of the actual test statistic distribution.

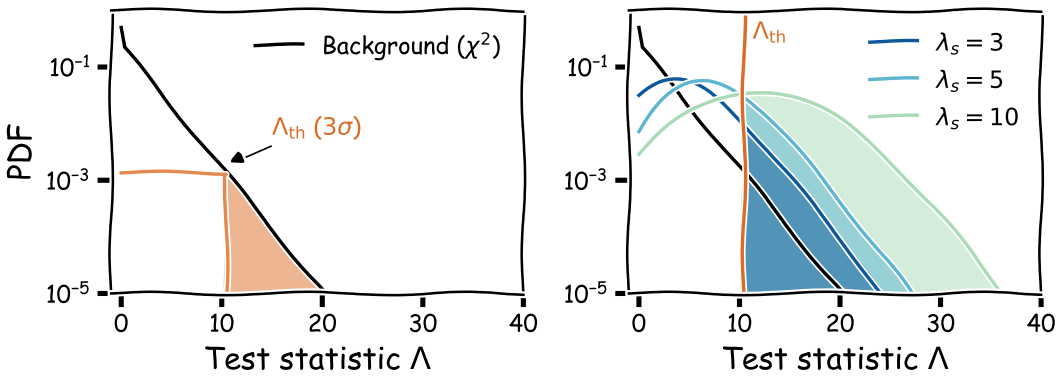

Figure 7.12: Schematic illustration of the sensitivity and discovery potential construction. In this sketch the 3σ discovery potential is evaluated. **Left:** Evaluation of Λ_{th}. **Right:** Distributions for different number of injected signal events λ_s. The shaded areas indicate the fraction of trials with a test statistic larger than Λ_{th}.

While these values could be in principle constructed from a full likelihood ratio test, their current definition in IceCube relies on the test statistic value Λ. Their construction is schematically illustrated in Figure 7.12. In both cases, initially the background test statistic threshold value Λ_{th} corresponding to the respective p-value is evaluated. In a second step the mean number of signal events λ_s that outperforms this threshold value at the desired confidence level is determined. Ultimately the number of signal events is transformed into a flux value by means of Equation (4.1) and (7.27)

$$\phi_{100} = \frac{\lambda}{\int \mathrm{d}t\, \mathrm{d}E_\nu\, A_{\text{eff}}(E_\nu) \left(\frac{E_\nu}{100\,\text{TeV}}\right)^{-\gamma}}. \tag{7.57}$$

Using a similar approach, upper limits can be calculated from outcomes below the significance threshold of the hypothesis test. The resulting test statistic serves as a threshold, while the remaining steps remain similar to above. In IceCube and in particular within this work, 90 % C.L. upper limits are quoted.

Ultimately it might also be of interest to calculate confidence regions for the true source parameters λ_0 and γ_0 after performing the analysis. In order to test the compatibility of the true parameters with the experimental data we formulate another likelihood ratio test with the corresponding test statistic

$$\bar{\Lambda}_{\text{2sd}} = -2 \log \left(\frac{\mathcal{L}(\lambda_s = \lambda_0, \gamma = \gamma_0)}{\sup_{\lambda_s \neq \lambda_0, \gamma \neq \gamma_0} \mathcal{L}(\lambda_s, \gamma)} \right) \tag{7.58}$$

In case the requirements for Wilks theorem are fulfilled, the p-values for each set of parameters λ_0 and γ_0 can be directly calculated from a χ^2_2 distribution with two degrees of freedom [152]. The true parameter combination λ_0 and γ_0 can be rejected if their p-value is smaller than $X\%$. The remaining parameter combinations form the $X\%$ C.L. contour for the true source parameters. An illustration of this construction can be seen in Figure 8.6 and 8.7.

8

Search for Steady Neutrino Emission from Blazar Populations

Blazars are among the most luminous objects in the entire Universe [54]. Depending on the conditions for particle acceleration at the site, they can be regarded as one of the most promising extragalactic source candidates for the emission of high energy neutrinos [164]. This conjecture intensified with the first evidence for neutrino emission from the direction of the blazar TXS 0506+056, observed by the IceCube neutrino telescope in September 2017 (Section 4.4). To further investigate the neutrino blazar correlation not only for individual objects but more general for large populations of blazars, we perform a search for steady neutrino emission from blazars, listed in the *third catalog of hard Fermi-LAT sources* (3FHL) [165]. The selection of the blazar populations used in this work is motivated in Section 8.1. The analysis method, as well as the outcomes of the studies, are summarized in Section 8.2 and 8.3. Finally, the implications of the analysis on the neutrino emission from blazar populations are outlined in Section 8.4.

8.1 Gamma-ray Emitting Blazars: The *third catalog of hard Fermi-LAT sources* (3FHL)

Blazars can generate photons that are observable over many order of magnitudes from radio ($\sim 10^{-17}\,\mathrm{GeV}$) to VHE gamma-ray ($\sim 10^{4}\,\mathrm{GeV}$) energies (Subsection 3.3.2). In the case of the presence of hadronic particle production processes, high-energy neutrinos are generated alongside gamma-rays at comparable energies [166]. While neutrinos are unaffected on their path towards the Earth, high-energy photons can either be reabsorbed at the source or perceive influences from extragalactic background radiation. High-energy gamma-rays above a few TeV escaping the site of acceleration are strongly attenuated, due to pair-production with these background photons (Subsection 2.2.1). Yet, while the highest energetic gamma-rays associated with high-energy neutrinos are

usually not directly apparent at the site of telescopes, they can generate subsequent gamma-rays at $\sim$ GeV energies that can be detected. Hence, although the direct correlation between neutrinos and gamma-rays is diluted by extragalactic background light and cosmic microwave background absorption, generally an associated flux of photons in the GeV to TeV range is expected from the site of high-energy neutrino production[1]. Note that gamma-ray sources do not always imply correlated neutrino emission, because these photons could be generated in purely leptonic models as well.

In order to emphasize the neutrino potential of GeV producing gamma-ray blazars, we can recollect the comparison between the total observed gamma-ray and neutrino flux mentioned in Section 4.3. Assuming an extreme scenario where the high-energy gamma-ray flux is purely generated in hadronic models, it is allowed to consider a simplified prediction for the expected neutrino flux at IceCube energies. In this scenario, the neutrino prediction resides above, yet within the magnitude of the actual measurement (Figure 4.4). Hence the majority of both messengers at high energies could potentially originate from the same population of sources. Within the photon component, $86^{+16}_{-14}\%$ of the extragalactic background radiation above 50 GeV can be allocated to resolved blazar sources [52]. The remaining fraction could arise from un-resolved blazars, which appear below the detection threshold of current observatories [52]. Consequently, GeV to TeV gamma-ray emitting blazars are amongst the most promising source candidates for the observed IceCube neutrinos.

As previously mentioned, this theoretically motivated neutrino-blazar correlation was further strengthened by the neutrino observations from the direction of TXS0505+056 (Section 4.4). Moreover, additional studies suggest a possible association between HBLs and high-energy neutrinos [164, 167]. While these analyses examined the correlation between neutrinos and individual or very few sources, we have performed a correlation analysis between all blazars resolved by the Fermi-LAT space telescope above 10 GeV (3FHL catalog) and IceCube neutrinos in the Northern Hemisphere. The observation of neutrinos from this population would not only confirm the existence of hadronic production mechanisms but could give detailed insight on the general conditions at the site of the sources. In the following section, the 3FHL catalog and the most relevant features used for the neutrino correlation are introduced.

The 3FHL catalog consist of 1556 sources observed above 10 GeV by the *Large Area Telescope* instrumented at the *Fermi Gamma-ray Space Telescope* during the first seven years of operation time [165, 168]. With overall 1301 objects, blazars constitute the

[1]Note that the correlation strongly depends on the specific conditions at the source. Moreover in the presence of intergalactic magnetic fields charged particles produced in pair-production processes can be deflected, yielding to a directional shift of the subsequent gamma-rays.

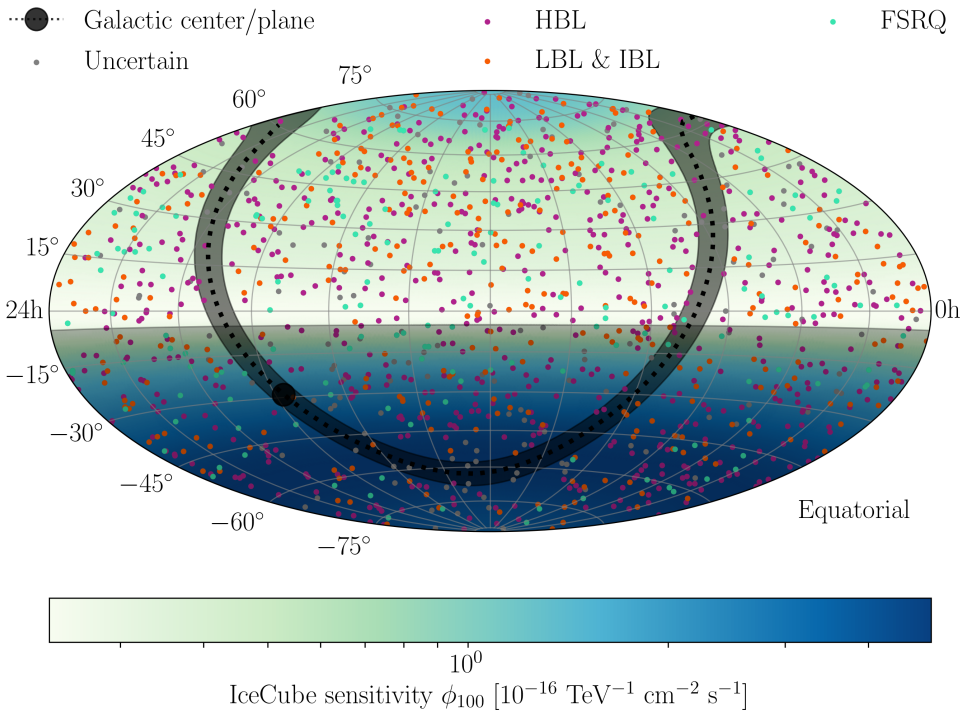

Figure 8.1: Location of identified blazars from the 3FHL catalog, split into the different categories mentioned in Table 8.1. The black shaded band illustrates the region around the galactic plane with galactic latitude $\|b_{||}\| < 5°$. The shaded region in the Southern Hemisphere indicates the region with $\delta < -5°$ which is not used in this analysis.

major fraction of the catalog. Amongst these, 1147 blazars can be associated with counterparts at other wavelengths. The spectral energy distributions of these objects have been further analyzed with tools provided by the *Open Universe* project[2], allowing an accurate estimation of the position of the synchtrotron peak ν_{peak} on a source by source basis. Together with the optical characteristics, this information is used to further classify these blazars into flat-spectrum radio quasars (FSRQ) and BL Lacs, which are further divided in low or intermediate synchtrotron peaked (LBL & IBL) and high synchtrotron peaked (HBL) objects (Subsection 3.3.2). The exact numbers of objects within the respective blazar category are listed in Table 8.1. The positions of all blazars in the 3FHL catalog are shown in Figure 8.1. Next to the position and classification of the sources, the 3FHL catalog provides information about the integrated

[2] `http://www.openuniverse.asi.it/`

Source Class	Total Number of Objects	Number of Objects $\delta > -5°$
HBL	637	356
LBL & IBL	339	212
FSRQ	171	101
Uncertain Type	154	76
All Blazars	1301	745

Table 8.1: Number of 3FHL objects in respective blazar category.

gamma-ray number flux above 10 GeV on a source by source basis defined as

$$\phi_{\mathrm{ph}} = \int_{10\,\mathrm{GeV}}^{1\,\mathrm{TeV}} \frac{\mathrm{d}N_{\mathrm{ph}}}{\mathrm{d}E_{\mathrm{ph}}\,\mathrm{d}\Omega\,\mathrm{d}t}\,\mathrm{d}E_{\mathrm{ph}}\,. \tag{8.1}$$

The source count distribution of the 3FHL blazars versus the number flux is shown in the left panel of Figure 8.2. Information on the redshift exist only for $\sim 41\,\%$ of the blazars and consequently will not be used in the following analysis.

8.2 Connecting Blazar Populations to High-energy Neutrinos

In the previous section, we emphasized the potential of gamma-ray emitting blazars as sources of the high-energy neutrino flux observed in IceCube. While gamma-ray observations alone will only yield limited information about the particle generation at these sources, high-energy neutrinos can be the smoking gun to shed light on these processes. Correlation analyses of large populations of resolved blazars and high-energy neutrino observations using the likelihood approach introduced in Subsection 7.3.3 depict a sensitive tool for such studies. In the following, we will summarize results from previous stacking analyses. Proximately, the analysis approach and outcomes of the correlation analysis with blazars from the 3FHL catalog and the selected sample of muon neutrinos from the Northern Hemisphere (Section 7.2) are introduced.

8.2.1 Previous Observations

Previous to the study in this thesis, blazar correlation analyses have been performed within IceCube. Similar to analysis in this work, these studies are based on the statistical method presented in Section 7.3. In [169] neutrino production from blazars from the second catalog of active galactic nuclei detected by *Fermi-LAT* (2LAC [170]) has been

analysed on the basis of four years of IceCube data between 2009 and 2012[3]. The 2LAC contains 862 blazars detected at energies above 100 MeV during the first two years of operation of the *Fermi-LAT*. The analysis studied the correlation of different blazar sub-categories assuming both, equally strong neutrino emission from each blazar and a neutrino emission proportional to the gamma-ray emission between 1 GeV and 100 GeV (Equation (7.53)). None of the tested categories showed any significant correlation with the observed neutrino data. Under the assumption of a global population spectrum similar to the one observed for the totality of astrophysical neutrinos [171], the contribution from the blazars in the 2LAC catalog to the median of the diffuse neutrino flux was constrained to maximally 27 % (7 %) for the scenario of equally strong neutrino fluxes from all blazars at the Earth (for a neutrino emission strength proportional to the observed gamma-ray flux).

Motivated by observations from correlation studies (based on simple counting statistics) with blazars from the *second catalog of hard Fermi-LAT sources* (2FHL) [172] and a selection of the highest energetic neutrinos in IceCube [161, 173], HBL objects from the same catalog were used to analyze the correlation with 7 years of through-going muon data from IceCube [174]. In contrast to the 2LAC, the source selection in the 2FHL catalog is solely based on photon observations above 50 GeV, yielding only 149 HBL objects[4]. According to the arguments made in the previous section, this is potentially the energy region where a proportionality between the observed photon and neutrino fluxes might appear. Similar to the analysis on the 2LAC blazars, the scenario with equal neutrino emission strength from all blazars was tested. In order to analyze a potential correlation with the gamma-ray flux above 50 GeV, these relative strengths are not incorporated in the analysis directly as for the 2LAC, but the blazars are classified recursively into sub-samples according to their integrated gamma-ray flux. Similar to the study on the 2LAC, no significant correlation between these blazars and the observed neutrino data was found. Assuming a power-law similar to the one observed for astrophysical muon neutrinos from Northern Hemisphere [66], the analysis confines the maximal contribution of the 2FHL HBLs to the median of the diffuse muon neutrino flux to maximally 5.7 % (3.8 % if the neutrino flux is proportional to the observed gamma-ray flux above 50 GeV). Theoretically more motivated models for the spectral shape of the populations can allow a maximal contribution of $\sim$ 27 % within certain energy regions [84, 174].

[3] Note that between 2009 and 2010 only a partially completed configuration of the IceCube detector with respectively 59 and 79 strings was available.

[4] 114 of these objects are also contained in the 2LAC catalog.

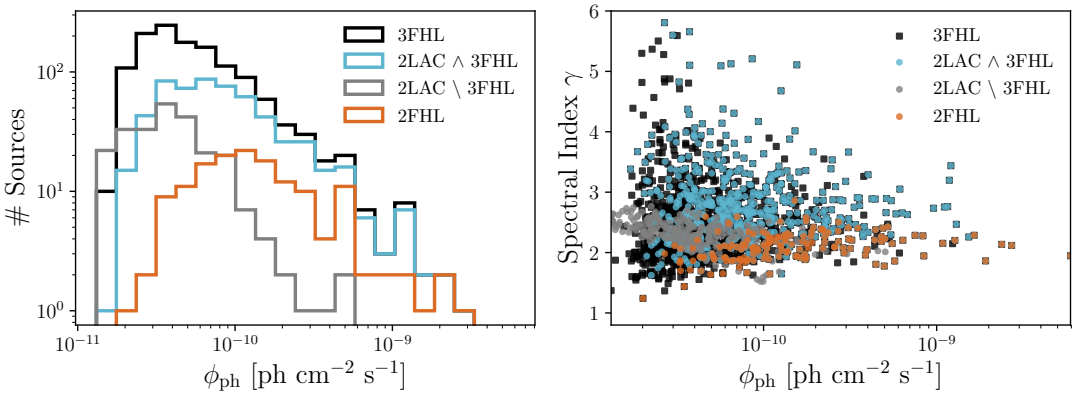

Figure 8.2: **Left:** Source count distribution of blazars from different *Fermi-LAT* Catalogs. **Right:** Distribution of blazars from different *Fermi-Lat* catalogs according to their spectral characteristics above 10 GeV. The spectral index γ corresponds to an unbroken power-law fit to the data above 10 GeV. Note that flux for the 2LAC sources that are not part of the 3FHL catalog (grey lines and dots) is approximated from the available data between 1 GeV and 100 GeV.

8.2.2 Analysis Approach

While neither the blazars from the 2LAC nor the HBLs from the 2FHL catalog were able to explain a major fraction of the observed diffuse muon neutrino flux, there is still a large number of resolved and un-resolved blazars left that potentially can. The analysis performed within this work fills the gap between the previous two blazar analyses. On the one hand, while the energy threshold for the source selection in the 2LAC might have been too loose[5], the catalog is missing a lot of potential sources with hard spectra appearing only at higher energies. On the other hand, the energy threshold might have been too strict in the case of 2FHL catalog, missing a large fraction of sources in the region above 10 GeV. Above this energy, blazars describe (48 ± 8) % of the extragalactic background light observed by the *Fermi-LAT* [51]. The 3FHL catalog contains 1301 blazars detected above this energy threshold, covering all but one of HBLs from the 2FHL catalog. 588 blazars within the 3FHL sample are also part of the 2LAC selection, yielding a total of 679 blazar objects that have not been analyzed in any of the previous studies[6]. The source count distribution for the different blazar catalogs are shown in Figure 8.2.

Next to the increased number of sources, the current study differs from the previous

[5] Too many very faint gamma-ray/neutrino sources might have been selected.
[6] 114 objects are part of the 2LAC and the 2FHL HBL selection.

searches in the available amount of neutrino data. For this search, we use the sample of muon neutrinos from the Northern Hemisphere during 8 years of operation time, introduced in Section 7.2. Hence in the following, we will only use the 3FHL blazars located in the Northern Hemisphere (Figure 8.1). The different blazar sub-categories introduced in the previous section exhibit diverse characteristics in their optical spectrum and therefore might significantly differ in their potential to generate and emit neutrinos. While FSRQ objects possess strong broad optical emission lines that could potentially serve as radiation targets for photomeson production [175, 176], a potential correlation between neutrinos and BL Lac objects was indicated in [164, 173, 177]. Hence we will separately study the neutrino emission from the blazar sub-samples mentioned in Table 8.1 as well as the full set of blazars. The exact analysis procedure is similar for each category and will be outlined in the following.

The statistical method used in this analysis follows the hypothesis test specified in Subsection 7.3.3. As indicated in this section, we assume that individual objects within the tested population meet the same unbroken power-law neutrino emission distribution with spectral index γ. This simplification is motivated by the presumption, that the neutrino production within this population is induced by the same processes. Next to the spectral shape, the relative neutrino production strength of the individual sources caused at the Earth folds in the expected outcome of the signal hypothesis (Equation 7.53). While certain models indicate that on average higher neutrino emission might be caused by sources with higher observed gamma-ray fluxes [176], it is neither clear at which gamma-ray energies these correlations might appear nor if the proportionality would also hold on a source by source basis. Imposing neutrino weights proportional to the corresponding gamma-ray fluxes in the 3FHL catalog would make the statistical test very insensitive to even little deviations from this assumption. This behavior is illustrated in the left panel of Figure 8.3.

The neutrino signal is supposed to originate from source populations with randomly distributed neutrino strengths[7]. While the analysis based on the equal-weighted sources is hardly affected by this simplified assumption, the sensitivity of the flux weighted method vastly declines. Hence we only test the populations based on the assumption that each source produced the same amount of neutrinos according to

$$\phi_0^j \coloneqq \phi_0 \quad \forall j \in M. \tag{8.2}$$

Nevertheless, we also want to study the correlation between the gamma-ray and a

[7] The source count distribution used for the sampling follows a dispersion similar to the source count distribution observed and modeled for gamma-ray (see Appendix G)

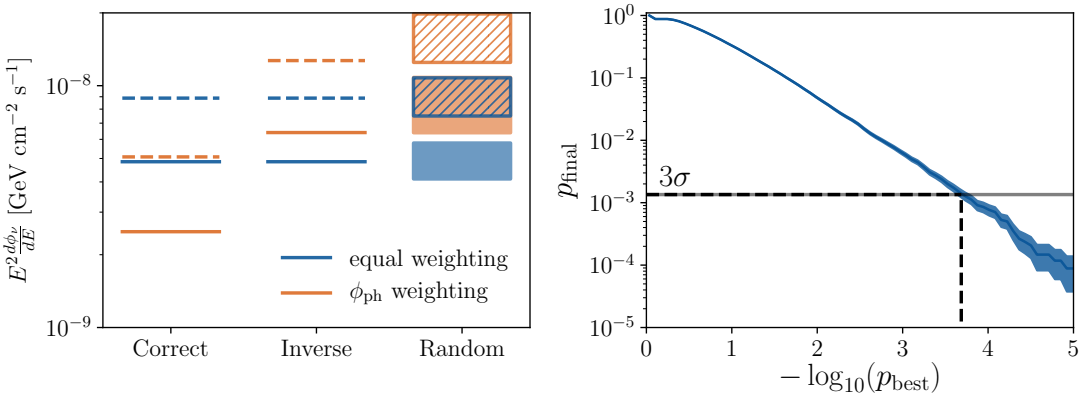

Figure 8.3: **Left:** Sensitivity (solid) and 3σ discovery potential (dashed) comparison between the population analysis based on the equal-weighting and the gamma-ray flux $\phi_{\rm ph}$ weighting assumption. In the *correct* scenario the true neutrino source count distribution ν-SCD is similar to the analysis assumption. In the *inverse* case the true ν-SCD is swapped between the two scenarios. Lastly, in the *random* case the true relative source strengths are randomly assigned from general photon SCD (Appendix G). The band illustrates the 68 % central band coming from multiple realizations. **Right:** Illustration of the trial correction for the best p-value $p_{\rm best}$ from the population scan according to the corresponding gamma-ray flux.

potential neutrino flux in this analysis. For this reason, similar to the previous analysis on the 2FHL catalog, we aim to conduct this survey by dividing the different blazar populations into cumulative sub-samples according to their observed integrated gamma-ray flux above 10 GeV. In this way the neutrino contribution from different $\phi_{\rm ph}$ can be studied, without penalizing the analysis with the strict presumption of a source by source correlation between the observable occurrence of both messengers. For this analysis, we have artificially chosen a partitioning into 10 cumulative sub-samples such that the number of additional sources stays approximately constant in each step [161]. For each of these sub-samples, the particular p-value value is calculated according to Equation (7.55). The best p-value ($p_{\rm best}$) from this scan is corrected for multiple trials[8], yielding a distinct post-trial p-value $p_{\rm final}$ for each blazar population according to

$$p_{\rm final}(p_{\rm best}) = \int_{p_{\rm best}}^{\infty} p(\bar{p}_{\rm best})\, \mathrm{d}\bar{p}_{\rm best}\,, \tag{8.3}$$

where p is the probability distribution of $p_{\rm best}$. Due to the strong correlation between

[8] Due to the repetition of the test in multiple correlated sub-samples, the trial correction compensates for the look elsewhere effect.

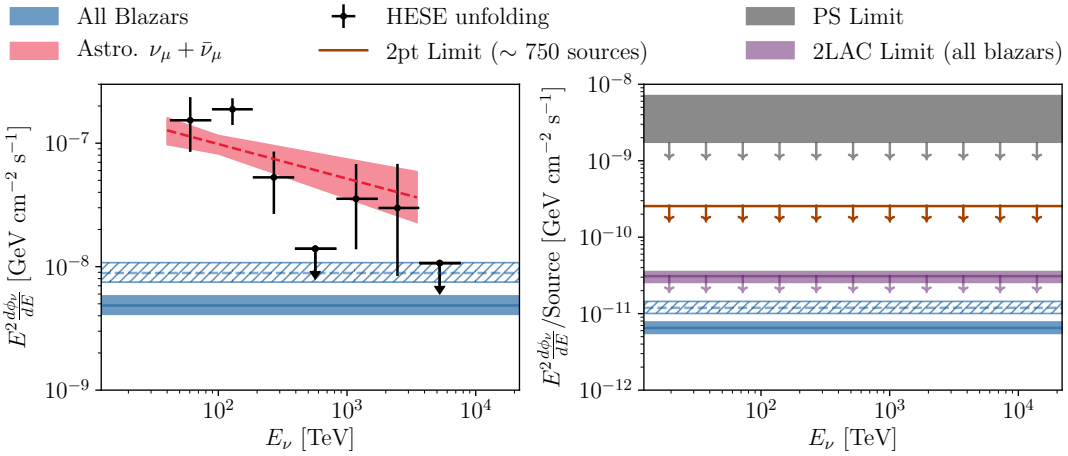

Figure 8.4: Sensitivity (solid blue line and band) and 3σ discovery potential (dashed blue line and band) of the blazar analysis in this work. The flux range of the respective limit corresponds to the 68 % confidence band arising from deviations of the relative neutrino emission strength of blazars from the uniform assumption. The corresponding energy ranges mark the 90 % region where IceCube has the highest exclusion power for the particular model (Appendix G). The diffuse muon neutrino fluxes are taken from [41, 68]. **Left:** Total flux of the population. **Right:** Fluxes per source assuming that their emission strength observed at the Earth is similar for all blazars. The limits from the comparative analyses are taken from [62, 169, 178].

the individual sub-samples, the correction factor is significantly smaller than the one for 10 independent observations. The trial correction distribution for the full sample of 3FHL blazars is illustrated in the right panel of Figure 8.3.

8.2.3 Sensitivity to Neutrino Emission from Fermi-detected Blazars

In order to validate the potential of an analysis, it seems obvious to compare its sensitivity and discovery potential (Section 7.4) to other analysis or general limitations. The sensitivity and 3σ discovery potential flux[9] for the 3FHL blazar population in the Northern Hemisphere is illustrated in the left panel of Figure 8.4. For comparison, the strength of the observed astrophysical muon neutrino flux in this region is illustrated as well [41]. Both the fluxes required for the sensitivity and 3σ discovery potential reside below this observed neutrino flux. Hence, in the scenario where blazars from the 3FHL catalog provide a significant fraction of the observed astrophysical neutrino flux, a significant observation by means of this analysis would not only be possible but also

[9]Based on the assumption of a single power-law distribution with $\gamma = 2$.

Source Class	p-value
HBL	0.31 ($+0.5\sigma$)
LBL & IBL	0.03 ($+1.9\sigma$)
FSRQ	0.56 ($+0.0\sigma$)
All blazars	0.12 ($+1.2\sigma$)

Table 8.2: Post-trial p-values for all tested 3FHL blazar categories.

very likely.

Other than in the search for individual point sources, population analyses such as the one in this work require an initial guess for the position of the sources. While introducing additional source assumptions, these analyses also provide a high sensitivity to the neutrino emission from the population compared to other techniques. This can be visualized by regarding the flux requirements from above, but instead of considering the total flux, we concentrate on the average fluxes per source. The sensitivity and 3σ discovery potential flux requirements per source, assuming an equal emission strength from all blazars observed at the Earth is illustrated in the right panel of Figure 8.4. The required flux per source resides orders of magnitude below the sensitivity and limits from the single point source search. This work is currently the most sensitive test performed on neutrino emission from blazars.

8.3 Results

Looking at the experimentally observed neutrino data, none of the tested blazar categories shows significant evidence for an astrophysical neutrino signal above the background expectations. The most significant post-trial p-value of 1.9σ arises from the sub-category of LBL&IBL. The final post-trial p-values p_{final} for each category are listed in Table 8.2.

The pre-trial p-value distributions of all blazar categories and their respective subsamples are shown in Figure 8.5. None of the observed p-value distributions indicates an obvious and clear correlation between the integrated gamma-ray flux ϕ_{ph} above 10 GeV and a potential neutrino signal. Having a direct correlation between gamma-rays and high-energy neutrinos would imply that sources with the highest ϕ_{ph} should at least on average dominate the neutrino signal and consequently the p-value. Adding more and more sources with lower neutrino power should then further improve the significance. For all tested blazars populations, except for the FSRQs, we can see an increase in significance up to a certain gamma-ray flux threshold ϕ_{ph}, which is followed by a drop in significance afterwards.

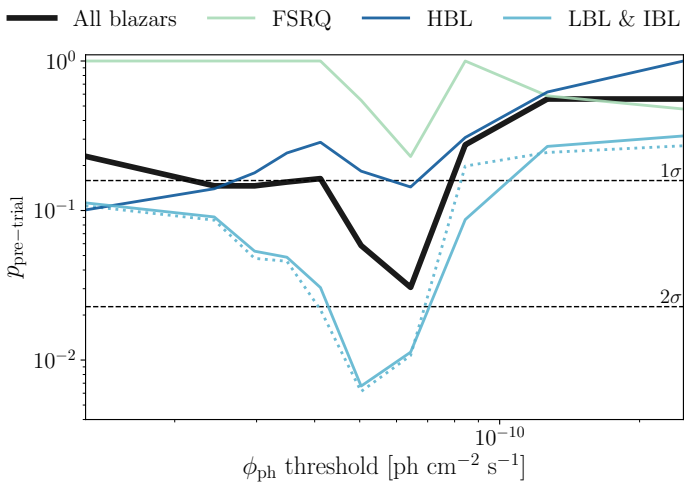

Figure 8.5: P-value distribution for all tested blazar populations from the 3FHL catalog. The x-axis depicts the ϕ_{ph} thresholds used to partition the blazar categories into cumulative sub-samples. The dotted-line illustrates the distribution of the LBL&IBL category without the blazar TXS 0506+056.

Although we observe a rise in significance up to a certain threshold, the largest contribution to the most significant p-values p_{best} does not necessarily arise from the blazars with the highest gamma-ray fluxes. Based on these observations a direct correlation between the gamma-ray flux above 10 GeV and a potential neutrino signal can neither be confirmed nor ruled out completely for HBLs, LBLs & IBLs as well as the total population of 3FHL blazars. Since we basically do not observe any excess for FSRQs at all, no qualitative statement about the correlation with ϕ_{ph} can be made [179].

8.3.1 Interpretation of the Observed Source Parameters

Next to the p-values, the free source parameters maximizing the corresponding likelihood ratio test (Equation (7.38)) can be of interest for the interpretation of the results. The likelihood spaces for the full population of blazars as well as for the most significant sub-sample from each category are illustrated in Figure 8.6 and 8.7 respectively.

While we would expect hard spectra for blazar populations (Section 4.2), all outcomes within this analysis prefer very soft distributions with very soft spectral indices γ between 3 and 4. Such soft spectra are similar to what we would expect from fluctuations of atmospheric background. The red lines in both figures indicate the confidence levels assuming Wilks theorem with two degrees of freedom (Section 7.4)[10]. In this

[10]Due to several approximations on the probability density functions in the likelihood, Wilks theorem is not achieved completely. Nevertheless assuming that the source parameters in the hypothesis

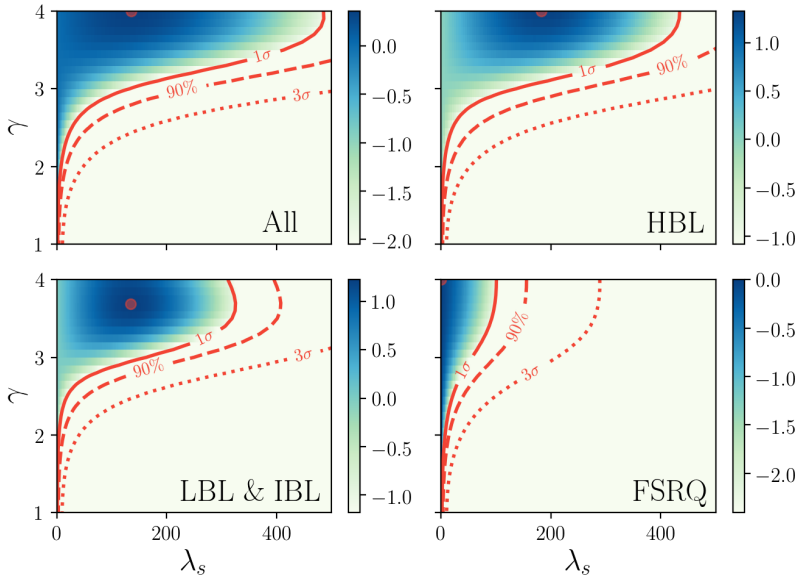

Figure 8.6: Likelihood scan for the full population of each blazar category. The color indicates the likelihood ratio for the corresponding λ_s and γ according to Equation (7.38). The dot indicates the best fit parameters maximizing the likelihood ratio. The red lines depict two-sided confidence levels based on Wilks Theorem with two degrees of freedom (Section 7.4).

scenario, hard spectra below $\gamma = 2$ are excluded for a large number of signal events for all blazar categories. Note that however, incorrect assumptions on the source population parameters can also yield systematic deviations in the observation of the free source parameters. This can, for instance, happen if the relative emission strength of sources is different from the fixed assumption (Subsection 8.2.2). In such scenarios, the global spectral index could attempt to compensate this deviation, by shifting the spectral index to values yielding the optimal detection efficiency for the strongest source (Equation (7.52)). In the case where the strongest neutrino sources are located at high declinations, this effect could yield a shift towards lower neutrino population spectra. A detailed summary of this effect can be found in Appendix F.2. While such situations on average only cause small ($\Delta\gamma \sim 0.5$) deviations in the observed spectrum, the general conclusion from the observation of all best-fit parameters suggests that at least a large fraction of the observed signal λ_s might be caused by fluctuations of atmospheric background.

Although both, p-values and observed source parameters indicate that a large con-

depict an accurate representation of the source population, Wilks theorem yields approximately correct results.

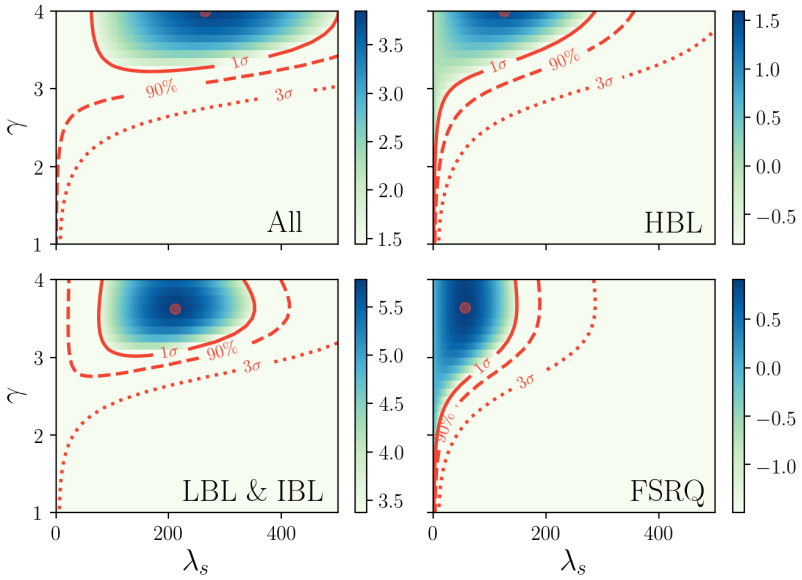

Figure 8.7: Likelihood scan for the most significant sub-population of each blazar category. The color indicates the likelihood ratio for the corresponding λ_s and γ according to Equation (7.38). The dot indicates the best-fit source parameters maximizing the likelihood ratio. The red lines depict two-sided confidence levels based on Wilks Theorem with two degrees of freedom (Section 7.4).

tribution to the observed signal is coming from atmospheric neutrinos, it is worth to further investigate what features of the data are at the origin of the observed results. In the following, we will study the correlation between certain characteristic of the source population and the observed data, while keeping all experimental information that was not part of the test in this analysis blind[11]. Since the most interesting observations arise from the LBL & IBL sources, we will only concentrate on this source category as well as the full sample of blazars in the following. Initially, we aim to figure out how many sources significantly contribute to the observed p-value. This can be achieved by removing individual sources from the population and re-evaluating the hypothesis test. The change in the re-evaluated test statistic value with respect to the original one can be interpreted as a measure for the contribution of individual sources. The number of sources significantly contributing to the final result can be determined by removing the most contributing sources step by step from the analysis hypothesis. This effect is illustrated in Figure 8.8 for the test statistic values of the LBL & IBL blazars. While our naive source hypothesis suggests, that the contribution from the individual sources only

[11]The significance study of individual blazar within the 3FHL catalog is not part of this analysis.

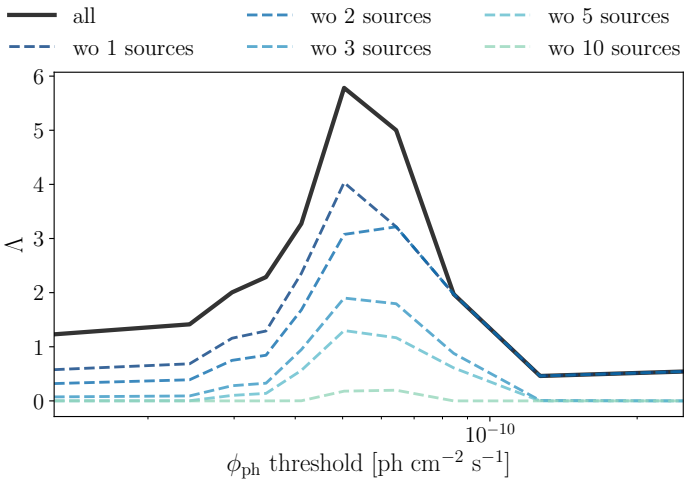

Figure 8.8: Test statistic evolution for the LBL & IBL category. The black line illustrates the full sample of 212 sources. The colored lines illustrate the re-evaluation of the analysis where the X most contributing sources are removed from the test.

differs by the declination dependent detection efficiency of the IceCube detector, we observe that actually only very few of LBL & IBL blazars generate the excess in the data. After removing the 10 most contributing sources from the 212 sources in this category, there is basically no more excess visible within any of the gamma-ray flux threshold ϕ_{ph} bins. This observation could either indicate that the observed excess is solely a result of background fluctuations or that our original assumption of equally strong neutrino emitting sources does most likely not represent the neutrino source count distribution within the catalog.

Next to the absolute number of objects that constitute the observed excess, we want to investigate a potential correlation of specific source characteristics. The distributions of the most contributing sources in the LBL&IBL category with respect to their synchrotron peak ν_{peak}, their declination δ and their integrated gamma-ray flux ϕ_{ph} are shown in Figure 8.9. For none of these source characteristics a clear correlation with the most contributing objects is observable. While the synchrotron peak of the most contributing blazars seems to cluster at the threshold to HBL blazars at 10^{15} Hz, no connection with the gamma-ray flux is visible. Yet, it is interesting to observe that all of the 10 sources that are responsible for the major part of the observed excess in the LBL&IBL blazar sample, are located at high declinations, with $\sin(\delta) > 0.4$. Since the most sensitive region of IceCube to detect neutrino point sources is located at the horizon, this is not what one might expect from the distribution of equally strong

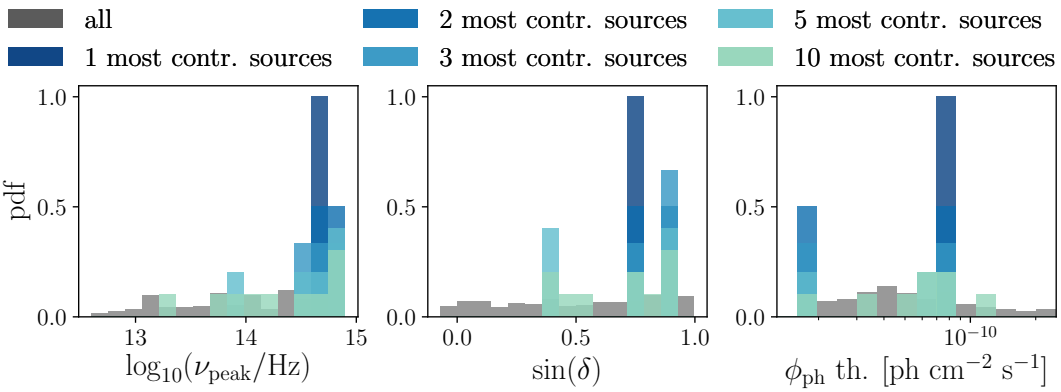

Figure 8.9: Correlation between the specific source characteristics and the objects responsible for the observed excess in the LBL&IBL category.

objects. This effect could be again attributed to background fluctuations or different neutrino source count distribution in the 3FHL catalog. Note that the location of the most contributing sources at high declination might be responsible for a putative shift towards softer observed spectra. This effect is studied in Appendix F.2.

8.3.2 Influence from TXS 0506+056

While none of the tested blazar categories revealed a significant neutrino signal, the largest excess is observed for the LBL&IBL objects with a post-trial p-value of 1.9σ. This is, in fact, the category in which the blazar TXS 0506+056 resides within the 3FHL catalog. As summarized in Section 4.4, this blazar is the first evidential candidate as a source of high-energy neutrinos. During the operation time of IceCube, both a high-energy neutrino alert as well as a neutrino flare of roughly 158 day duration have been observed from the direction of this blazar. Hence it seems obvious to verify if the observed excess seen in this analysis is correlated to this object. As before, the influence of individual sources is investigated by removing them from the tested sample. The outcome for the LBL&IBL sources without TXS 0506+056 is illustrated by the dotted line in Figure 8.5. Comparing this line to the results including TXS 0506+056 shows that TXS 0506+056 hardly influences the outcome of the analysis in this category. While this outcome might seem surprising at first sight, it is not if we closely consider the observations made in the previous subsections. Although from the direction of TXS 0506+056, a neutrino flare was observed at 3.5σ level, the time-integrated neutrino emission from this blazar during the first 8 years of IceCube data[12]

[12]Exactly the same data period that is used for this analysis.

only yields a p-value of $\sim 3\,\%$. The fitted spectrum of TXS 0506+056 tends to prefer hard spectra close to $\gamma = 2$ [5, 180]. In particular, the spectral shape is very different from the one connected to the excess of the LBL&IBL sample. The neutrino signal in this sample is dominated by sources following very soft spectra. In this scenario, the high-energy neutrino events from the moderately strong object TXS 0506+056 lose their discrimination power against the atmospheric background. As a consequence, TXS 0506+056 hardly influences the outcome of this population analysis.

8.4 Implications for the Neutrino Emission from Blazars

Since none of the tested blazar categories showed any significant evidence for neutrino emission above background expectations, upper limits on the $\nu_\mu + \bar{\nu}_\mu$ flux from these blazars are calculated in the following. Assuming a global spectrum for the tested source population, C.L. limits can be evaluated according to the procedure mentioned in Section 7.4. The 90 % C.L. upper limits for all four blazar populations for an unbroken power-law spectrum with $\gamma = 2$ are illustrated in Figure 8.10. Similar to before, the flux range of the respective limit corresponds to the 1σ band arising from deviations of the relative neutrino emission strength of blazars from the equality assumption (Equation (8.2)). The corresponding energy ranges mark the 90 % region where IceCube has the highest exclusion power for the particular model. The procedures used to access these quantities are outlined in Appendix G.

8.4.1 Maximal Contribution of the 3FHL Blazars to the Astrophysical Muon Neutrino Flux

The astrophysical muon neutrino flux observed by IceCube yields a spectrum compatible with a single unbroken power law (Equation (4.1)) with spectral index of $\gamma = 2.28^{+0.08}_{-0.09}$ and $\phi_{100} = 1.44^{+0.25}_{-0.24} 10^{-18}\,\mathrm{GeV}^{-1}\,\mathrm{cm}^{-2}\,\mathrm{s}^{-1}\,\mathrm{sr}^{-1}$ between 40 TeV and 3.5 PeV [41]. The integrated muon neutrino flux in the Northern Hemisphere above $\delta = -5^\circ$ is illustrated as complementary information in Figure 8.10[13].

The upper limit for the neutrino emission from 3FHL blazars resides clearly below this observed muon neutrino flux. In order to quantify the maximally possible contribution of the 3FHL blazars to the total observed astrophysical muon neutrino flux, we can compare the respective energy fluxes in the energy range between 40 TeV and 3.5 PeV

[13] Since the astrophysical muon neutrino flux is consistent with an isotropic distribution, the integration over the Northern Hemisphere with $\delta > -5^\circ$ yields a constant multiplication factor $2\pi \cdot \int_{-5^\circ}^{90^\circ} \cos(\delta)\,\mathrm{d}\delta \sim 2\pi \cdot 1.09$.

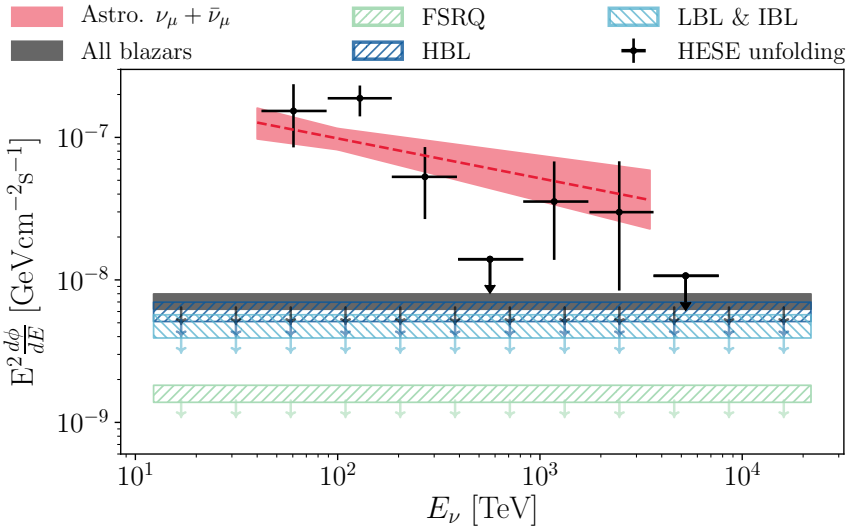

Figure 8.10: 90 % C.L. upper limits for all tested blazar populations assuming an unbroken power-law spectrum with $\gamma = 2$. The illustration of the astrophysical muon neutrino flux is based on data from [41, 68].

defined as

$$\phi_E = \int_{40\,\mathrm{TeV}}^{3.5\,\mathrm{PeV}} E \cdot \frac{\mathrm{d}\phi_\nu}{\mathrm{d}E}\,\mathrm{d}E\,. \tag{8.4}$$

The ratio $r \coloneqq \phi_E^{\mathrm{pop}}/\phi_E^{\mathrm{astro}}$ then depicts the maximally feasible contribution of the tested population to the total astrophysical muon neutrino energy flux ϕ_E^{astro}. Assuming an unbroken power-law with $\gamma = 2$, the blazar population in the 3FHL catalog can maximally account for 8.6 % to 11.0 % of the average astrophysical muon neutrino flux (6.6 % to 14.5 % if we account for the entire 1σ uncertainty band of the diffuse measurement as well) in the Northern Hemisphere. While most of the contribution in such scenarios would arise from BL Lacs (HBL and LBL & IBL), the maximal share from the FRSQ population in the 3FHL catalog would add up to 1.9 % to 2.5 % (1.5 % to 3.3 % accounting for the 1σ uncertainty band of the diffuse flux).

The exact fractions depend strongly on the hypothetical source spectrum. Assuming different spectral shapes allows the description of a larger share of the total muon neutrino flux within certain energy ranges. The limits for different hypothetical source spectra are illustrated in both panels of Figure 8.11. Their maximal contributions r to the astrophysical muon neutrino flux from the Northern Hemisphere are listed in Table 8.3. Since there is no indication for the blazar populations to follow a single unbroken power-law, also other scenarios are investigated. As introduced in Subsection 4.2.1,

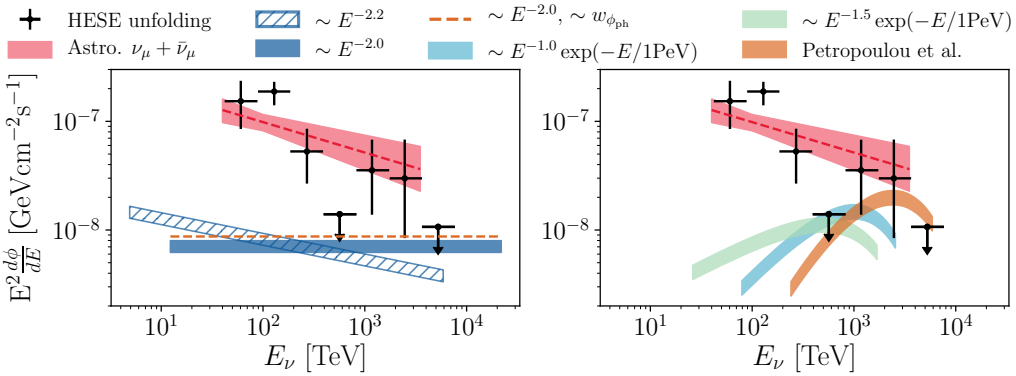

Figure 8.11: 90 % C.L. upper limits for various hypothetical source spectra. The data of the astrophysical muon neutrino spectrum are taken from [41, 68]. The data for the theoretical model from Petropoulou et al. is taken from [84].

theoretical models allow blazars to follow very hard spectra. In such cases, an energy cut-off is expected once the hadronic acceleration of protons at the source breaks off. Such scenarios are illustrated in the right panel of Figure 8.11.

Next to these arbitrary source spectra, additional theoretical predictions for blazars can be tested. The authors in [84] modeled the SED of several HBL objects by means of a multi-wavelength leptohadronic emission model, automatically yielding a prediction for the neutrino emission. For the blazar Mrk 421 the prediction was found to be in good agreement with the neutrino flux implied by a cascade-like IceCube event located in the vicinity of the object [164]. Using the neutrino emission shape from Mrk 421 for all blazars in the 3FHL catalog, this population can account for no more than 38 % of the astrophysical muon neutrino flux between 240 TeV and 3.5 PeV.

In summary, we conclude that the maximal contribution r to the diffuse muon neutrino flux from the 3FHL blazar population within certain energy regions can significantly vary based on the choice of the global source spectrum. Nevertheless, independent of the selected spectrum, the 3FHL blazars cannot describe the bulk of the observed astrophysical muon neutrinos over the entire energy range between 40 TeV and 3.5 PeV.

8.4.2 Constraints on the Neutrino Emission from GeV Blazars

The outcomes in the previous subsection illustrate that the blazars detected by the *Fermi LAT* above 10 GeV within the first seven years of observations cannot explain the bulk of the observed astrophysical muon neutrino emission. In order to integrate these neutrino observations in the multi-messenger picture of blazars, it is interesting to compare these numbers to the associated values in the gamma-ray sector. The con-

Spectrum $\frac{\mathrm{d}\phi}{\mathrm{d}E}$	E_{min} [TeV]	E_{max} [TeV]	r [%]
E^{-2}	40	3.5×10^3	$6.6 - 14.5$
$E^{-2.2}$	40	3.5×10^3	$6.1 - 13.6$
$E^{-2.2}, \sim w_{\phi_{\mathrm{ph}}}$	40	3.5×10^3	$9.2 - 15.8$
$E^{-1.0} \exp(-E/1\,\mathrm{PeV})$	79	2.5×10^3	$9.4 - 22.3$
$E^{-1.5} \exp(-E/1\,\mathrm{PeV})$	40	1.7×10^3	$7.4 - 16.7$
Petropoulou et al. [84]	240	3.5×10^3	$14.1 - 38.0$

Table 8.3: Maximal fraction r of the diffuse muon neutrino energy flux that can be explained by blazars from the 3FHL catalog for different hypothetical source spectra. The ratios are based on the limits illustrated in Figure 8.11. The energy ranges used for the comparison consist of the overlapping most relevant regions of the diffuse flux and the respective limit. The ratio r accounts for both, the 68 % uncertainties of the limits as well as the 68 % uncertainties of the diffuse muon neutrino flux measurements [41].

tribution of blazars[14] to the extra-galactic background light above 10 GeV aggregates to (42 ± 8) % [51]. Assuming a power-law with spectral index $\gamma = 2$, the 3FHL blazar population can maximally constitute 14.5 % of the astrophysical muon neutrino flux above 40 TeV. Hence the relative contribution in the respective messenger sector differs by at least a factor of 3 in this scenario. While different shapes of a global neutrino spectrum allow larger contribution to the astrophysical neutrino flux in certain energy ranges, no assumption on a global spectral shape permits a significantly larger contribution to the total astrophysical muon neutrino flux over the whole observed energy range. Consequently, the difference by a factor of 3 depicts a conservative lower-limit estimate, nearly independent of the spectral assumption of the neutrino emission. Assuming a direct correlation between the integrated gamma-ray flux ϕ_{ph} above 10 GeV and the neutrino flux in the IceCube energy region on a source-by-source basis, the maximal possible contribution to the astrophysical neutrino flux from the 3FHL blazars would be $9.2 - 15.8$ % (Table 8.3), yielding a difference in the relative contribution of the two messengers by a factor of ~ 3.

A possible interpretation of this difference is not trivial. In principle, this could indicate that a large fraction of the observed gamma-ray flux above 10 GeV from the 3FHL blazars is generated by leptonic processes. Assuming optically thin environments at the site of the blazars and following the strategy mentioned in Section 4.3 [79], we can place simplified upper-limits on the relative contribution of hadronic production mechanisms in the 3FHL catalog. This approach is illustrated in Figure 8.12. In [79] the distribution of the observed EBL emission at gamma-ray energies is modeled by

[14] Nearly all of the contribution attributes to sources resolved in the 3FHL catalog

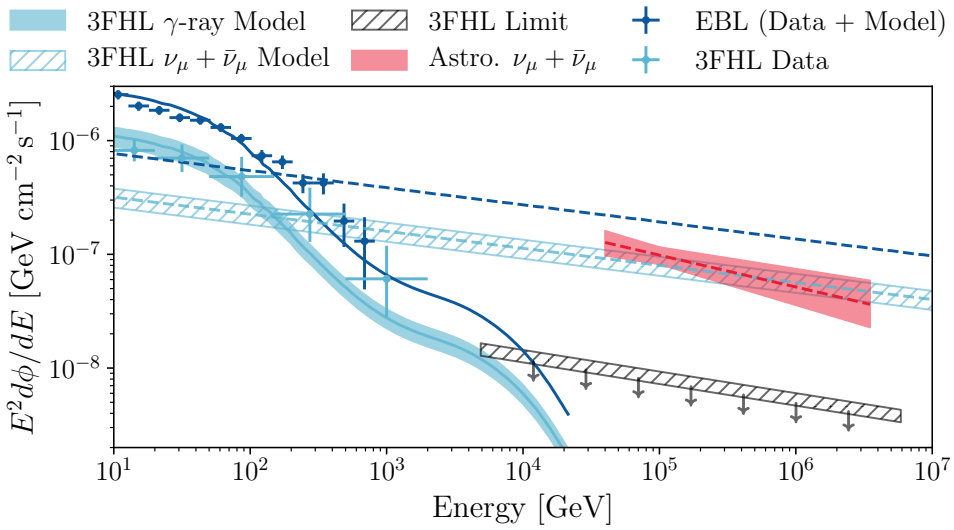

Figure 8.12: Comparison of neutrino predictions for 3FHL Blazars in purely pionic scenarios and the observed limits from this analysis. The plot follows the format in Figure 4.4 and [79]. The error-bars for the 3FHL blazars are taken from data in the 3FHL catalog [165]. More details on the content of the plot can be found in the text.

an initial power-law spectrum with spectral index $\gamma \sim 2.15$. The photon flux above $\sim 100\,\mathrm{GeV}$ is strongly attenuated by interactions with cosmic background radiation. The production rates of gamma-rays and neutrinos from pion decays[15] are correlated according to Equation (4.24). Assuming that all gamma-rays are products of such pion decays, yields an upper limit on the associated neutrino flux (dashed line in Figure 8.12). This approach can be easily adapted to the blazars from the 3FHL catalog. Above 10 GeV, these blazars roughly contribute $(42 \pm 8)\,\%$ to the extragalactic background light. This gamma-ray flux can be used to calculate the maximal possible neutrino flux from the 3FHL blazars (hashed band) in the scenario where gamma-rays are generated from pion decays. Comparing this neutrino flux prediction to the actually observed limits within this analysis yields a limit on the relative fraction of hadronic generation processes within these sources. Assuming a neutrino power-law shape similar to the one from the gamma-ray prediction, the maximal fraction of hadronically generated gamma-rays evaluates to 8.5 % to 16.2 % if the decaying pions itself are produced in proton hadron interactions (17.0 % to 32.4 % if the pions are generated in photo-hadronic interactions).

The argumentation in the preceding discussion presumes that the gamma-ray emission

[15] These pions can be produced in both *pp* and photo-hadronic interactions (Section 3.2).

rate from the acceleration site of the source is equal to its generation rate. In particular, in the case of gamma-ray production in photo-hadronic processes, such a scenario seems very unlikely. The photon field required for photo-hadronic processes, not only serves as a target for accelerated protons but most likely also efficiently reduces the rate of the resulting gamma-rays due to pair-production [181]. In these source scenarios, the correlation between observable gamma-rays and neutrinos is strongly obliterated and requires detailed modeling of the environment at the site of acceleration. However, the specific evaluation of the maximal possible fraction of hadronic processes from the previous paragraph also applies for the hadronic generation of gamma-rays at the site of the source. Note that the arguments used throughout this section are based on the assumption that IceCube neutrinos are generated through the decay of charged pions and that both the generation spectra of gamma-rays and neutrinos follow a power-law distribution. More exotic generation models might change the whole picture, but will not be treated within this work.

In summary, the results within this analysis state that the blazars from the 3FHL catalog cannot explain the majority of the astrophysical muon neutrino flux observed in IceCube. Since the 3FHL blazar catalog depicts a rather complete selection of objects contributing to the blazar induced gamma-ray flux above 10 GeV [51], it is also very likely that these blazars, in general, do not depict the major origin of high-energy neutrinos. Moreover, the neutrino limits suggest that the largest fraction of gamma-rays from these sources are likely to be generated from accelerated electrons. However, it is worth noting that these results do not claim that blazars, in general, cannot be the origin of IceCube neutrinos. For instance, blazars that are faint at 3FHL or generally *Fermi-LAT* energies could in principle still produce the flux observed in IceCube. Such scenarios can be studied in dedicated multi-messenger analyses.

8.4.3 3FHL Blazar Limits in the context of TXS 0506+056 and Transient Sources

The blazar TXS 0506+056 is the found to be the first candidate with high evidence[16] to generate astrophysical neutrinos observable at IceCube energies. Although TXS 0506+056 is part of the 3FHL blazar catalog, we did not observe any significant sign for neutrino emission from this population. The two observations by itself do not constitute an obvious contradiction. Yet, it seems obvious to check if the outcomes from this analysis and the TXS 0506+056 studies are in agreement. In Figure 8.13 the average

[16] Note that neutrino observations of TXS 0506+056 do not count as a discovery but only depict high evidence for a correlation (Section 4.4).

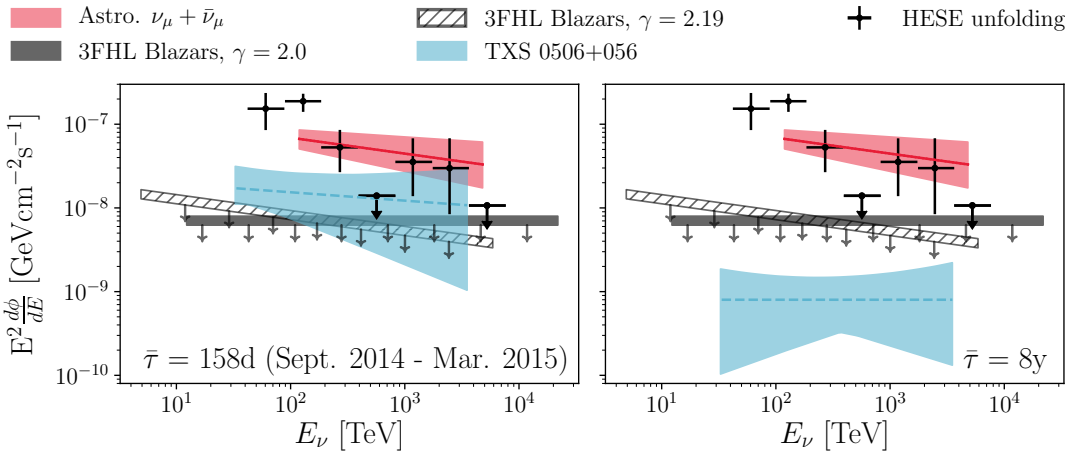

Figure 8.13: 90 % C.L. limit on the flux from the blazar population in the 3FHL catalog for two different spectral assumptions compared to two different scenarios of the blazar TXS 0506+056. **Left:** Average flux of TXS 0506+056 during the 158 d flaring period in 2014/2015. **Right:** Average Flux of TXS during $\sim$ 8 years of measurement.

neutrino flux from the position of TXS 0506+056 is shown for two different scenarios. In the left panel, the 68 % C.L. band for the average neutrino flux TXS 0506+056 is illustrated, assuming that it is a steady neutrino source over the whole lifetime of the IceCube detector measurements [5]. In contrary the flux in the right panel represents the average flux scenario in which this blazar can be interpreted as a flaring source, producing neutrinos only within a 158 d flare in 2014 and 2015 [5]. For comparison, the 90 % C.L. limits for the blazar population from the 3FHL catalog are shown as well for $\gamma = 2$ and $\gamma = 2.19$. Corresponding to the definition of the population analysis in this work, these limits are produced under the assumption that the whole blazar population consists of steady emitting sources following a single global power-law. During the short flaring period of TXS 0506+056 the average flux of this source is on average higher than the 90 % C.L. limit from the whole 3FHL blazar population. On the other hand, once the average neutrino activity of TXS 0506+056 over the whole 8 years of IceCube exposure is compared to the limits from the blazar catalog one can observe that on average the neutrino emission from TXS 0506+056 is much lower. Since the limits from the 3FHL population analysis are only giving rejection power for the average neutrino emission of steady sources, it is not absolutely surprising that individual sources can outshine these limits over shorter periods of time. The neutrino observations of TXS 0506+056 and the limits presented in this work show very good agreement but also emphasize how exceptional the neutrino flare of TXS 0506+056 in 2014/2015 was [179].

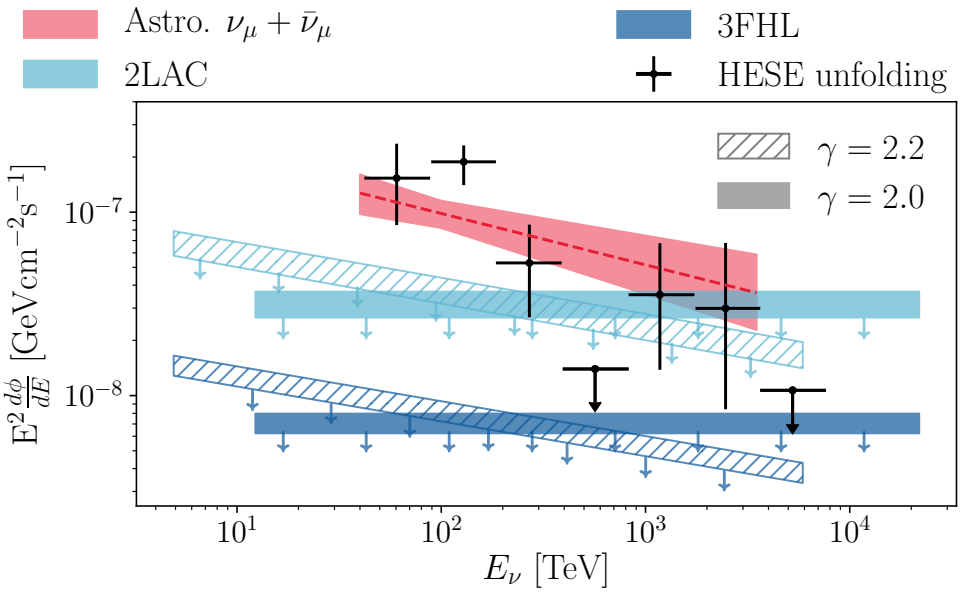

Figure 8.14: Comparison between the neutrino limits from the 2LAC and the 3FHL blazar catalog. The data for the 2LAC limits are taken from [169]. The data for the observed diffuse muon neutrino spectrum are taken from [41, 68].

8.5 Outlook

Despite not being able to explain the entire origin of IceCube's high-energy neutrinos, the scenario of neutrino production from the 3FHL blazar population is not ruled out by this analysis but only restricted by the upper limits set in the previous section. Adding more IceCube data might slightly improve the sensitivity (Subsection 8.2.3) of the analysis, yet most likely will not vastly change the general observation made in this work[17]. Moreover, the implementation of the hypothesis test in this work uses numerous approximations for the evaluation of the respective probability densities. An implementation with more accurate characterizations of the emerging probability density distributions is current work in progress. However, similar to increasing the statistics of neutrino data, this update will most likely only have marginal effects on the outcome of the analysis.

Although the population of blazars that is dominant at gamma-ray energies above 10 GeV is not responsible for the bulk of the astrophysical muon neutrino flux, blazars

[17] This depends on the putative time variability of the sources. For highly variable sources one could by chance pick up a lot of neutrino signal even within short time periods.

	$\gamma = 2.0$	$\gamma = 2.2$
3FHL	$(6.6 - 14.4)\%$	$(6.1 - 13.6)\%$
2LAC	$(28.1 - 66.9)\%$	$(26.6 - 63.4)\%$

Table 8.4: Maximal fraction of the diffuse muon neutrino energy flux between 40 TeV and 3.5 PeV that could be explained by blazars from the respective *Fermi-LAT* catalog.

that do not appear at gamma-ray energies, or only appear at the lower energies, can in principle still contribute a significant fraction. Previous neutrino limits from the 2LAC catalog (detected above 100 MeV, Subsection 8.2.1) constrained the maximal contribution of these blazars to the astrophysical muon neutrino flux to 27 % [169]. In their publication, the authors used the derivation of an all-flavor neutrino flux for the comparison. In order to allow a fair relation to their limits, this flux was reduced to account for muon neutrinos by assuming a flavor ratio of $(\hat{\nu}_e : \hat{\nu}_\mu : \hat{\nu}_\tau) \sim (1 : 1 : 1)$ (Subsection 4.2.3). Comparing the limits to an updated version of the actually observed muon neutrino flux in the Northern Hemisphere (Figure 8.14), a larger contribution of up to $\sim 67\,\%$ might be feasible.

The possible contributions for both, the 2LAC and the 3FHL catalog to the muon neutrino flux between 40 TeV and 3.5 PeV are listed in Table 8.4 respectively for two different hypothetical source spectra. An updated version of the 2LAC, namely the 4LAC based on 8 years of observation time was recently released by the *Fermi LAT* collaboration [46]. Compared to its predecessor 2LAC, this catalog contains nearly three times the amount of sources detected with a slightly lower energy threshold of 50 MeV. A re-evaluation of the previous 2LAC blazar population analysis with the updated source catalog in combination with a vastly increased amount of available neutrino data can give further insight into this blazar scenario.

Ultimately it is worth pointing out again, that the analysis in this work was implemented with the aim to observe time-integrated neutrino emission from the 3FHL blazar population. However, the hypothesis test can be easily extended to include assumptions on potential time-dependent neutrino emission features. This could, for instance, involve studies correlating gamma-ray and neutrino flaring periods.

9

Future Prospects for High-energy Neutrino Astronomy

The history of neutrino physics and in particular high-energy neutrino astronomy at the South Pole depicts a success story over many decades. The major milestones along the path towards our current knowledge are illustrated in Figure 9.1. With the detection of atmospheric neutrinos in AMANDA in 2001 [183], and the discovery of astrophysical neutrinos in 2013 with the successor IceCube [2], both detectors achieved their primary objective shortly after their completion. Since then the IceCube collaboration confirmed this discovery in different distinct analyses. Yet no sources of these astrophysical neutrinos have been discovered within the first 10 years of detector lifetime. In 2018 the blazar TXS 0506+056 revealed first evidence for high-energy neutrino emission in multi-messenger studies (Section 4.4). As shown in the previous chapter such evidence could not be confirmed for the general case of blazar or any other source populations yet. Consequently, it seems reasonable to re-think the possible search strategies for the origin of high-energy astrophysical neutrinos. For this reason, we summarize the current status, potential, and issues of point source searches performed in IceCube in the first

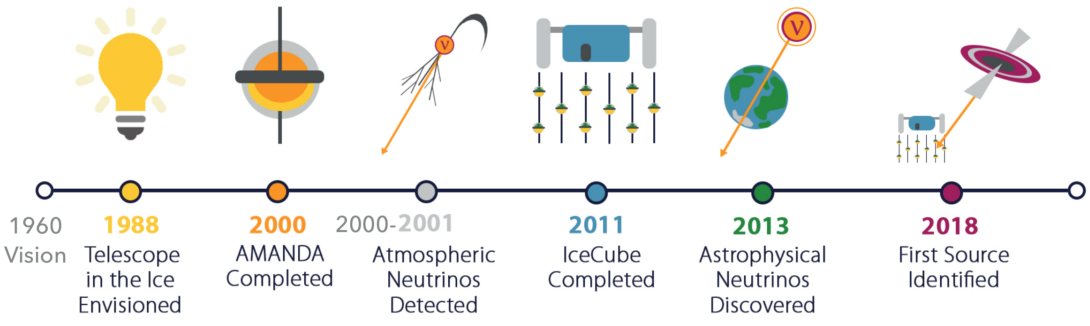

Figure 9.1: Timeline of the history of neutrino astronomy at the South Pole. The figure is taken from [182].

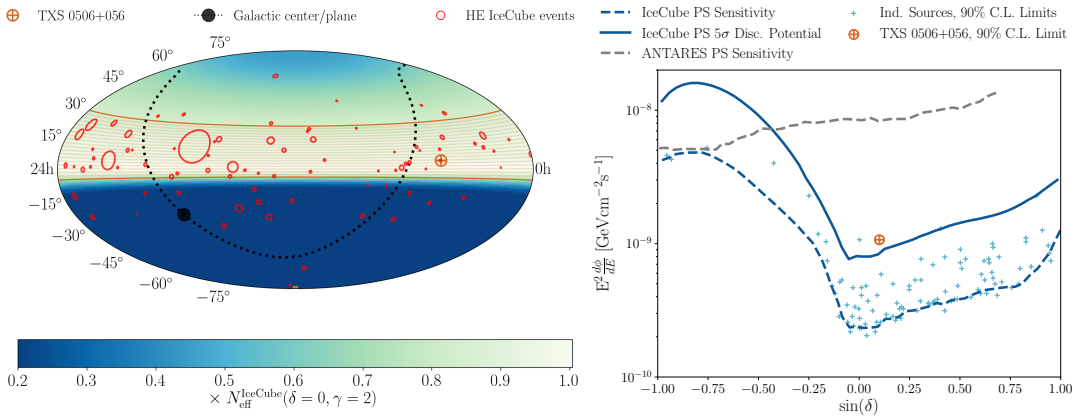

Figure 9.2: **Left:** Detection efficiency N_{eff} of the IceCube detector. The orange band indicates the most optimal region for neutrino point source searches with this setup. **Right:** Sensitivity and 5σ discovery potential for neutrino point sources with 10 years of IceCube data. The data are taken from [3].

section of this chapter. Afterward, we propose a global neutrino telescope network of existing and prospective neutrino observatories and study its potential in Section 9.2.

9.1 Current Status of High-energy Neutrino Point Source Searches

Since the first discovery of an astrophysical neutrino flux in 2013, the IceCube collaboration has raised large efforts to localize the origin of these events. Next to independent searches within neutrino data, several known astrophysical objects and populations (e.g. the 3FHL blazar population in Chapter 8) have been studied for their neutrino emission. While one of these multi-messenger studies revealed evidence for neutrino emission from the blazar TXS 0506+056, no source has been discovered at a 5σ level within the first 10 years of detector lifetime. In order to develop further strategies of neutrino point source searches, the status and the potential of current analyses with IceCube is illustrated in both panels of Figure 9.2. The sky map in the left panel illustrates the detection efficiency N_{eff} of the IceCube detector defined as

$$N_{\text{eff}}(\delta, \gamma) = \int_0^\infty A_{\text{eff}}(\delta, E_{\nu_\mu}) E_{\nu_\mu}^{-\gamma} \, \mathrm{d}E_{\nu_\mu} \,, \tag{9.1}$$

for a source with spectral index $\gamma = 2$. In general, the detection efficiency is proportional to the number of expected astrophysical events N_{ν_μ} (Equation (7.27)) from a source

with spectral index γ. The distribution in the left panel of Figure 9.2 nicely shows that for sources with hard $\gamma = 2$ power-law spectra, the detection efficiency rapidly drops in the Southern Hemisphere below $\delta \sim -5°$. This effect is caused by atmospheric muons vastly dominating the event rate in this region. Above $\delta = 30°$ the detection efficiency of the IceCube observatory also drops in the Northern Hemisphere due to the absorption of high-energy neutrinos inside the core of the Earth. Hence the optimal region of the IceCube detector for such sources is limited to the region around the horizon from approximately $-5°$ to $30°$. Although IceCube constantly observes neutrinos from every direction in the Universe, this means that only $\sim 30\,\%$ of the sky is covered with optimal sensitivity. The distribution of high-energy track-like events, most likely representing astrophysical muon neutrino events clarify this observation. The vast majority of these events are located in the region around the horizon. Some high-energy events are also detected in the Southern Hemisphere by means of vetoing techniques, that only yield minor enhancements for statistical searches of neutrino point sources. Two more points are worth to be noted from the illustration of this sky map. Firstly, the blazar TXS 0506+056 is located exactly within the optimal region of the IceCube detector and thus has an maximal probability to be detected. Secondly, we can see that only a small part of the galactic plane is covered by the region around the horizon, while a large part including the galactic center can only be studied with the considerably worse sensitivity in the Southern Hemisphere.

The distribution of the sensitivity and discovery potential sources with a $\gamma = 2$ spectrum, shown in the right panel of Figure 9.2 reassures the improved sensitivity of IceCube at the horizon for hard sources. Besides it also provides additional information about the potential of future neutrino point source discoveries. Next to the sensitivity and discovery potential of IceCube[1], the flux limits of several potentially interesting sources are shown (blazars, etc.). Several of these sources reveal limits close to the one observed for TXS 0506+056 and in particular close to the flux threshold required for discovery. Hence it might be possible that we just reached the threshold for many more neutrino sources similar to TXS 0506+056. Improving the performance of the current analyses might shed light on this speculation. The fundamental question is, if such improvements can be realized by means of additional data from the IceCube detector. In order to answer this question we have to contemplate the temporal evolution of the sensitivity and discovery potential with increasing amount of data. We can identify theoretical boundaries by considering two extreme scenarios. Assuming that the region around the hypothetical source is dominated by background, then the statistical

[1]Note that both thresholds are not corrected for the look elsewhere effect that arises from scanning the whole sky.

fluctuations of these background events evolve with the square root of the total amount of events[2] and hence the measuring time t. The amount of the signal events on the other hand increases linearly with t (Equation (7.27)), yielding an improvement of the discrimination between signal and background that is proportional to

$$\frac{\mathrm{d}\phi^{\mathrm{min}}_{\mathrm{thr}}}{\mathrm{d}E_\nu}(t, t_0) \propto \frac{1}{\sqrt{t/t_0}}, \tag{9.2}$$

where $\frac{\mathrm{d}\phi_{\mathrm{thr}}}{\mathrm{d}E_\nu}$ can be both, the flux threshold for the sensitivity as well as the discovery potential and t_0 depicts an artificial reference time. In a background free environment, the improvement of the analyses performance only depends on the linear growth of the signal event rate, yielding

$$\frac{\mathrm{d}\phi^{\mathrm{max}}_{\mathrm{thr}}}{\mathrm{d}E_\nu}(t, t_0) \propto \frac{1}{t/t_0}. \tag{9.3}$$

The actual evolution of the discovery potential for single point source searches as well as for population searches such as the 3FHL blazar stacking in Chapter 8 depict an average of both scenarios [158]. Assuming a single power-law with spectral index $\gamma = 2$, the performance for both analyses improves with

$$\frac{\mathrm{d}\phi_{\mathrm{thr}}}{\mathrm{d}E_\nu}(t, t_0) \propto\sim \frac{1}{(t/t_0)^{0.8}}. \tag{9.4}$$

This means that the performance of point source analyses can be improved by $\sim 40\,\%$ when doubling the amount of experimental data. Hence additional data represent a powerful tool to improve the sensitivity of point source analyses throughout the first years of data-taking. Nevertheless current point source analyses in IceCube already make use of ~ 10 years of data. Hence significant improvements in the performance of the analyses can not be expected from the collection of more data[3].

In 2014 the IceCube collaboration proposed an extension of the current IceCube detector, called *IceCube-Gen2* [184]. This successor is supposed to instrument $10\,\mathrm{km}^3$ of glacial ice, with the spacing of the modules optimized for high-energy muon neutrino tracks. Due to the potential improvements of the reconstructions (a long lever arm allows both, improved directional as well as energy reconstructions) and a vast increase in statistics, this detector aims to improve the performance of point source analyses by a factor of ~ 5 with respect to the current IceCube detector. While *IceCube-Gen2* could

[2] Similar to the standard deviation of a poissonian distribution.

[3] Note that neutrino flares could by chance still yield discoveries of neutrino sources with the current setup.

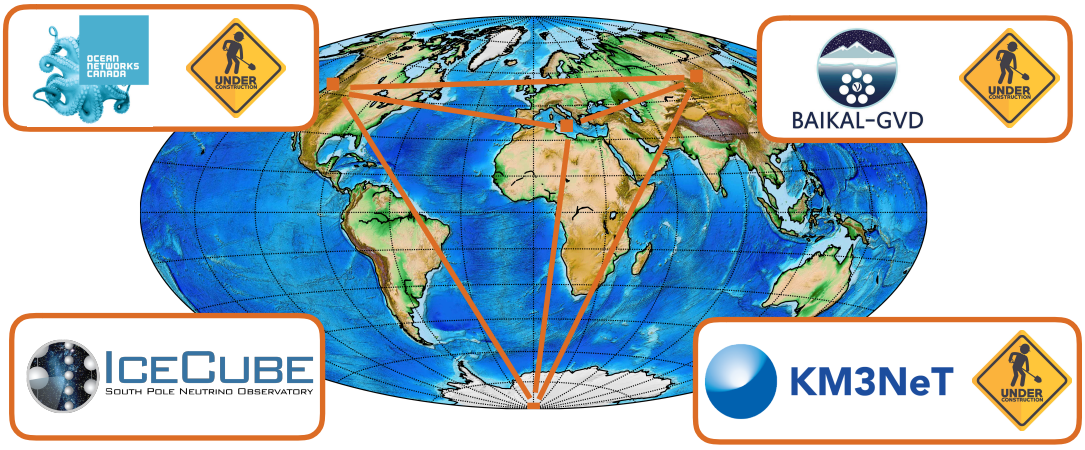

Figure 9.3: Location of the observatory sites of the available large volume neutrino telescopes.

overcome the flux threshold to discover neutrino sources at the horizon, its optimal performance is limited to the region around the horizon, hence missing roughly 70 % of the entire sky[4].

9.2 Prospects towards a Global Neutrino Telescope Network

Despite being the only neutrino telescope build in ice, IceCube is not the only neutrino observatory on our planet that aims to detect high-energy neutrinos. With the Baikal Gigaton Volume Detector (Baikal-GVD)[135], the Cubic Kilometer Neutrino Telescope (KM3NeT)[133] and the Pacific-Ocean Neutrino Explorer (P-ONE)[185] three more neutrino detectors based in water are under construction or running in partially finished configurations (Subsection 6.4.2). All of these neutrino observatories attempt to find the origin of high-energy astrophysical neutrinos, bringing light into the physics involved in multi-messenger astronomy. The different sites of these observatories are marked on the world map shown in Figure 9.3.

In order to improve the sensitivity for a discovery of high-energy neutrino sources, we investigate the combined performance of a global network of all four neutrino telescopes. We will call this global network *Planetary Neutrino Monitoring system* (PLEνM) throughout this thesis [185]. Using a combined effort of all existing resources

[4]Note that both IceCube and IceCube-Gen2 are actually observing these parts in the sky as well but only with limited sensitivity.

will not only offer maximal sensitivity towards the detection of neutrino sources but can also solve the challenges obtained by the individual detectors (such as for instance the declination dependent analysis performance in IceCube). In the following chapter, we will study the potential of PLEνM. In a first step, we compare the optimal field of views from the respective detection site before we derive estimates for the sensitivity and discovery potential of the global telescope network based on simplified, yet conservative detector assumptions.

9.2.1 Combined Field Of View of PLEνM

As mentioned repeatedly throughout this thesis, the performance of point source analysis in IceCube is optimal for sources located at the horizon. In this region, the event rate is neither dominated by atmospheric muons (because of the shielding of the Earth) nor affected strongly by the absorption of the high-energy part of the neutrino flux in the Earth's core. These effects are not the result of any specific detector geometry but are solely caused by the particular location of the detection site. Hence we expect a similar behavior for each of the other telescopes as well. Yet, instead of the actual horizon, their best field of view will be at the respective detector *horizon* of their observation site. A combined field of view of all four neutrino telescopes is shown in Figure 9.4, assuming that the optimal detection range of each telescope is similar to the one from IceCube from $\delta \in \{-5°, 30°\}$.

Although being an extremely simplified consideration, this illustration already provides valuable information about the behavior and the potential of a combined telescope network. While IceCube's performance constantly peaks at the horizon, the optimal detection regions of the other telescopes shift throughout one day due to the rotation of the Earth. These shifts are illustrated by the four panels in Figure 9.4, which are respectively shifted by 6 h (corresponds to 90°). From each of these skymaps, it is obviously visible that a large region of the Universe is covered by at least one of the telescopes in optimal configuration at any point in time. Based on the optimal angular observation range chosen for this illustration roughly 85 % of the sky are provided with optimal exposure of PLEνM. The missing fraction mostly resides in the region close to the North Pole, which is not covered by any of the telescopes.

Despite the extension of the total exposure of the Universe by nearly a factor of 3, the potential of PLEνM compared to IceCube can be highlighted by means of two specific examples. As previously mentioned, a large fraction of the galactic plane including the galactic center is located in the low-performance region of the IceCube detector. Using a combined telescope network completely changes this picture. As visible in Figure 9.4

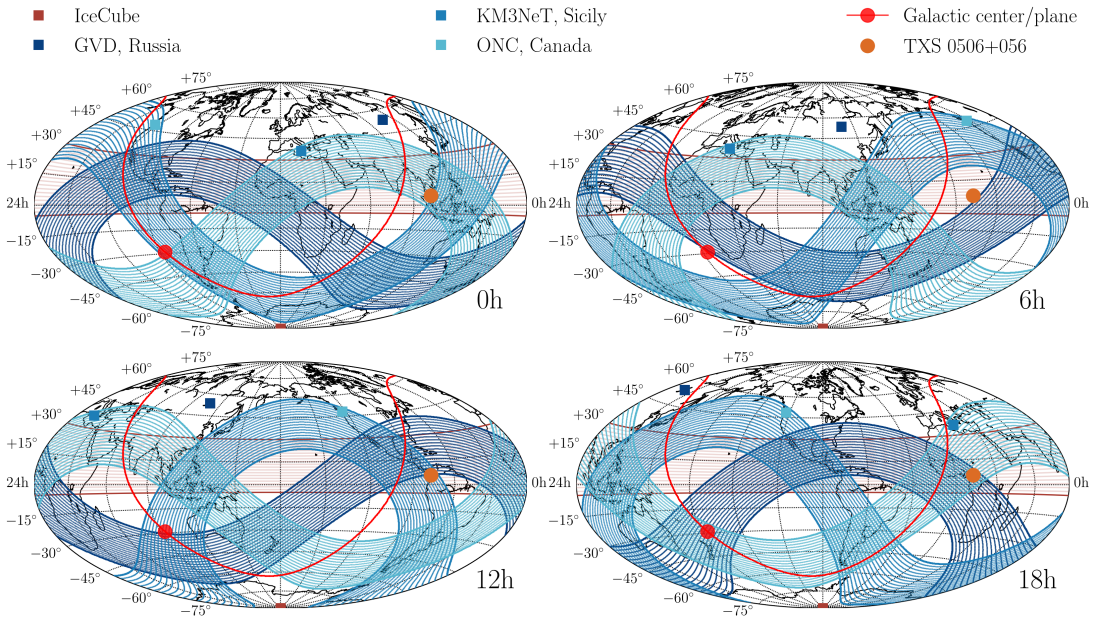

Figure 9.4: Optimal field of views from different detection sites at different observation times. While IceCube is not affected by the rotation of the Earth due to its exceptional location, the optimal field of views of the Universe from the other telescope sites are shifted with time.

the galactic center, as well as a large fraction of the galactic plane, constantly appear within the optimal detector performance region of one of the observatories. In this way, not only the time-integrated flux but even short transient emission of sources from this region could be observed. Note that in principle this improvement is not restricted to galactic phenomena, but could be applied to any kind of neutrino source that is not located close to the North Pole.

Next to the study of galactic phenomena, a combined neutrino telescope network could be also used to strengthen or rule out the discovery of neutrino sources for instance at the horizon. This can be exemplary demonstrated by looking at the particular example of the blazar TXS 0506+056, that showed evidence for neutrino emission at a 3.5σ level within IceCube data between September 2014 and March 2015 [5]. From Figure 9.4, it becomes clear that in the case of TXS 0506+056 being a source, a roughly similar neutrino signal should have been visible in a combined effort of the remaining three telescopes. Observing a signal at a similar level (3.5σ) would boost the individual IceCube result to a combined outcome of PLEνM very close to a point source discovery at $\sim 4.8\sigma$[5]. In a similar way, the signal observation by IceCube could have been

[5]Based on Fisher's method for two independent results bearing upon the same null hypothesis [186].

sanctioned and potentially ruled out by not detecting any signal by any of the other telescopes.

9.2.2 Neutrino Point Source Discovery Potential of PLEνM

In the previous subsection, we pointed out the potential of PLEνM that arises from the superposition of the best field of views from the individual telescopes. Nevertheless, in this simplified view, we completely neglect that each of these observatories also observes neutrinos outside these regions with lower sensitivity towards point source searches. In this subsection, we want to include the full potential of each telescope in order to derive a realistic estimation of the sensitivity and discovery potential of a combined network. Since none of the telescopes apart from IceCube reached their final detector configuration yet, we cannot rely on performance measurements from these sites. In order to estimate the combined potential of PLEνM anyway, we built our study on the basic detector assumptions from IceCube. In the following, we will assume that each of the neutrino telescopes included in PLEνM performs exactly like the IceCube detector, but at its respective telescope location. Since each of the new telescopes under construction (KM3NeT, Baikal-GVD and P-ONE) are designed to outperform IceCube in the search for high-energy neutrino sources, this depicts a very conservative assumption. Consequently also the values for the discovery potential that will be shown depict conservative estimates, that will most likely be outperformed by the actual implementation of PLEνM.

Since all of the telescopes within the network of PLEνM can be de treated as independent observatories, we can use a linear superposition of the individual effective areas

$$A_{\text{eff}}^{\text{PLE}\nu\text{M}} = \sum_k A_{\text{eff}}^k, \tag{9.5}$$

with $k \in \{\text{IceCube, KM3NeT, Baikal-GVD, P-ONE}\}$. On the basis two essential facts we can use this effective area to evaluate the combined potential. Initially we recall from Equation (7.27), that the number of observable events from a steady emitting source with flux $\frac{\mathrm{d}^2\phi_{\nu_\mu}}{\mathrm{d}t\mathrm{d}E}$ is defined as

$$N_{\nu_\mu} = \int_{\Delta E} A_{\text{eff}}(E,\delta)\frac{\mathrm{d}^2\phi_{\nu_\mu}}{\mathrm{d}t\,\mathrm{d}E}\,\mathrm{d}E\,\tau, \tag{9.6}$$

where τ depicts the total observation time. Similar to the total observation time τ, the effective area A_{eff} incorporates linearly in this definition. Hence constant changes in

either of the two parameters have similar effects on the number of signal events. In this sense we observe twice the amount of signal events N_{ν_μ} from doubling the effective area as well as from doubling the total observation time. In the beginning of this chapter we have observed that the performance quantities such as the sensitivity and the discovery potential evolve with $\tau^{-0.8}$ (Equation (9.4)) for point source analyses in IceCube. For the performance study in this section we will attribute changes of the effective area to relative changes in the observation time. The observation time τ that the IceCube detector needs to observe the similar amount of events as PLEνM within τ_0 is

$$\tau = \tau_0 \frac{\int_{\Delta E} A_{\text{eff}}^{\text{PLE}\nu\text{M}}(E,\delta) \frac{\mathrm{d}^2\phi_{\nu_\mu}}{\mathrm{d}t\mathrm{d}E}\,\mathrm{d}E}{\int_{\Delta E} A_{\text{eff}}^{\text{IceCube}}(E,\delta) \frac{\mathrm{d}^2\phi_{\nu_\mu}}{\mathrm{d}t\mathrm{d}E}\,\mathrm{d}E}. \tag{9.7}$$

In this sense, the PLEνM network can be interpreted as extension of IceCube's observation time by a factor of τ/τ_0. Ultimately using the time evolution monitored in IceCube allows an approximate evaluation of the sensitivity and discovery potential of PLEνM.

Using the approximated effective areas, based on the assumption that detectors are similar to IceCube we can evaluate these performance magnitudes for the PLEνM network. The effective area depends on both declination and energy. Hence on grounds of better manageability, we make use of the detection efficiency N_{eff} instead. Assuming a source following a single power-law distribution, both parameters are correlated according to Equation (9.1). The detection efficiencies of all four telescopes for one specific but artificial moment in time are shown in Figure 9.5. Similar to IceCube, the performance of the other telescopes is best at their respective horizon and drops vastly towards their respective southern hemisphere that is dominated by atmospheric muons. While the rotation of the Earth hardly affects neutrino studies for IceCube[6], the local detection efficiency of the other telescopes rapidly changes throughout one day. Since we are mostly interested in time-integrated neutrino emission studies over many months up to years, we only care for the detection efficiency averaged over time periods larger than a few days day. These average detection efficiencies with respect to IceCube are shown in Figure 9.6. Note that due to very similar latitude (or declination) of the observation sites of KM3NeT, Baikal-GVD and P-ONE their average detection efficiencies are very similar.

In order to generate the scenario of PLEνM, we can simply take the sum of the average detection efficiencies of the individual observatories[7]. By comparing this sum

[6] Note that this only counts for analysis that search for neutrino emission in time windows that are larger than a few days.

[7] For sources following a single power-law this shows a similar effect as the superposition of the effective areas (Equation (9.5).

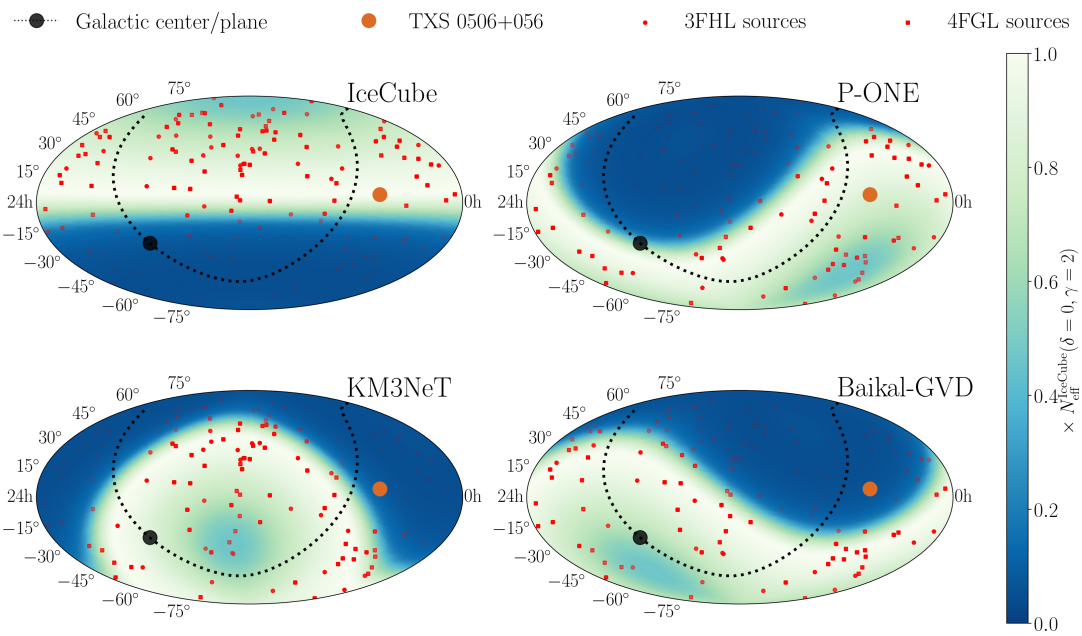

Figure 9.5: Detection efficiency for a source following a single power-law spectrum with $\gamma = 2$ at one artificial moment in time for all neutrino telescopes that are part of the PLEνM performance study. The respectively 100 sources with the highest gamma-ray emission within the 3FHL and the 4FGL catalog are illustrated as well [165, 187].

to the respective values for IceCube yields estimates for the increase in observation time τ/τ_0. In the following we will use three different expressions for the resulting sensitivity and discovery potential values. Next to the absolute values $\frac{\mathrm{d}\phi_{\mathrm{thr}}^{\mathrm{conf}}}{\mathrm{d}E_\nu}$ for these performance parameters, we also show the improvement of the detector configuration compared to IceCube at its optimal location $\delta = 0$ defined as

$$R_0(\delta, \gamma) \coloneqq \frac{\mathrm{d}\phi_{\mathrm{thr}}^{\mathrm{IceCube}}}{\mathrm{d}E_\nu}(\delta = 0, \gamma) \quad / \quad \frac{\mathrm{d}\phi_{\mathrm{thr}}^{\mathrm{conf}}}{\mathrm{d}E_\nu}(\delta, \gamma), \tag{9.8}$$

and the relative improvement at the actual location defined as

$$R_{\mathrm{rel}}(\delta, \gamma) \coloneqq \frac{\mathrm{d}\phi_{\mathrm{thr}}^{\mathrm{IceCube}}}{\mathrm{d}E_\nu}(\delta, \gamma) \quad / \quad \frac{\mathrm{d}\phi_{\mathrm{thr}}^{\mathrm{conf}}}{\mathrm{d}E_\nu}(\delta, \gamma). \tag{9.9}$$

The improvements of PLEνM compared to IceCube for similar observation times and sources with unbroken power-law $\gamma = 2$ is shown in Figure 9.7. The skymap in the left panel directly reveals that PLEνM opens a window to basically every point in the Universe with at least the optimal sensitivity of IceCube at the horizon. Even in the

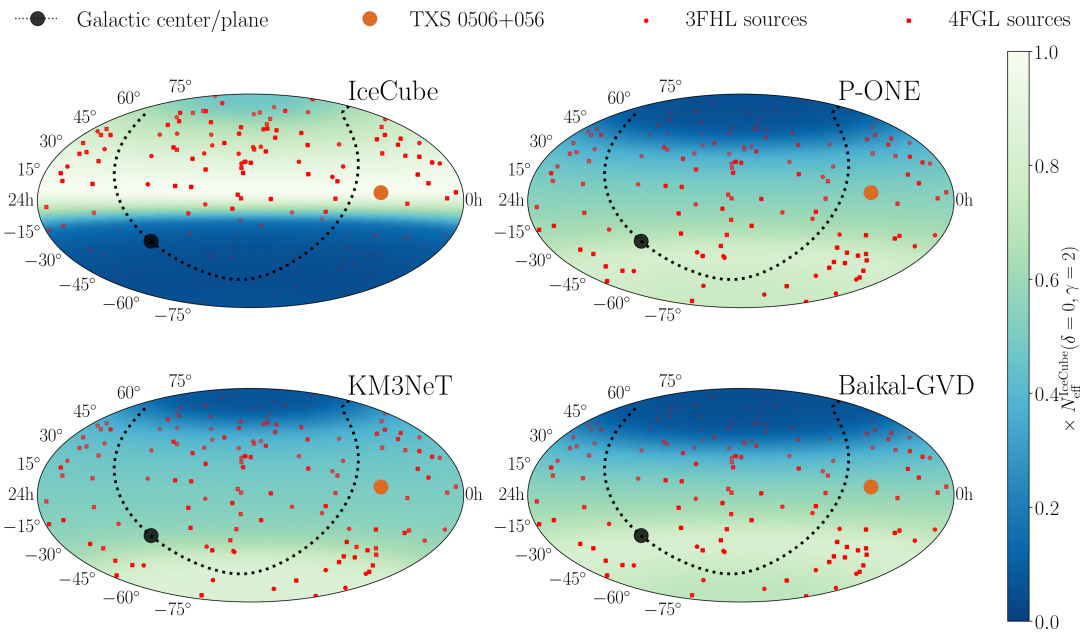

Figure 9.6: Detection efficiency for a source following a single power-law spectrum with $\gamma = 2$ averaged over time periods of > 1 d for all neutrino telescopes that are part of the PLEνM performance study. The respectively 100 sources with the highest gamma-ray emission within the 3FHL and the 4FGL catalog are illustrated as well [165, 187].

region close to the North Pole approximately 75 % of IceCube's optimal performance are reached. Hence a global neutrino telescope network could accomplish a complete survey of the sky for these kinds of neutrino sources. Comparing the explicit performance at each declination directly reveals that PLEνM improves the point source analysis performance by more than a factor of 20 in the Southern Hemisphere and at least a factor of 2 everywhere else.

The spectral shape of potential neutrino sources is still unknown. In fact, while for instance, most theoretical models for blazars predict spectral shapes harder than the general assumption of $\gamma = 2$, the IceCube measurements reveal that the spectral shape of the entity of astrophysical neutrinos most likely follows a power-law distribution with a softer spectral index. In order to study both scenarios in the context of PLEνM, similar comparisons as shown in Figure 9.7 for $\gamma = 2$, are shown in Figure 9.8 for sources with $\gamma = 1.5$ and $\gamma = 2.5$ respectively. Similar to the scenario for $\gamma = 2$ neutrino sources, the skymaps in the left panels illustrate that by means of PLEνM nearly the whole Universe can be studied with at least the optimal sensitivity of IceCube at the horizon. The explicit improvements at the respective declinations R_{rel} are differing for

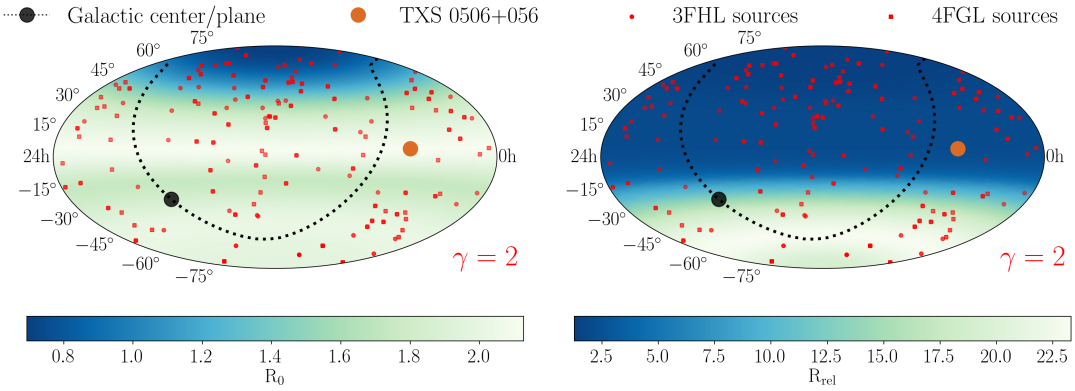

Figure 9.7: Performance of PLEνM with respect to IceCube for similar run times and sources following an unbroken power-law distribution with spectral index $\gamma = 2$. The respectively 100 sources with the highest gamma-ray emission within the 3FHL and the 4FGL catalog are illustrated as well [165, 187].

the two scenarios. For sources with a hard spectral index of $\gamma = 1.5$, IceCube performs best at the horizon. Nevertheless also the sensitivity in the Southern Hemisphere enhances compared to softer sources because the on average higher energies of the neutrino events offer a better discrimination power with respect to low-energy atmospheric muons. Consequently the explicit improvement R_{rel} (top right panel of Figure 9.8) in the Southern Hemisphere is less than for softer sources, yet still achieves a factor of ~ 5. While the relative performance of IceCube in the Southern Hemisphere increases for hard sources, the absorption of high-energy neutrinos in the core of the Earth yields a decline in the region close to the North Pole. Hence the combined telescope network will also yield improvements by a factor ~ 5 for sources with $\gamma = 1.5$. For sources following a softer power-law distribution of $\gamma = 2.5$ the situation is exactly the other way round. In the region above the horizon, PLEνM will outperform IceCube by more than a factor of ~ 2.5. In the Southern Hemisphere, IceCube's sensitivity for neutrino point sources drops drastically for soft sources. This is caused by the poor energy discrimination between atmospheric muons and neutrinos and low-energy astrophysical neutrinos. The remaining telescopes in the PLEνM framework can compensate IceCube's weak performance, yielding improvements of more than a factor of 160 in this region.

Up to now we always showed comparisons of PLEνM and IceCube based on the assumption that both instruments measure over the same time period. Nonetheless, the IceCube collaboration already measured neutrino data by means of its full detector configuration for more than 10 years. In order to display a more realistic scenario for the PLEνM network, we want to account for this fact. In the following, we will investigate

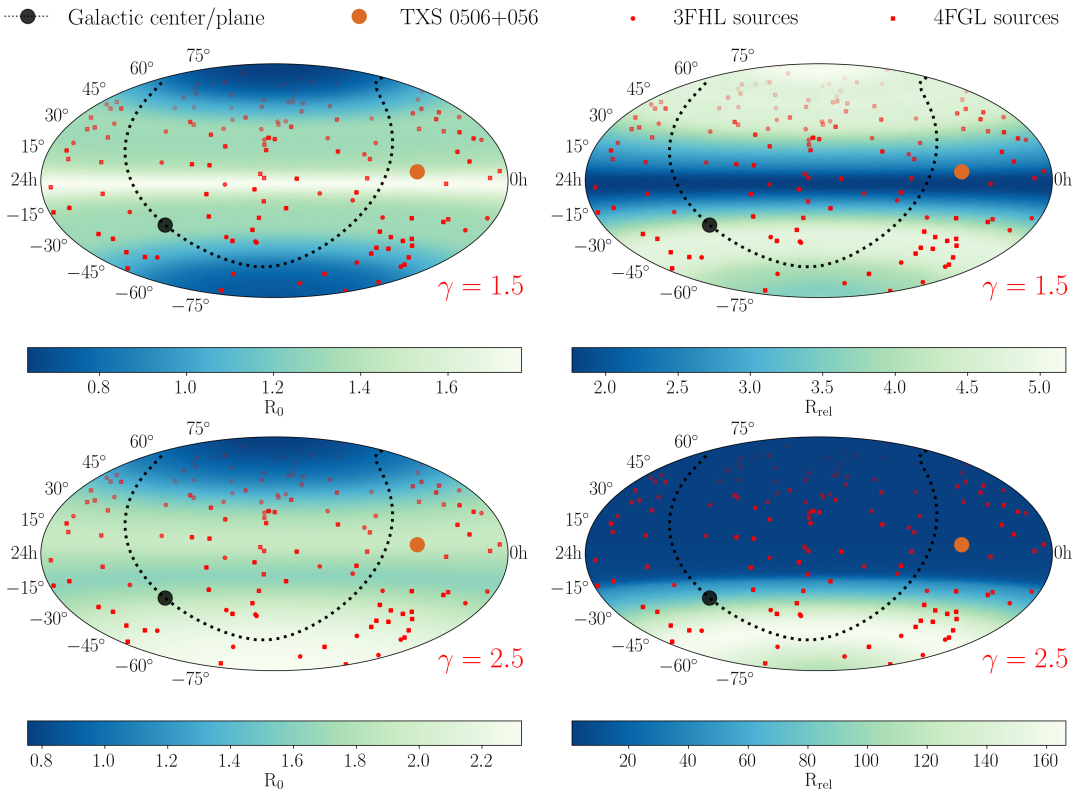

Figure 9.8: Performance of PLEνM with respect to IceCube for similar run times and sources following an unbroken power-law distribution with spectral index $\gamma = 1.5$ and $\gamma = 2.5$. The respectively 100 sources with the highest gamma-ray emission within the 3FHL and the 4FGL catalog are illustrated as well [165, 187].

the improvements of PLEνM, if we turn on this global network after 10 years of exclusive runtime of IceCube. The evolution of the relative improvements R_{rel} with increasing lifetime for sources following a power-law distribution with $\gamma = 2$ is illustrated in Figure 9.9. We can see that even after the first year of PLEνM the sensitivity towards point sources improves by a factor of four in the Southern Hemisphere. After three years the performance in the south already enhances by a factor of ~ 8 evolving to a factor of ~ 14 after 10 years. At the horizon PLEνM enhances the sensitivity by $\sim 50\,\%$ after 5 years and $\sim 70\,\%$ after 10 years.

9.2.3 PLEνM and IceCube Gen-2

As previously mentioned at the beginning of this chapter, not only new neutrino telescopes are under construction but also the IceCube collaboration itself plans a high-

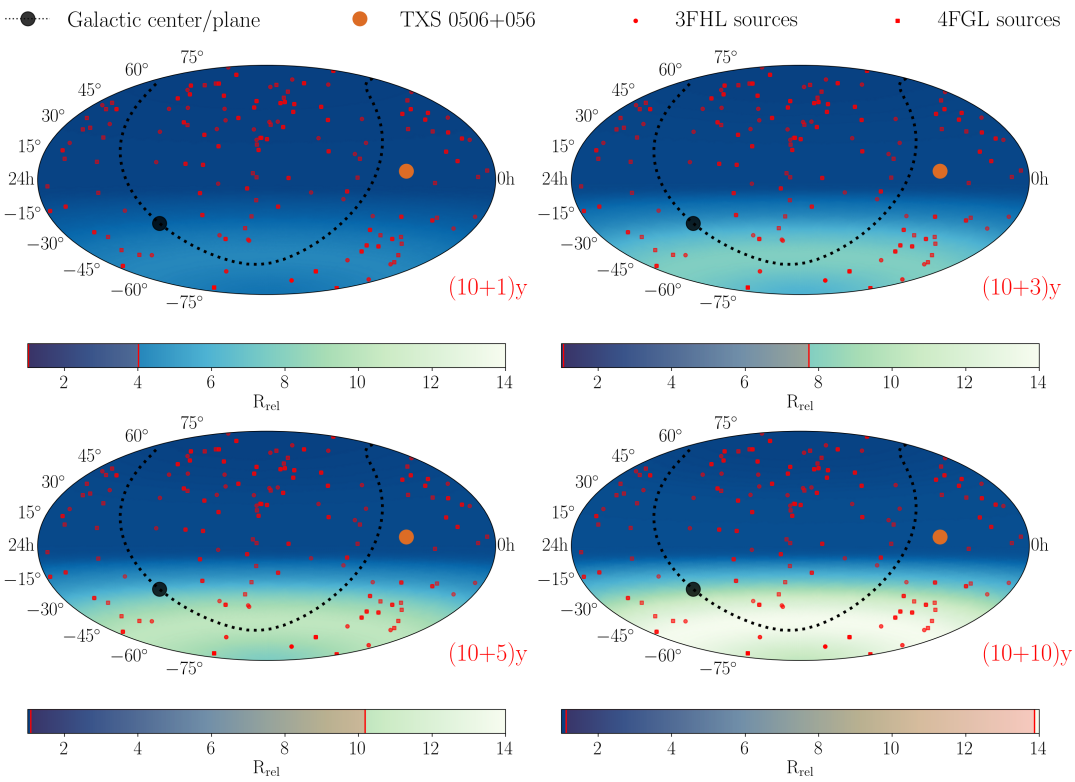

Figure 9.9: Relative improvements due to (x)yr of PLEνM compared to IceCube running for $(10+x)$yr. The red band in the colorbar indicates the range of the values apparent in the respective skymap. The respectively 100 sources with the highest gamma-ray emission within the 3FHL and the 4FGL catalog are illustrated as well [165, 187].

energy extension, called IceCube Gen-2, around the currently existing detector volume that could yield a gain for point source sensitivities by a factor of ~ 5. In the following, we will include this successor in the scenario of PLEνM. In the left panel of Figure 9.10 the relative improvement R_{rel} of a global neutrino telescope network including IceCube Gen-2 compared to IceCube is shown for sources following a power-law with $\gamma = 2$. Similar to before we presume for this study that IceCube already measured data for 10 years before PLEνM and the IceCube upgrade start their operation for additional 10 years. Similar to the before the largest improvement compared to IceCube arises in the Southern Hemisphere. Yet, as a result of the IceCube upgrade Gen-2 also the performance at the horizon and in the Northern Hemisphere increases by nearly a factor of 4.

In the right panel of Figure 9.10 the influence of KM3NeT, Baikal-GVD, and P-ONE

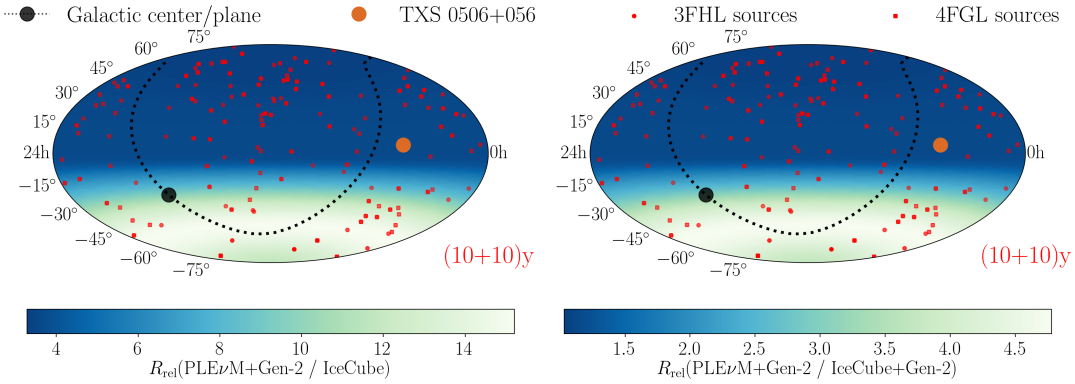

Figure 9.10: **Left:** Relative improvements for sources with spectral index $\gamma = 2$ due to additional 10 yr of PLEνM and Gen-2 compared to IceCube running for 20 yr. **Right:** Relative improvements due to additional 10 yr of PLEνM and Gen-2 compared to IceCube and Gen-2 running for $(10+10)$yr respectively. The respectively 100 sources with the highest gamma-ray emission within the 3FHL and the 4FGL catalog are illustrated as well [165, 187].

within this scenario is illustrated. Including these detectors to IceCube and IceCube-Gen2 yields large improvements to sensitivity in the Southern Hemisphere. Nevertheless in the Northern Hemisphere and at the horizon IceCube Gen-2 dominates the sensitivity in this scenario. Note that this specific outcome is strongly affected by the primary assumption made in this study, which established that all other telescopes (except IceCube Gen-2) operate similar to the IceCube detector. In fact, since probably all of these detectors will outperform IceCube in terms of point source sensitivities, all results shown in this study can be interpreted as conservative estimates.

Ultimately the absolute values for the 5σ discovery potential for the previous scenario are shown in Figure 9.11. As visible, the discovery potential of the combined network of PLEνM+Gen2 would cover the 90 % C.L. upper limits for all tested sources from [3]. In order to reach the discovery potential of the combined network of PLEνM and IceCube Gen-2 at the horizon and the Northern Hemisphere after 10 years of runtime, IceCube would need to observe the sky for additional $\sim$ 100 years. To accomplish a similar performance in the Southern Hemisphere, IceCube would need to run for auxiliary $\sim$ 350 years.

9.3 Conclusion

The study described in this chapter revealed that a combined network of neutrino telescopes at different detection sites can vastly improve the point source sensitivity of

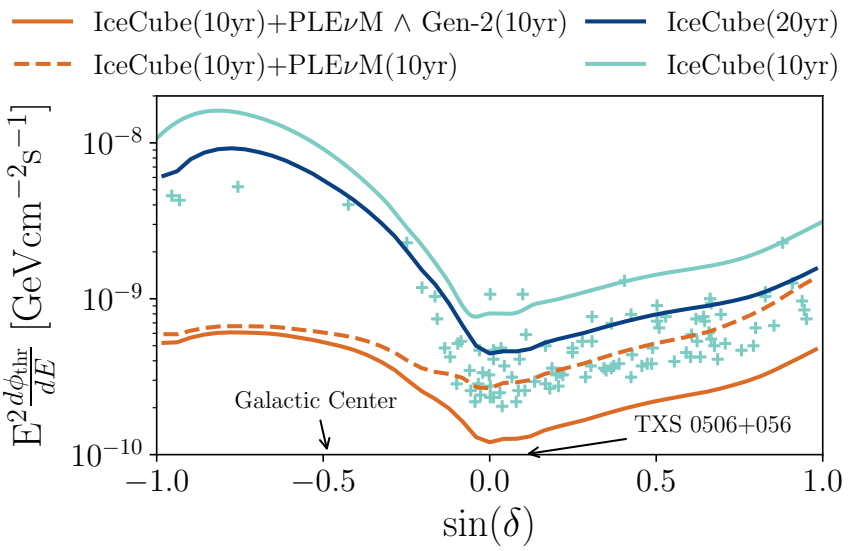

Figure 9.11: 5σ discovery potential of different telescope networks. The markers indicate the current limits for interesting objects tested by IceCube [3]. The location of the galactic center and TXS 0506+056 are indicated by the black arrows.

IceCube within a few years. While a large factor of this enhancement at the horizon and in the Northern hemisphere can be attributed to the IceCube upgrade Gen-2, the Southern Hemisphere can only be accessed by means of the other telescopes. In order to optimally access the region close to the North Pole, another neutrino telescope located somewhere in the Southern Hemisphere would be necessary.

The study in this chapter only consider point source searches based on track-like events mainly induced by muons and muon neutrinos. In ice, these track-like events allow for a median angular resolution of less than 1° at energies above 1 TeV. Hence they depict the optimal event type to observe the local clustering of neutrinos from astrophysical sources. In contrast, due to scattering and their spherical appearance, cascade-like events from electron neutrinos and NC interactions can only be reconstructed with a median accuracy of 10° to 15° in IceCube (Subsection 6.4.1). As a consequence cascade-like events in ice are barely valuable in the search of their sources.

This situation changes for neutrino telescopes in water. In water, the propagation of Cherenkov light is mainly dictated by absorption effects, while scattering only depicts a minor influence. Hence, depending on the spacing of the detector modules, more direct un-scattered photons can be observed which subsequently yields the chance for enhanced reconstructions. The median angular resolution for track-like events in KM3NeT is roughly 0.2° above 10 TeV, while cascade-like events above 100 TeV can

still be reconstructed with a median angular uncertainty of 1.5° [188]. In this scenario, not only track-like events but also the second major event topology can be used for the study of neutrino point sources. While track-like events still outperform the directional reconstruction of cascade-like events, the latter appears to obtain other major advantages for point source searches. In contrast to track-like events, the energy of observable cascade-like events is mostly contained inside detector volume, allowing for an accurate energy reconstruction. The accurate knowledge of their energy can be utilized to discriminate against the atmospheric background. Moreover, the total event rate of cascade-like events at higher energies is not influenced by atmospheric muons that dominate the rate of track-like events. Hence their total rate is mainly constituted by atmospheric and astrophysical neutrino events. In combination with the accurate energy estimation, cascade-like events in water-based neutrino telescopes can introduce a second alternative facility to discover astrophysical neutrino sources. The exact potential of these events in this context requires a detailed dedicated study for the respective telescope.

A

Theory: Variable Conversions

Experimental results of particle collisions can be measured and interpreted in different kinds of variables. Hence in order to combine multiple different data sets, it may often be necessary to convert all these results to values in terms of one common specific variable. The hadronic production yield data in Section 5.3 represent such a case. In the following, we will introduce all particle conversions that are necessary to convert all of these experimental data to the x_{Lab} frame (Equation 5.6).

A.1 Particle Interactions

The inclusive production of a particle c in the interaction of particle a and b can be written as

$$\mathrm{a} + \mathrm{b} \longrightarrow \mathrm{c} + \mathrm{X}, \tag{A.1}$$

where X denotes all other possible products of the interaction. Due to energy and momentum conservation the following equation holds

$$p_a + p_b = p_c + p_X \tag{A.2}$$

with p_i being the 4-momentum vector of particle $i \in \{a, b, c, X\}$. More explicitely this can be written as

$$\begin{pmatrix} E_a \\ \mathbf{p}_a \end{pmatrix} + \begin{pmatrix} E_b \\ \mathbf{p}_b \end{pmatrix} = \begin{pmatrix} E_c \\ \mathbf{p}_c \end{pmatrix} + \begin{pmatrix} E_X \\ \mathbf{p}_X \end{pmatrix}, \tag{A.3}$$

with E_i being the energy and $\mathbf{p}_i$ being the respective momentum vector. Moreover the energy momentum relation

$$p^2 = E^2 - \mathbf{p}^2 = m^2 \tag{A.4}$$

Figure A.1: View on the collision of two particles from two different reference frames.

applies universally for relativistic particles. The center of mass energy (c.m. energy) of this particle collision is defined as

$$E_{c.m.} = \sqrt{(p_a + p_b)^2} \tag{A.5}$$

A.2 Frame of Reference

Particle collisions can be considered within different reference frames. In the situation of fixed target experiments the target material is at rest, hence $\mathbf{p}_b = \mathbf{0}$. Throughout this thesis, we will refer to this perspective as the laboratory or fixed target frame. The situation is illustrated in the left panel of Figure A.1. The center of mass energy can be written as

$$E_{c.m.}^2 = (E_a + E_b)^2 - \mathbf{p}_a^2 \tag{A.6}$$

$$\overset{(A.4)}{=} 2E_a m_b + m_b^2 + m_a^2 \tag{A.7}$$

$$\overset{E_a \gg m_{a,b}}{\approx} 2E_a m_b \tag{A.8}$$

On the other hand, in the reference frame of collider experiments, particles a and b collide with opposite momentum, $\mathbf{p}_a = -\mathbf{p}_b \coloneqq \mathbf{p}$. The representation of the collision is displayed in the left panel of Figure A.1. In case both a and b are of the same particle type they also have the same mass and hence the same energy $E_a = E_b \coloneqq E$ (refer to (A.4)). In the following we will refer to this view as the center of mass frame, with all particles being written with an asterix *. The center of mass energy in this scenario can be written as

$$E_{c.m.}^2 = (E_a^* + E_b^*)^2 \tag{A.9}$$

A.3 Transformation between Reference Frames

Each situation in a specific reference frame of an observer can be expressed also in the view of another observer by doing a linear Lorentz transformation between the respective coordinate systems

$$p^* = \mathbf{\Lambda} p, \tag{A.10}$$

where $\mathbf{\Lambda}$ represents the Lorentz matrix. A boost along the z-direction from a system at rest to a system moving with velocity $\mathbf{v}$ is characterized by the Lorentz matrix

$$\mathbf{\Lambda} = \begin{pmatrix} \gamma & 0 & 0 & -\gamma\beta \\ 0 & 1 & 0 & 0 \\ 0 & 0 & 1 & 0 \\ -\gamma\beta & 0 & 0 & \gamma \end{pmatrix}, \tag{A.11}$$

where $\beta = \mathbf{v}/c$ and $\gamma = \frac{1}{\sqrt{1-\beta^2}}$ is the Lorentz factor. According to Equation (A.10), this transformation yields a relation between the energy and momentum in the frame at rest and the moving system

$$E^* = \gamma\left(E - \beta p_z\right) \tag{A.12}$$

$$p_x^* = p_x \tag{A.13}$$

$$p_y^* = p_y \tag{A.14}$$

$$p_z^* = \gamma\left(p_z - \beta E\right). \tag{A.15}$$

These relations can be used to describe the transformation of a system from the center of mass frame to the laboratory frame which is boosted with $\beta = \frac{v_z}{c}$ relative to the center of mass system such that the particle b is at rest. Following Equation (A.15) yields

$$0 = \gamma\left(p_z^* - (-\beta)E_b^*\right) \tag{A.16}$$

$$\Longrightarrow \beta = \frac{p_z^*}{E_b^*}. \tag{A.17}$$

Assuming that both particles have the same mass $m_a = m_b \coloneqq m$, the energy of the particles in the center of mass frame can be written as

$$E^{*2} \overset{(A.9)}{=} \frac{E_{c.m.}^2}{4} \overset{(A.8)}{=} \frac{1}{2} m(E_a + m). \tag{A.18}$$

Using this expression the boost factor β can be expressed as

$$\beta^2 = \frac{p_z^{*2}}{E_b^{*2}} \tag{A.19}$$

$$\overset{(A.4)}{=} \frac{E_b^{*2} - m^2}{E_b^{*2}} \overset{(A.18)}{=} \frac{E_a - m}{E_a + m} \tag{A.20}$$

The Lorentz factor γ is defined as a variable of β and can be written as

$$\gamma^2 = \frac{1}{1 - \beta^2} \tag{A.21}$$

$$\overset{(A.20)}{=} \frac{1}{1 - \frac{E_a - m}{E_a + m}} = \frac{E_a + m}{2m} \tag{A.22}$$

$$= \frac{(E_a + m)^2}{2m(E_a + m)} \overset{(A.8)}{=} \frac{(E_a + m)^2}{E_{c.m.}^2}. \tag{A.23}$$

A.4 Variable Conversions

As mentioned at the beginning of this chapter the measured data of hadronic interactions that are used in this work are all evaluated in terms of different variables. In this section, we will use the formulas that were previously introduced in order to express them in terms of

$$x_{Lab} = \frac{E_c}{E_a}, \tag{A.24}$$

which is defined in the laboratory frame as the ratio of the energy of the secondary particle c with respect to the projectile energy E_a.

A.4.1 Conversion from x_F (c.m. frame) to $x_{\mathbf{Lab}}$

The Feynman variable x_F is defined in the center of mass frame as the fraction of longitudinal momentum of the secondary particle c and the overall center of mass energy

$$x_F = \frac{2p_{c,z}^*}{E_{c.m.}}. \tag{A.25}$$

Hence the range of possible values for x_F is between -1 and 1. Different to the Feynman x_F, x_{Lab} can only obtain values between 0 and 1. In order to convert x_F to variables in the lab frame and finally x_{Lab} one has to boost the c.m. system to the lab frame. The

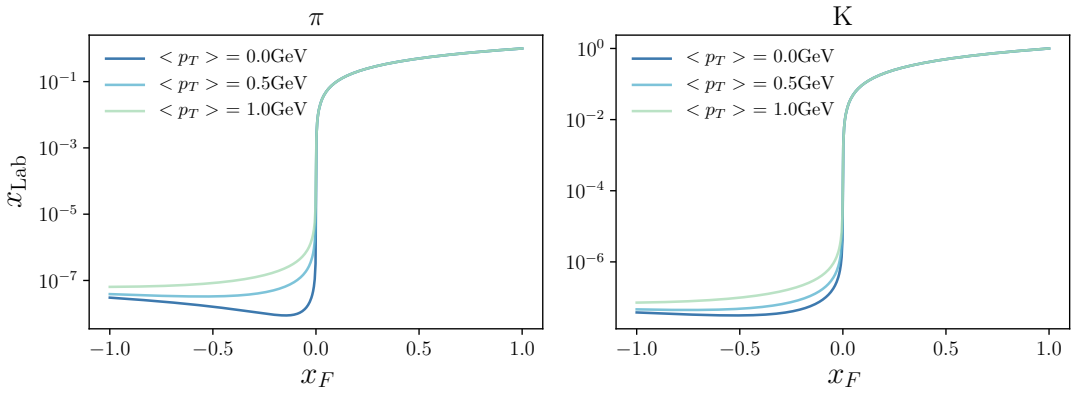

Figure A.2: Relation between x_{Lab} and x_F for pions and kaons. The different colors illustrate different transverse momenta $p_{c,T}$.

energy of the secondary particle in the lab frame can be estimated as

$$E_c \overset{(A.15)}{=} \gamma \left(E_c^* - (-\beta) p_{c,z}\right) \tag{A.26}$$

$$\overset{(A.4)}{=} \gamma \left(\sqrt{m_c^2 + p_{c,z}^{*2} + p_{c,T}^{*2}} + \beta p_{c,z}^*\right) \tag{A.27}$$

$$\overset{(A.25)}{=} \gamma \left(\sqrt{m_c^2 + \frac{1}{4} x_F^2 E_{c.m.}^2 + p_{c,T}^{*2}} + \frac{1}{2} \beta x_F^2 E_{c.m.}\right) \tag{A.28}$$

Using this one can convert x_F to x_{Lab} according to

$$x_{Lab} = \frac{E_c}{E_a} = \frac{\gamma \sqrt{m_c^2 + \frac{1}{4} x_F^2 E_{c.m.}^2 + p_{c,T}^{*2}} + \frac{1}{2} \gamma \beta x_F^2 E_{c.m.}}{E_a} \tag{A.29}$$

Despite the properties of the interacting particles this conversion does not only depend on x_F but also on the transverse momentum $p_{c,T}^*$ of the secondary particle. An illustration of the effect of the transverse momentum on the conversion is shown in Figure A.2

A.4.2 Conversion from rapidity y (c.m. frame) to x_{Lab}

The rapidity of a particle a is defined in the center of mass frame as

$$y = \operatorname{arctanh}\left(\frac{p_{a,z}^*}{E_a^*}\right) \tag{A.30}$$

Given this equation the longitudinal momentum $p^*_{a,z}$ can be written as

$$p^*_{a,z} = \tanh(y) \cdot E^*_a \overset{(A.4)}{=} \tanh(y) \cdot \sqrt{m_a^2 + p^{*2}_{a,z} + p^{*2}_{a,T}} \tag{A.31}$$

$$\Rightarrow p^{*2}_{a,z} = \tanh^2(y) \cdot \left(m_a^2 + p^{*2}_{a,z} + p^{*2}_{a,T}\right) \tag{A.32}$$

$$\Leftrightarrow p^{*2}_{a,z} = \frac{\tanh^2(y) \cdot \left(m_a^2 + p^{*2}_{a,T}\right)}{1 - \tanh^2(y)} \tag{A.33}$$

$$\Rightarrow p^*_{a,z} = \frac{\tanh(y) \cdot \sqrt{m_a^2 + p^*_{a,T}}}{\sqrt{1 - \tanh^2(y)}} \tag{A.34}$$

Using the context of the longitudinal momentum $p^*_{a,z}$ and the Feynman x_F from Equation (A.25) in combination with the conversion introduced in the previous subsection we can directly get an expression for x_{Lab} in terms of rapidity. The Feynman x_F is defined in Equation (A.25) as a function of p^*_z. Using this definition and the expression from Equation (A.34) one can write x_F in terms of rapidity y as

$$x_F \overset{(A.25)}{=} \frac{2p^*_{c,z}}{E_{c.m.}} \tag{A.35}$$

$$\overset{(A.34)}{=} \frac{2\tanh(y) \cdot \sqrt{m_c^2 + p^*_{c,T}}}{E_{c.m.}\sqrt{1 - \tanh^2(y)}} \tag{A.36}$$

Inserting the above derived expression for x_F into Equation (A.29) yields

$$x_{Lab} \overset{(A.29)}{=} \frac{\gamma\sqrt{m_c^2 + \frac{1}{4}x_F^2 E^2_{c.m.} + p^{*2}_{c,T}} + \frac{1}{2}\gamma\beta x_F^2 E_{c.m.}}{E_a} \tag{A.37}$$

$$\overset{(A.36)}{=} \frac{\gamma\sqrt{m_c^2 + \frac{\tanh^2(y)\left(m_c^2 + p^{*2}_{c,T}\right)}{1-\tanh^2(y)} + p^{*2}_{c,T}} + 2\gamma\beta\frac{\tanh^2(y)\left(m_c^2 + p^{*2}_{c,T}\right)}{E_{c.m.}\left(1-\tanh^2(y)\right)}}{E_a} \tag{A.38}$$

Similar to above above the expression explicitly depends on the transverse momentum of the secondary particle c. The influence of the transverse momentum on this conversion is illustrated in Figure A.3 for pions, kaons and protons.

A.4.3 Conversion from the total momentum p (lab frame) to x_{Lab}

The full energetics of a particle with mass m can be described by x_{Lab} and the transverse momentum p_T of the particle. The longitudinal momentum of the particle can be derived using Formula (A.4). Yet, of course, this is not the only possible represen-

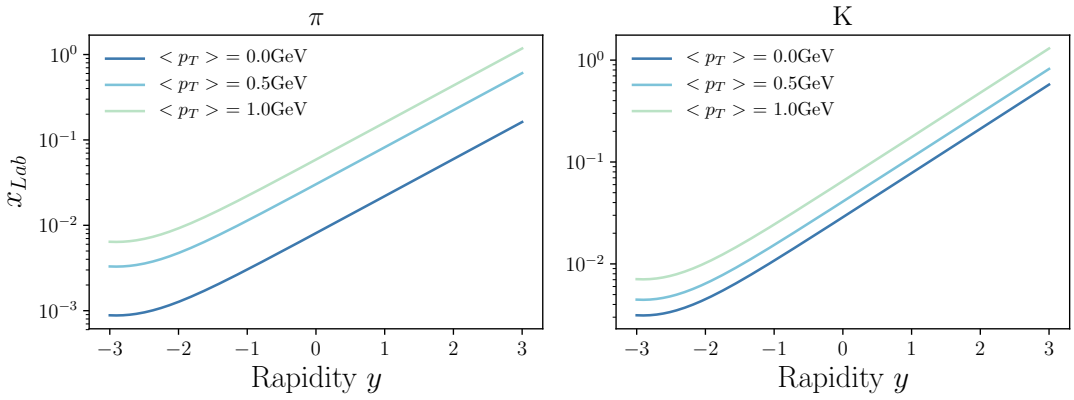

Figure A.3: Relation between x_{Lab} and rapidity y for pions and kaons. The different colors illustrate different transverse momenta $p_{a,T}$.

tation of the properties of a particle in the lab frame. The absolute value of the total momentum $\mathbf{p}$ and the polar angle θ, defined as the angle between the direction of the projectile particle a and the secondary particle c represent an alternate description.

Using Formula (A.4), these variables can be easily transformed to x_{Lab} and transverse momentum p_T values. Since both variable sets are defined in the lab frame no Lorentz transformation is necessary. The lab momentum can be expressed as

$$x_{Lab} = \frac{E_c}{E_a} = \frac{\sqrt{m_c^2 + \mathbf{p}_c^2}}{E_a} \tag{A.39}$$

The transverse momentum can be written as

$$p_T = \sin(\theta) \cdot |\mathbf{p}| \tag{A.40}$$

Different to the conversion in the previous two subsection the conversion from the total momentum to x_{Lab} doesn not depend on the transverse momentum of the secondary particle c.

A.5 Transformation of Particle Yields

Experiments like the NA49 and the NA61/SHINE collaboration measure inclusive particle production yields from hadronic particle collisions. These data are measured in fixed target experiments, whereas the results are either presented in terms of x_F, rapidity y or total momentum $\mathbf{p}$. Throughout this work we aim to use these data to compute atmospheric lepton fluxes. In order to solving a set of of coupled cascade equations

we are in particularly interested in the p_T-integrated particle production yields as a variable of x_L

$$\frac{\mathrm{d}N}{\mathrm{d}x_{\mathrm{Lab}}} = \int \frac{\mathrm{d}^2N}{\mathrm{d}x_{\mathrm{Lab}}\,\mathrm{d}p_T}\,\mathrm{d}p_T \tag{A.41}$$

Hence in the following section we will concentrate on providing the technical apparatus to convert the experimental outputs from Table 5.1 to Equation (A.41).

The total particle multiplicity is defined as

$$N = \iint \frac{\mathrm{d}^2N}{\mathrm{d}x_{\mathrm{Lab}}\,\mathrm{d}p_T}\,\mathrm{d}x_{\mathrm{Lab}}\,\mathrm{d}p_T \tag{A.42}$$

Assuming we have a different set of variables u and v which can be related to $x_{\mathrm{Lab}} = x_{\mathrm{Lab}}(u,v)$ and $p_T = p_T(u,v)$ and also cover the full momentum phase-space, the multiplicity integral can be written in terms of u and v as

$$N = \iint \frac{\mathrm{d}^2N}{\mathrm{d}x_{\mathrm{Lab}}\,\mathrm{d}p_T}(u,v)\cdot J\,\mathrm{d}u\,\mathrm{d}v \coloneqq \iint \frac{\mathrm{d}^2N}{\mathrm{d}u\,\mathrm{d}v}\,\mathrm{d}u\,\mathrm{d}v\,, \tag{A.43}$$

where J is the Jacobian of the transformation to the new coordinates that is defined as

$$J = \begin{vmatrix} \frac{\partial x_{\mathrm{Lab}}}{\partial u} & \frac{\partial x_{\mathrm{Lab}}}{\partial v} \\ \frac{\partial p_T}{\partial u} & \frac{\partial p_T}{\partial v} \end{vmatrix} = \frac{\partial x_{\mathrm{Lab}}}{\partial u}\frac{\partial p_T}{\partial v} - \frac{\partial x_{\mathrm{Lab}}}{\partial v}\frac{\partial p_T}{\partial u}. \tag{A.44}$$

For all the data in Table 5.1 the contribution to the transverse component of the momentum is measured. Hence we can set $v = p_T$ yielding the jacobian

$$J = \frac{\partial x_{\mathrm{Lab}}}{\partial u}. \tag{A.45}$$

Ultimately according to Equations (A.43) and (A.45) the required p_T integrated production yield from Equation (A.41) can be evaluated from the new coordinates as

$$\frac{\mathrm{d}N}{\mathrm{d}x_{\mathrm{Lab}}} = \int \frac{\mathrm{d}^2N}{\mathrm{d}u\,\mathrm{d}p_T}\cdot\frac{\partial u}{\partial x_{\mathrm{Lab}}}\,\mathrm{d}p_T \tag{A.46}$$

In case the derivate $\frac{\partial u}{\partial x_{\mathrm{Lab}}}$ is independent of the transverse momentum p_T, the integrated production yields in terms of u can be used directly for the conversion

$$\frac{\mathrm{d}N}{\mathrm{d}x_{\mathrm{Lab}}} = \int \frac{\mathrm{d}^2N}{\mathrm{d}u\,\mathrm{d}p_T}\,\mathrm{d}p_T\cdot\frac{\partial u}{\partial x_{\mathrm{Lab}}}. \tag{A.47}$$

While this is not the case for $u \in \{x_F, y\}$ (refer to Equation (A.29) and (A.38)), the

derivative of the total momentum $\mathbf{p}$ with respect to x_{Lab} is independent of p_T.

B

Application: Variable Conversions

The measured particle production data from hadronic interactions that are used throughout this work are summarized in Table 5.1. In order to apply these measurements to MCEq, they have to be reproduced to transverse momentum integrated production yields in terms of x_{Lab} (refer to Equation (A.41)). Since each of these data sets is evaluated in terms of different variables we have to apply an independent conversion respectively. The technical instruments that are required for these transformations are summarized in Appendix A. Since each measurement has its own parameter representation each transformation has its own puzzles. In the following, we will address the actual conversions of all data sets given in Table 5.1.

B.1 Inclusive Particle Production in Proton Carbon Interactions at 158 GeV

The NA49 experiment at CERN analyzed the particle production within collisions of protons moving at 158 GeV and a carbon target [99]. As a result, the inclusive production yields of charged pions, protons, anti-protons, and neutrons were measured as variables of x_F. The analyzers published both the p_T dependent as well as p_T integrated results of the analysis According to Appendix A and in particular Equation (A.46) the data can be converted to the required quantity. Since the derivate of x_F with respect to x_{Lab} is not independent of the transverse momentum we can not apply Equation (A.47) and use the integrated data directly, but have to make use of the p_T dependent data. This fact becomes more obvious if we look at the conversion of the phase-space binning scheme that was used in the analysis. This transformation is illustrated for π^+ in Figure B.1. The curved shape of the original binning in the x_{Lab} space indicates that the integration along the p_T direction differs strongly between the two coordinate systems, with the biggest effect appearing at low values of x_{Lab}. The situation for the other secondary particles is mostly similar to the effect of this p_T dependence weakening

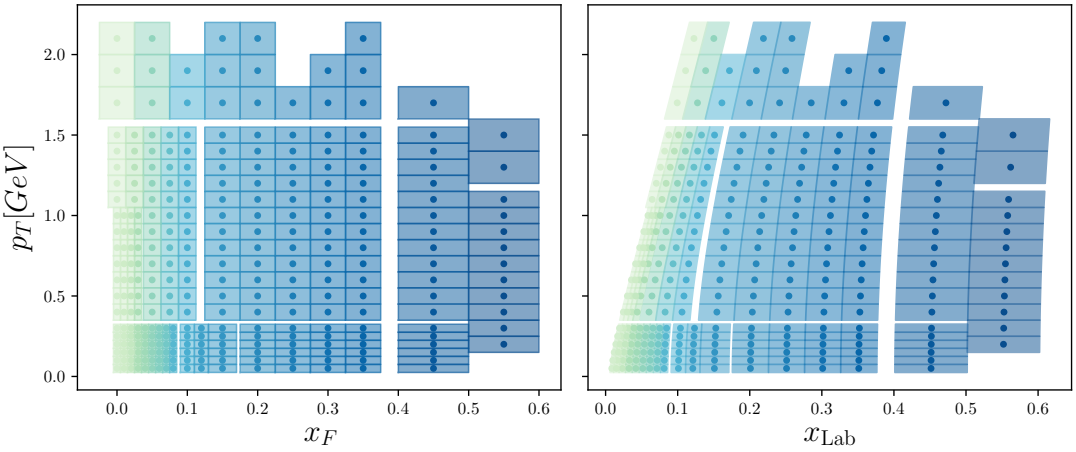

Figure B.1: Binning scheme used for the π^+ production yields measurement performed at the NA49 experiment [99]. The shaded colors indicate the width of the respective x_F bin in the left panel and the affiliated bin width in terms of x_{Lab} on the right side.

for the heavier particles.

Consequently, we have to use the double differential data to carry out a proper unbiased conversion. In the following, we will only show the conversion of the production yields of positively charged pions explicitly, with the general transformation method being identical for all the other secondary particles. The measured double differential production yields of π^+ in the corresponding binning scheme are illustrated in the left panel of Figure B.2. According to Equation (A.46) we transform the result of the respective bin to the corresponding bin in the lab frame coordinate system. In a next step, we define a reasonable binning scheme in the new x_{Lab}-p_T coordinates and calculate the mean values in these bins. The transformed outcome from π^+ in the new coordinate system is shown in the right panel of Figure B.2. Ultimately we can integrate these values along the transverse momentum to obtain the p_T integrated production yields in terms of x_{Lab}.

The uncertainties of the original data are propagated along with this procedure, yielding the resulting uncertainties of the desired variables. In case this conversion method does not introduce any further uncertainties, these values can be seen as the total error of the transformed data. In theory, this conversion method could introduce additional deviation due to the choice of the binning scheme. In order to quantify this effect, we applied this procedure to Monte Carlo simulated distributions from different theoretical interaction models. The additional deviation on these simulations is of the order of $\lesssim 5\,\%$. Hence to be conservative we introduce an additional uncertainty of $5\,\%$

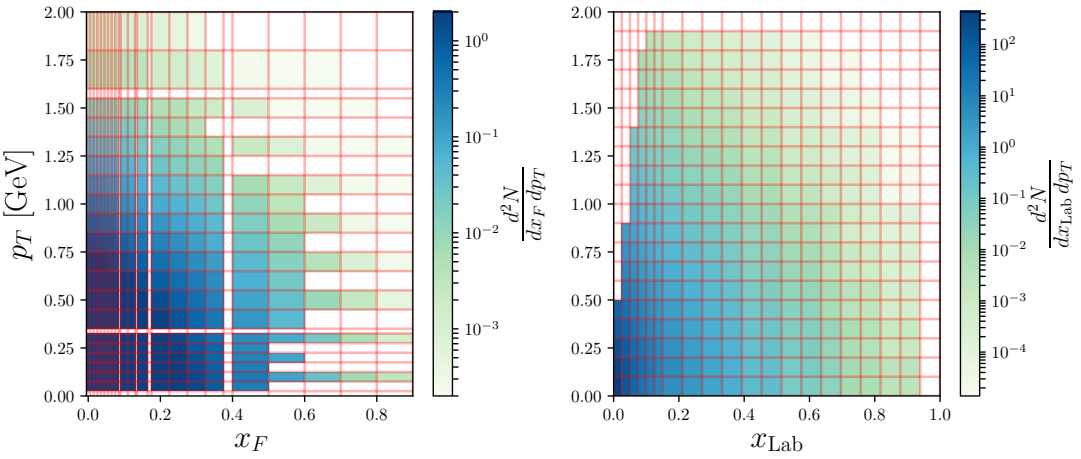

Figure B.2: Double differential π^+ production yield from proton carbon interactions at 158 GeV beam momentum. The red lines show the binning used in the respective coordinate system. **Left:** Originally measured data. **Right:** Converted production yields. The binning scheme was chosen according to the phase space coverage of these data.

to all converted data points.

The final converted and integrated outcomes including their uncertainties are illustrated in Figure 5.4.

B.2 Inclusive Particle Production in Proton Proton Interactions

The NA61/SHINE collaboration analyzed the particle production within collisions of protons moving at different GeV energies and a proton target [102]. As a result, the inclusive production yields of charged pions, kaons, protons, and neutrons were measured as variables of the rapidity y. The analyzers published both the p_T dependent as well as p_T integrated results of the analysis Similar to the previous section the integrated data can not be used directly, since the derivate of the rapidity y with respect to x_{Lab} in Equation (A.46) is not independent of the transverse momentum. This fact becomes more obvious if we look at the conversion of the phase-space binning scheme that was used in the analysis. This transformation is illustrated in Figure B.3 for the π^+ production yield at at 158 GeV beam momentum. Similar to above the curved shape of the original binning in the x_{Lab} space indicates that the integration along the p_T direction differs strongly between the two coordinate systems. The situation for the other

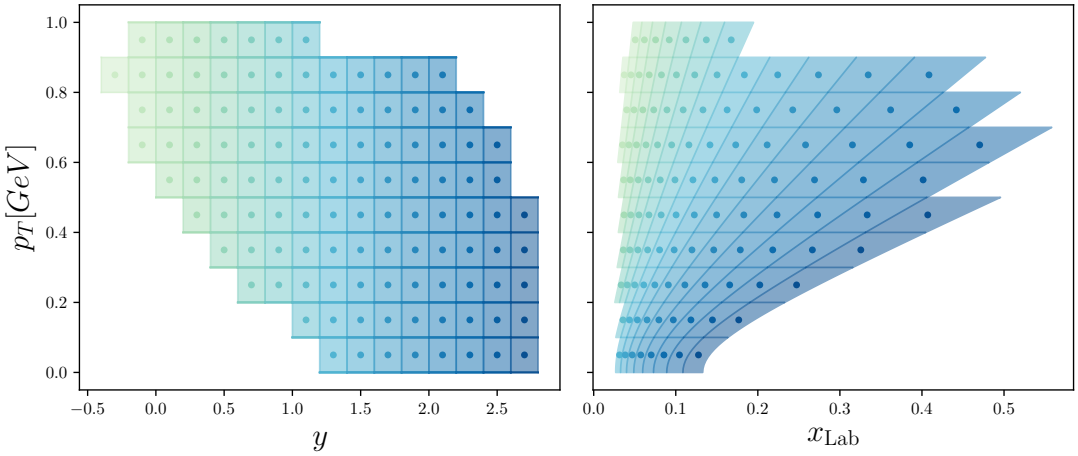

Figure B.3: Binning scheme used for the π^+ production yields measurement performed at the NA61/SHINE detector [102]. The shaded colors indicate the width of the respective rapidity y bin in the left panel and the affiliated bin width in terms of x_{Lab} on the right side.

secondary particles is mostly similar to the effect of this p_T dependence weakening for the heavier particles but being even stronger for lower beam energies.

As a consequence, we have to use the double differential data to carry out a proper unbiased conversion. In the following, we will only show the conversion of the production yields of positively charged pions explicitly, with the general transformation method being identical for all the other secondary particles. The measured double differential production yields of π^+ in the corresponding binning scheme are illustrated in the left panel of Figure B.4. The transformation to the x_{Lab}-p_T coordinate system follows the exact same step as described in the previous section. The transformed outcome from π^+ in the new coordinate system is shown in the right panel of Figure B.4. The p_T integration of converted yields requires a little bit more effort than the one in Appendix B.1 since no data for low p_T values exist above $x_{\mathrm{Lab}} \gtrsim 0.2$. In order to compensate for this lack of data, we apply a theoretically motivated fit function to these data [102]. The integrated values are then derived from these fits.

Similar to the method in the previous section, the uncertainties of the original data are propagated along with this procedure. Tests based on Monte Carlo simulations revealed that the conversion procedure also introduces small additional deviations. Similar to above we established an additional uncertainty of 5 % to cover these deviations.

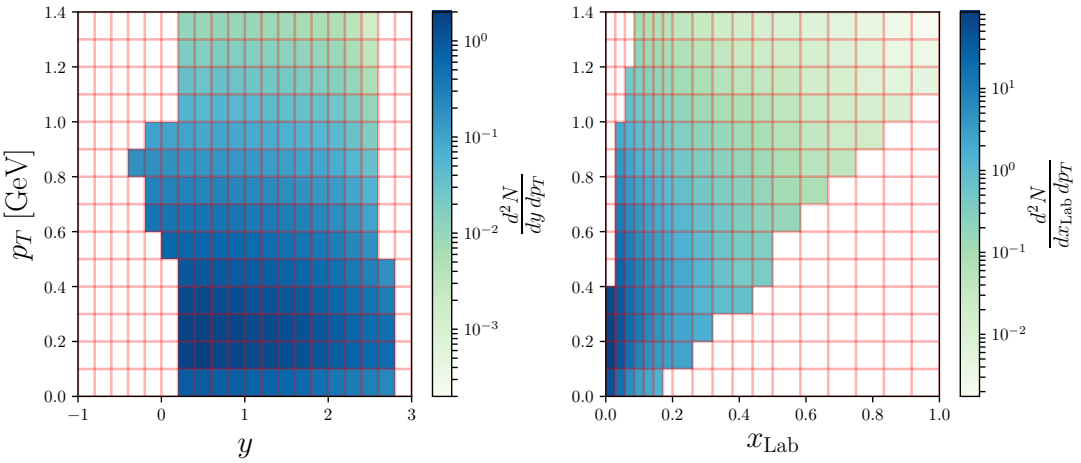

Figure B.4: Double differential π^+ production yield from proton-proton interactions at 158 GeV beam momentum. The red lines show the binning used in the respective coordinate system. **Left:** Originally measured data. **Right:** Converted production yields. The binning scheme was chosen according to the phase space coverage of these data.

B.3 Inclusive Particle Production in Proton Carbon and Pion Carbon Interactions

Next to the proton-proton data set from Appendix B.2 the NA61/SHINE also took data with a carbon target. Next to protons as projectile particles, also measurements with a π^- beam exist. Both data sets were analyzed in terms of the total momentum of the secondary particles. Since the partial derivative of the total momentum with respect to x_{Lab} does not depend on the transverse momentum the integrated data can be converted directly according to Equation (A.47).

The converted production yields of both data sets are illustrated in Figure 5.4 and 5.5.

C

Integration of Hadronic Models in MCEq

MCEq can solve a set of coupled cascade equations in order to compute the flux of particles generated along the path of a cosmic-ray induced air shower. Within the numerical implementation hadronic interactions are treated within the interaction matrix (Equation (5.25)) which contains the elements

$$c_{k(E_j)\to h(E_i)} = \Delta E_j \frac{\mathrm{d}N^{\mathrm{int}}_{k(E_j)\to h(E_i)}}{\mathrm{d}E_i}, \tag{C.1}$$

where the index j indicates the projectile particle and i the secondary product (refer to Equation (5.21)).

After the unification of all measured data sets mentioned in Table 5.1, these measurements can be used to describe the hadronic interactions in MCEq. In order to describe the elements of the interaction matrix, these data have to be converted according to

$$c_{k(E_j)\to h(E_i)} = \Delta E_j \frac{\mathrm{d}N^{\mathrm{int}}}{\mathrm{d}x_{\mathrm{Lab}}} \frac{\mathrm{d}x_{\mathrm{Lab}}}{\mathrm{d}E_i} = \Delta E_j \frac{\mathrm{d}N^{\mathrm{int}}}{\mathrm{d}x_{\mathrm{Lab}}} \frac{1}{E_j}, \tag{C.2}$$

where we used the definition of x_{Lab} from Equation (5.6) in the last step.

D

Uncertainty Propagation in MCEq

Using coupled cascade equations, MCEq can calculate atmospheric particle flux within the order of seconds. Hence MCEq is perfectly suited for the study of the effects from different components on these outcomes. We can even go one step further and propagate the uncertainties of the input parameters through the whole cascade. As a result, we obtain the uncertainties on the final outcomes. In this chapter, we will shortly introduce the principal concept of uncertainty propagation that we use here and its application to MCEq.

Assuming we have a function

$$f(x|a_0 \cdots a_n), \tag{D.1}$$

that depends on set of correlated coefficients $\{a_0 \cdots a_n\}$. Each of these coefficients is measured with a given gaussian uncertainty σ_{ii}. The correlation between the individual parameters can be described by the correlation coefficient σ_{ij}. The effect of these uncertainties on the function f can be quantified by making use of the principle of quadratic uncertainty propagation. The total uncertainty of f can be written as

$$\Delta f(x|a_0 \cdots a_n) = \sqrt{\sum_{i,j}^{n} \left(\frac{\partial f}{\partial a_i} \frac{\partial f}{\partial a_j} \right) \sigma_{ij}} \tag{D.2}$$

$$= \sqrt{\begin{pmatrix} \frac{\partial f}{\partial a_0} & \cdots & \frac{\partial f}{\partial a_n} \end{pmatrix} \Sigma \begin{pmatrix} \frac{\partial f}{\partial a_0} \\ \vdots \\ \frac{\partial f}{\partial a_n} \end{pmatrix}}, \tag{D.3}$$

where Σ indicates the covariance matrix containing the uncertainty coefficients σ_{ij}

$$\Sigma = \begin{pmatrix} \sigma_{00}^2 & \cdots & \sigma_{0n} \\ \vdots & \ddots & \vdots \\ \sigma_{n0} & \cdots & \sigma_{nn}^2 \end{pmatrix}. \tag{D.4}$$

Hence if can access the derivatives of f with respect to the coefficients a_i, we can compute the absolute error Δf caused by the uncertainties of the coefficients.

This principle can be directly applied to the situation in MCEq. In the following, we will show this based on a short simplifying example, which can be generally extended to all other situations. Let us assume that we want to compute the flux of atmospheric muon neutrinos at the surface of the Earth. This can be easily calculated with MCEq (Subsection 5.1.3). In a next step, we want to quantify how this result is affected by the hadronic production of pions in interactions of protons within the atmosphere.

Assuming that these production yields can be described by a function g

$$\frac{dN_{p\to\pi}^{\text{int}}}{dE_\pi}(E_p) = g\left(E_\pi, E_p | a_0 \cdots a_n\right), \tag{D.5}$$

which depends on n correlated coefficients $\{a_i\}_{i\in\{0\cdots n\}}$, with respective uncertainties σ_i, then the total uncertainty of the muon neutrino flux caused by the uncertainties of the hadronic pion production can be written as (Equation (D.3))

$$\Delta\phi_{\nu_\mu}(E|dN_{p\to\pi}^{\text{int}}) = \sqrt{\left(\frac{\partial\phi_{\nu_\mu}}{\partial\pi}\right)^T \cdot \Sigma_\pi \cdot \frac{\partial\phi_{\nu_\mu}}{\partial\pi}}, \tag{D.6}$$

where similar to above Σ_π corresponds to the covariance matrix of the coefficients in g and

$$\frac{\partial\phi_{\nu_\mu}}{\partial\pi} = \begin{pmatrix} \frac{\partial\phi_{\nu_\mu}}{\partial a_0} \\ \vdots \\ \frac{\partial\phi_{\nu_\mu}}{\partial a_n} \end{pmatrix}. \tag{D.7}$$

The computed atmospheric fluxes in MCEq are numerical solutions of a set of coupled cascade equations (Subsection 5.1.3). Consequently the simplest way to estimate the derivatives from Equation (D.7) we apply the approach of finite difference derivatives in order to get a numerical approximation. In case of the example above these derivatives

this yields

$$\left.\frac{\partial \phi_{\nu_\mu}}{\partial a_i}\right|_{\hat{a}} = \lim_{h\to 0} \frac{\phi_{\nu_\mu}(\cdots, \hat{a}_i + h, \cdots) - \phi_{\nu_\mu}(\cdots, \hat{a}_i - h, \cdots)}{2h} \tag{D.8}$$

$$\overset{h \ll |\hat{a}_i|}{\approx} \frac{\phi_{\nu_\mu}(\cdots, \hat{a}_i + h, \cdots) - \phi_{\nu_\mu}(\cdots, \hat{a}_i - h, \cdots)}{2h}, \tag{D.9}$$

where $\hat{a}$ illustrates the set of expectation values $\{\hat{a}_i\}_{i\in\{0\cdots n\}}$.

E

Data-driven Hadronic Interaction Model: Additional Material

Projectile	Secondary	E_p [GeV]	Z_{ps}^{DDM}	$\Delta Z_{ps}^{\mathrm{DDM}}$	Z_{ps}^{SIB}(C)	Z_{ps}^{SIB}(air)
p	π^+	31	0.0474	0.0009 (1.9 %)	0.0505	0.0502
		158	0.0477	0.0033 (7.0 %)	0.0414	0.0412
p	π^-	31	0.0292	0.0002 (0.8 %)	0.0287	0.0288
		158	0.0265	0.0005 (1.8 %)	0.0261	0.0262
p	K^+	31	0.0067	0.0008 (12.3 %)	0.0038	0.0038
p	K^-	31	0.0015	0.0001 (5.1 %)	0.0017	0.0017
p	p	158	0.1531	0.0044 (2.9 %)	0.1821	0.1784
p	$\bar{p}$	158	0.0010	0.0001 (12.4 %)	0.0010	0.0010
p	n	158	0.0737	0.0080 (10.8 %)	0.0681	0.0682
π^-	π^+	158	0.0504	0.0003 (0.7 %)	0.0465	0.0467
		350	0.0417	0.0025 (6.0 %)	0.0462	0.0467
π^-	π^-	158	0.1556	0.0437 (28.1 %)	0.2120	0.2118
		350	0.1409	0.0390 (27.7 %)	0.2152	0.2151
π^-	K^+	158	0.0075	0.0001 (1.9 %)	0.0045	0.0045
		350	0.0039	0.0004 (10.3 %)	0.0047	0.0047
π^-	K^-	158	0.0093	0.0002 (1.8 %)	0.0082	0.0083
		350	0.0056	0.0014 (24.4 %)	0.0092	0.0091
π^-	p	158	0.0070	0.0002 (2.9 %)	0.0026	0.0025
		350	0.0039	0.0002 (3.9 %)	0.0026	0.0025
π^-	$\bar{p}$	158	0.0067	0.0001 (0.9 %)	0.0044	0.0044
		350	0.0061	0.0013 (21.7 %)	0.0049	0.0048

Table E.1: Spectrum weighted moments for the inclusive particle production yields shown in Figure 5.4 and 5.5. The experimental data from the DDM are generated with a carbon target. Comparable values from SIBYLL 2.3c for carbon and air targets are shown in the last two columns.

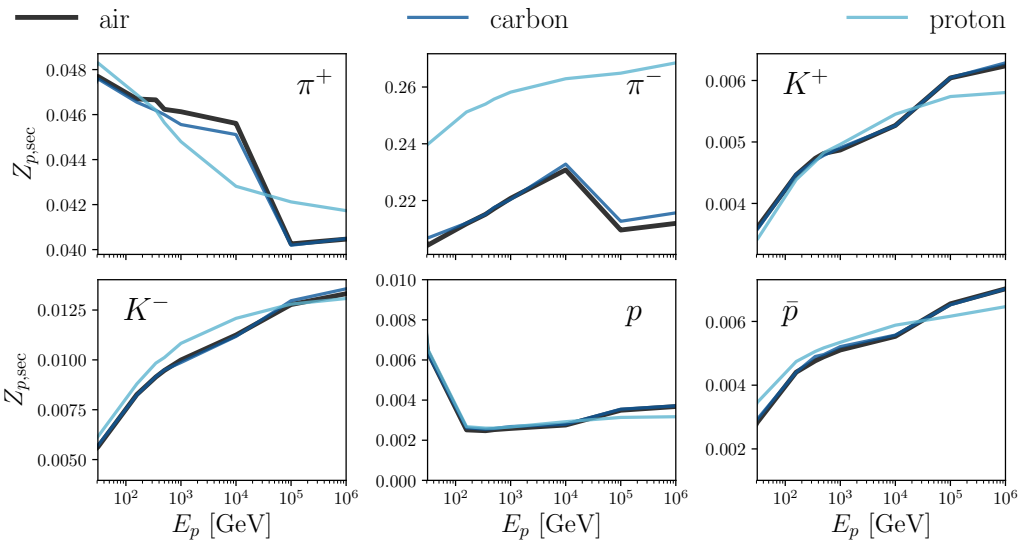

Figure E.1: Z-factor distributions for the inclusive particle interactions shown in Figure 5.5. The colors indicate the different target materials for the respective interaction. Note that the values in these plots are calculated by means of the interaction model SIBYLL 2.3c [90].

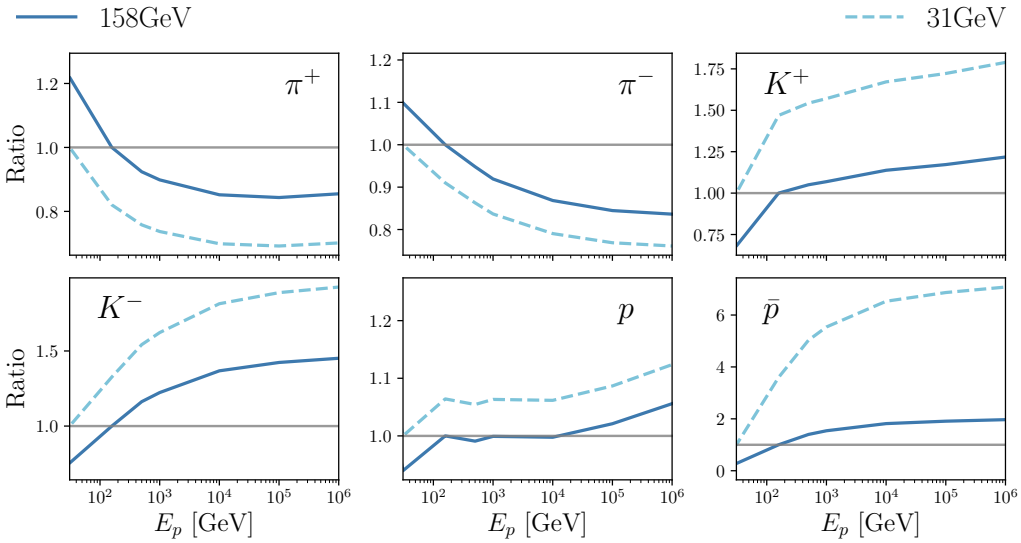

Figure E.2: Change of the Z-factor with respect to the values at proton projectile energies of 31 GeV and 158 GeV for the inclusive particle interactions shown in Figure 5.4. Note that the values in these plots are calculated by means of the interaction model SIBYLL 2.3c with air-like target material [90].

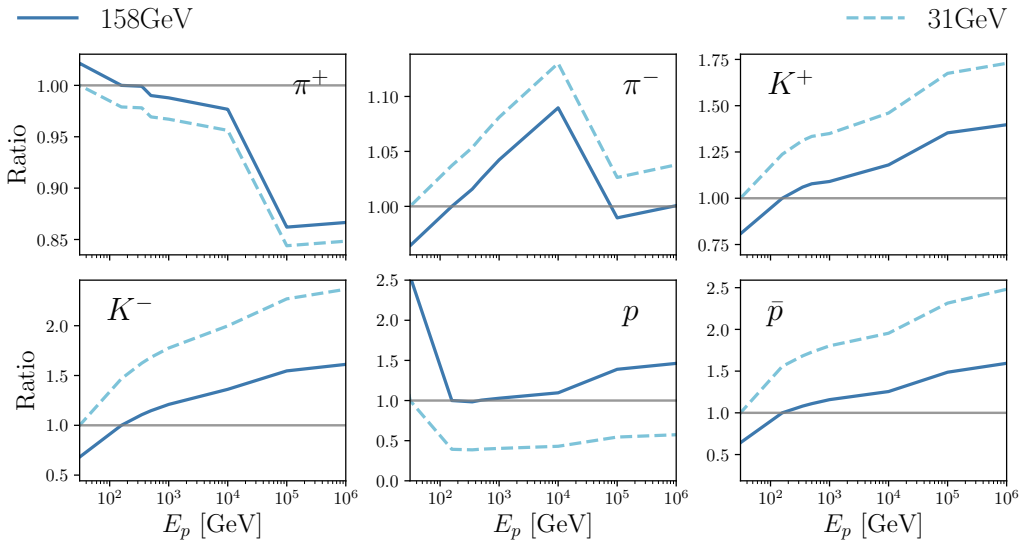

Figure E.3: Change of the Z-factor with respect to the values at π^- projectile energies of 31 GeV and 158 GeV for the inclusive particle interactions shown in Figure 5.5. Note that the values in these plots are calculated by means of the interaction model SIBYLL 2.3c with air-like target material [90].

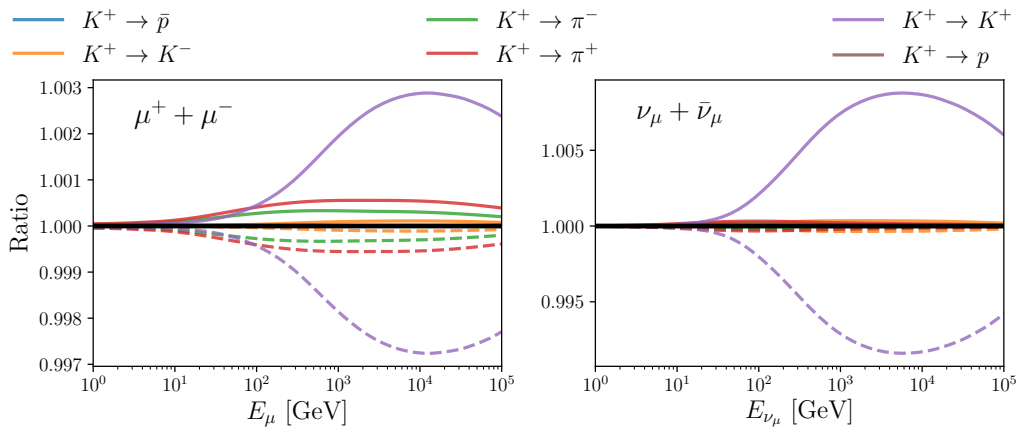

Figure E.4: Illustration of the influence of positively charged koan interactions for the development of air-shower and resulting lepton fluxes. In these plots the respective particle yields (projectile → secondary) are extended (solid lines) or lowered (dashed lines) by 20 %. The resulting effect on muon and muon neutrino fluxes resides in the sub-percent region. The hadronic interactions in this plot are modeled with SIBYLL 2.3c [90].

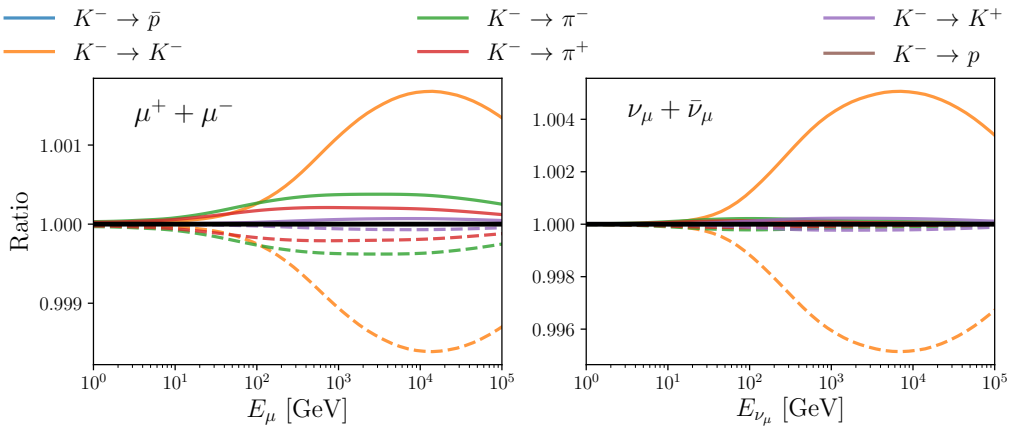

Figure E.5: Illustration of the influence of negatively charged koan interactions for the development of air-shower and resulting lepton fluxes. In these plots the respective particle yields (projectile → secondary) are extended (solid lines) or lowered (dashed lines) by 20 %. The resulting effect on muon and muon neutrino fluxes resides in the sub-percent region. The hadronic interactions in this plot are modeled with SIBYLL 2.3c [90].

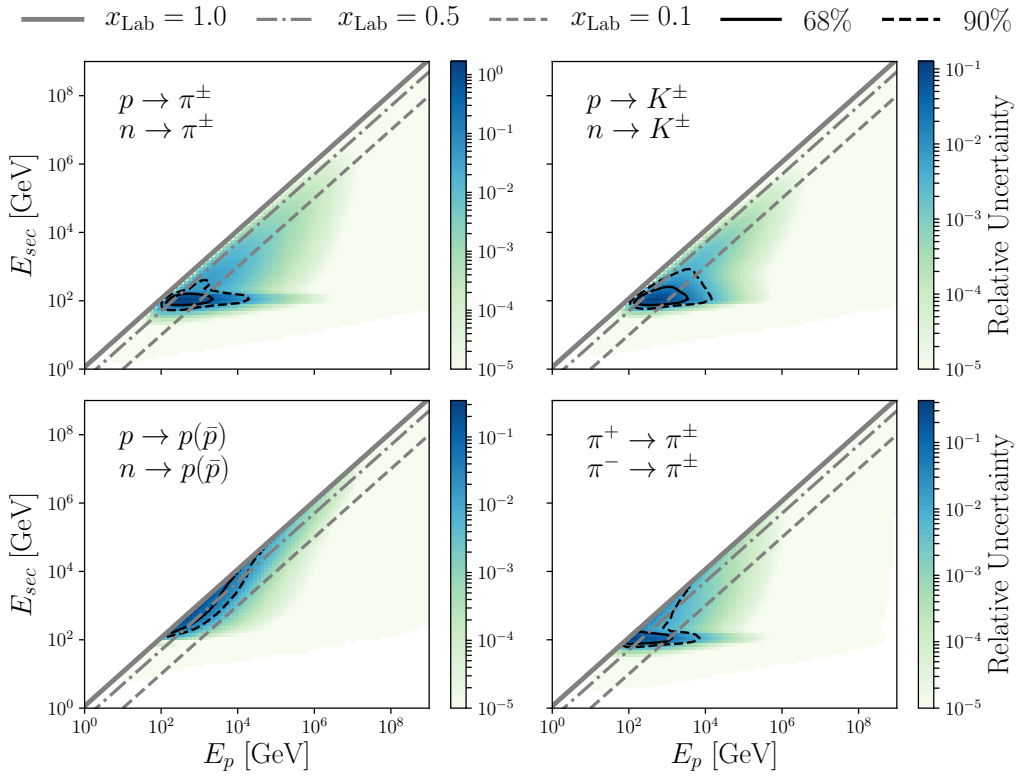

Figure E.6: Relative contribution of different phase space elements to the atmospheric muon flux at 100 GeV. These relative contributions are shown for different particle interactions. The black contour lines illustrate the 68 % and 90 % phase space regions that contribute most to the total uncertainty.

F

3FHL Blazar Stacking: Analysis Performance

F.1 Background Test Statistic Distributions

The background test statistic distributions of all four blazar categories apparent in the 3FHL catalog are illustrated in Figure F.1. Assuming that all required conditions for Wilks theorem are fulfilled, the distributions should follow the modified χ^2 function defined in Equation (7.56). This distribution is illustrated by the black lines in Figure F.1. Due to the multiplicity of approximations applied for the underlying probability density functions of the hypothesis test, Wilks theorem does not describe the actual distributions correctly. Hence we use the actual test statistic distributions generated from background trials for the evaluation of the p-value (Subsection 7.3.4) and the sensitivity (Section 7.4). In order to access the tails of the distribution at high test statistic values we make use of another modified χ^2 fit

$$f(\Lambda|x,y) \sim \begin{cases} x & \text{if } \Lambda = 0 \\ (1-x)\cdot\chi^2_{n_{\mathrm{dof}}=y}(\Lambda) & \text{else .} \end{cases}, \tag{F.1}$$

where x and y depict the free parameters of f. These distributions are illustrated by the orange lines in Figure F.1.

F.2 Recovery of Physics Parameters

In order to verify the functionality of the hypothesis test, we want to investigate if we can recover the true physics parameters λ_s and γ of a hypothetical neutrino source. In the following, we will exemplarily assume all sources following a power-law with spectral index $\gamma = 2$. Under the assumption of this spectrum, the recovery of the physics parameters will be shown exemplarily for the FSRQ sub-category for different

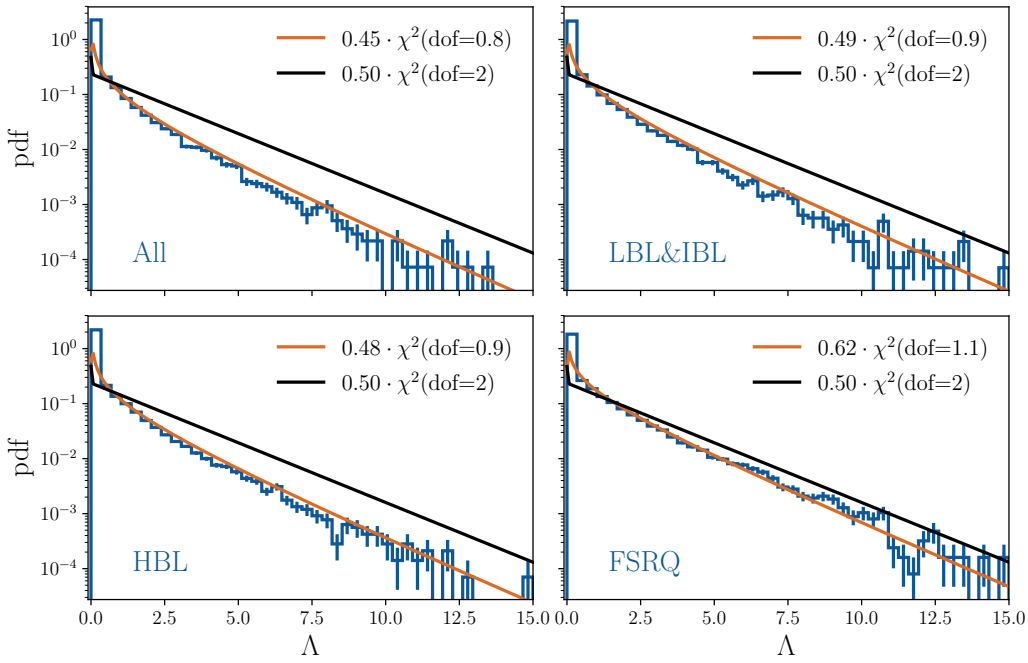

Figure F.1: Background test statistic Λ distribution for all tested 3FHL blazar categories.

scenarios. The generally observed behavior of all other blazar categories is similar to the one of the FSRQ objects.

In general, the hypothesis analysis in this thesis performs best once the model assumptions correspond to the actual true parameters of the source population. Hence, in order to study the effect coming from putative deviations, we initially recall the assumptions made for the 3FHL blazar population analysis in Subsection 8.2.2:

- Location of M neutrino sources at the position of 3FHL objects
- A global power-law spectrum with spectral index γ that is valid for all sources.
- All sources constantly emit the neutrinos at a steady rate
- The relative neutrino emission strength of the individual sources follows a predefined distribution according to Equation (7.53). In the case of the 3FHL population analysis we fix the relative weights w_j of each source j to $w_j \sim \phi_0^j := \phi_0$. Hence all sources are assumed to generate observable neutrinos at the Earth at the exact same rate with $w_j = 1/M$.

The recovery of the true number of signal events λ_s and the true spectral index γ for the case where all these assumptions are correct are shown in Figure F.2. After

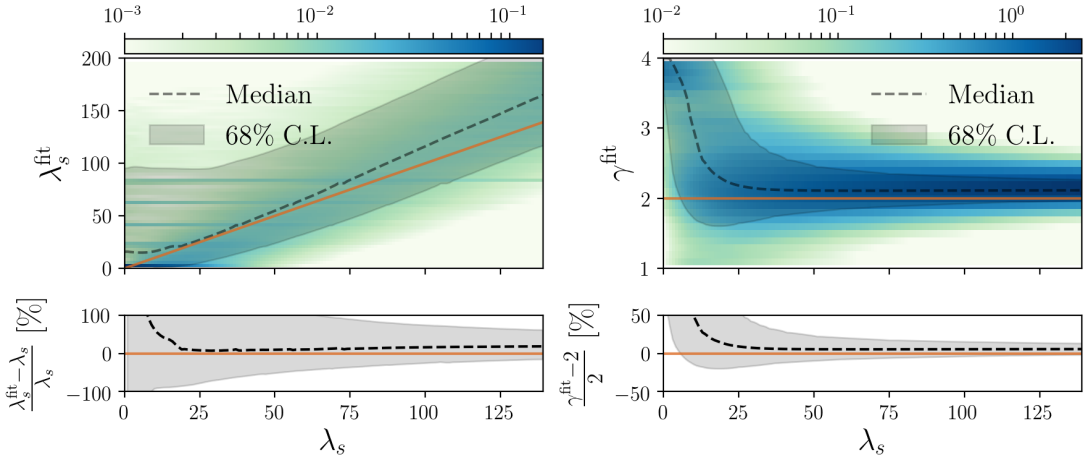

Figure F.2: Recovery of the true physics parameters of the FSRQ source population based on the assumption that $\phi_0^j = \phi_0$.

reaching a certain source strength ($\lambda_s \sim 25$), both the number of signal events λ_s and the spectral index γ can be nicely recovered within the 68 % uncertainties.

F.2.1 Deviations from the Uniform Neutrino Emission Assumption

Nevertheless this situation changes if the relative source weights w_j do not follow a uniform distribution anymore. The potential influence of these weights becomes clear if we recall the signal likelihood function for the hypothesis of multiple sources defined in Equation (7.51)

$$p(x_i|\{\mathbf{x}_{\mathrm{src}}^k, \phi_0^k\}_{k\in M}, \gamma) = \sum_{j=1}^{M} p(x_i|\mathbf{x}_{\mathrm{src}}^j, \phi_0^j, \gamma) \cdot r_j(\gamma) \cdot w_j, \tag{F.2}$$

where $r_j(\gamma)$ depicts the relative detection efficiency at the position of source j according to Equation (7.54). As highlighted in this formula, the spectral index γ appears in both the signal likelihood of the individual source as well as the relative detection efficiency $w_j(\gamma)$. The declination distribution of the latter for different spectral indices is shown in Figure F.3. In case all sources emit neutrinos at the same strength as predicted by the fixed theoretical weights $w_j = 1/M$, the fitted global spectral index γ^{fit} should be able to recover the true spectral shape for a strong signal. This expectation is confirmed by the outcome in Figure F.2.

Nevertheless, once the real signal strength distribution differs from the uniform assumption fixed in the likelihood method, then the fitted spectral index γ^{fit} will try to

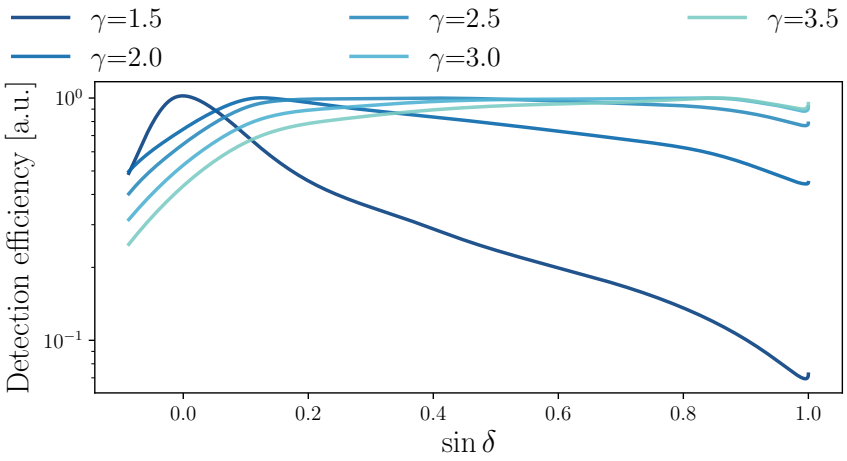

Figure F.3: Detection efficiency for different source spectra based on simulated events from IC86 2012-2016.

compensate this false assumption by means of the relative detection efficiency $r_j(\gamma)$. In this case, γ^{fit} deviates from the truth value γ even if all pdfs within the analysis are known perfectly. This behavior will be illustrated by means of two extreme examples in the following.

F.2.2 Example 1: Major Contribution from the Horizon

In the first example signal events are injected according to the randomly assigned emission strength distribution shown in the left panel of Figure In this scenario, the strongest sources come from the region close to the horizon. Nevertheless as before, within the likelihood method, we assume an equal emission strength with $w_j = 1/M$ for all sources j. The median fitted spectral index γ^{fit} and the median fitted number of signal events λ_s^{fit} are shown in Figure F.5. Above a certain signal strength, the median fitted spectral index settles far below the true value of $\gamma = 2$ at values around $\gamma^{\text{fit}}0.5$. To a large extent, this deviation can be attributed to the false neutrino strength assumption in the analysis. In this scenario, the fitted spectral index γ^{fit} not only tries to maximize the test statistic Λ with respect to the individual signal pdfs, but also tries to account for the deviation of the assumed source strength distribution with respect to the truth. Since most of the signal contribution comes from sources around the horizon, the relative detection efficiency $r_j(\gamma)$ tend to prefer hard spectra (for hard spectra the detection efficiency at the horizon is significantly larger than for sources located at high declinations, Figure F.3). In total, the fitted spectral index compensates the wrong assumption yielding a spectral shape that is ~ 1.5 harder than the true spectrum.

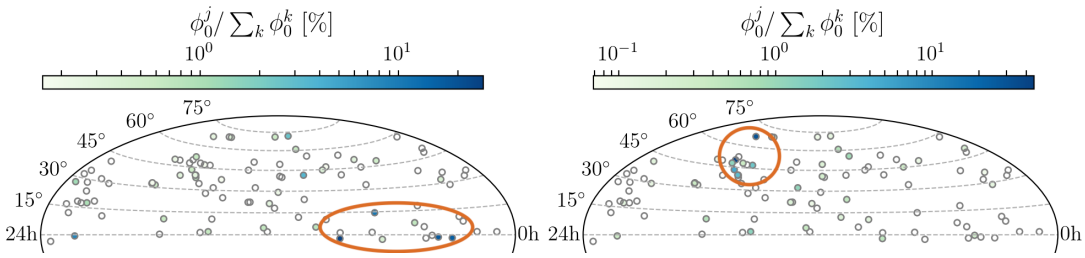

Figure F.4: **Left:** Relative neutrino strength distributions for example 1. **Right:** Relative neutrino strength distributions for example 2. The colors indicate the relative neutrino strengths w_j. The orange circles depict the region where the strongest sources are located in the respective example.

Ultimately, it seems reasonable to look at the other fit parameter, namely the fitted number of signal events λ_s as well. The distributions of λ_s^{fit} for an increasing number of injected signal events λ_s is shown in the left panel of Figure F.5. Since both fit variables, λ_s and γ are strongly correlated (high energy events from a source can be easier discriminated from the atmospheric background than low energy events), it is not surprising that also the fitted number of signal events does not recover the true number of injected signal events. In fact, since the fitted spectrum is much harder than the true spectrum it seems obvious that fewer signal events are required.

F.2.3 Example 2: Major Contribution from the High Declinations

The relative source strength distribution of the second example is illustrated in the right panel of Figure F.4. In contrast to the first example, the major neutrino signal now comes from sources located at high declinations. The median values of the fitted source population parameters are illustrated in Figure F.6. The outcome of this second scenario basically depicts the exact opposite of the observations from the first example. According to Figure F.3 soft spectra tend to yield high detection efficiencies r_j for sources located at higher declinations. Hence in order to compensate the false source strength distribution assumption, the fitted spectral index γ^{fit} yields a soft spectrum with values around 2.5. Correspondingly the fitted number of signal events λ_s^{fit} overestimates the true value λ_s.

Based on the observation from these two extreme examples we can state that the interpretation of the fit parameters λ_s^{fit} and γ^{fit} is not obvious. The interpretation as the true physical population parameters is only valid as long as all model assumptions are correct. If the true source strength distribution deviates from the fixed assumption, the estimated parameters can strongly deviate from the corresponding truth. At this

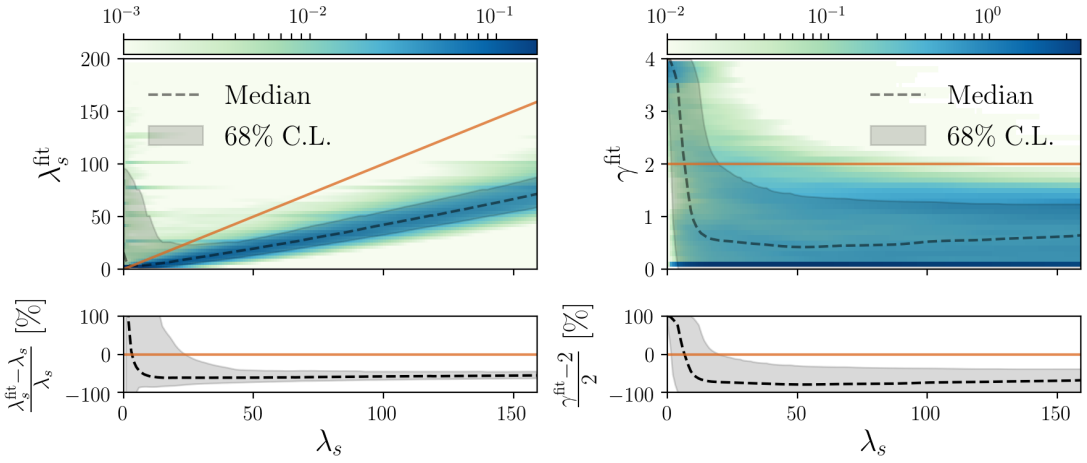

Figure F.5: Recovery of the true physics parameters of the FSRQ source population based on the relative source strength distribution in example 1.

point it is worth noting that this issue does not appear if we treat the relative source strength w_j as free parameters in the analysis[1].

F.2.4 Implications on the p-value

The fitted population parameters strongly depend on the correctness of the relative flux strength distribution within the hypothesis test. Yet, it is not necessarily clear what the observations from the previous section mean for the p-value and the sensitivity or upper limits of the analysis. These questions will be treated in the following.

If the model assumption is different from the actual truth this affects of course also the result and hence the p-value of the analysis. The more correct the model assumptions, the more power is assigned to the corresponding hypothesis test.

If we inject signal events, assuming that all of these sources actually have the same neutrino strength, then the free fit parameters of the test statistic Λ and in particular the spectral index try to optimize the signal likelihood of the individual sources in Equation (F.2). The second highlighted term in this equation will naturally account for declination dependent detection effects of the detector since the true source strength distribution is recovered correctly by the model weights w_j. In this case, the analysis builds up the most optimal for the true population scenario. The signal of each source is accounted for with the correct weight and including detector effects.

[1] Unfortunately this could not be realized for this analysis since this introduces an enormous number (M) of additional free parameters. The minimizer used in this work was not able to properly handle these.

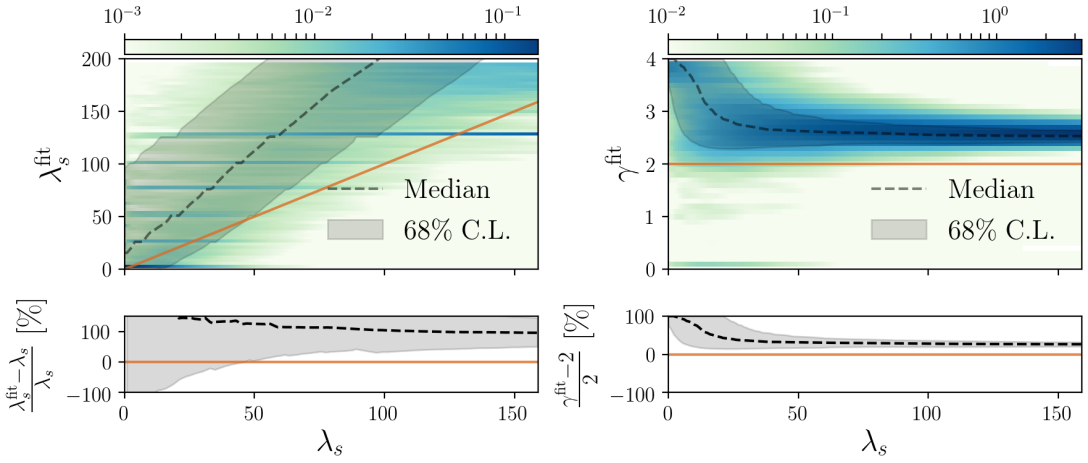

Figure F.6: Recovery of the true physics parameters of the FSRQ source population based on the relative source strength distribution in example 2.

Now, let us assume again a scenario of a population of neutrino sources, which all emit neutrinos at a different strength. Yet within the likelihood analysis, we assume that all sources obtain an equal emission strength. As before, in order to maximize the test statistic Λ, the spectral index γ^{fit} does not only try to optimize the individual source signal probabilities, but now also tries to account for the false theoretical source strength assumption via the detector weight r_j. While the fitted source parameters deviate from the truth, it is still possible to observe test statistic values Λ larger than 0 from such a source class. Yet the analysis would on average behave more optimal if the correct source strength weights w_j would have been chosen. This is mainly caused by the fact, that the most driving factor for every point source analysis in IceCube is the spatial accumulation of signal events. The energy term adds additional information to distinguish between astrophysical signal and background. These energy terms can not be recovered perfectly once the true source strength distribution is different from the model assumption. Yet it is still possible to detect the accumulation of signal in space from all sources.

In summary, one can state that even in the case where the source strength model assumption is wrong, it is possible to detect a signal from the tested source class (at least if the model assumption is equal weighting) and hence get a meaningful p-value. Of course, this p-value could be stronger when choosing the correct model assumption. The exact effect of false relative neutrino strength assumptions can be estimated by means of comparing sensitivity values. This is shown in the following subsection.

Scenario	Sensitivity [GeV cm^{-2} s^{-1}]
1	1.7×10^{-9}
2	6.7×10^{-10}
3	2.1×10^{-9}
4	2.7×10^{-9}

Table F.1: Sensitivity of the FSRQ blazar population for different source strength realizations. More details can be found in the text.

F.2.5 Implications on the Sensitivity and Upper Limits

If the model assumption of the relative neutrino emission strength distribution is different from the actual truth also the sensitivity and upper limit evaluations are influenced. In the following, we will calculate the sensitivity of the 3FHL FSRQ blazars for four extreme scenarios with different true source strength distributions. Within the likelihood method, equal emission strength is assumed for all of these scenarios. The first scenario depicts the case where all sources emit the same amount of neutrinos. The remaining three scenarios constitute realizations with only one source in the whole sample emitting neutrinos. The respective scenarios differ by the declination of this one neutrino source, with one being located at $\delta \sim 0^\circ$ (scenario 2), one at $\delta \sim 30^\circ$ (scenario 3) and one at $\delta \sim 50^\circ$ (scenario 4). The corresponding sensitivity values to each of these scenarios are listed in Table F.1. The first scenario and the last two scenarios yield a rather similar sensitivity, while the flux threshold in the second scenario is significantly lower. This results from the fact that the IceCube detector is most sensitive to sources located around the horizon (at least for not too soft spectra). Hence from such sources less signal events are needed than for sources at higher declinations.

In fact from this observation it seems, that it is beneficial to have only one source at the horizon even if the model assumption in the likelihood method is not correct. This is of course only true for the absolute number of signal events. For the case where all sources emit neutrinos at the same strength only a weak signal is needed from each source. On the other hand, once only one source emits neutrinos and all the others do not, it has to be a very strong source. In this case, a stacking analysis is by definition not the optimal analysis to find the signal.

In summary, one can state that for the sensitivity it is, in fact, crucial where the strongest sources are located. If they are located close to the horizon, fewer signal events are required in total. Nevertheless, if only a few sources contribute, the requirement for these few sources is much higher than it would be for the case where all sources contribute. Everything that is mentioned here for the sensitivity values, accounts simi-

larly for upper limits. In fact, for both sensitivity and upper limit fluxes, we estimate uncertainties that account for deviations of the actual source strength distribution from the uniform assumption. These uncertainties are based on the assumption, that the general neutrino source count distribution of the 3FHL population follows a development similar to the respective gamma-ray source count distribution. The exact procedure is explained in more detail in Appendix G.

G

Determination of Flux Uncertainties and Energy Ranges for Sensitivity, Discovery Potential and Upper Limits.

For all fluxes derived in this work we evaluate the 68 % uncertainties of the flux value corresponding to possible deviations of the equal neutrino strength assumption from the actual relative neutrino strength distribution. Besides we also estimate the 90 % energy region for the respective scenario where IceCube has the highest exclusion power. Both procedures follow the strategies introduced in [169]. In the following, both approaches are shortly outlined here.

In order to account for deviations of the actual neutrino source count distribution (SCD) from the equal emission strength assumption, we generally assume that neutrino source count distribution follows a similar shape as the corresponding photon source count distribution at 3FHL energies [51]. In this sense, we expect a lot of sources with faint neutrino fluxes and only a few sources with a significantly larger neutrino emission rate. Although we do not have any confirmed knowledge about the neutrino source count distribution of any source population, this assumption might, in fact, depict a realistic scenario. In order to evaluate uncertainties sensitivity and upper limit fluxes, we randomly assign source weights w_j to the individual sources according to this SCD and re-evaluate the desired flux thresholds. The 68 % uncertainty of the flux values assembles from the 68 % central region of these random outcomes.

In order to determine the 90 % energy region that contributes most to the respective flux, we compare the respective flux to the differential sensitivity of the analysis in IceCube. The IceCube data have the highest exclusion power at the energies where the ratio between the flux and the differential sensitivity is maximal. The central interval

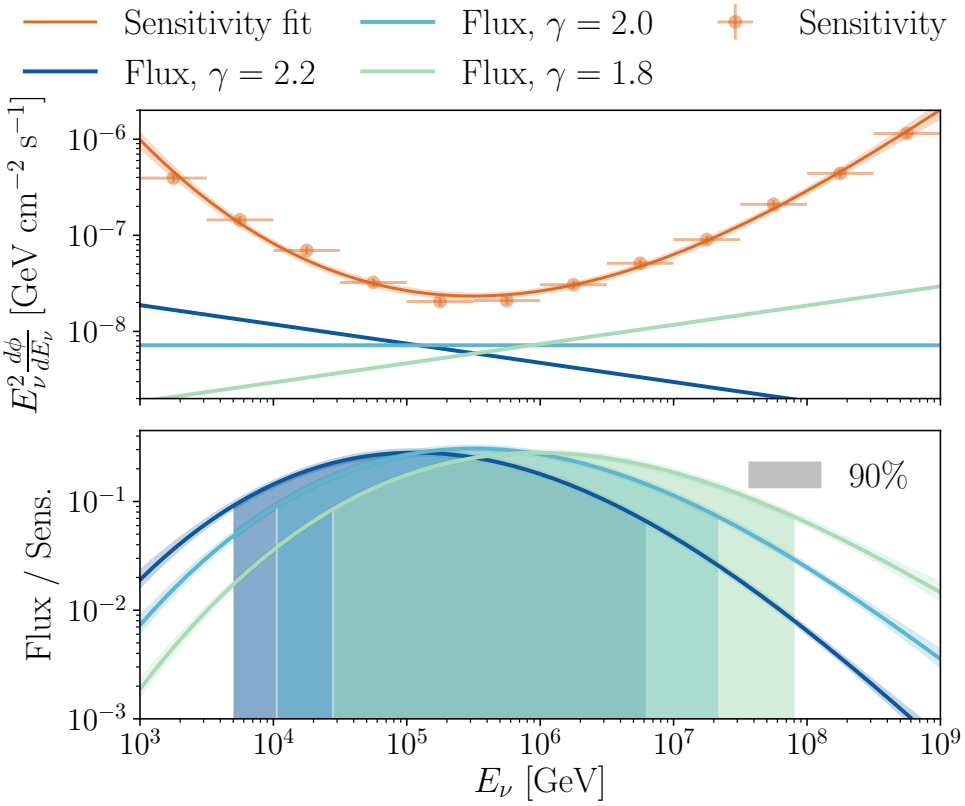

Figure G.1: Determination of the energy range that contributes most to the sensitivity for different source spectra.

enclosing 90 % of the area under the flux-sensitivity ratio is used to define the energy range that contributes 90 % to the sensitivity for a given spectrum. This procedure is illustrated for three exemplary neutrino spectra in Figure G.1

Acknowledgments

The work presented in this thesis would not have been possible without the support of many friends and colleagues that I would like to thank here. First of all I would like to thank my supervisor, Prof. Elisa Resconi, for giving me the chance to work in the fascinating field of multi-messenger astronomy, guiding me through these past years and always encouraging me to follow my interests. It has been a real pleasure to be part of this working group at the TUM for the last few years. I also want to thank Anatoli Fedynitch for the many hours of supervision and fruitful discussions and also for inviting me to work with him in Japan. Many thanks to Prof. Susanne Mertens for being the second reviewer of this work, and Prof. Andreas Weiler for agreeing to be the chair of the review commission. Very special thanks go to all my colleagues, the members of the ECP group, that made the days at the office very enjoyable and became friends over the years. Thanks for always being available for advice and important refreshment breaks in the Coffice. In particular I would like to thank Andrea, Stefan, Theo, Kai, Stephan, Hans and Martina for being good collaborators in the office and great friends outside. Finally I would also like to thank my family and especially my girlfriend Isabella for being at my side all the time without complaining too much :). Without all of you the last four years would have been much less enjoyable.

Bibliography

[1] Victor F. Hess. "Über Beobachtungen der durchdringenden Strahlung bei sieben Freiballonfahrten." In: *Phys. Z.* 13 (1912), pp. 1084–1091.

[2] M. G. Aartsen et al. "Evidence for High-Energy Extraterrestrial Neutrinos at the IceCube Detector." In: *Science* 342 (2013), p. 1242856. DOI: 10.1126/science.1242856. arXiv: 1311.5238.

[3] M. G. Aartsen et al. "Time-integrated Neutrino Source Searches with 10 years of IceCube Data." In: *Phys. Rev. Lett.* 124.5 (2020), p. 051103. DOI: 10.1103/PhysRevLett.124.051103. arXiv: 1910.08488 [astro-ph.HE].

[4] M. G. Aartsen et al. "Multimessenger observations of a flaring blazar coincident with high-energy neutrino IceCube-170922A." In: *Science* 361.6398 (2018), eaat1378. DOI: 10.1126/science.aat1378. arXiv: 1807.08816 [astro-ph.HE].

[5] M. G. Aartsen et al. "Neutrino emission from the direction of the blazar TXS 0506+056 prior to the IceCube-170922A alert." In: *Science* 361.6398 (2018), pp. 147–151. DOI: 10.1126/science.aat2890. arXiv: 1807.08794 [astro-ph.HE].

[6] T. K. Gaisser, R. Engel, and E. Resconi. *Cosmic Rays and Particle Physics.* Cambridge University Press, 2016.

[7] Carl D. Anderson. "The Positive Electron." In: *Phys. Rev.* 43 (6 Mar. 1933), pp. 491–494. DOI: 10.1103/PhysRev.43.491. URL: https://link.aps.org/doi/10.1103/PhysRev.43.491.

[8] S.H. Neddermeyer and C.D. Anderson. "Note on the Nature of Cosmic Ray Particles." In: *Phys. Rev.* 51 (1937), pp. 884–886. DOI: 10.1103/PhysRev.51.884.

[9] Y. Fukuda et al. "Evidence for oscillation of atmospheric neutrinos." In: *Phys. Rev. Lett.* 81 (1998), pp. 1562–1567. DOI: 10.1103/PhysRevLett.81.1562. arXiv: hep-ex/9807003.

[10] V. L. Ginzburg and S. I. Syrovatskii. *The Origin of Cosmic Rays.* Macmillan, 1964.

[11] M. Aguilar et al. "Precision Measurement of the Proton Flux in Primary Cosmic Rays from Rigidity 1 GV to 1.8 TV with the Alpha Magnetic Spectrometer on the International Space Station." In: *Physical Review Letters* 114 (2015), p. 171103. DOI: 10.1103/PhysRevLett.114.171103.

[12] Y. S. Yoon et al. “Proton and Helium Spectra from the CREAM-III Flight.” In: *The Astrophysical Journal* 839.1 (2017), p. 5. DOI: 10.3847/1538-4357/aa68e4. arXiv: 1704.02512.

[13] R. Alfaro et al. “All-particle cosmic ray energy spectrum measured by the HAWC experiment from 10 to 500 TeV.” In: *Physical Review* D96.12 (2017), p. 122001. DOI: 10.1103/PhysRevD.96.122001. arXiv: 1710.00890.

[14] M. Amenomori et al. “The all-particle spectrum of primary cosmic rays in the wide energy range from 10^{14} eV to 10^{17} eV observed with the Tibet-III air-shower array.” In: *The Astrophysical Journal* 678 (2008), pp. 1165–1179. DOI: 10.1086/529514. arXiv: 0801.1803.

[15] M. G. Aartsen et al. “Measurement of the cosmic ray energy spectrum with IceTop-73.” In: *Physical Review* D88.4 (2013), p. 042004. DOI: 10.1103/PhysRevD.88.042004. arXiv: 1307.3795.

[16] S. Ter-Antonyan. “Sharp knee phenomenon of primary cosmic ray energy spectrum.” In: *Physical Review* D89.12 (2014), p. 123003. DOI: 10.1103/PhysRevD.89.123003. arXiv: 1405.5472.

[17] T. Antoni et al. “KASCADE measurements of energy spectra for elemental groups of cosmic rays: Results and open problems.” In: *Astroparticle Physics* 24 (2005), pp. 1–25. DOI: 10.1016/j.astropartphys.2005.04.001. arXiv: astro-ph/0505413.

[18] W. D. Apel et al. “The spectrum of high-energy cosmic rays measured with KASCADE-Grande.” In: *The Astrophysical J.* 36 (2012), pp. 183–194. DOI: 10.1016/j.astropartphys.2012.05.023. arXiv: 1206.3834.

[19] T. Abu-Zayyad et al. “Measurement of the cosmic ray energy spectrum and composition from 10^{17} eV to $10^{18.3}$ eV using a hybrid fluorescence technique.” In: *The Astrophysical Journal* 557 (2001), pp. 686–699. DOI: 10.1086/322240. arXiv: astro-ph/0010652.

[20] R. U. Abbasi et al. “First observation of the Greisen-Zatsepin-Kuzmin suppression.” In: *Physical Review Letters* 100 (2008), p. 101101. DOI: 10.1103/PhysRevLett.100.101101. arXiv: astro-ph/0703099.

[21] Y. Tsunesada et al. “Energy Spectrum of Ultra-High-Energy Cosmic Rays Measured by The Telescope Array.” In: *Proceedings of the 35th International Cosmic Ray Conference*. Vol. ICRC2017. Proceedings of Science, 2017, p. 535.

[22] The Pierre Auger Collaboration. "The cosmic ray energy spectrum measured using the Pierre Auger Observatory." In: *Proceedings of the 35th International Cosmic Ray Conference*. Vol. ICRC2017. Proceedings of Science, 2017, p. 486. arXiv: 1708.06592.

[23] M. Spurio. *Particles and Astrophysics: A Multi-Messenger Approach*. Astronomy and Astrophysics Library. Springer International Publishing, 2017. ISBN: 9783319345390. URL: https://books.google.de/books?id=u8rgAQAACAAJ.

[24] B. Peters. "Primary cosmic radiation and extensive air showers." In: *Il Nuovo Cimento (1955–1965)* 22.4 (1961), pp. 800–819. DOI: 10.1007/BF02783106.

[25] T. K. Gaisser. "Spectrum of cosmic-ray nucleons, kaon production, and the atmospheric muon charge ratio." In: *Astroparticle Physics* 35 (2012), pp. 801–806. DOI: 10.1016/j.astropartphys.2012.02.010. arXiv: 1111.6675.

[26] A. M. Hillas. "The Origin of Ultra-High-Energy Cosmic Rays." In: *Annual Review of Astronomy and Astrophysics* 22.1 (1984), pp. 425–444. DOI: 10.1146/annurev.aa.22.090184.002233.

[27] K. Greisen. "End to the Cosmic-Ray Spectrum?" In: *Physical Review Letters* 16 (17 1966), pp. 748–750. DOI: 10.1103/PhysRevLett.16.748.

[28] G. T. Zatsepin and V. A. Kuzmin. "Upper limit of the spectrum of cosmic rays." In: *JETP Letters* 4 (1966), pp. 78–80.

[29] J. A. Simpson. "Elemental and isotopic composition of the galactic cosmic rays." In: *Ann. Rev. Nucl. Part. Sci.* 33 (1983), pp. 323–382. DOI: 10.1146/annurev.ns.33.120183.001543.

[30] Katharina Lodders. "Solar System Abundances and Condensation Temperatures of the Elements." In: *Astrophys. J.* 591 (2003), pp. 1220–1247. DOI: 10.1086/375492.

[31] T. Pierog and Klaus Werner. "Muon Production in Extended Air Shower Simulations." In: *Phys. Rev. Lett.* 101 (2008), p. 171101. DOI: 10.1103/PhysRevLett.101.171101. arXiv: astro-ph/0611311 [astro-ph].

[32] Karl-Heinz Kampert and Michael Unger. "Measurements of the Cosmic Ray Composition with Air Shower Experiments." In: *Astropart. Phys.* 35 (2012), pp. 660–678. DOI: 10.1016/j.astropartphys.2012.02.004. arXiv: 1201.0018 [astro-ph.HE].

[33] K. Nakamura et al. "Review of particle physics." In: *J. Phys.* G37 (2010), p. 075021. DOI: 10.1088/0954-3899/37/7A/075021.

[34] Alexander Aab et al. "Evidence for a mixed mass composition at the 'ankle' in the cosmic-ray spectrum." In: *Phys. Lett.* B762 (2016), pp. 288–295. DOI: 10.1016/j.physletb.2016.09.039. arXiv: 1609.08567 [astro-ph.HE].

[35] Anthony M. Hillas. "Cosmic Rays: Recent Progress and some Current Questions." In: *Conference on Cosmology, Galaxy Formation and Astro-Particle Physics on the Pathway to the SKA Oxford, England, April 10-12, 2006*. 2006. arXiv: astro-ph/0607109 [astro-ph].

[36] Alexander Aab et al. "Searches for Anisotropies in the Arrival Directions of the Highest Energy Cosmic Rays Detected by the Pierre Auger Observatory." In: *Astrophys. J.* 804.1 (2015), p. 15. DOI: 10.1088/0004-637X/804/1/15. arXiv: 1411.6111 [astro-ph.HE].

[37] R.U. Abbasi et al. "Search for Anisotropy in the Ultra High Energy Cosmic Ray Spectrum using the Telescope Array Surface Detector." In: (July 2017). arXiv: 1707.04967 [astro-ph.HE].

[38] Alexander Aab et al. "An Indication of anisotropy in arrival directions of ultra-high-energy cosmic rays through comparison to the flux pattern of extragalactic gamma-ray sources." In: *Astrophys. J.* 853.2 (2018), p. L29. DOI: 10.3847/2041-8213/aaa66d. arXiv: 1801.06160 [astro-ph.HE].

[39] A. Aab et al. "Observation of a Large-scale Anisotropy in the Arrival Directions of Cosmic Rays above 8×10^{18} eV." In: *Science* 357.6537 (2017), pp. 1266–1270. DOI: 10.1126/science.aan4338. arXiv: 1709.07321.

[40] M. Ackermann et al. "The spectrum of isotropic diffuse gamma-ray emission between 100 MeV and 820 GeV." In: *Astrophys. J.* 799 (2015), p. 86. DOI: 10.1088/0004-637X/799/1/86. arXiv: 1410.3696 [astro-ph.HE].

[41] Joeran Stettner. "Measurement of the Diffuse Astrophysical Muon-Neutrino Spectrum with Ten Years of IceCube Data." In: *HAWC Contributions to the 36th International Cosmic Ray Conference (ICRC2019)*. 2019. arXiv: 1908.09551 [astro-ph.HE].

[42] The IceCube Collaboration. *IceCube Multi-Messenger Propagation*. Jan. 2018. URL: https://gallery.icecube.wisc.edu/internal/d/318865-1/physicus.pdf.

[43] Markus Ahlers. "Multi-messenger aspects of cosmic neutrinos." In: *EPJ Web Conf.* 116 (2016). Ed. by A. Capone et al., p. 11001. DOI: 10.1051/epjconf/201611611001.

[44] Alberto Franceschini, Giulia Rodighiero, and Mattia Vaccari. "The extragalactic optical-infrared background radiations, their time evolution and the cosmic photon-photon opacity." In: *Astron. Astrophys.* 487 (2008), p. 837. DOI: 10.1051/0004-6361:200809691. arXiv: 0805.1841 [astro-ph].

[45] J.A. Hinton and W. Hofmann. "Teraelectronvolt Astronomy." In: *Annual Review of Astronomy and Astrophysics* 47.1 (Sept. 2009), pp. 523–565. ISSN: 1545-4282. DOI: 10.1146/annurev-astro-082708-101816. URL: http://dx.doi.org/10.1146/annurev-astro-082708-101816.

[46] "The Fourth Catalog of Active Galactic Nuclei Detected by the Fermi Large Area Telescope." In: (May 2019). arXiv: 1905.10771 [astro-ph.HE].

[47] ENRICO Fermi. "On the Origin of the Cosmic Radiation." In: *Phys. Rev.* 75 (8 Apr. 1949), pp. 1169–1174. DOI: 10.1103/PhysRev.75.1169. URL: https://link.aps.org/doi/10.1103/PhysRev.75.1169.

[48] M.T. Dova. "Ultra-High Energy Cosmic Rays." In: *7th CERN–Latin-American School of High-Energy Physics*. 2015, pp. 169–190. DOI: 10.5170/CERN-2015-001.169. arXiv: 1604.07584 [astro-ph.HE].

[49] M.G. Aartsen et al. "An All-Sky Search for Three Flavors of Neutrinos from Gamma-Ray Bursts with the IceCube Neutrino Observatory." In: *Astrophys. J.* 824.2 (2016), p. 115. DOI: 10.3847/0004-637X/824/2/115. arXiv: 1601.06484 [astro-ph.HE].

[50] P. Padovani et al. "Active galactic nuclei: what's in a name?" In: *Astron. Astrophys. Rev.* 25.1 (2017), p. 2. DOI: 10.1007/s00159-017-0102-9. arXiv: 1707.07134 [astro-ph.GA].

[51] M. Di Mauro et al. "Deriving the contribution of blazars to the Fermi-LAT Extragalactic γ-ray background at $E > 10$ GeV with efficiency corrections and photon statistics." In: *Astrophys. J.* 856.2 (2018), p. 106. DOI: 10.3847/1538-4357/aab3e5. arXiv: 1711.03111 [astro-ph.HE].

[52] Mattia Di Mauro. "The origin of the Fermi-LAT γ-ray background." In: *Proceedings, 14th Marcel Grossmann Meeting on Recent Developments in Theoretical and Experimental General Relativity, Astrophysics, and Relativistic Field Theories (MG14) (In 4 Volumes): Rome, Italy, July 12-18, 2015*. Vol. 3. 2017, pp. 3098–3104. DOI: 10.1142/9789813226609_0393. arXiv: 1601.04323 [astro-ph.HE].

[53] Daniel J. Mortlock et al. "A luminous quasar at a redshift of z = 7.085." In: *Nature* 474 (2011), p. 616. DOI: 10.1038/nature10159. arXiv: 1106.6088 [astro-ph.CO].

[54] C. M. Urry and P. Padovani. "Unified schemes for radio-loud active galactic nuclei." In: *Publications of the Astronomical Society of the Pacific* 107 (1995), p. 803. DOI: 10.1086/133630. arXiv: astro-ph/9506063.

[55] Paolo Padovani. "On the two main classes of Active Galactic Nuclei." In: *Nat. Astron.* 1 (2017), p. 194. DOI: 10.1038/s41550-017-0194. arXiv: 1707.08069 [astro-ph.GA].

[56] R.F. Mushotzky, C. Done, and K.A. Pounds. "X-ray spectra and time variability of active galactic nuclei." In: *Ann. Rev. Astron. Astrophys.* 31 (1993), pp. 717–761. DOI: 10.1146/annurev.aa.31.090193.003441.

[57] "Search for Gamma-ray Emission from X-ray Selected Seyfert Galaxies with Fermi-LAT." In: *Astrophys. J.* 747 (2012), p. 104. DOI: 10.1088/0004-637X/747/2/104. arXiv: 1109.4678 [astro-ph.HE].

[58] P. Giommi, P. Padovani, and G. Polenta. "A simplified view of blazars: the gamma-ray case." In: *Mon. Not. Roy. Astron. Soc.* 431 (2013), p. 1914. DOI: 10.1093/mnras/stt305. arXiv: 1302.4331 [astro-ph.HE].

[59] Paolo Padovani. "The faint radio sky: radio astronomy becomes mainstream." In: *Astron. Astrophys. Rev.* 24.1 (2016), p. 13. DOI: 10.1007/s00159-016-0098-6. arXiv: 1609.00499 [astro-ph.GA].

[60] P. Padovani and P. Giommi. "The Connection between x-ray and radio-selected BL Lacertae objects." In: *The Astrophysical J.* 444 (1995), p. 567. DOI: 10.1086/175631. arXiv: astro-ph/9412073.

[61] A. A. Abdo et al. "The Spectral Energy Distribution Of FERMI Bright Blazars." In: *The Astrophysical Journal* 716.1 (May 2010), pp. 30–70. ISSN: 1538-4357. DOI: 10.1088/0004-637x/716/1/30. URL: http://dx.doi.org/10.1088/0004-637X/716/1/30.

[62] A. Turcati. "Multimessenger searches for the sources of high energy cosmic rays: IceCube, Fermi, Auger, TA." Dissertation. Technische Universität München, 2018. URL: https://mediatum.ub.tum.de/603847.

[63] R.A. Jansen et al. "Spectrophotometry of nearby field galaxies: the data." In: *Astrophys. J. Suppl.* 126 (2000), pp. 331–398. DOI: 10.1086/313308. arXiv: astro-ph/9910095.

[64] Janet Torrealba et al. "Optical Spectroscopic ATLAS of the MOJAVE/2cm AGN Sample (1)." In: *Rev. Mex. Astron. Astrofis.* 48 (2012), p. 9. arXiv: 1107.3416 [astro-ph.CO].

[65] Markus Boettcher and Charles D. Dermer. "Timing Signatures of the Internal-Shock Model for Blazars." In: *Astrophys. J.* 711 (2010), pp. 445–460. DOI: 10.1088/0004-637X/711/1/445. arXiv: 1001.1606 [astro-ph.CO].

[66] M. G. Aartsen et al. "Observation and Characterization of a Cosmic Muon Neutrino Flux from the Northern Hemisphere using six years of IceCube data." In: *The Astrophysical Journal* 833.1 (2016), p. 3. DOI: 10.3847/0004-637X/833/1/3. arXiv: 1607.08006.

[67] Hans Martin Niederhausen and Yiqian Xu. "High Energy Astrophysical Neutrino Flux Measurement Using Neutrino-induced Cascades Observed in 4 Years of IceCube Data." In: *PoS* ICRC2017 (2018), p. 968. DOI: 10.22323/1.301.0968.

[68] Austin Schneider. "Characterization of the Astrophysical Diffuse Neutrino Flux with IceCube High-Energy Starting Events." In: *36th International Cosmic Ray Conference (ICRC 2019) Madison, Wisconsin, USA, July 24-August 1, 2019.* 2019. arXiv: 1907.11266 [astro-ph.HE].

[69] P. S. Bhupal Dev et al. "Heavy right-handed neutrino dark matter and PeV neutrinos at IceCube." In: *JCAP* 08 (2016), p. 034. DOI: 10.1088/1475-7516/2016/08/034. arXiv: 1606.04517 [hep-ph].

[70] F. Halzen and E. Zas. "Neutrino fluxes from active galaxies: A Model independent estimate." In: *Astrophys. J.* 488 (1997), pp. 669–674. DOI: 10.1086/304741. arXiv: astro-ph/9702193 [astro-ph].

[71] H. Athar, M. Jezabek, and O. Yasuda. "Effects of neutrino mixing on high-energy cosmic neutrino flux." In: *Phys. Rev. D* 62 (2000), p. 103007. DOI: 10.1103/PhysRevD.62.103007. arXiv: hep-ph/0005104.

[72] Ziro Maki, Masami Nakagawa, and Shoichi Sakata. "Remarks on the unified model of elementary particles." In: *Prog. Theor. Phys.* 28 (1962), pp. 870–880. DOI: 10.1143/PTP.28.870.

[73] F. Capozzi et al. "Status of three-neutrino oscillation parameters, circa 2013." In: *Phys. Rev. D* 89 (2014), p. 093018. DOI: 10.1103/PhysRevD.89.093018. arXiv: 1312.2878 [hep-ph].

[74] Juliana Stachurska. "First Double Cascade Tau Neutrino Candidates in IceCube and a New Measurement of the Flavor Composition." In: *HAWC Contributions to the 36th International Cosmic Ray Conference (ICRC2019).* 2019. arXiv: 1908.05506 [astro-ph.HE].

[75] P. Giommi et al. “Dissecting the regions around IceCube high-energy neutrinos: growing evidence for the blazar connection.” In: (Jan. 2020). arXiv: 2001.09355 [astro-ph.HE].

[76] Tessa Carver. “Ten years of All-sky Neutrino Point-Source Searches.” In: *HAWC Contributions to the 36th International Cosmic Ray Conference (ICRC2019).* 2019. arXiv: 1908.05993 [astro-ph.HE].

[77] C. Patrignani et al. “Review of Particle Physics.” In: *Chinese Physics* C40.10 (2016), p. 100001. DOI: 10.1088/1674-1137/40/10/100001.

[78] Luis A. Anchordoqui et al. “Cosmic Neutrino Pevatrons: A Brand New Pathway to Astronomy, Astrophysics, and Particle Physics.” In: *JHEAp* 1-2 (2014), pp. 1–30. DOI: 10.1016/j.jheap.2014.01.001. arXiv: 1312.6587 [astro-ph.HE].

[79] Markus Ahlers and Francis Halzen. “Opening a New Window onto the Universe with IceCube.” In: *Prog. Part. Nucl. Phys.* 102 (2018), pp. 73–88. DOI: 10.1016/j.ppnp.2018.05.001. arXiv: 1805.11112 [astro-ph.HE].

[80] Eli Waxman. “Cosmological origin for cosmic rays above 10**19-eV.” In: *Astrophys. J.* 452 (1995), pp. L1–L4. DOI: 10.1086/309715. arXiv: astro-ph/9508037 [astro-ph].

[81] Eli Waxman and John N. Bahcall. “High-energy neutrinos from astrophysical sources: An Upper bound.” In: *Phys. Rev.* D59 (1999), p. 023002. DOI: 10.1103/PhysRevD.59.023002. arXiv: hep-ph/9807282 [hep-ph].

[82] M. G. Aartsen et al. “The IceCube Realtime Alert System.” In: *Astropart. Phys.* 92 (2017), pp. 30–41. DOI: 10.1016/j.astropartphys.2017.05.002. arXiv: 1612.06028.

[83] A. Dominguez et al. “Extragalactic Background Light Inferred from AEGIS Galaxy SED-type Fractions.” In: *Mon. Not. Roy. Astron. Soc.* 410 (2011), p. 2556. DOI: 10.1111/j.1365-2966.2010.17631.x. arXiv: 1007.1459 [astro-ph.CO].

[84] M. Petropoulou et al. “Photohadronic origin of γ-ray BL Lac emission: implications for IceCube neutrinos.” In: *Monthly Notices of the Royal Astronomical Society* 448.3 (2015), pp. 2412–2429. DOI: 10.1093/mnras/stv179. arXiv: 1501.07115.

[85] K. Abe et al. “Atmospheric neutrino oscillation analysis with external constraints in Super-Kamiokande I-IV.” In: *Phys. Rev. D* 97.7 (2018), p. 072001. DOI: 10.1103/PhysRevD.97.072001. arXiv: 1710.09126 [hep-ex].

[86] Soebur Razzaque, Olga Mena, and Irina Mocioiu. "Determination of Neutrino Mass Hierarchy from the Deep Core Extension of the IceCube data on Atmospheric Neutrinos." In: *APS April Meeting Abstracts*. APS Meeting Abstracts. May 2009, E1.043.

[87] A. Capella et al. "Dual parton model." In: *Phys. Rept.* 236 (1994), pp. 225–329. DOI: 10.1016/0370-1573(94)90064-7.

[88] Anatoli Fedynitch. "Cascade equations and hadronic interactions at very high energies." PhD thesis. KIT, Karlsruhe, Dept. Phys., Nov. 2015. DOI: 10.5445/IR/1000055433.

[89] Richard P. Feynman. "Very high-energy collisions of hadrons." In: *Phys. Rev. Lett.* 23 (1969). [,494(1969)], pp. 1415–1417. DOI: 10.1103/PhysRevLett.23.1415.

[90] Felix Riehn et al. "The hadronic interaction model Sibyll 2.3c and extensive air showers." In: (Dec. 2019). arXiv: 1912.03300 [hep-ph].

[91] Hans Peter Dembinski et al. "Data-driven model of the cosmic-ray flux and mass composition from 10 GeV to 10^{11} GeV." In: *PoS* ICRC2017 (2018). [35,533(2017)], p. 533. DOI: 10.22323/1.301.0533. arXiv: 1711.11432 [astro-ph.HE].

[92] S. Roesler, R. Engel, and J. Ranft. "The Monte Carlo event generator DPMJET-III." In: *Advanced Monte Carlo for radiation physics, particle transport simulation and applications*. 2001, pp. 1033–1038. DOI: 10.1007/978-3-642-18211-2_166. arXiv: hep-ph/0012252.

[93] S. Ostapchenko. "Monte Carlo treatment of hadronic interactions in enhanced Pomeron scheme: I. QGSJET-II model." In: *Physical Review* D83 (2011), p. 014018. DOI: 10.1103/PhysRevD.83.014018. arXiv: 1010.1869.

[94] Felix Riehn et al. "A new version of the event generator Sibyll." In: *PoS* ICRC2015 (2016), p. 558. DOI: 10.22323/1.236.0558. arXiv: 1510.00568 [hep-ph].

[95] Ralph Engel, Dieter Heck, and Tanguy Pierog. "Extensive air showers and hadronic interactions at high energy." In: *Ann. Rev. Nucl. Part. Sci.* 61 (2011), pp. 467–489. DOI: 10.1146/annurev.nucl.012809.104544.

[96] F. Riehn et al. "The hadronic interaction model SIBYLL 2.3c and Feynman scaling." In: *Proceedings of the 35th International Cosmic Ray Conference*. Vol. ICRC2017. Proceedings of Science, 2017, p. 301. arXiv: 1709.07227.

[97] Wolfgang Rauch et al. "The NA49 data acquisition system." In: *IEEE Trans. Nucl. Sci.* 41 (1994), p. 30. DOI: 10.1109/23.281452.

[98] Andras Laszlo et al. "Na61/Shine at the CERN SPS." In: *PoS* CPOD07 (2007), p. 054. DOI: 10.22323/1.047.0054. arXiv: 0709.1867 [nucl-ex].

[99] C. Alt et al. "Inclusive production of charged pions in p+C collisions at 158-GeV/c beam momentum." In: *Eur. Phys. J.* C49 (2007), pp. 897–917. DOI: 10.1140/epjc/s10052-006-0165-7. arXiv: hep-ex/0606028 [hep-ex].

[100] N. Abgrall et al. "Measurements of $\pi^{\pm}$, $K^{\pm}$, K^0_S , Λ and proton production in proton–carbon interactions at 31 GeV/c with the NA61/SHINE spectrometer at the CERN SPS." In: *Eur. Phys. J. C* 76.2 (2016), p. 84. DOI: 10.1140/epjc/s10052-016-3898-y. arXiv: 1510.02703 [hep-ex].

[101] Alexander E. Hervé. "Results from pion-carbon interactions measured by NA61/SHINE for better understanding of extensive air showers." In: *PoS* ICRC2015 (2016), p. 330. DOI: 10.22323/1.236.0330. arXiv: 1509.06586 [nucl-ex].

[102] A. Aduszkiewicz et al. "Measurements of $\pi^{\pm}$, $\mathrm{K}^{\pm}$, p and $\bar{\mathrm{p}}$ spectra in proton-proton interactions at 20, 31, 40, 80 and 158 GeV/c with the NA61/SHINE spectrometer at the CERN SPS." In: *Eur. Phys. J.* C77.10 (2017), p. 671. DOI: 10.1140/epjc/s10052-017-5260-4. arXiv: 1705.02467 [nucl-ex].

[103] G. D. Barr et al. "Uncertainties in Atmospheric Neutrino Fluxes." In: *Phys. Rev.* D74 (2006), p. 094009. DOI: 10.1103/PhysRevD.74.094009. arXiv: astro-ph/0611266 [astro-ph].

[104] Juan-Pablo Yáñez, Anatoli Fedynitch, and Tyler Montgomery. "Calibration of atmospheric neutrino flux calculations using cosmic muon flux and charge ratio measurements." In: *PoS* ICRC2019 (2019), p. 881. arXiv: 1909.08365 [astro-ph.HE].

[105] David Griffiths. *Introduction to elementary particles*. 2008. ISBN: 978-3-527-40601-2.

[106] Anatoli Fedynitch. *MCEq - Matrix cascade equations*. Version 1.2. 2015. URL: https://github.com/afedynitch/MCEq/.

[107] Bert G. Petersen. "The cosmic ray induced muon spectrum measured with the L3 detector." PhD thesis. Nijmegen U., 2002.

[108] M Motoki et al. "Precise measurements of atmospheric muon fluxes with the BESS spectrometer." In: *Astropart. Phys.* 19 (2003), pp. 113–126. DOI: 10.1016/S0927-6505(02)00195-0. arXiv: astro-ph/0205344.

[109] O. C. Allkofer et al. "Muon spectra from DEIS up to 7 TeV." In: *International Cosmic Ray Conference*. Vol. 10. International Cosmic Ray Conference. Jan. 1981, pp. 321–324.

[110] T. Kitamura et al. "Measurement of Muon Spectrum by Mutron." In: *14th International Cosmic Ray Conference*. Jan. 1975, pp. 2031–2036.

[111] P. Adamson et al. "Measurement of the atmospheric muon charge ratio at TeV energies with MINOS." In: *Phys. Rev. D* 76 (2007), p. 052003. DOI: 10.1103/PhysRevD.76.052003. arXiv: 0705.3815 [hep-ex].

[112] M. Aldaya and Pablo Garcia-Abia. "Measurement of the Charge Ratio of Cosmic Muons using CMS Data." In: (Oct. 2008). arXiv: 0810.3515 [hep-ex].

[113] E. Richard et al. "Measurements of the atmospheric neutrino flux by Super-Kamiokande: energy spectra, geomagnetic effects, and solar modulation." In: *Phys. Rev. D* 94.5 (2016), p. 052001. DOI: 10.1103/PhysRevD.94.052001. arXiv: 1510.08127 [hep-ex].

[114] M.G. Aartsen et al. "Development of a General Analysis and Unfolding Scheme and its Application to Measure the Energy Spectrum of Atmospheric Neutrinos with IceCube." In: *Eur. Phys. J. C* 75.3 (2015), p. 116. DOI: 10.1140/epjc/s10052-015-3330-z. arXiv: 1409.4535 [astro-ph.HE].

[115] Patrick Heix et al. "Seasonal Variation of Atmospheric Neutrinos in IceCube." In: *PoS* ICRC2019 (2020), p. 465. DOI: 10.22323/1.358.0465. arXiv: 1909.02036 [astro-ph.HE].

[116] S. Adrian-Martinez et al. "Measurement of the atmospheric ν_μ energy spectrum from 100 GeV to 200 TeV with the ANTARES telescope." In: *Eur. Phys. J. C* 73.10 (2013), p. 2606. DOI: 10.1140/epjc/s10052-013-2606-4. arXiv: 1308.1599 [astro-ph.HE].

[117] M. Honda et al. "Atmospheric neutrino flux calculation using the NRLMSISE-00 atmospheric model." In: *Phys. Rev. D* 92.2 (2015), p. 023004. DOI: 10.1103/PhysRevD.92.023004. arXiv: 1502.03916 [astro-ph.HE].

[118] J. A. Formaggio and G. P. Zeller. "From eV to EeV: Neutrino Cross Sections Across Energy Scales." In: *Reviews of Modern Physics* 84 (2012), pp. 1307–1341. DOI: 10.1103/RevModPhys.84.1307. arXiv: 1305.7513.

[119] S. L. Glashow. "Resonant Scattering of Antineutrinos." In: *Physical Review* 118 (1960), pp. 316–317. DOI: 10.1103/PhysRev.118.316.

[120] R. Gandhi et al. "Ultrahigh-energy neutrino interactions." In: *Astroparticle Physics* 5 (1996), pp. 81–110. DOI: 10.1016/0927-6505(96)00008-4. arXiv: hep-ph/9512364.

[121] I. M. Frank and I. E. Tamm. "Coherent visible radiation of fast electrons passing through matter." In: *Comptes Rendus Acad. Sci. URSS* 14.3 (1937), pp. 109–114. DOI: 10.1007/978-3-642-74626-0_2.

[122] T. K. Gaisser. "Neutrino astronomy: Physics goals, detector parameters." In: 1997. arXiv: astro-ph/9707283 [astro-ph].

[123] M. Ackermann et al. "Optical properties of deep glacial ice at the South Pole." In: *Journal of Geophysical Research: Atmospheres* 111.D13 (2006), p. D13203. DOI: 10.1029/2005JD006687.

[124] Shujiro Mitani, Keiji Sakai, and Kenshiro Takagi. "Dependence of Transport Mean Free Path on Size of Scatterer." In: *Japanese Journal of Applied Physics* 39.Part 1, No. 1 (Jan. 2000), pp. 146–149. DOI: 10.1143/jjap.39.146. URL: https://doi.org/10.1143%2Fjjap.39.146.

[125] M. G. Aartsen et al. "Measurement of South Pole ice transparency with the IceCube LED calibration system." In: *Nuclear Instruments and Methods in Physics Research* A711 (2013), pp. 73–89. DOI: 10.1016/j.nima.2013.01.054. arXiv: 1301.5361.

[126] M. G. Aartsen et al. "Energy Reconstruction Methods in the IceCube Neutrino Telescope." In: *Journal of Instrumentation* 9 (2014), P03009. DOI: 10.1088/1748-0221/9/03/P03009. arXiv: 1311.4767.

[127] Leif Radel and Christopher Wiebusch. "Calculation of the Cherenkov light yield from electromagnetic cascades in ice with Geant4." In: *Astropart. Phys.* 44 (2013), pp. 102–113. DOI: 10.1016/j.astropartphys.2013.01.015. arXiv: 1210.5140 [astro-ph.IM].

[128] Donald E. Groom, Nikolai V. Mokhov, and Sergei I. Striganov. "Muon stopping power and range tables 10-MeV to 100-TeV." In: *Atom. Data Nucl. Data Tabl.* 78 (2001), pp. 183–356. DOI: 10.1006/adnd.2001.0861.

[129] Dmitry Chirkin and Wolfgang Rhode. "Muon Monte Carlo: A High-precision tool for muon propagation through matter." In: (2004). arXiv: hep-ph/0407075 [hep-ph].

[130] R. Abbasi et al. "An improved method for measuring muon energy using the truncated mean of dE/dx." In: *Nucl. Instrum. Meth.* A703 (2013), pp. 190–198. DOI: 10.1016/j.nima.2012.11.081. arXiv: 1208.3430.

[131] M. G. Aartsen et al. "Search for Time-independent Neutrino Emission from Astrophysical Sources with 3 yr of IceCube Data." In: *Astrophys. J.* 779 (2013), p. 132. DOI: 10.1088/0004-637X/779/2/132. arXiv: 1307.6669 [astro-ph.HE].

[132] A. Achterberg et al. "First Year Performance of The IceCube Neutrino Telescope." In: *Astroparticle Physics* 26 (2006), pp. 155–173. DOI: 10.1016/j.astropartphys.2006.06.007. arXiv: astro-ph/0604450.

[133] V. Aynutdinov. "The prototype string for the km3-scale Baikal neutrino telescope." In: *Nucl. Instrum. Meth.* A602 (2009), pp. 227–234. DOI: 10.1016/j.nima.2008.12.149. arXiv: 0811.1110 [astro-ph].

[134] Immacolata Carmen Rea et al. "STRAW-Strings for Absorption Length in Water Pathfinder for a Potential New Neutrino Telescope Site in the Pacific Ocean." In: *JPS Conf. Proc.* 27 (2019), p. 011016. DOI: 10.7566/JPSCP.27.011016.

[135] K. Antipin et al. "The Baikal Neutrino Telescope: Status and plans." In: *Proceedings, 30th International Cosmic Ray Conference (ICRC 2007): Merida, Yucatan, Mexico, July 3-11, 2007.* Vol. 3. 2007, pp. 1261–1264. arXiv: 0710.3063 [astro-ph]. URL: http://indico.nucleares.unam.mx/contributionDisplay.py?contribId=1084&confId=4.

[136] M. G. Aartsen et al. "The IceCube Neutrino Observatory: Instrumentation and Online Systems." In: *Journal of Instrumentation* 12.03 (2017), P03012. DOI: 10.1088/1748-0221/12/03/P03012. arXiv: 1612.05093.

[137] R. Abbasi et al. "IceTop: The surface component of IceCube." In: *Nuclear Instruments and Methods in Physics Research* A700 (2013), pp. 188–220. DOI: 10.1016/j.nima.2012.10.067. arXiv: 1207.6326.

[138] The IceCube Collaboration. *IceCube Detector Array.* Jan. 2020. URL: https://gallery.icecube.wisc.edu/internal/v/GraphicRe/visuals/detetor/arraygraphics2011/ArrayWSeasonsLabels.jpg.html.

[139] R. Abbasi et al. "Calibration and Characterization of the IceCube Photomultiplier Tube." In: *Nuclear Instruments and Methods in Physics Research* A618 (2010), pp. 139–152. DOI: 10.1016/j.nima.2010.03.102. arXiv: 1002.2442.

[140] The IceCube Collaboration. *IceCube Digital Optical Module.* Jan. 2018. URL: https://gallery.icecube.wisc.edu/internal/v/graphics/dom/DOMNoHarnessWhiteback_lg.jpg.html?g2_imageViewsIndex=2.

[141] R. Abbasi et al. “The Design and Performance of IceCube DeepCore.” In: *Astroparticle Physics* 35 (2012), pp. 615–624. DOI: 10.1016/j.astropartphys.2012.01.004. arXiv: 1109.6096.

[142] Dmitry Chirkin. “Evidence of optical anisotropy of the South Pole ice.” In: *Proceedings, 33rd International Cosmic Ray Conference (ICRC2013): Rio de Janeiro, Brazil, July 2-9, 2013*, p. 0580. URL: http://www.cbpf.br/%7Eicrc2013/papers/icrc2013-0580.pdf.

[143] M. G. Aartsen et al. “Observation of the cosmic-ray shadow of the Moon with IceCube.” In: *Phys. Rev.* D89.10 (2014), p. 102004. DOI: 10.1103/PhysRevD.89.102004. arXiv: 1305.6811.

[144] J. Lundberg et al. “Light tracking for glaciers and oceans: Scattering and absorption in heterogeneous media with Photonics.” In: *Nuclear Instruments and Methods in Physics Research* A581 (2007), pp. 619–631. DOI: 10.1016/j.nima.2007.07.143. arXiv: astro-ph/0702108.

[145] A. Avrorin et al. “The gigaton volume detector in Lake Baikal.” In: *Nucl. Instrum. Meth. A* 639 (2011). Ed. by R. Forty et al., pp. 30–32. DOI: 10.1016/j.nima.2010.09.137.

[146] J. A. Aguilar et al. “Transmission of light in deep sea water at the site of the ANTARES Neutrino Telescope.” In: *Astropart. Phys.* 23 (2005), pp. 131–155. DOI: 10.1016/j.astropartphys.2004.11.006. arXiv: astro-ph/0412126 [astro-ph].

[147] G. Riccobene and A. Capone. “Deep seawater inherent optical properties in the Southern Ionian Sea.” In: *Astropart. Phys.* 27 (2007), pp. 1–9. DOI: 10.1016/j.astropartphys.2006.08.006. arXiv: astro-ph/0603701 [astro-ph].

[148] J. Ahrens et al. “Muon track reconstruction and data selection techniques in AMANDA.” In: *Nuclear Instruments and Methods in Physics Research* A524 (2004), pp. 169–194. DOI: 10.1016/j.nima.2004.01.065. arXiv: astro-ph/0407044.

[149] J. G. Learned and K. Mannheim. “High-energy neutrino astrophysics.” In: *Ann. Rev. Nucl. Part. Sci.* 50 (2000), pp. 679–749. DOI: 10.1146/annurev.nucl.50.1.679.

[150] N. van Eijndhoven, O. Fadiran, and G. Japaridze. “Implementation of a Gauss convoluted Pandel PDF for track reconstruction in Neutrino Telescopes.” In: *Astroparticle Physics* 28 (2007), pp. 456–462. DOI: 10.1016/j.astropartphys.2007.09.001. arXiv: 0704.1706.

[151] N. Whitehorn, J. van Santen, and S. Lafebre. "Penalized Splines for Smooth Representation of High-dimensional Monte Carlo Datasets." In: *Computer Physics Communications* 184 (2013), pp. 2214–2220. DOI: 10.1016/j.cpc.2013.04.008. arXiv: 1301.2184.

[152] S. S. Wilks. "The Large-Sample Distribution of the Likelihood Ratio for Testing Composite Hypotheses." In: *Annals Math. Statist.* 9.1 (1938), pp. 60–62. DOI: 10.1214/aoms/1177732360.

[153] T. Neunhoffer. *Die Entwicklung eines neuen Verfahrens zur Suche nach kosmischen Neutrino-Punktquellen mit dem AMANDA-Neutrinoteleskop*. May 2004.

[154] T. Neunhoffer. "Estimating the angular resolution of tracks in neutrino telescopes based on a likelihood analysis." In: *Astroparticle Physics* 25 (2006), pp. 220–225. DOI: 10.1016/j.astropartphys.2006.01.002. arXiv: astro-ph/0403367.

[155] Eric Per Vogel. "Noboloid - An improved likelihood estimation for angular uncertainties of muon tracks in IceCube." Masterthesis. RWTH Aachen, 2017. URL: https://www.institut3b.physik.rwth-aachen.de/global/show_document.asp?id=aaaaaaaaaawhudl.

[156] L. Rädel. "Measurement of High-Energy Muon Neutrinos with the IceCube Neutrino Observatory." Dissertation. RWTH Aachen University, 2017. DOI: 10.18154/RWTH-2017-10054.

[157] René Reimann. "Search for the sources of the astrophysical high-energy muon-neutrino flux with the IceCube neutrino observatory." PhD thesis. RWTH Aachen U., 2019. DOI: 10.18154/RWTH-2019-11012.

[158] S. Coenders. "High-energy cosmic ray accelerators: searches with IceCube neutrinos." Dissertation. Technische Universität München, 2016. URL: https://mediatum.ub.tum.de/1327578.

[159] Stefan Schonert et al. "Vetoing atmospheric neutrinos in a high energy neutrino telescope." In: *Phys. Rev. D* 79 (2009), p. 043009. DOI: 10.1103/PhysRevD.79.043009. arXiv: 0812.4308 [astro-ph].

[160] T. K. Gaisser et al. "Generalized self-veto probability for atmospheric neutrinos." In: *Physical Review* D90.2 (2014), p. 023009. DOI: 10.1103/PhysRevD.90.023009. arXiv: 1405.0525.

[161] Elisa Resconi et al. "The neutrino filter: connecting blazars with ultra high energy cosmic rays and astrophysical neutrinos." In: *PoS* ICRC2017 (2018), p. 1016. DOI: 10.22323/1.301.1016.

[162] Marcel Zoll. "A search for solar dark matter with the IceCube neutrino detector : Advances in data treatment and analysis technique." In: 2016.

[163] F. Pedregosa et al. "Scikit-learn: Machine Learning in Python." In: *Journal of Machine Learning Research* 12 (2011), pp. 2825–2830.

[164] P. Padovani and E. Resconi. "Are both BL Lacs and pulsar wind nebulae the astrophysical counterparts of IceCube neutrino events?" In: *Mon. Not. Roy. Astron. Soc.* 443.1 (2014), pp. 474–484. DOI: 10.1093/mnras/stu1166. arXiv: 1406.0376 [astro-ph.HE].

[165] M. Ajello et al. "3FHL: The Third Catalog of Hard Fermi-LAT Sources." In: *Astrophys. J. Suppl.* 232.2 (2017), p. 18. DOI: 10.3847/1538-4365/aa8221. arXiv: 1702.00664 [astro-ph.HE].

[166] S. R. Kelner and F. A. Aharonian. "Energy spectra of gamma rays, electrons, and neutrinos produced at interactions of relativistic protons with low energy radiation." In: *Phys. Rev. D* 78 (3 Aug. 2008), p. 034013. DOI: 10.1103/PhysRevD.78.034013. URL: https://link.aps.org/doi/10.1103/PhysRevD.78.034013.

[167] P. Padovani et al. "Extreme blazars as counterparts of IceCube astrophysical neutrinos." In: *Mon. Not. Roy. Astron. Soc.* 457.4 (2016), pp. 3582–3592. DOI: 10.1093/mnras/stw228. arXiv: 1601.06550 [astro-ph.HE].

[168] W. B. Atwood et al. "The Large Area Telescope on the Fermi Gamma-ray Space Telescope Mission." In: *The Astrophysical Journal* 697 (2009), pp. 1071–1102. DOI: 10.1088/0004-637X/697/2/1071. arXiv: 0902.1089.

[169] M. G. Aartsen et al. "The contribution of Fermi-2LAC blazars to the diffuse TeV-PeV neutrino flux." In: *Astrophys. J.* 835.1 (2017), p. 45. DOI: 10.3847/1538-4357/835/1/45. arXiv: 1611.03874 [astro-ph.HE].

[170] "The Second Catalog of Active Galactic Nuclei Detected by the Fermi Large Area Telescope." In: *Astrophys. J.* 743 (2011), p. 171. DOI: 10.1088/0004-637X/743/2/171. arXiv: 1108.1420 [astro-ph.HE].

[171] M. G. Aartsen et al. "A combined maximum-likelihood analysis of the high-energy astrophysical neutrino flux measured with IceCube." In: *The Astrophysical Journal* 809.1 (2015), p. 98. DOI: 10.1088/0004-637X/809/1/98. arXiv: 1507.03991.

[172] M. Ackermann et al. "2FHL: The Second Catalog of Hard Fermi-LAT Sources." In: *Astrophys. J. Suppl.* 222.1 (2016), p. 5. DOI: 10.3847/0067-0049/222/1/5. arXiv: 1508.04449 [astro-ph.HE].

[173] Elisa Resconi et al. "Connecting blazars with ultrahigh-energy cosmic rays and astrophysical neutrinos." In: *Mon. Not. Roy. Astron. Soc.* 468.1 (2017), pp. 597–606. DOI: 10.1093/mnras/stx498. arXiv: 1611.06022 [astro-ph.HE].

[174] Matthias Huber and Kai Krings. "Results of IceCube searches for neutrinos from blazars using seven years of through-going muon data." In: *PoS* ICRC2017 (2018), p. 994. DOI: 10.22323/1.301.0994.

[175] Armen Atoyan and Charles D. Dermer. "High-energy neutrinos from photomeson processes in blazars." In: *Phys. Rev. Lett.* 87 (2001), p. 221102. DOI: 10.1103/PhysRevLett.87.221102. arXiv: astro-ph/0108053 [astro-ph].

[176] Kohta Murase, Yoshiyuki Inoue, and Charles D. Dermer. "Diffuse Neutrino Intensity from the Inner Jets of Active Galactic Nuclei: Impacts of External Photon Fields and the Blazar Sequence." In: *Phys. Rev.* D90.2 (2014), p. 023007. DOI: 10.1103/PhysRevD.90.023007. arXiv: 1403.4089 [astro-ph.HE].

[177] A. Muecke et al. "BL Lac Objects in the synchrotron proton blazar model." In: *Astropart. Phys.* 18 (2003), pp. 593–613. DOI: 10.1016/S0927-6505(02)00185-8. arXiv: astro-ph/0206164 [astro-ph].

[178] M. G. Aartsen et al. "All-sky Search for Time-integrated Neutrino Emission from Astrophysical Sources with 7 yr of IceCube Data." In: *The Astrophysical Journal* 835.2 (2017), p. 151. DOI: 10.3847/1538-4357/835/2/151. arXiv: 1609.04981.

[179] Matthias Huber. "Searches for steady neutrino emission from 3FHL blazars using eight years of IceCube data from theNorthern hemisphere." In: *PoS* ICRC2019 (2020), p. 916. DOI: 10.22323/1.358.0916. arXiv: 1908.08458 [astro-ph.HE].

[180] M. G. Aartsen et al. "Search for steady point-like sources in the astrophysical muon neutrino flux with 8 years of IceCube data." In: *Eur. Phys. J.* C79.3 (2019), p. 234. DOI: 10.1140/epjc/s10052-019-6680-0. arXiv: 1811.07979 [hep-ph].

[181] Markus Ahlers and Francis Halzen. "High-energy cosmic neutrino puzzle: a review." In: *Rept. Prog. Phys.* 78.12 (2015), p. 126901. DOI: 10.1088/0034-4885/78/12/126901.

[182] The IceCube Collaboration. *IceCube Gallery*. Jan. 2018. URL: https://gallery.icecube.wisc.edu/.

[183] J. Ahrens et al. "Observation of high-energy atmospheric neutrinos with the Antarctic Muon and Neutrino Detector Array." In: *Phys. Rev. D* 66 (2002), p. 012005. DOI: 10.1103/PhysRevD.66.012005. arXiv: astro-ph/0205109.

[184] M. G. Aartsen et al. “IceCube-Gen2: A Vision for the Future of Neutrino Astronomy in Antarctica.” In: *Proceedings, Frontier Research in Astrophysics - II*. Vol. FRAPWS2016. Proceedings of Science, 2017, p. 004. arXiv: 1412.5106.

[185] M. Agostini et al. “The Pacific Ocean Neutrino Experiment.” In: (May 2020). arXiv: 2005.09493 [astro-ph.HE].

[186] S. C. Pearce. “Introduction to Fisher (1925) Statistical Methods for Research Workers.” In: *Breakthroughs in Statistics: Methodology and Distribution*. Ed. by Samuel Kotz and Norman L. Johnson. New York, NY: Springer New York, 1992, pp. 59–65. ISBN: 978-1-4612-4380-9. DOI: 10.1007/978-1-4612-4380-9_5. URL: https://doi.org/10.1007/978-1-4612-4380-9_5.

[187] S. Abdollahi et al. “Fermi Large Area Telescope Fourth Source Catalog.” In: *Astrophys. J. Suppl.* 247.1 (2020), p. 33. DOI: 10.3847/1538-4365/ab6bcb. arXiv: 1902.10045 [astro-ph.HE].

[188] S. Adrian-Martinez et al. “Letter of intent for KM3NeT 2.0.” In: *J. Phys. G* 43.8 (2016), p. 084001. DOI: 10.1088/0954-3899/43/8/084001. arXiv: 1601.07459 [astro-ph.IM].